

137738

NHTSA - 98-3588  
- 119

**Evaluation of Motor Vehicle Fire Initiation and Propagation  
Part 3: Propagation of an Engine Compartment Fire in a 1996 Passenger  
Van**

Jeffrey Santrock  
General Motors Corporation

**ABSTRACT**

This report describes a vehicle fire propagation test conducted pursuant to an agreement between General Motors and the United States Department of Transportation. The test described in this report was conducted on November 13, 1996. The test vehicle was a crash-tested 1996 Dodge Caravan Sport. An electrical igniter was used to artificially ignite the battery and power distribution center housing. The fire was allowed to burn until flames spread into the passenger compartment and along the headliner toward the rear of the passenger compartment. Flames spread from the engine compartment into the passenger compartment through the windshield. Flames penetrated the dash through the A/C evaporator- and condenser-line pass-through, where the pass-through closures had been dislodged in the crash test. Flames also penetrated the dash through the HVAC air intake, where the recirculation door had been dislodged in the crash test. The rate of flame spread through the openings in the dash was slower than through the windshield. Flames in the passenger compartment were extinguished approximately 11 minutes after flames were first noted above the igniter.

01 AUG 30 PM 2:06Z '98

DEPT OF TRANSPORTATION

## Table of Contents

Section 1	Introduction and Test Summary	page 1
Section 2	Vehicle Condition and Test Protocol	page 5
Section 3	Ignition	page 10
Section 4	Flame-spread in the Engine Compartment	page 20
Section 5	Flame-spread into the Passenger Compartment through the Windshield	page 31
Section 5.1	Ignition of the Windshield Inner-Layer	page 34
Section 5.2	Flame-spread into the Passenger Compartment	page 37
Section 5.3	Flame-spread Downward into the Instrument Panel	page 43
Section 5.4	Flame-spread to the Front Seats	page 48
Section 6	Flame-spread into the Passenger Compartment through the Dash Panel	page 50
Section 6.1	Development of a Pressure Gradient Across the Dash Panel	page 53
Section 6.2	The Heater Pass-Through	page 55
Section 6.3	The A/C Pass-Through	page 60
Section 6.4	The HVAC Air Intake	page 64
Section 7	Combustion Conditions	page 70
Section 8	Estimation of Skin Temperature Profiles from Measured Heat Flux Data, Fractional Equivalent Dose Parameters from Measured Gas Concentration Data, and Thermal Damage to the Respiratory Tract from Measured Air Temperature Data	page 78
Section 8.1	The BURNSIM Model	page 78
Section 8.1.1	Estimation of Skin Temperature Profiles using BURNSIM	page 79
Section 8.2	The FAA Combined Hazard Survival Model and Purser's Model of Combustion Gas Toxicity	page 83
Section 8.2.1	Estimation of Fractional Equivalent Dose Parameters	page 88
Section 8.3	Estimation of Burn-Injury to the Respiratory Tract	page 93
	Acknowledgements	page 96
	References	page 97
Appendix A	Video Camera Set-Up	

- Appendix B Infrared Thermography**
- Appendix C Thermocouple Data**
- Appendix D Aspirated Thermocouple Data**
- Appendix E Heat Flux Transducer/Radiometer Data**
- Appendix F Pressure and Flow Data**
- Appendix G Directional Flame Thermometer Measurements, Time-compensated Aspirated Thermocouple Measurements, and Estimated Heat Fluxes**
- Appendix H Fire Products Collector Data**
- Appendix I Passenger Compartment Combustion Gas Data  
Fourier Transform Infrared Spectroscopy**
- Appendix J Passenger Compartment Combustion Gas Data  
Gas Chromatography/Mass Spectroscopy**

## List of Figures

Figure 1	Photograph of the test vehicle used in Fire Test F961115 after the impact in Crash Test C11167.	page 2
Figure 2	Photograph of the left side of the engine compartment of the test vehicle after Crash Test C11167.	page 3
Figure 3	Photograph of the test vehicle positioned in the fluid containment pan at the test facility before the fire test.	page 6
Figure 4	Photograph of igniter used in Fire Test F961115.	page 7
Figure 5	Photograph of the igniter inserted between the battery and power distribution center before the start of the test.	page 8
Figure 6	Video still from Camera 1 at 540 seconds after the start of the test.	page 10
Figure 7	Plots of temperatures recorded by thermocouples located around the battery and PDC for the first 11 minutes of the test.	page 11
Figure 8	Video still from Camera 5 and infrared thermogram from IR2 at 200 seconds before ignition	page 12
Figure 9	Video still from Camera 5 (upper panel) and infrared thermogram from IR 2 (lower panel) at ignition (602 seconds after the start of the test).	page 13
Figure 10	Video still from Camera 1 (upper panel) and infrared thermogram from IR 1 (lower panel) at 17 seconds before ignition (585 seconds after the start of the test).	page 15
Figure 11	Video still from Camera 1 (upper panel) and infrared thermogram from IR 1 (lower panel) at the time of ignition (602 seconds after the start of the test).	page 16
Figure 12	Video still from Camera 1 (upper panel) and infrared thermogram from IR 1 (lower panel) at 5 seconds post-ignition (607 seconds after the start of the test).	page 17
Figure 13	Video still from Camera 1 (upper panel) and infrared thermogram from IR 1 (lower panel) at 10 seconds post-ignition (612 seconds after the start of the test).	page 18
Figure 14	Video still from Camera 1 (upper panel) and infrared thermogram from IR 1 (lower panel) at 15 seconds post-ignition (617 seconds after the start of the test).	page 19
Figure 15	Video still from Camera 7 at 15 seconds post-ignition.	page 20

Figure 16	Video still from Camera 7 at 60 seconds post-ignition.	page 22
Figure 17	Video still from Camera 1 at 88 seconds post-ignition.	page 23
Figure 18	Video still from Camera 7 at 90 seconds post-ignition.	page 24
Figure 19	Video still from Camera 7 at 120 seconds post-ignition.	page 25
Figure 20	Video still from Camera 7 at 180 seconds post-ignition.	page 26
Figure 21	Plots of the progress of flame fronts along different paths in the engine compartment.	page 27
Figure 22	Video still from Camera 7 at 5 minutes post-ignition.	page 28
Figure 23	Video still from Camera 1 at 5 minutes post-ignition.	page 29
Figure 24	Video still from Camera 1 at 7½ minutes post-ignition.	page 29
Figure 25	Plots of temperatures recorded from Thermocouples F1, F2, F3, and F4.	page 31
Figure 26	Video still from Camera 5 at 4 minutes post-ignition.	page 32
Figure 27	Plot of the vertical flame contact with the windshield versus time post-ignition as determined from the view of Camera 5.	page 33
Figure 28	Infrared thermogram from IR4 at 110 seconds post-ignition.	page 35
Figure 29	Infrared thermogram from IR4 at 196 seconds post-ignition.	page 35
Figure 30	Infrared thermogram from IR4 at 224 seconds post-ignition.	page 36
Figure 31	Infrared thermogram from IR4 at 316 seconds post-ignition.	page 36
Figure 32	Video still from Camera 4 at 260 seconds post-ignition.	page 37
Figure 33	Plots of temperatures recorded from Thermocouples D7, D8, D9, and D10.	page 38
Figure 34	Video still from Camera 4 at 316 seconds post-ignition.	page 39
Figure 35	Video still from Camera 4 at 445 seconds post-ignition.	page 40
Figure 36	Plots of air temperature recorded from the aspirated thermocouples.	page 41
Figure 37	Plot of airflow measured using the bi-direction airflow probe.	page 42
Figure 38	Plots of temperatures recorded from Thermocouples D1, D3, D4, D5, D8, and D9.	page 43
Figure 39	Photograph of the instrument panel top cover after this fire test.	page 44
Figure 40	Photograph the front of the instrument panel and front carpet in the	page 45

test vehicle after this fire test.

Figure 41	Photograph showing the lower surfaces of the distribution duct assembly from the test vehicle after this fire test.	page 46
Figure 42	Photographs showing to the top and bottom of the HVAC distribution housing from the test vehicle after this fire test.	page 47
Figure 43	Photograph showing the front seats from the test vehicle after this fire test.	page 48
Figure 44	Photograph showing the front of the test vehicle after this fire test.	page 52
Figure 45	Plots of pressures measured at the dash panel.	page 54
Figure 46	Diagrams showing the locations of thermocouples and a heat flux transducer in the dash panel and the HVAC air intake cowl around the heater feed-through.	page 56
Figure 47	Plots of the data recorded by thermocouples and a heat flux transducer in the dash panel and the HVAC air intake cowl around the heater feed-through.	page 57
Figure 48	Photograph showing the forward exterior surface of the HVAC distribution housing from the test vehicle after this fire test.	page 58
Figure 49	Photographs showing the passenger-compartment-dash-panel silencer pad and dash panel around the heater feed-through after this fire test.	page 59
Figure 50	Diagrams showing the location of thermocouples and a heat flux transducer in the dash panel and HVAC air intake cowl around the A/C feed-through.	page 61
Figure 51	Plots of the data recorded by the thermocouples and heat flux transducer in the dash panel and HVAC air intake cowl around the A/C feed-through.	page 62
Figure 52	Photographs of the interior surface of the dash around the A/C feed-through after this fire test.	page 63
Figure 53	Diagrams showing the locations of thermocouples in the dash panel and HVAC module around the HVAC air intake.	page 65
Figure 54	Plots of the data recorded by the thermocouples B8, B12, B18, C11, C12, and D2.	page 66
Figure 55	Photograph of the HVAC recirculation door from the test vehicle after the test.	page 67

Figure 56	Photographs showing the passenger compartment dash panel silencer pad (upper photograph) and the dash panel (lower photograph) around the HVAC air intake after this fire test.	page 68
Figure 57	Photograph of the HVAC module from the test vehicle after the test	page 69
Figure 58	Plot of $[G_{CO}]/[G_{CO2}]$ versus time post-ignition determined from the carbon dioxide and carbon monoxide release rates measured by the Fire Products Collector.	page 72
Figure 59	Plots of $[C_{CO} \times d_{CO}]/[C_{CO2} \times d_{CO2}]$ and the concentration of carbon monoxide in the passenger compartment.	page 75
Figure 60	Plots of $[C_{HC} \times d_{HC}]/[C_{CO2} \times d_{CO2}]$ and the concentration of total hydrocarbons in the passenger compartment.	page 75
Figure 61	Plots of $[C_{CO2} \times d_{CO2}]/[t_{air} \times Cp]$ and the concentration of carbon dioxide in the passenger compartment.	page 76
Figure 62	Plots of $[C_{CO} \times d_{CO}]/[t_{air} \times Cp]$ and the concentration of carbon monoxide in the passenger compartment.	page 76
Figure 63	Plots of $[C_{HC} \times d_{HC}]/[t_{air} \times Cp]$ and the concentration of hydrocarbons in the passenger compartment.	page 77
Figure 64	Skin temperature profile estimated from heat flux to a forward-facing vertical surface at the drivers head level.	page 80
Figure 65	Skin temperature profile estimated from heat flux to a forward-facing vertical surface at the drivers knee level.	page 80
Figure 66	Skin temperature profile estimated from heat flux to a forward-facing vertical surface at the passenger head level.	page 81
Figure 67	Skin temperature profile estimated from heat flux to a forward-facing vertical surface at the passenger knee level.	page 81
Figure 68	Skin temperature profile estimated from heat flux to a upward-facing horizontal surface at the passenger head level.	page 82
Figure 69	Skin temperature profile estimated from heat flux to a downward-facing horizontal surface at the passenger head level.	page 82
Figure 70	Plots of estimates of $FED(I)_{CO}$ versus time post-ignition computed using the FAA Combined Hazard Survival Model, the Purser model with a respiratory minute volume of 8.5 L/min, and the Purser model with a respiratory minute volume of 25 L/min. A plot of $C_{CO}$ is included for reference.	page 90

- Figure 71 Plots of  $EFD(I)_{HCN}$  versus time post-ignition: FAA Combined Hazard Survival Model and Purser's model. A plot of  $C_{HCN}$  is included for reference. page 90
- Figure 72 Plots of  $FED(I)_{CO_2}$  versus time post-ignition: FAA Combined Hazard Survival Model and Purser's model. A plot of  $C_{CO_2}$  is included for reference. page 91
- Figure 73 Plots of  $FED(I)_{TOTAL}$  versus time post-ignition: FAA Combined Hazard Survival Model; Purser's model with  $RMV = 8.5$  L/min and Purser's model with  $RMV = 25$  L/min. page 91
- Figure 74 Plots of  $FED(L)_{CO}$ ,  $FED(L)_{HCN}$ , and  $FED(L)_{TOTAL}$  versus time post-ignition computed using the FAA Combined Hazard Survival Model. page 93
- Figure 75 Plots of air temperature at 1, 4, 7, 10, 13, and 16 inches below the lower surface of the headlining versus time post-ignition. page 94

**List of Tables**

**Table 1**      **Fire Products for Well-ventilated Fires.**

**page 71**

## **1 Introduction and Test Summary**

The work described in this report was conducted by General Motors (GM) pursuant to an agreement between GM and the United States Department of Transportation. According to this agreement, GM and the National Highway Traffic Safety Administration (NHTSA) jointly developed fifteen separate vehicle fire safety research projects. One of these projects, entitled "Fire Initiation and Propagation Tests", involves conducting 1) vehicle crash tests to investigate potential ignition events that occur in vehicle crashes, and 2) subsequent vehicle fire tests to characterize fire propagation in these crash-tested vehicles. The vehicle models to be tested, and the crash- and fire-test methods to be used for Project B.3 are described in another report [1]. The objectives of the fire tests are:

- To determine the principal fire paths and time-lines for flame propagation into the passenger compartment under the test conditions;
- To identify which components burn and to measure the thermal environments around those components associated with their ignition under the test conditions; and
- To measure air temperatures, heat fluxes, and combustion gas concentrations in the passenger compartment under the test conditions.

These tests were conducted under carefully designed test conditions noted throughout this and other reports. They cannot be relied upon to predict the specific nature and characteristics of actual post-collision fires in the field.

The test described in this report was conducted on November 13, 1996. The vehicle was a 1996 Dodge Caravan Sport (VIN: 1B4GP45R1TB376396) with the following options: 3.3 liter V-6 engine, air conditioning, four speed automatic transmission, a driver's side rear sliding door, and the SE sport package. This vehicle was crash tested on June 26, 1996 [2]. In the crash test, this vehicle was stationary and was struck in the left front (driver's side) by a moving barrier. The moving barrier had a deformable aluminum honeycomb face as described in FMVSS214 [3]. The test vehicle was parked with the brakes on and positioned at a  $25 \pm 2^\circ$  angle relative to the velocity vector of the moving barrier. The barrier face struck the front left corner of the test vehicle. The mass of the vehicle was 1981 kg (4,367 lbs.). The mass of the barrier was 1638 kg (3611 lbs.). The barrier speed was 105.7 km/h (65.6 mph). The change in velocity of the test vehicle was 53 km/h (32.9 mph) in the direction of the barrier's initial longitudinal axis. The maximum velocity change occurred in the first 110 msec after impact [2].

Figure 1 is a photograph of the test vehicle after the impact in Crash Test C11167. The glass in the outer-layers of the windshield was cracked, but the broken glass remained attached to the

inner-layer, which kept the windshield in place after the crash. The front left door was buckled, but remained latched. The window in the left front door was shattered. The residual crush on the left side of the vehicle was approximately 585 mm. The powertrain was displaced rearward 131 mm into the center of the dash panel.

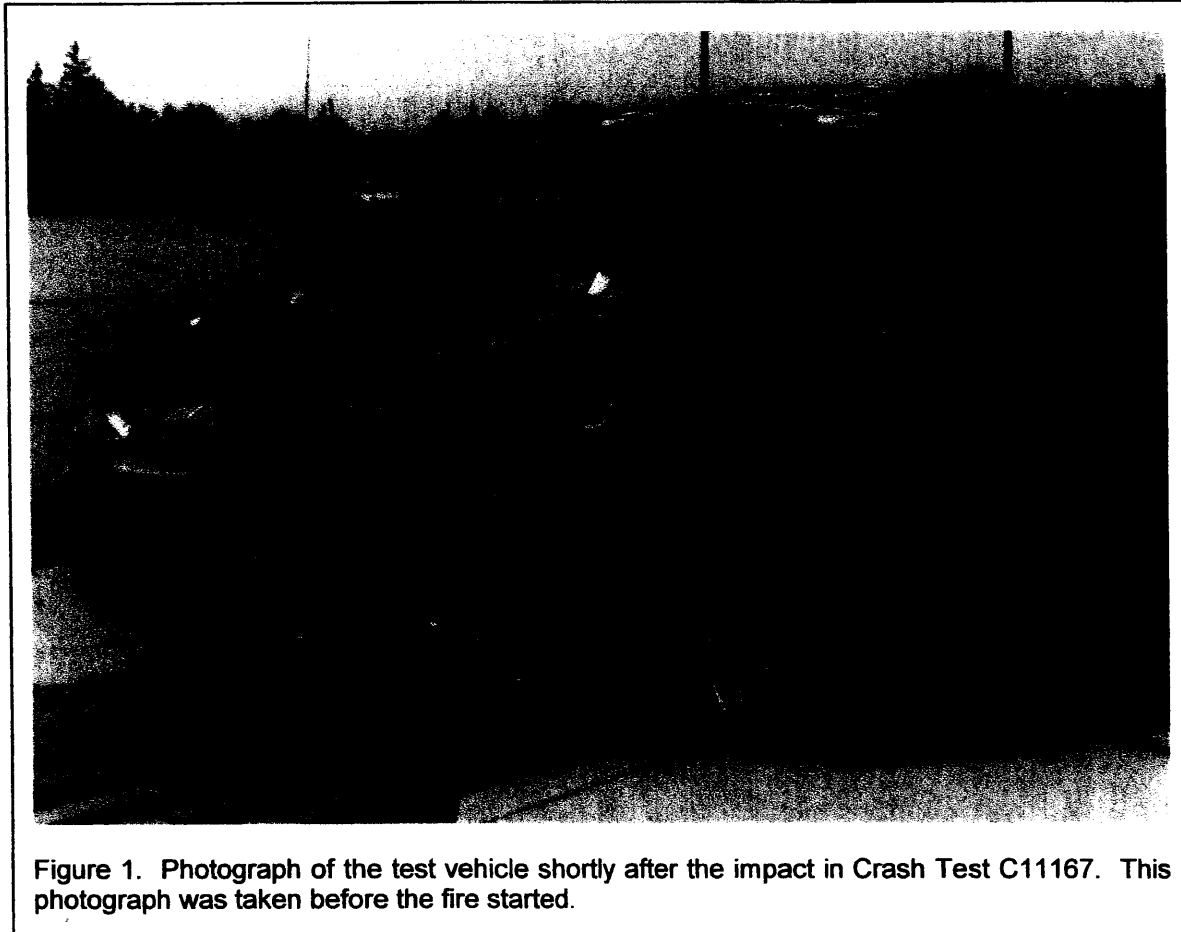


Figure 1. Photograph of the test vehicle shortly after the impact in Crash Test C11167. This photograph was taken before the fire started.

Instrumented Hybrid III Anthropomorphic Test Devices (crash-test dummies) were located in the two front outboard seating positions. An analysis of the recorded data indicated that all head, neck, and chest measurements for both dummies were below their respective Injury Assessment Reference Values (IARV). The left femur compression, right upper tibia moment, right lower tibia moment, and left lower tibia moment in the dummy in the driver's seat were above their respective IARV values. The left lower tibia moment in the dummy in the front passenger's seat was above its IARV [2].<sup>1</sup>

<sup>1</sup> Instrumented crash-test dummies may be used in vehicle crash tests to assess the probability of sustaining specific types of trauma-injuries under similar crash conditions. In general, measurements below the IARV indicate a smaller probability of injury, while measurements above the IARV indicate a greater probability of injury.

Approximately 5 minutes after the impact, a fire started in the area of the battery and the power distribution center (PDC). The fire was allowed to burn for approximately five minutes, then extinguished with a hand-held fire extinguisher. Figure 2 is a photograph of the left side of the engine compartment showing the battery top and PDC melted and charred by the fire. The cause of the fire was determined to have been a series of shorts in the vehicle electrical system. The environmental housing around the battery, the battery case, the battery tray, the PDC, and left headlamp assembly ignited. A detailed analysis of the crash test, including a determination of the cause of the fire, appears in another report [2].

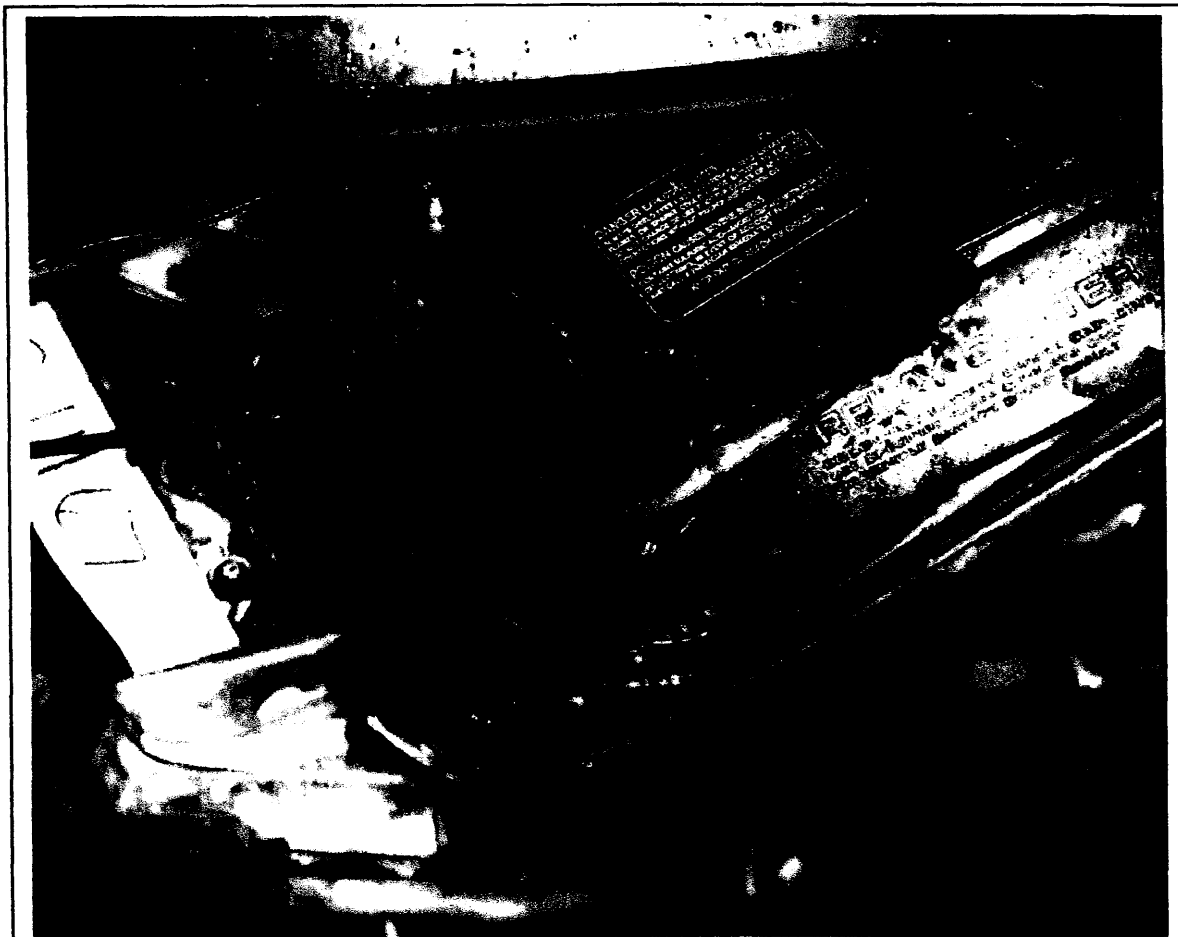


Figure 2. Photograph of the left side of the engine compartment after the fire had been extinguished. The burned battery and power distribution center are in the center of this photograph.

The results of a limited number of crash tests cannot be extrapolated reliably to real-world fire events. Since a fire did occur during this crash test, this vehicle was selected as one of the test vehicles for a fire propagation test. For the fire test, the fire was started artificially using an

electrical igniter placed between the battery and power distribution center (PDC). Heat from the igniter caused plastic in the igniter and in the components contacting the igniter to thermally degrade, producing a plume of gray smoke that rose from the left side of the engine compartment for approximately 10 minutes before the gaseous thermal degradation products ignited spontaneously. Flames were first detected in the area above the battery and PDC. The hood liner<sup>2</sup> ignited shortly after the battery and PDC. Flames spread to the right side of the engine compartment along the hood liner and the heating, ventilation, and air conditioning (HVAC) air intake cowl. Burning thermoplastic melt flowing into the left head lamp assembly eventually ignited the bumper fascia and other combustible components in the front of the engine compartment. More detailed descriptions of ignition and flame spread in the engine compartment are provided in **SECTIONS 3.1** and **3.2**, respectively.

A small fire plume emerged from the rear edge of the hood approximately 15 seconds after ignition. As more combustible material in the engine compartment ignited, the fire plume grew in height. Increasing pressure in the engine compartment created by the growing fire also increased the velocity of gas flow from the engine compartment, pushing the fire plume rearward against the windshield. The polymer film in the windshield started to burn about 4 minutes after ignition. Pieces of flaming windshield fell into the passenger compartment, igniting the top of the instrument panel, the carpet in front of the passenger seat, the deployed passenger airbag, and the inboard armrest of the front passenger seat. Hot gases produced by the burning objects in the passenger compartment accumulated below the roof, causing the front of the headliner and upper sections of the A-pillar trim to ignite between 10 and 11 minutes after flames were first observed in the engine compartment. Flames spread along the headliner toward the rear of the vehicle, with the interior of the vehicle approaching the flashover stage when the fire was extinguished starting at 11 minutes after ignition. A more detailed description of flame-spread into the passenger compartment through the windshield is given in **SECTION 3.3**.

Physical inspection of the test vehicle after the test and analysis of the test data indicated that flames also spread into the instrument panel through two of the openings in the dash panel. These included the pass-through for the refrigerant lines and the air intake for HVAC system. The pass-through closures in both of these openings were dislodged during the crash test. Flame-spread through the openings in the dash was slower than flame-spread through the windshield, and appeared to have been driven by a pressure gradient across the dash panel that developed as the fire in the engine compartment grew. A more detailed description of flame-spread into the passenger compartment through the dash panel is given in **SECTION 3.4**.

---

<sup>2</sup> The hood was removed from the test vehicle for the crash test. The hood was dynamically crushed in a drop-tower apparatus. The artificially crushed hood was reinstalled on the test vehicle before this fire test.

The fire test described in this report was conducted at the Factory Mutual Test Center in West Gloucester, Rhode Island. The crash-tested vehicle was prepared at the General Motors Technical Center in Warren, Michigan, and shipped to the Factory Mutual Test Center for the test. The test vehicle was returned to the GM Technical Center after the fire test, where it was systematically disassembled to permit closer inspection of the fire damage and identification of fire spread paths that were not obvious during the tests.

A detailed record of this test was obtained by video cameras located both inside and outside the test vehicle (**APPENDIX A**). Thermal radiation signatures from the burning vehicle were measured using infrared imaging systems (IR cameras), also located inside and outside the test vehicle (**APPENDIX B**). Flame spread in areas not visible to the video or infrared cameras, such as in the instrument panel, was tracked by thermocouples and heat flux transducers installed in the test vehicle before the fire test (**APPENDICES C and E**). The air temperature in the passenger compartment was measured using an aspirated thermocouple probe assembly containing six shielded thermocouples (**APPENDIX D**). Pressure measurements were made to determine the pressure gradient across the dash panel and airflow through the driver's side window during this test (**APPENDIX F**). Heat transfer to six locations in the passenger compartment was measured using differential flame thermometers (**APPENDIX G**). The heat release rate of the fire was measured using the Fire Products Collector (FPC) at the test facility (**APPENDIX H**). The gaseous combustion products in the passenger compartment were measured by FTIR gas analysis of gas sampled continuously from the passenger compartment during the test (**APPENDIX I**) and by GC/MS analysis of grab-samples acquired from the passenger compartment during the test (**APPENDIX J**).

The test vehicle was placed in a fluid containment pan<sup>2</sup> and centered under the fire products collector at the test facility. Figure 3 is a photograph of the test vehicle in place on the fluid containment pan before the test. All doors in the test vehicle were closed. The driver's side window was broken in the crash test and was not replaced. All other windows were intact and raised to their fully closed positions. No attempt was made to heat the engine or exhaust system. All components in the vehicle were at ambient temperature at the start of the fire test. The hood,

---

<sup>2</sup> The fluid containment pan was a rectangular steel pan (length = 25 ft. (7.6 m) width = 15 ft. (4.6 m), height = 4 in. (0.10 m)) to prevent spilled and leaking automotive fluids from spreading in the test facility. This fluid containment pan was fabricated from two sheets of carbon steel. Angle-braces were welded to the underside of the pan to keep it from flexing under the weight of the vehicle. The bottom of the fluid containment pan was lined with concrete landscaping paving blocks on a level bed of sand. The joints between the paving blocks were filled with sand. The purpose of this treatment was to place the test vehicle on a non-metal, semi-porous surface with absorptive properties similar to an asphalt or concrete road surface.

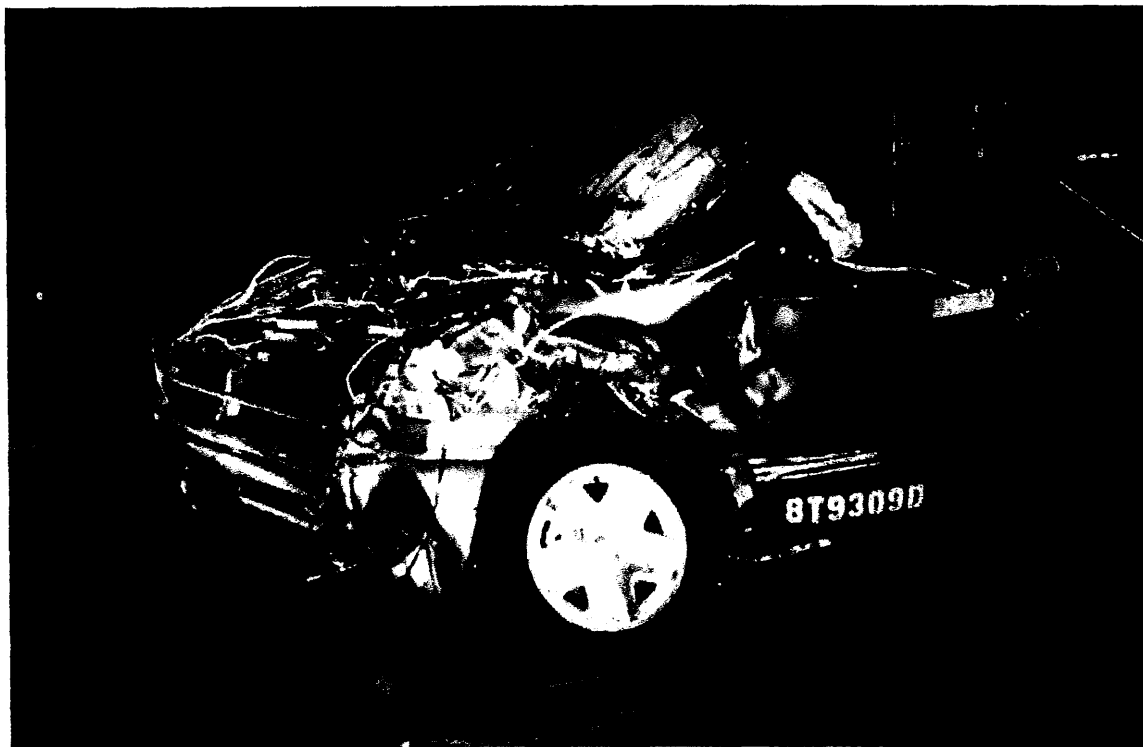


Figure 3. Fire Test F961115. Photograph of the test vehicle positioned in the fluid containment pan before the fire test. The hood was removed for this picture, and was replaced before the test.

which was removed from the vehicle for the crash test [2], was dynamically crushed to approximate the crush that would have occurred during the crash and replaced for the fire test.

Underhood fluids were poured into the engine compartment and under the vehicle before the hood was replaced. A 1:1 mixture of antifreeze and water (2 gal. (7.8L)) was poured over the front of the engine compartment. Washer fluid (1 gal. (3.85L)) was added to the broken windshield washer fluid reservoir and allowed to drain onto the ground. Transmission fluid (1 qt. (0.95 L)) was poured onto the concrete paving blocks under the transaxle housing. Motor oil (SAE 5W-30, 1 qt. (0.95L)) was added to the engine through the engine oil filler neck and allowed to drain onto the ground through the broken oil pan. Brake fluid (approximately 1 pt. (0.47 L)) was poured into the engine compartment at the location of the brake fluid reservoir.

The electrical igniter consisted of nicrome heating wire wrapped around several pieces of plastic cut from the environmental housing around the battery from another Dodge Caravan. The igniter had a maximum power output of 1.2 kW with 120 VAC. This plastic material was included in the igniter to replace material in the engine compartment consumed by fire following the crash test.

The igniter was placed between the battery and PDC, close to where flames were first observed during the crash test.

Figure 4 is a photograph of an igniter similar to the one used in this test.<sup>3</sup> Figure 5 is a photograph showing the igniter between the battery and PDC of the test vehicle shortly before the start of the test. Electrical power was supplied to the igniter from a variable-tap transformer. The electrical cable for the igniter can be seen in Figure 3 coiled on the ground under the left front corner of the test vehicle.

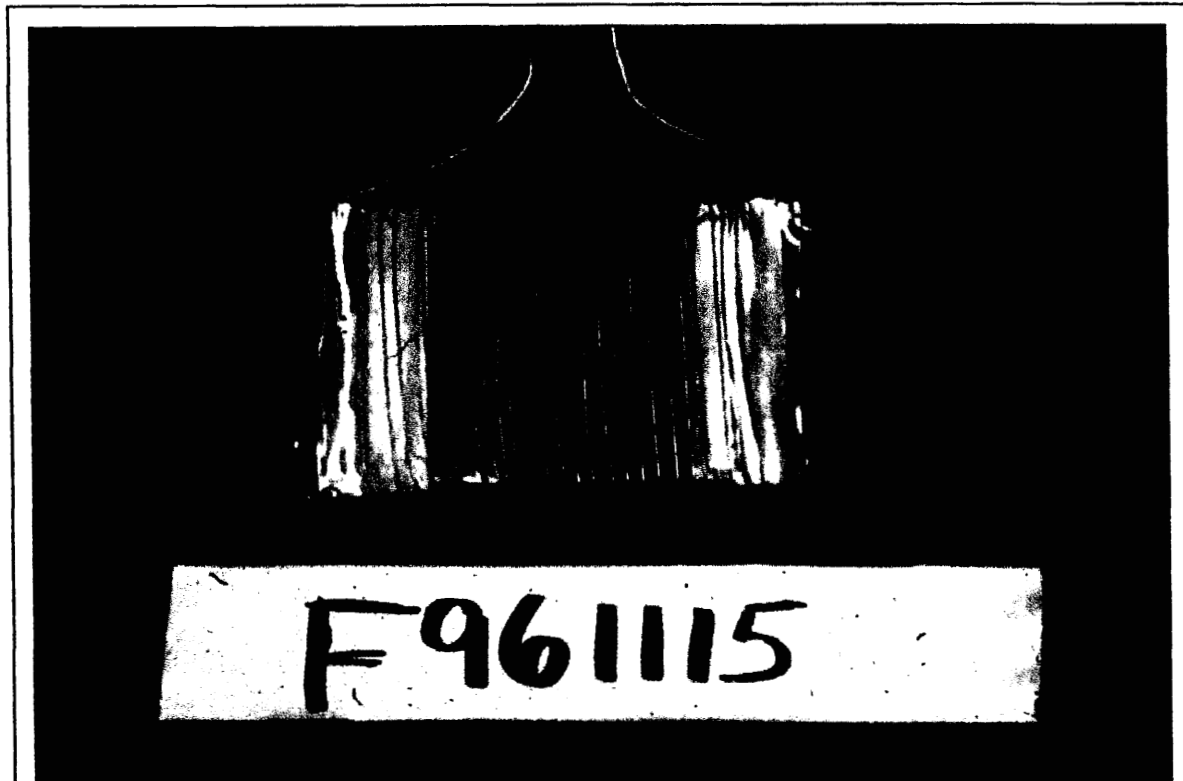


Figure 4. Fire Test F961115. Photograph of an igniter similar to the one used in this test.

At the start of this test, the power output of the transformer was adjusted to approximately 80% of full power (approximately 95 VAC). The power-output of the transformer was increased to 100% of full power (approximately 118 VAC) approximately 330 seconds after the start of the test. Neither the temperature of the igniter, nor the current through the heating wire was measured

<sup>3</sup> The igniter was made by winding Nichrome wire (24 AWG, length = 350 cm, resistance = 12  $\Omega$ ) around four pieces of poly(propylene) sheet (0.1 x 10 x 15 cm, mass = 110 g) cut from the environmental housing of a Dodge Caravan battery. The poly(propylene) sheet was included in the igniter to replace material consumed by the fire during the crash test.

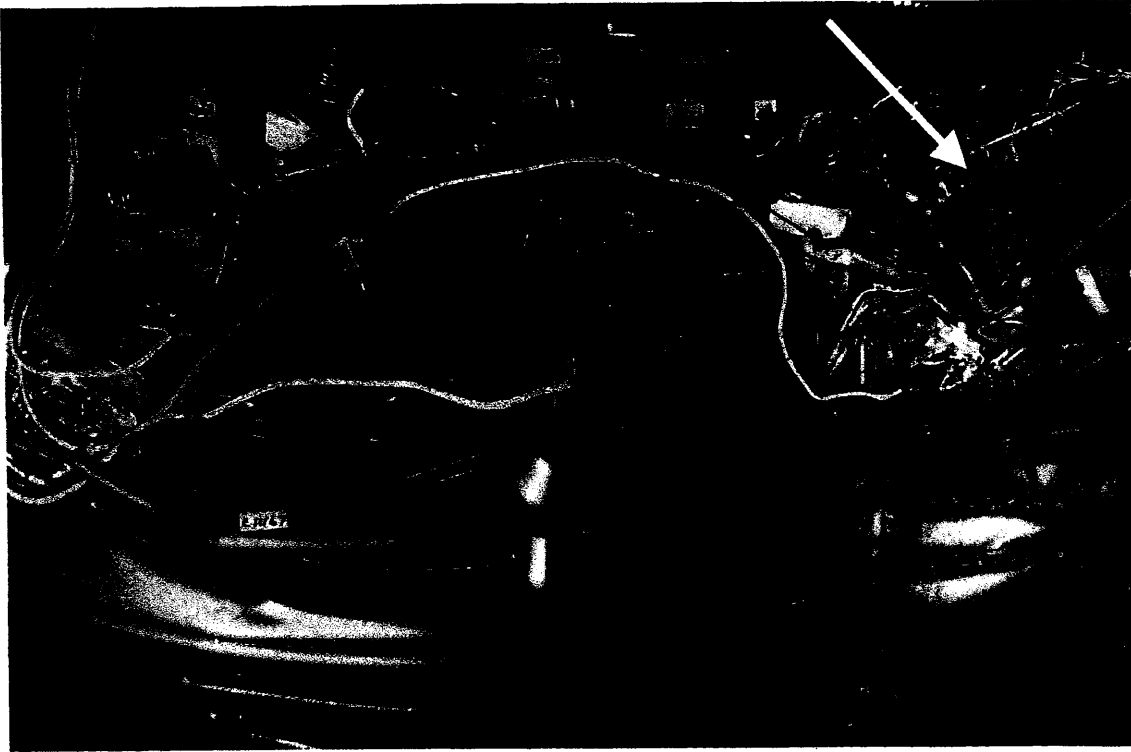


Figure 5. Fire Test F961115. Photograph of the igniter (arrow) inserted between the battery and power distribution center before the fire test. The hood was removed for this picture, and was replaced before the fire test was started.

during this test. Heat generated by the igniter was estimated from the resistance of the heating wire and the applied voltage: 0.8 kW at 95 VAC and 1.2 kW at 120 VAC.

The transformer was turned-off, cutting electrical power to the igniter, when flames were observed in the engine compartment. The test was stopped shortly after observing flames along the entire lower surface of the headliner, and the air horn was sounded a second time to signal the end of the test. The fire was extinguished with a fine water mist. At first, the water mist was directed through the drivers' side window to extinguish burning objects in the passenger compartment. The fire in the engine compartment, the burning front grill and bumper fascia, and several small burning pools of melted plastic under the vehicle were extinguished after suppressing flames inside the vehicle.

Five criteria were established before the test to guide the decision to stop the tests and extinguish the fire. The intent of these criteria was to allow flames to spread into the passenger compartment sufficiently so that the principle fire paths could be determined while preserving physical evidence

of fire paths that were not readily visible during the test or in any of the videos of the test. This physical evidence would be lost if the test vehicle were allowed to burn completely.

- When the air temperature in the passenger compartment measured between the front seats at the height of an adult occupant exceeded 200°C and was increasing rapidly, or
- When the concentration of carbon monoxide in the passenger compartment exceeded 1% and was rising rapidly, or
- When flames visibly impinged on one or both front seats, or
- When the head-lining covering the forward section of the roof was in flames, or
- When flashover in the passenger compartment was evident.

After flames were first observed in the engine compartment, an attempt was made to evaluate these criteria continuously. As flames spread into the passenger compartment, conditions changed rapidly allowing insufficient time for objective evaluation of each of these criteria. The test was stopped after observing that flames had spread along the entire lower surface of the headliner.

### 3 Ignition

Smoke started to rise from the area of the battery and PDC within 5 seconds of the start of the test<sup>4</sup>, and continued for approximately the next 10 minutes (Fig. 6).<sup>5</sup>



Figure 6. Fire Test F961115. Video still from Camera 1 showing pyrolysate rising from the engine compartment 540 seconds after the start of the test.

The rising smoke was deflected by the inner surface of the hood, and emerged from the rear and left edges of the hood. Heating from the igniter was localized to the battery, the PDC, and the hood liner above these components. Thermocouples located on top of the battery and PDC closest to the igniter (A1, A2, and A3) recorded temperature increases of approximately 25°C (*i.e.*, from ambient to 40°C) during the first 5 minutes of the test (Fig 7). However, the sections of the battery case and PDC housing in contact with the igniter coils must have been heated to greater

<sup>4</sup> In this report, The start of the test is defined as the time when electrical power was first applied to the ignitor. The time of ignition (see p. 14) is defined as the time when flames were first detected in the engine compartment in the area of the battery and PDC.

<sup>5</sup> Refer to APPENDIX A for the locations of the video cameras relative to the test vehicle during this fire test.

than 350°C for these materials to thermally decompose.<sup>6</sup> When the power output of the transformer was increased to 100% approximately 5½ minutes after the start of the test, the temperatures recorded by thermocouples A2 and A3 increased to approximately 80 and 150°C, respectively. Temperatures recorded by thermocouples located on the rear of the battery and PDC (A4 and A5, respectively) remained less than 50°C for the first 10 minutes of the test.

Localized heating of objects near the igniter before and at the time of ignition can be seen in the infrared thermograms from IR Camera 2 (Fig.'s 8 and 9). Although flames were not seen in the video (upper panel, Fig. 8), the radiant temperature from the left side of the engine compartment increased from 20°C at the start of the test to greater than 30°C during the first 10 minutes of the test (lower panel, Fig. 8). The temperature of a small area on the exterior surface of the hood above the igniter increased from 25°C at the start of the test to approximately 30°C during the initial 10 minutes of the test. The small amount of heat and smoke rising from the vehicle before ignition of the battery and PDC housing was not detected by the fire products collector (APPENDIX G).

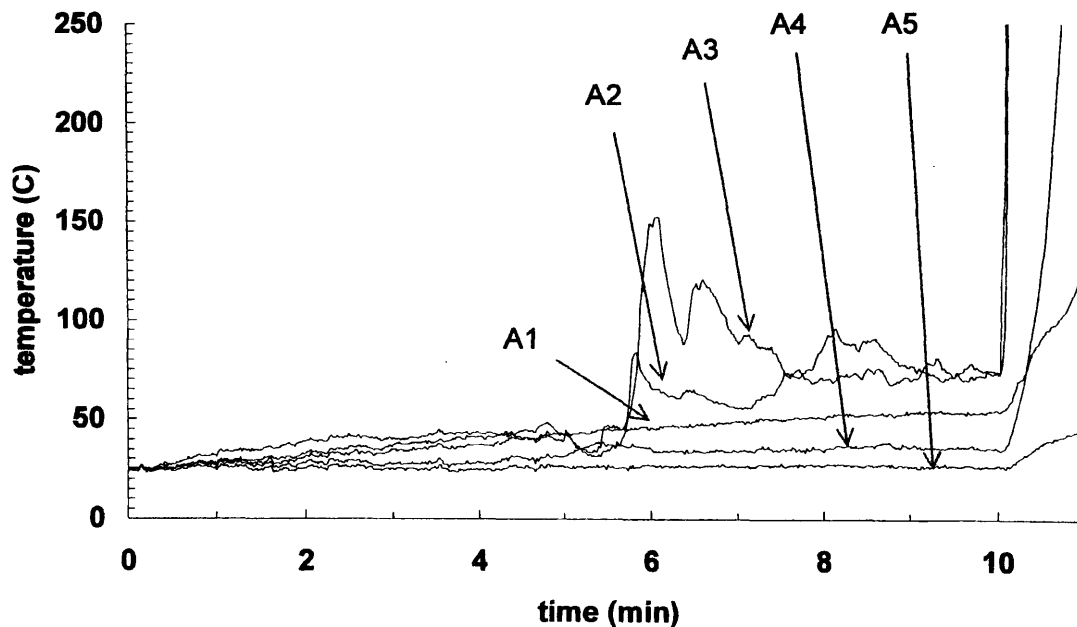


Figure 7. Fire Test F961115. Temperatures recorded by thermocouples A1 through A5 for the first 11 minutes of the test.

<sup>6</sup> The battery case was poly(ethylene). The battery environmental housing was a (propylene/ethylene copolymer). The PDC housing was poly(ethylene terphthalate) with 30% (wt/wt) glass filler. These materials typically undergo thermal decomposition between 350 and 450°C in air.



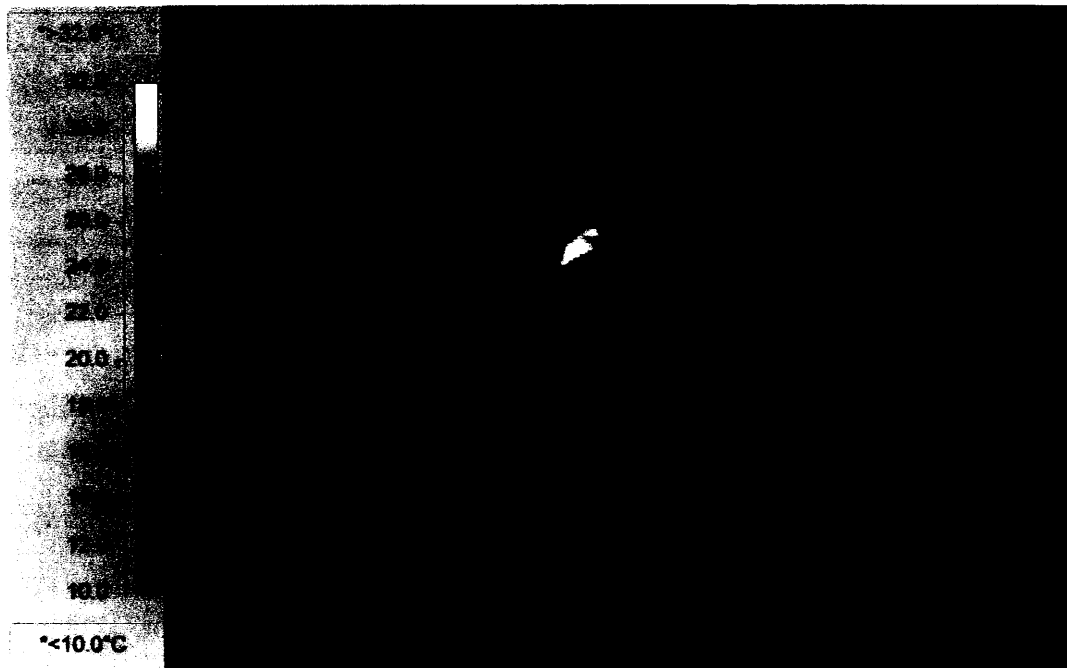


Figure 8. Fire Test F961115. Video still from Camera 5 (upper panel) and infrared thermogram from IR 2 (lower panel) 402 seconds after the start of the test (200 seconds before ignition of the battery and PDC housing).

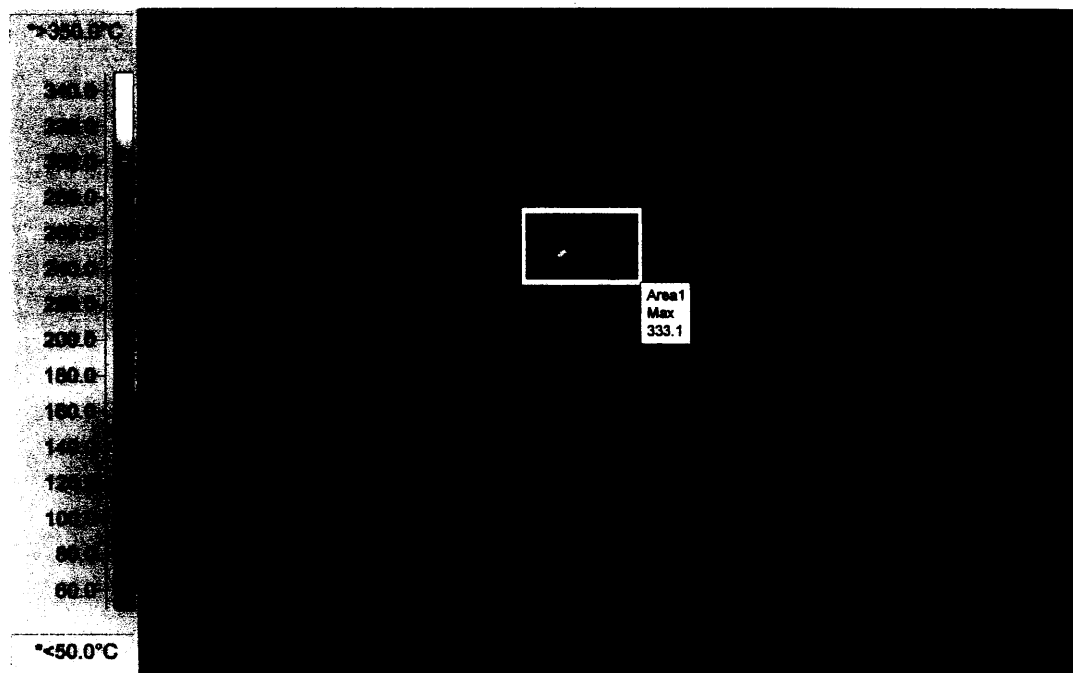


Figure 9. Fire Test F961115. Video still from Camera 5 (upper panel) and infrared thermogram from IR 2 (lower panel) 602 seconds after the start of the test (the time of ignition of the battery and PDC housing). The dynamic range of this thermal imaging system was insufficient to measure both radiation from the initial fire plume and from the vehicle at room temperature simultaneously.

Pyrolysate from the battery case and PDC housing ignited spontaneously 602 seconds after the start of the test (Fig. 9). The video of the left side of the engine compartment showed flames above the battery and PDC at this time (the bright area under the hood visible in the video still (upper panel) in Fig. 9). Thermal radiation from objects in the engine compartment also increased at this time (lower panel, Fig. 9), as did temperatures recorded by thermocouples A2, A3, and A4 (Fig. 7).

The sequence of video stills and infrared thermograms in Figures 10 through 14 shows that flames started to emerge from the left and rear edges of the hood about 13 seconds after ignition, with a small flame was visible at the rear edge of the hood by 15 seconds post-ignition.

The infrared thermograms showed heated gas venting from the rear edge of the hood 3 seconds after ignition. The infrared thermograms also show large plumes of heated gas and particulate venting from both the rear and left edges of the hood 5 seconds post-ignition. The size and temperature of the hot gas/particulate plume increased as the fire under the hood increased. As seen by the increase in thermal radiation from the engine compartment through the front grill and the gap under the right front corner of the hood (Fig.'s 11 through 14), the fire started to irradiate objects throughout the engine compartment almost immediately. IR1 was set to a more sensitive range at this time, with a maximum temperature of < 45°C.

Apparent hot spots on the bumper fascia and front grill seen in the thermogram 17 seconds before ignition (Fig. 10) are reflections from the video lights.

The discussions in all proceeding sections (**SECTIONS 3 through 7**) reference the timing of events to the time when flames were first observed in the engine compartment (602 seconds after the start of the test).

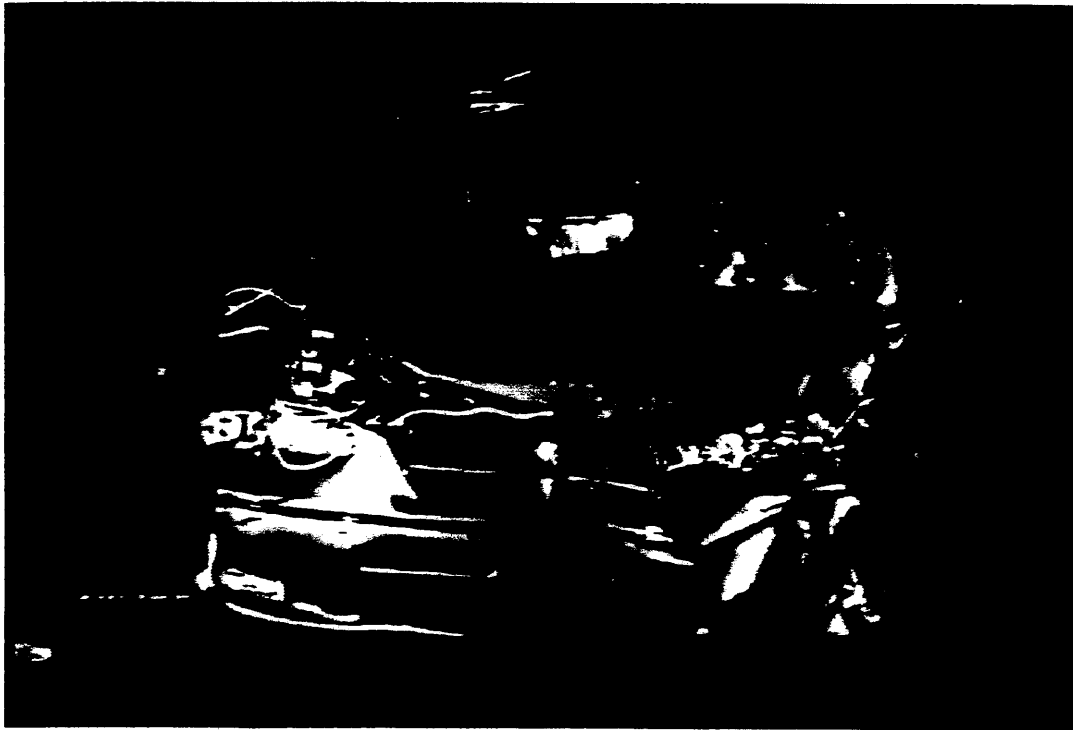


Figure 10. Fire Test F961115. Video still from Camera 1 (upper panel) and infrared thermogram from IR 1 (lower panel) at 585 seconds after the start of the test (17 seconds before ignition of the battery and PDC housing).

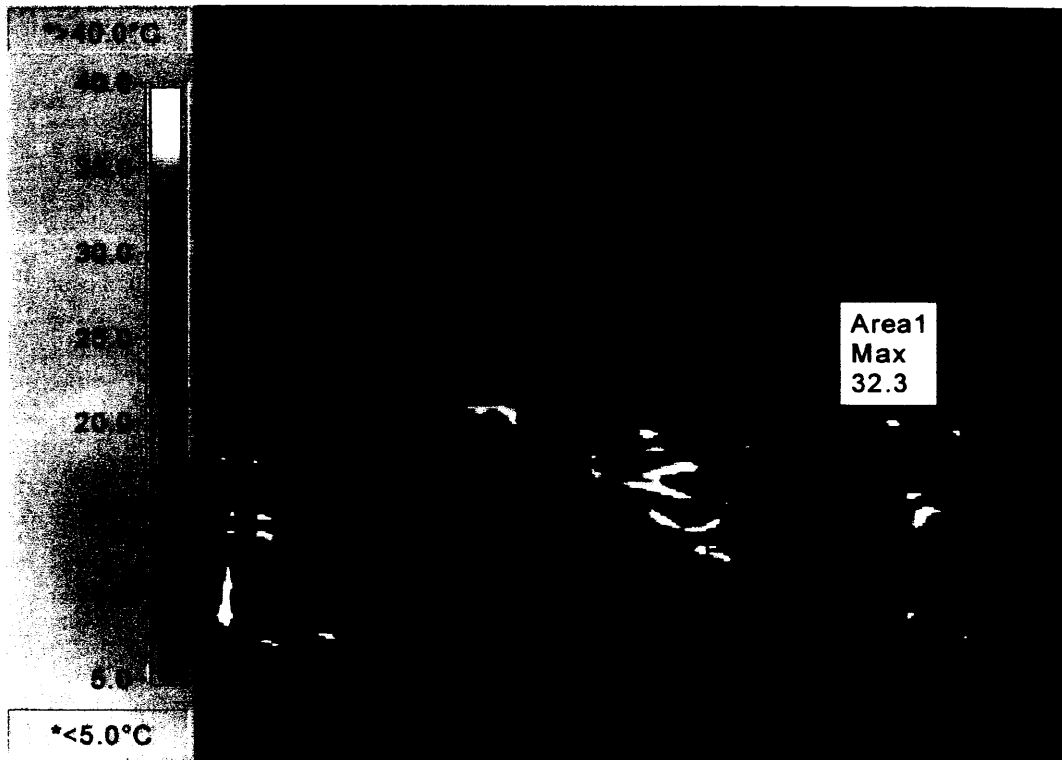


Figure 11. Fire Test F961115. Video still from Camera 1 (upper panel) and infrared thermogram from IR 1 (lower panel) at 602 seconds after the start of the test (the time of ignition of the battery and PDC housing).



Figure 12. Fire Test F961115. Video still from Camera 1 (upper panel) and infrared thermogram from IR 1 (lower panel) at 607 seconds after the start of the test (5 seconds after ignition of the battery and PDC housing).



Figure 13. Fire Test F961115. Video still from Camera 1 (upper panel) and infrared thermogram from IR 1 (lower panel) at 612 seconds after the start of the test (10 seconds after ignition of the battery and PDC housing).

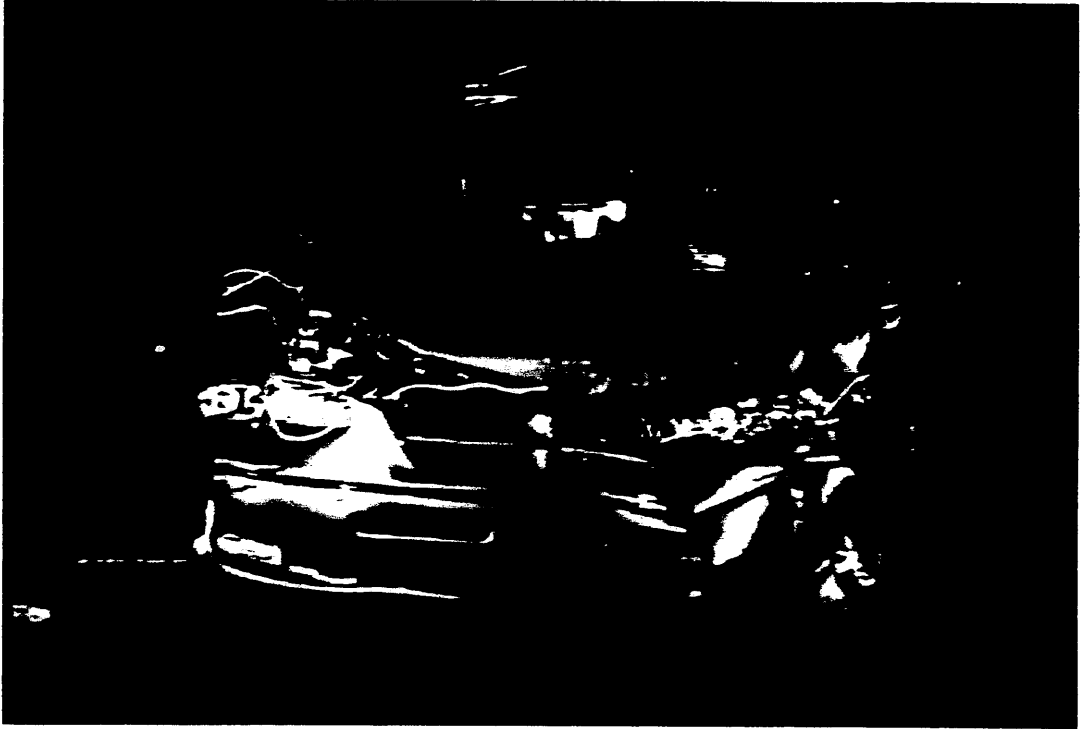


Figure 14. Fire Test F961115. Video still from Camera 1 (upper panel) and infrared thermogram from IR 1 (lower panel) at 617 seconds after the start of the test (15 seconds after ignition of the battery and PDC housing).

#### 4 Flame-Spread in the Engine Compartment

Fifteen seconds after ignition, flames were localized to the front of the battery and PDC (Fig. 15). Thermocouples A4 and A5, located on the rear of the battery and PDC, respectively, recorded temperatures of 72 and 33°C at this time, indicating that flames had not progressed significantly toward the rear of the engine compartment (Fig. 7).



Figure 15. Fire Test F961115. Video still from Camera 7 showing flames localized to the battery and PDC 15 seconds post-ignition.

Flaming melted plastic dripping from the burning battery and PDC appeared to have ignited the air cleaner housing, which was broken and pushed under the battery during the crash test. Although it cannot be seen clearly in the video images, it is likely that the hood liner above the battery and PDC also ignited at this time. The hood liner in this vehicle was a composite structure consisting of a polyester and glass fiber mat with a cotton-felt (cotton-shoddy) backing. This assembly was attached to the hood by thermoplastic clips, with the polyester mat exposed to the engine compartment and the cotton felt backing against the lower surface of the inner hood panel. The exposed lower surface of the hood liner above the battery and PDC was heated directly by the fire plume. The hood liner appeared to ignite during the first 15 seconds post-ignition.

Most components in the engine compartment, including the hood liner, were near ambient temperature at the time of ignition. Infrared thermograms of the left side of the vehicle show localized heating on the exterior surface of the hood above the igniter before ignition (Fig. 8). This indicates that heated gases rising from the igniter during the first 10 minutes of the test heated the hood and hood liner directly above the battery and PDC. This pre-heating may have accelerated ignition of this area of the hood liner by flames from the burning battery and PDC, but was not sufficient to cause the hood liner to ignite in the absence of a pilot flame.

Radiation from the burning hood liner may have accelerated lateral flame-spread by pre-heating other objects in the engine compartment slightly, but would not have been sufficient to ignite the materials used in the engine compartment of the test vehicle. In separate flammability tests, combustion of an exemplar hood liner produced a steady-state heat release rate of 10 to 20 kW and a downward heat flux of 12 to 15 kW/m<sup>2</sup> at the level of in the top of the engine compartment [4]. The heat release rate from a fire localized to a small area of the hood liner above the battery would not have been substantially less and would not have added greatly to the total heat output at this time. And only objects near the point of ignition would have been effected by radiative pre-heating from such a localized fire.

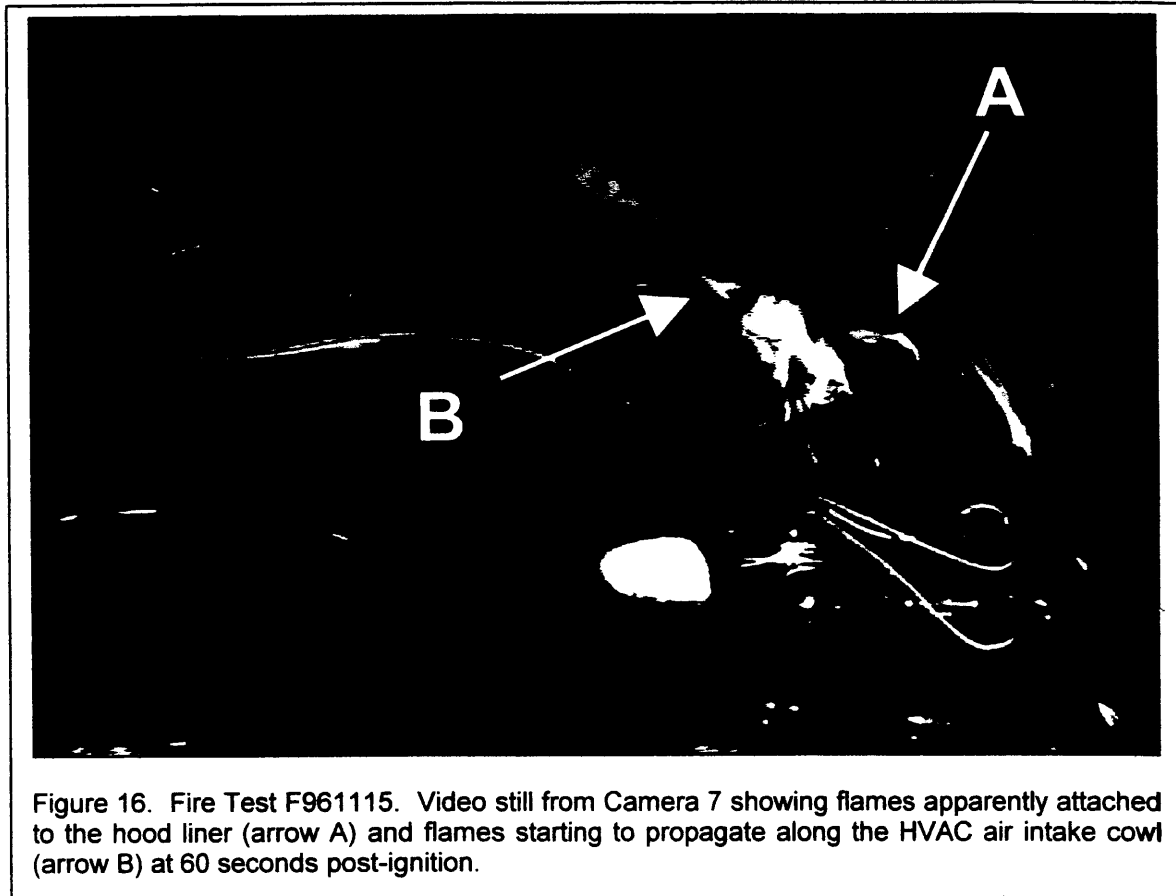
The location of the flame front and the rate of flame spread in the engine compartment were estimated from the video images and the temperature data recorded by thermocouples located on objects in the engine compartment<sup>7</sup>. In analyzing the video recordings, the flame front was defined as the outer edge of the visible fire plume. The location of the actual attached flame front on the various solid objects could not be seen in the video recordings. In clean lateral flame spread conditions, the attached flame front is close, usually within millimeters of the edge of the fire plume. The dynamics of fire propagation in this test were more complex, and the separation between the outer edges of the visible flame front and the point of attachment could have been larger, resulting in overestimation of the extent of the ignited region at any given time.

The fire had expanded only slightly in the area of the battery and PDC by 60 seconds post-ignition. But the fire on the hood liner had grown toward the front and rear of the vehicle at this time. Flames could be seen apparently attached to the hood liner 13 to 15 cm forward of where

---

<sup>7</sup> In analyzing the thermocouple data, a temperature of 600°C was defined as the threshold for the presence of flame at a specific thermocouple location. However, the timing of flame-spread could not be determined precisely because of the inherent time lag in the response of the thermocouples. The thermocouples used in this test contained enclosed junctions contacting the thermocouple sheath (see APPENDIX C). It was estimated that these thermocouples had a 3 to 5 seconds delay in their temperature response. Moreover, many of the thermocouples recorded rapid, extreme changes in temperature that were probably the result of flame turbulence, making it impossible to accurately correct for the inherent time delay in the thermocouple response when measuring flame spread.

the fire plume from the battery contacted the hood liner (Fig. 16). The exact point of attachment could not be seen clearly in these videos. Thermocouples located on the top of the battery (A2) and PDC housing (A3), both of which were adjacent to the igniter, and at the rear of the PDC housing (A1) recorded temperatures of 809, 453, and 689°C at 60 seconds post-ignition. Thermocouples located toward the right edge of the battery (A4 and A5) recorded temperatures of 130 and 51°C at this time. Thermocouples located above the battery and under the HVAC air intake cowl (B4, B4, and B10) recorded temperatures < 100°C at this time (**Appendix C**).



Flame-spread along the hood liner toward the front of the engine compartment required the flame front move downward along the slope of the crumpled hood (Fig. 16). This type of flame movement is called opposed-flow spread because flame movement is against the buoyancy-induced airflow. Flame-spread on the hood liner toward the windshield was in the direction of the buoyancy-induced airflow, and would be expected to have been faster because of the coincident flow of gaseous fuel and heat. It was impossible to estimate directional flame-spread rates accurately because the exact point of flame attachment to the hood liner could not be determined from the video tapes. The video still in Figure 16 indicates that by one minute

post-ignition, the hood liner was burning from the rear-edge of the hood to approximately 15 cm forward of the battery and PDC. The maximum width of the burning area of the hood liner was approximately 30 cm, estimated from the width of the fire plume emerging from the rear edge of the hood: (Fig. 17). As noted above, the flaming hood liner would have been a source of radiant heating to objects below it in the engine compartment, which would have been a factor in the spread of flames to other objects beyond the site of ignition.



Figure 17. Fire Test F961115. Video still from Camera 1 showing flames emerging from the side and rear of the hood 88 seconds post-ignition.

Camera 7 also showed flames starting to spread along the HVAC air intake cowl at about 1 minute post-ignition (Fig. 16). The fire plume on the top of the battery and PDC began to contact the forward edge of the cowl<sup>8</sup> by 15 seconds post-ignition (see Fig. 15). Ignition of other components under the battery added to the heat release in the left side of the engine compartment and contributed to the subsequent ignition on the HVAC air intake cowl (Fig. 18).

<sup>8</sup> The air intake cowl was a fiberglass-reinforced sheet molding compound composite. The cowl cover was polycarbonate with a flexible urethane foam weather seal along its forward edge. Separate flammability tests showed that the assembled air intake cowl yielded a moderately high rate of heat release and lateral flame spread [5].

These components, which were not visible in Figure 18 because of the crush on the left side of the test vehicle, included the battery tray, the air intake resonator, the air cleaner housing, and the air intake boot<sup>9</sup>. The locations of these components were documented before the test. The brake fluid reservoir,<sup>10</sup> which was located behind the battery, broken and pushed against the brake master cylinder during the crash test, also contributed to the fire load in the upper left side of the engine compartment at this time. The buoyancy of the fire plume forced flames rearward against the upward slope of the hood, directly against the front of the air intake cowl and across the cowl cover.



Figure 18. Fire Test F961115. Video still from Camera 7 showing flames emerging from under the battery (arrow) at 90 seconds post-ignition.

The hood liner started to separate from the hood at about 2 minutes post-ignition, allowing the previously unexposed cotton shoddy to ignite. When held in place to the underside of the hood by thermoplastic clips, the cotton felt backing of the hood liner was shielded from exposure to open flames. As the thermoplastic clips melted, the hood liner pulled away from the hood on the left side of the vehicle, exposing the cotton felt backing to flames. Once ignited, the cotton felt burned more

<sup>9</sup> The battery tray was poly(propylene) with 30% inorganic filler. The air intake resonator and air cleaner housing were poly(propylene) with 20% inorganic filler. The air intake boot was EPDM elastomer with 40% carbon black.

vigorously than the polyester mat. The additional heat released by the burning cotton felt enhanced flame-spread along the HVAC air intake cowl and, secondarily, also ignited the paint on the exterior surface of the hood (Fig. 19).

Most of the battery, the PDC, and the forward edge of the HVAC air intake cowl in the left side of the engine compartment were burning 3 minutes post-ignition (Fig. 20).



Figure 19. Fire Test F961115. Video still from Camera 7 showing the hood liner starting to sag (arrow A) and the paint on the hood starting to blister and burn (arrow B) 120 seconds post-ignition.

Gravity-induced flow of flaming melted thermoplastic aided downward flame spread in the left side of the engine compartment. Flaming streams of molten thermoplastic were seen flowing downward and forward from the site of ignition 3 minutes post-ignition. However, no molten plastic was observed on the ground under the vehicle at this time. The left front wheel-house, the left frame rail, the transaxle housing, and the bumper reinforcement<sup>11</sup> appear to have impeded the downward flow of molten thermoplastic, and prevented the formation of a significant thermoplastic

<sup>10</sup> The brake fluid reservoir was poly(ethylene).

<sup>11</sup> These structures were pushed together when the left side of the vehicle was crushed during the crash test, forming a barrier that impeded the downward flow of molten thermoplastic from the area of ignition.

pool fire on the ground until about 6 minutes post-ignition. The combustible material pooling on these higher structures strengthened the fire in the upper engine compartment.

The fire plume emerging from the rear of the hood also grew taller between 3 and 6 minutes. One possible cause of the observed increase in flame height (length) at this time was an increase in the heat release rate in the region behind the advancing lateral flame front in the engine compartment. At least one laboratory study has shown a correlation between flame height (length) and heat release rate for flames attached to a wall [5]. This observation suggests that flame-spread to combustible material forward and downward in the engine compartment, which resulted in an increase in the heat release rate in the engine compartment, contributed to the growing fire plume at the rear of the hood.



Figure 20. Fire Test F961115. Video still from Camera 7 showing flames emerging from under the battery 180 seconds post-ignition.

Figure 21 shows plots of the position of the flame front relative to the point of ignition on the hood liner (fire plume at the rear edge of the hood), and on the upper-, front-, lower-, and interior-surfaces of the air intake cowl. The rates of lateral flame spread (slopes) along the hood liner and the exterior surfaces of the HVAC air intake cowl were similar, suggesting that flame spread along

these objects was coupled by convective and radiative heat transfer throughout the spreading flame zones. The small vertical spacing between the hood liner and those on the cowl cover (top of the air intake cowl) facilitated radiative heat exchange between these flame zones. The rate of flame spread inside the air intake cowl was apparently slower, and the reason for this is not known (Fig. 21).

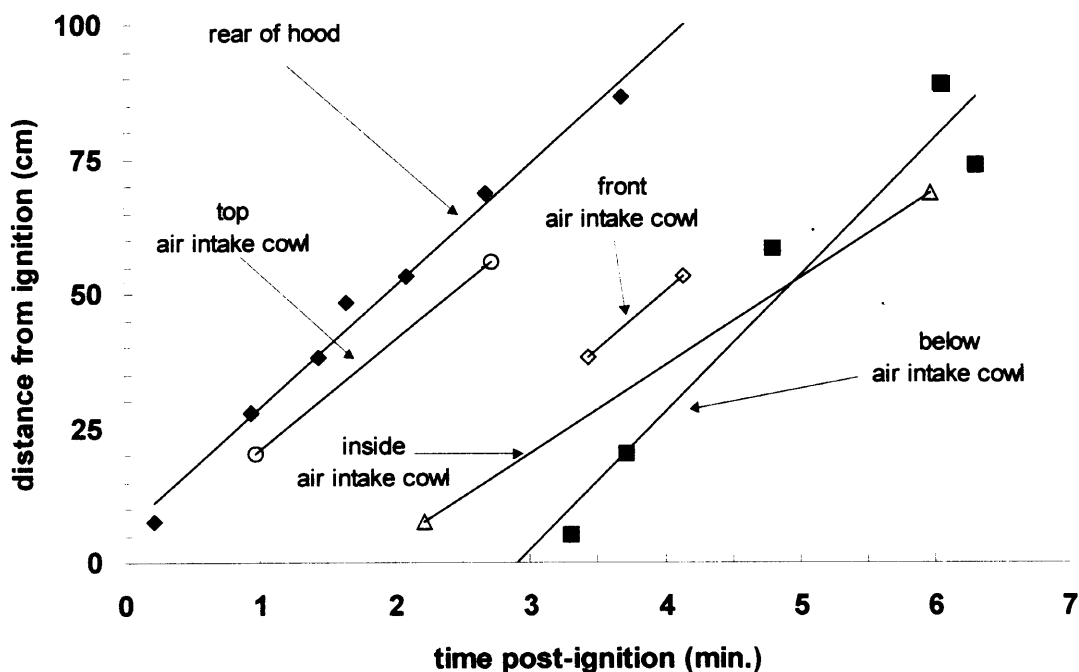


Figure 21. Fire Test F961115. Lateral flame spread along different paths in the engine compartment. The distance from the point of ignition (the y-axis) was determined by estimating the lateral separation between the flame front and the steering column, which was approximately in-line with the igniter. Flame spread along the rear of the hood was determined from Camera 1. Flame front along the air intake cowl was measured by noting the times when the flame front reached recognizable features at known locations in the video from Camera 7. Flame spread inside and below the air intake cowl was determined from the temperatures recorded by thermocouples B1 through B8 and B9 through B13, respectively.

The cause of lateral fire growth in the engine compartment is difficult to discern from the videos. It seems to have been associated with ignition of the exposed cotton shoddy on the detached hood liner. The hood liner detached from the front left side of the hood about 2 minutes post-ignition (see Fig. 19), and fell on top of the engine approximately 5½ minutes post-ignition. It seems unlikely that the additional heat released by ignition of the cotton shoddy [4] was sufficient by itself to cause flames to spread across the engine compartment. However, flames were observed in the right side of the engine compartment by 5 minutes post-ignition (Fig. 22), indicating that material not visible in these videos had ignited and was contributing to the overall heat release rate during this time. Combustible components in the right side of the engine



Figure 22. Fire Test F961115. Video still from Camera 7 at 5 minutes post-ignition showing flames had spread to the right side of the engine compartment at this time.

compartment included the windshield washer fluid reservoir, the engine coolant overflow reservoir, and the power steering fluid reservoir (refer to Fig. 5).

Figures 23 and 24 contain video stills from Camera 1 showing the front of the test vehicle at 5 and 7½ minutes post-ignition, respectively. The video still in Figure 23 shows that flames had spread into the left head lamp assembly by 5 minutes post-ignition. Burning molten thermoplastic flowing forward in the left side of the engine compartment entered the rear of the head lamp assembly through crash induced fractures. Ignition of the head lamp assembly occurred between 3 and 4 minutes post-ignition. Temperatures recorded by thermocouples along the front of the vehicle (A7 through A11) indicated that the bumper fascia and energy absorber started to burn below the left head light between 5 and 6 minutes post-ignition. The forward edge of the hood captured the fire plume, directing it rearward along the upward slope of the deformed hood, apparently causing the radiator support cross member to ignite. Flames began to spread downward on the bumper fascia and bumper energy absorber about 6 minutes post-ignition. A small melt/drip fire, fueled by melted material dripping from the bumper fascia and bumper energy absorber also began to form on the ground below the left front corner of the test vehicle at this time.



Figure 23. Fire Test F961115. Video stills from Camera 1 showing the front of the test vehicle at 5 minutes post-ignition.



Figure 24. Fire Test F961115. Video stills from Camera 1 showing the front of the test vehicle at 7½ minutes post-ignition.

By 7½ minutes post-ignition, flames were visible along the entire length of a tear on the left side of the bumper fascia that occurred in the crash test of this vehicle (Fig. 24). Combustion of the front bumper fascia and energy absorber contributed to the overall heat release rate during the latter stages of the fire; however, only a small portion of the fire plume from the front of the vehicle was captured by the hood and deflected rearward toward the passenger compartment.

## 5 Flame-spread into the Passenger Compartment through the Windshield

For the first several minutes after ignition, the fire plume emerging from the rear edge of the hood was short and had little momentum toward the windshield, staying several centimeters away from the base of the glass. The temperatures recorded by thermocouples on the windshield remained below 35°C for the first 60 seconds after ignition, indicating that the windshield underwent predominantly low-level radiative heating during the early stage of the fire (Fig. 25).

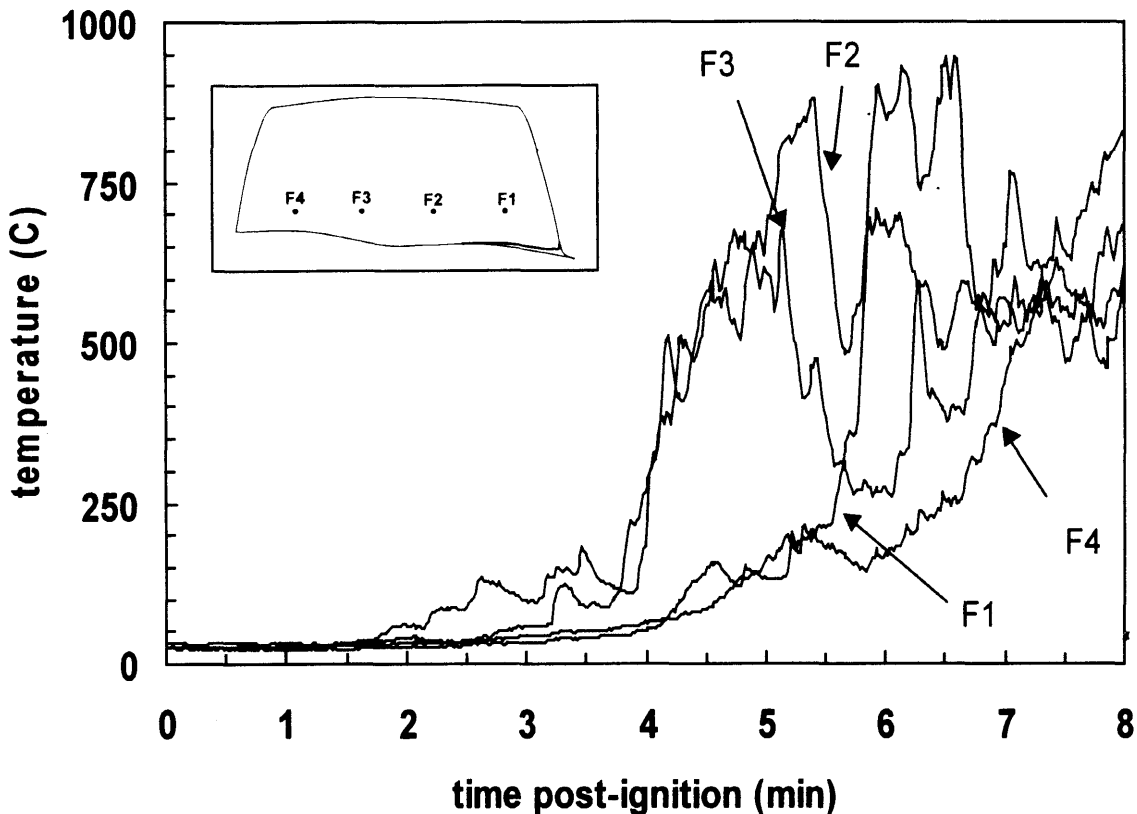


Figure 25. Fire Test F961115. Plots of temperatures recorded by thermocouples F1 through F4 attached to the windshield. The insert is a view of the windshield (looking rearward from the front of the vehicle) showing the locations of thermocouples F1 through F4. The thermocouples were located approximately 20 cm above the lower edge of the windshield.

Flames began to contact the windshield directly along its lower edge between 1 and 2 minute post-ignition. The fire plume grew to approximately half the height of the windshield, with roughly the lower half of the plume making contact with the exterior surface of the glass slightly to the left of the center of the windshield. The thermocouples on the windshield were above the area of flame contact. Temperatures recorded from Thermocouples F2 and F3 in the center of the windshield were less than 200°C for the first 3½ minutes post-ignition (Fig. 25). Temperatures recorded from Thermocouples F1 and F4 on the right and left side of the windshield, respectively,

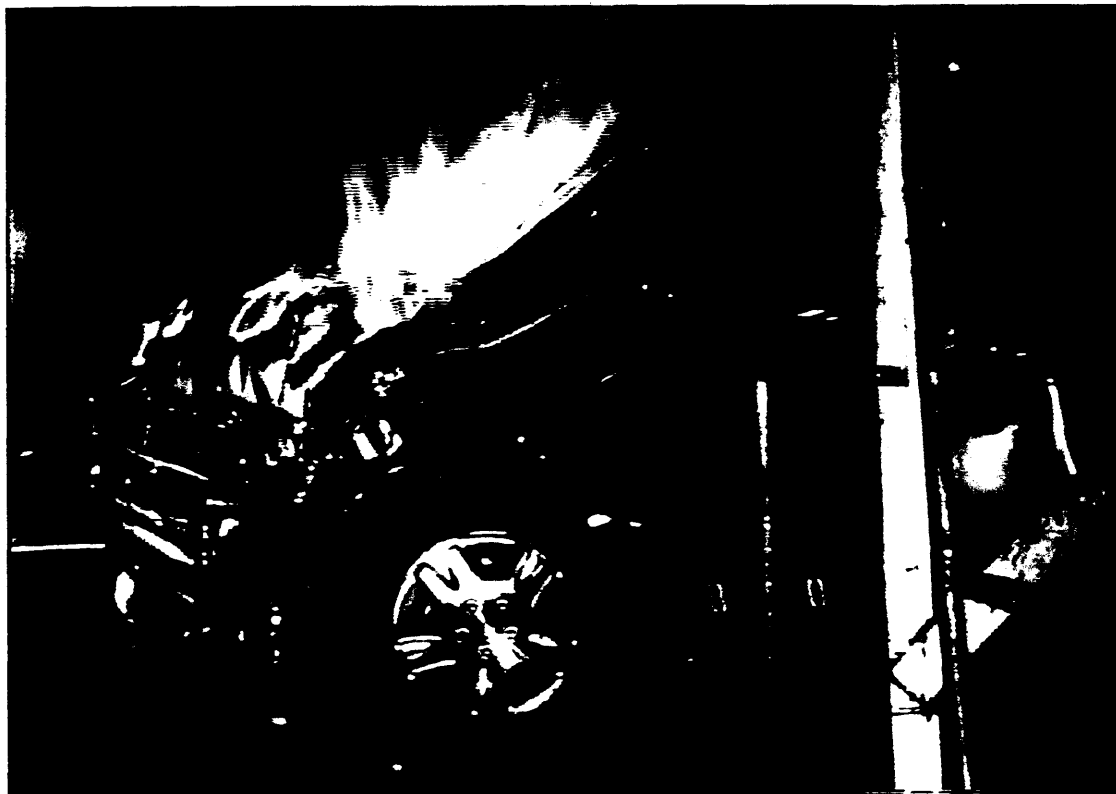


Figure 26. Fire Test F961115. Video still from Camera 5 showing flame contact on the windshield 4 minutes post-ignition.

were slightly higher than at the start of the test (Fig. 25). This temperature data confirms that flame contact was localized to the lower center of the windshield for the first 3 ½ minutes post-ignition. Radiation from the flames in front of the windshield heated the area where Thermocouples F2 and F3 were located.

As flames spread laterally in the engine compartment, the size of the fire plume emerging from the rear of the hood increased, which resulted in an increase in the area of flame contact on the windshield (Fig. 26). By 4 minutes post-ignition, flames had spread to the center of the air intake cowl, and further to the right along the hood liner. Temperatures recorded from Thermocouples F2 and F3 increased from approximately 250 to > 600°C between 4 and 5 minutes post-ignition (Fig. 25), indicating that the fire plume impinged directly upon the area where these thermocouples were located.

The shape of the deformed hood and growth of the fire in the engine compartment contributed to the increase in the flame contact on the windshield. Figure 27 is a plot of the height of flame contact on the exterior surface of the windshield versus time post-ignition. The growth in the fire

plume at the rear of the hood and the contact height on the windshield correlated with an increase the heat release- and product release-rates of the fire (see **APPENDIX H**), which had not spread outside of the engine compartment. The gap between the rear edge of the hood and the HVAC air intake cowl acted as a fixed orifice, causing the velocity of the vent flow toward the windshield to increase as the production of heat and gaseous combustion products increased. The increasing rearward momentum of the flames resulted in an increasing contact height on the windshield. This analysis does not distinguish between flame contact and flame attachment. In this case, flame contact describes the phenomenon of the flames from the engine compartment being forced against the exterior surface of the windshield. Flame attachment describes the phenomenon of flames coming from the burning windshield. The principle combustible material in the windshield is the inner-layer.

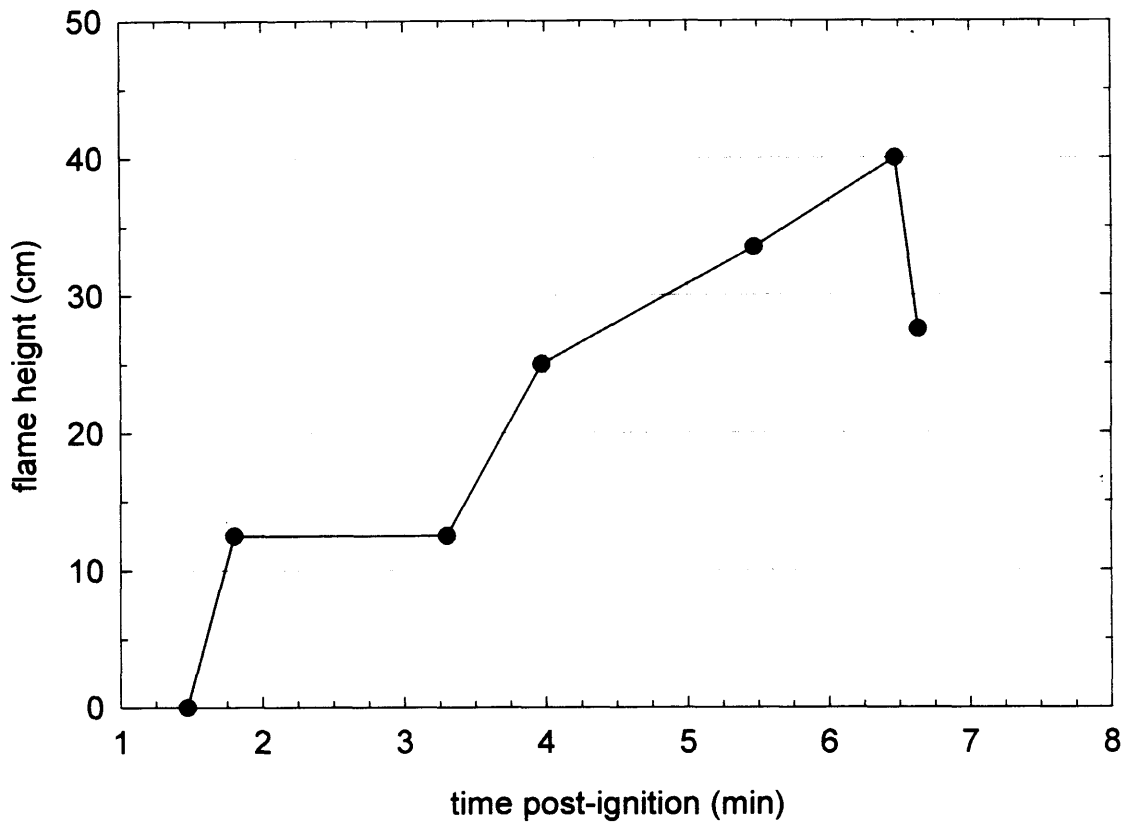


Figure 27. Fire Test F961115. Plot of the height of vehicle flame contact with the windshield versus time post-ignition as determined from the view of Camera 5.

## 5.1 Ignition of the Windshield Inner-layer

The time of ignition of the inner-layer<sup>13</sup> in the windshield could not be determined precisely. Both layers of glass were shattered during the crash test. The impinging fire plume heated the glass outer-layer on the exterior surface of the windshield. In addition, the inner-layer was exposed to the fire plume through numerous cracks in the outer-layer of glass, and in several places where small fragments of glass were dislodged from the windshield. Thus, the inner-layer was heated by the flames both indirectly by conduction from through the glass outer-layer and by direct flame contact in areas where the glass outer-layer was cracked or missing. The following analysis the temperature data from thermocouples on the windshield and the Infrared thermograms from IR4 attempts to estimate when the windshield inner-layer ignited.

Figures 28 through 29 show a series of infrared thermograms of the interior surface of the windshield. The outline of the top surface of the instrument panel and the steering wheel are faintly visible in upper part of Figure 28. These features were lost in Figures 29 through 31 when the temperature range was increased to measure the hotter flame temperatures along the lower edge of the windshield. In these thermograms, the temperature of the interior glass inner-layer in the lower central section of the windshield increased from approximately 50°C at 110 seconds post-ignition (Fig. 28) to greater than 600°C at 316 seconds post-ignition (Fig. 31).

Initially, a small area along the lower edge of the windshield was exposed directly to flames. At 2 minutes post-ignition, flames contacted the lower 13 cm of the central portion of the windshield d (Fig. 27). The temperature of the interior surface of the windshield behind the fire plume was only 50°C (Fig. 28). The fire plume was too small to contact the thermocouples located on the exterior surface of the windshield, and the temperatures recorded by thermocouples F2 and F3 at this time were less than 50°C (Fig. 2). The temperature of the exterior surface of the windshield was estimated to have been < 200°C at 2 minutes post-ignition.<sup>14</sup> This temperature was below the thermal decomposition temperature of vinyl butyral/vinyl alcohol copolymer and thus would not have resulted in ignition of the inner-layer at this time.

---

<sup>13</sup> Motor vehicle windshields generally are composite structures, consisting of two outer-layers of tempered glass and an inner-layer of a vinyl butyral/vinyl alcohol copolymer. The polymer in the windshield of the test vehicle contained dihexyl adipate (plasticizer) and 2-(2H-benzotriazol-2-yl)-4-methylphenol (UV-inhibitor). In separate laboratory tests, the inner-layer began to thermally decompose at a temperature of approximately 250°C by elimination of n-butanal and water. Continued heating produces acetaldehyde, 2-butenal, dihydrofuran, propane, benzene, and a mixture of aliphatic hydrocarbons.

<sup>14</sup>A transient, one-dimensional heat conduction model was used to estimate the temperature differential across the windshield for incident heat fluxes of 25 and 50 kW/m<sup>2</sup>. These calculations suggest that the temperature of the exterior surface of the windshield was 80 to 150°C hotter than the temperature of the interior surface of the windshield at these heat fluxes. This estimated temperature differential was used to estimate the temperature of the exterior of the windshield from the infrared thermograms.

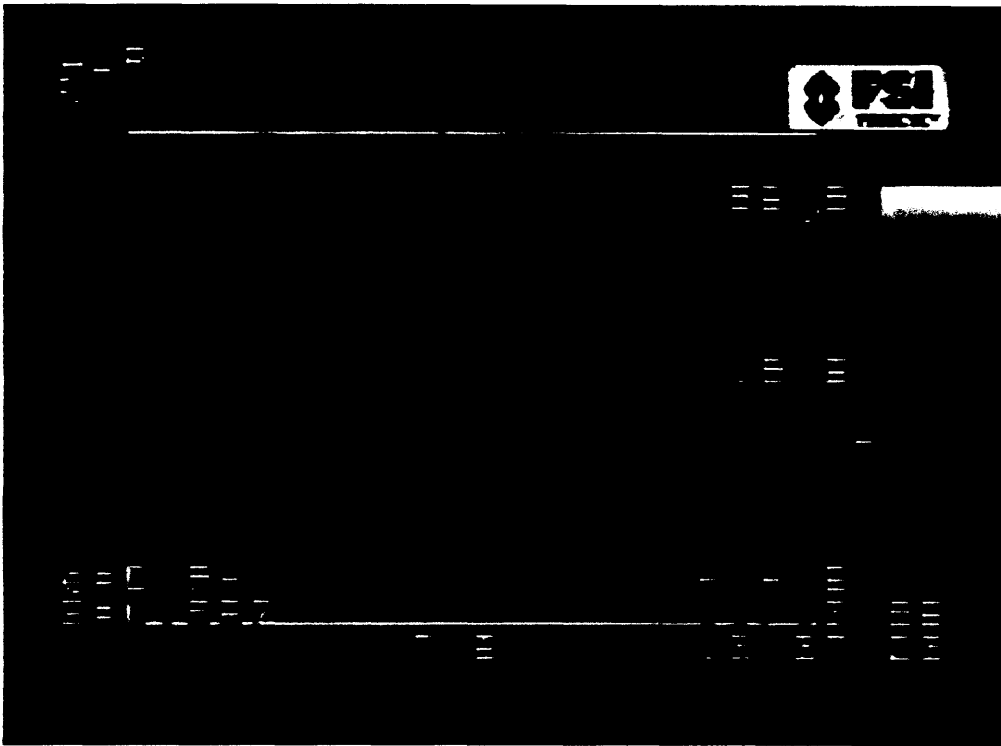


Figure 28. Fire Test F961115. Infrared thermogram from IR4 showing the temperature profile of the interior surface of the windshield 110 seconds post-ignition.



Figure 29. Fire Test F961115. Infrared thermogram from IR4 showing the temperature profile of the interior surface of the windshield 196 seconds post-ignition.



Figure 30. Fire Test F961115. Infrared thermogram from IR4 showing the temperature profile of the interior surface of the windshield 224 seconds post-ignition.



Figure 31. Fire Test F961115. Infrared thermogram from IR4 showing the temperature profile of the interior surface of the windshield 316 seconds post-ignition.

By 224 seconds post-ignition, the maximum temperature of the interior glass inner-layer on the lower central portion of the windshield was approximately 320°C (Fig. 30). The temperature of the exterior glass outer-layer was estimated from the thermocouple data to have been between 400 and 570°C. As the temperature of the inner-layer would have been > 320°C, greater than both its melting and thermal decomposition temperatures. According to these estimates, the temperature of the windshield inner-layer was high enough for it to have ignited between 3½ and 4 minutes post-ignition. The infrared thermogram in Figure 30 shows temperatures greater than 600°C along the lower central section of the windshield at approximately 5¼ minutes post-ignition, indicating that flames were inside the windshield at this time.

## 5.2 Flame-Spread into the Passenger Compartment

A triangular section of the windshield fell onto the top of the instrument panel at approximately 4½ minutes post-ignition (Fig. 32), leaving a hole roughly 15 cm wide in the windshield in front of the steering wheel. The size of the hole in the windshield increased horizontally by a factor of about three and vertically by a factor of about two as several other pieces of the windshield fell inward

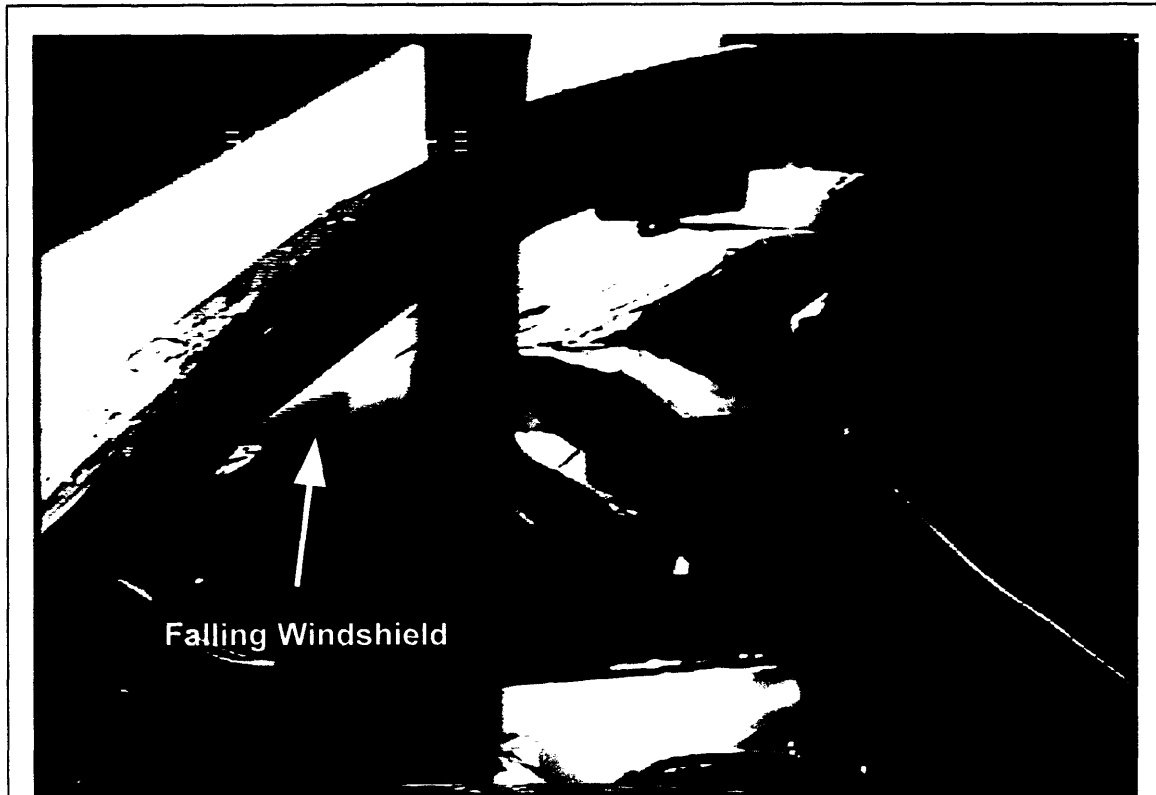


Figure 32. Figure Test F96115. Video still from Camera 4 at 260 seconds post-ignition showing a piece of windshield falling (arrow) onto the IP top cover.

over the next two minutes. At first, the pieces of glass appear to have shielded the instrument panel from the flames. A combination of radiation from the flames in front of the windshield and pieces of burning windshield falling inward ignited the instrument panel top cover between 6 and 7 minutes post-ignition (see thermocouples D8 and D9, Fig. 33). Flames then spread laterally toward the left and right, and downward into the underlying defroster duct assembly over the next few minutes.

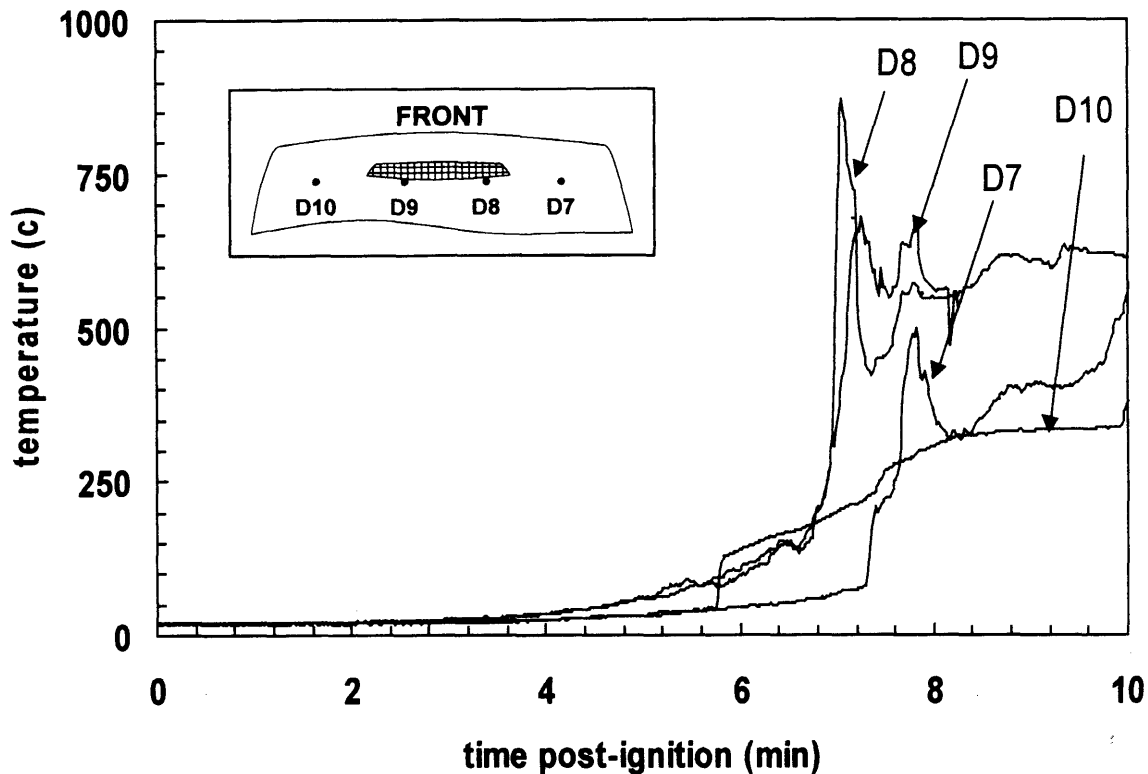


Figure 33. Fire Test F961115. Plots of temperatures recorded by thermocouples on the instrument panel top cover. The thermocouple junction of D9 failed shortly after 8 minutes post-ignition. The inset shows the locations of the thermocouples on the instrument panel top cover. See Figures A9 through A11 in **APPENDIX C** for the locations of the D thermocouples.

Flames did not spread rapidly from the instrument panel to other components in the passenger compartment. One factor that slowed fire growth in the passenger compartment was the direction of airflow during this stage of the fire. As is usual for a free fire plume, the flames at the rear edge of the hood created a lower pressure in front of the windshield than in the passenger compartment, drawing hot gases out of the passenger compartment through the hole in the windshield. This was evident by the movement of smoke in the passenger compartment in the video from Camera 4. Smoke from the engine compartment entered the passenger compartment through openings in the forward bulkhead. The infiltrating smoke emerged from seams at the top of the instrument cluster and was drawn out through the hole in the windshield (Fig. 34). Except



Figure 34. Fire Test F961115. Video still from Camera 4 at 316 seconds post-ignition showing smoke drawn out through the windshield (indicated by the arrows) in front of the steering wheel. The motion of the smoke cannot be determined from this video still, but was clearly visible in the video. The arrows in this figure point to streamers of smoke that were being drawn out through the windshield.

for flames attached to the polymer film around the edge of the hole in the windshield, outward airflow prevented flames from entering the passenger compartment around this time. The flames attached to the windshield around the edge of the hole typically were less than 10 cm in length, probably contributing minimally to the overall heat release of the fire.

Another factor in limiting fire growth in the passenger compartment was the lack of obstacles to direct the flames from the pieces of burning windshield on top of the instrument panel rearward into the passenger compartment. The windshield fell into the passenger compartment piece-wise, creating a hole in the center of the windshield above the instrument panel. Most of the pieces of windshield that fell into the passenger compartment between about 4½ and 7½ minutes post-ignition fell onto the instrument panel top cover. Flames on top of the instrument panel were drawn out through the hole in the windshield. Although components in the front of the passenger compartment were heated by radiation from the fire on the instrument panel, this was insufficient to cause them to ignite at this time. And heat transfer to objects in the passenger compartment by

convection would have been minimal as the air temperature inside the passenger compartment was less than 50°C during this time (see **APPENDIX D**).

Several large sections of the windshield fell into the right side of the passenger compartment between 7 and 8 minutes post-ignition (Fig. 35), igniting the deployed passenger airbag, the passenger seat, and the carpet in front of the passenger seat.

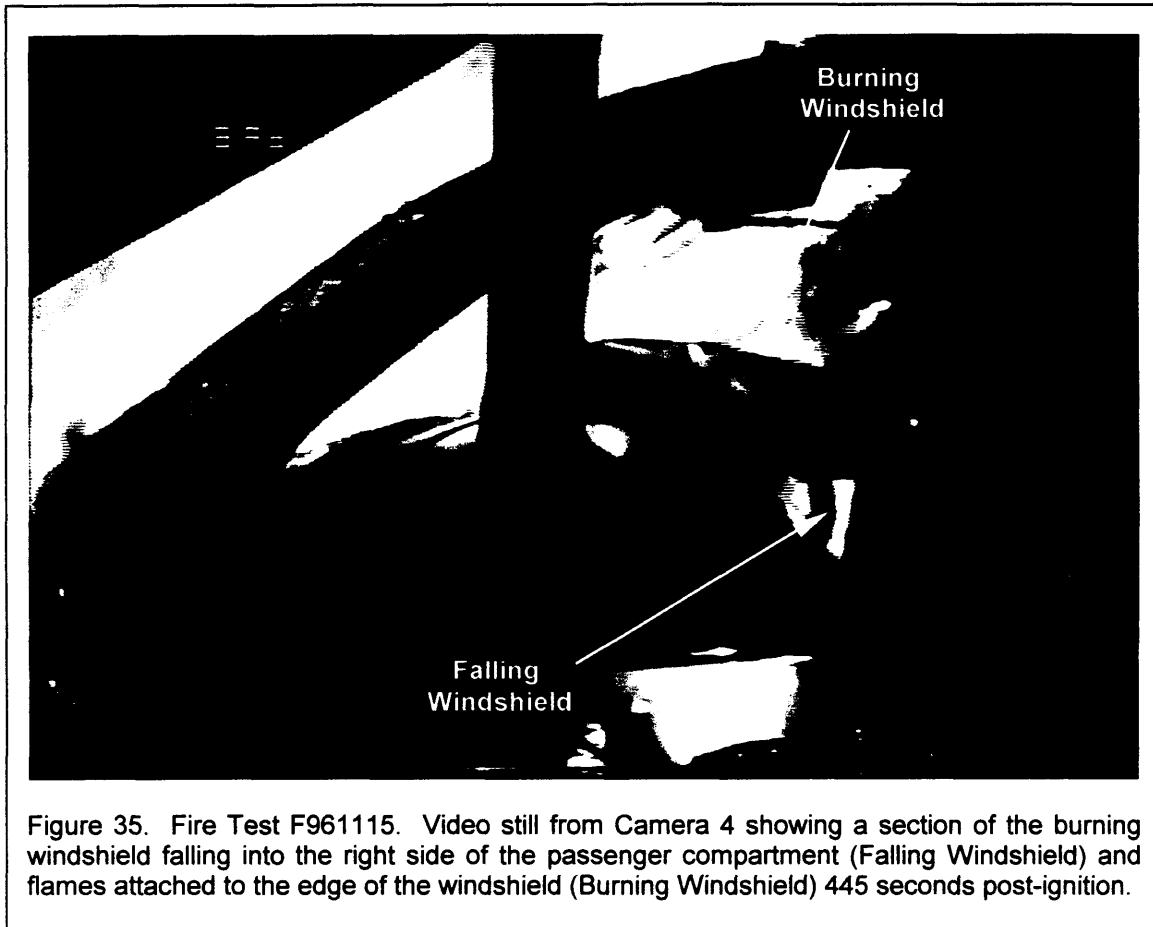


Figure 35. Fire Test F961115. Video still from Camera 4 showing a section of the burning windshield falling into the right side of the passenger compartment (Falling Windshield) and flames attached to the edge of the windshield (Burning Windshield) 445 seconds post-ignition.

These components are out of the field-of-view in Figure 33, but flames are visible behind the lower right edge of the steering wheel in the area of the deployed passenger airbag. Once objects in the passenger compartment behind the roof-line (rearward of the forward edge of the roof) ignited, heat and combustion gases started to accumulate in the passenger compartment.

Figure 36 shows plots of air temperature at six heights in the passenger compartment: 1, 4, 7, 10, 13, and 16 inches below the lower surface of the headliner. The temperature of the layer of air just below the headliner (1 inch, Fig. 36) increased from about 50°C to greater than 100°C

between 7 and 8 minutes post-ignition. The air temperature 16 inches below the headliner was only 32°C. The concentrations of the measured combustion gases (measured 6 inches below the headliner) also started to accumulate in the passenger compartment between 7 and 8 minutes post-ignition (see **SECTION 8** and **APPENDIX I**).

A layer of heated combustible gasses produced by thermal decomposition of materials in the instrument panel, the deployed air bags, the interior trim panels, the front seats, and the carpet accumulated below the headliner of the test vehicle, and ignited between 9 and 10 ½ minutes post-ignition. The temperature recorded from the thermocouple closest to the headliner increased from approximately 150 to > 800°C between 9 and 10½ minutes post-ignition.

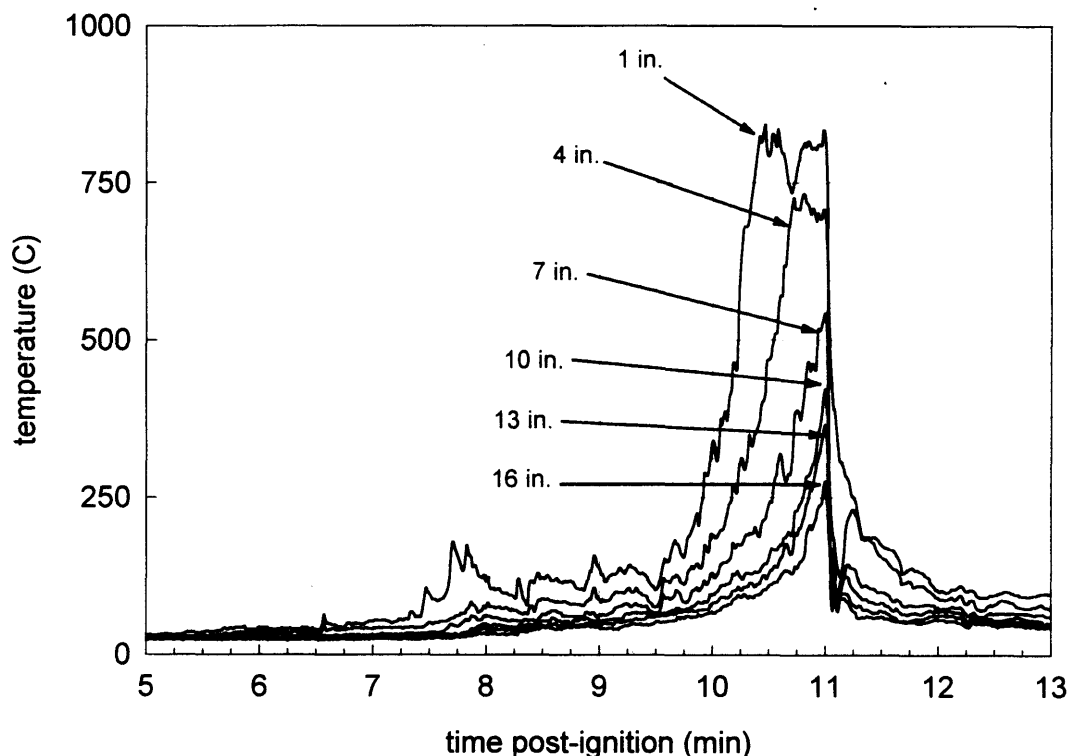


Figure 36. Fire Test F961115. Plots of air temperature in the passenger compartment measured 1, 4, 7, 10, 13, and 16 inches below the lower surface of the headlining.

Flames began to emerge from the driver's door window starting at about 10 minutes post-ignition, indicating that the burning upper layer filled the space from the lower surface of the headliner to the top edge of the window frame. A rapid expansion of the gases in the burning zone lead to an efflux of gases through the top of the window opening in the driver's door (Fig. 37). A net inflow of air was detected through the driver's door window beginning at 2 minutes post-ignition, which continued until about 9½ minutes post-ignition. This was consistent with the observation of

smoke being drawn out through the windshield (see Fig. 34). The linear velocity of airflow during this time varied between -0.15 and -0.25 m/s. The direction of airflow reversed and the velocity of airflow through the window opening increased at 9½ minutes post-ignition (Fig. 37). The measured airflow through the top of the driver's window was -0.25 m/s at 9½ minutes post-ignition (before ignition of the upper layer) and +1.5 m/s – net outflow of air from the passenger compartment – at 11 minutes post-ignition.

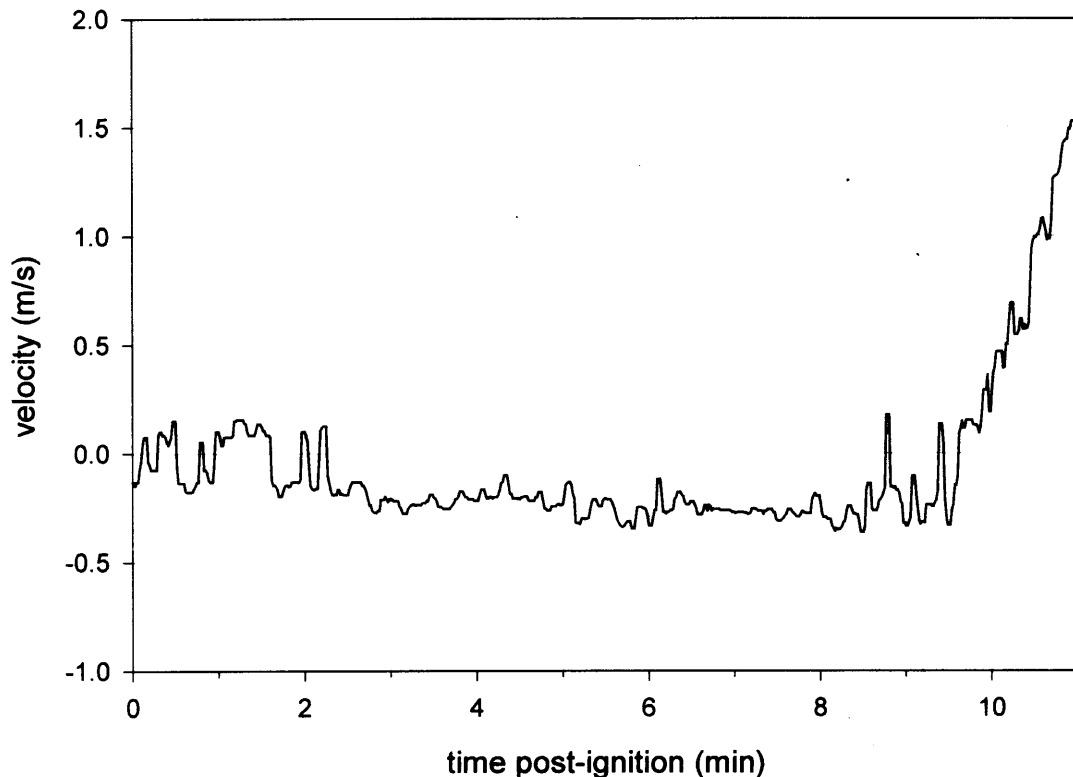


Figure 37. Fire Test F961115. Plot of airflow through the window in the driver's door. Velocity was measured using a bi-directional probe located at the top of the window opening in the driver's door. A positive velocity indicated net outflow and a negative velocity indicated net inflow.

Radiation from the burning upper layer ignited the deployed driver's air bag and the upper surfaces of the seat backs on the driver and front passenger seats. The signal to end the test was given at about 10¾ minutes post-ignition. A fine water mist was sprayed into the passenger compartment through the window in the driver's door. The water mist extinguished the burning upper layer within a few seconds, causing a rapid drop in air temperature in the passenger compartment (see Fig. 34). The water mist was then directed into the hole in top of the instrument panel, which extinguished the fire in the instrument panel and cooled melted plastic components rapidly without appreciably disrupting their shapes. Finally, the water mist was

sprayed through the gaps between the crushed hood and left fender to suppress flames in the engine compartment.

### 5.3 Flame-spread Downward into the Instrument Panel

The thermocouple data and physical evidence obtained during inspection of the vehicle after the test indicated that flames spread from the instrument panel top cover downward into the HVAC demister and distribution ducts, and partially into the HVAC distribution housing. The center of the instrument panel top cover ignited about 7 minutes post-ignition (thermocouples D8 and D9, Fig. 38).

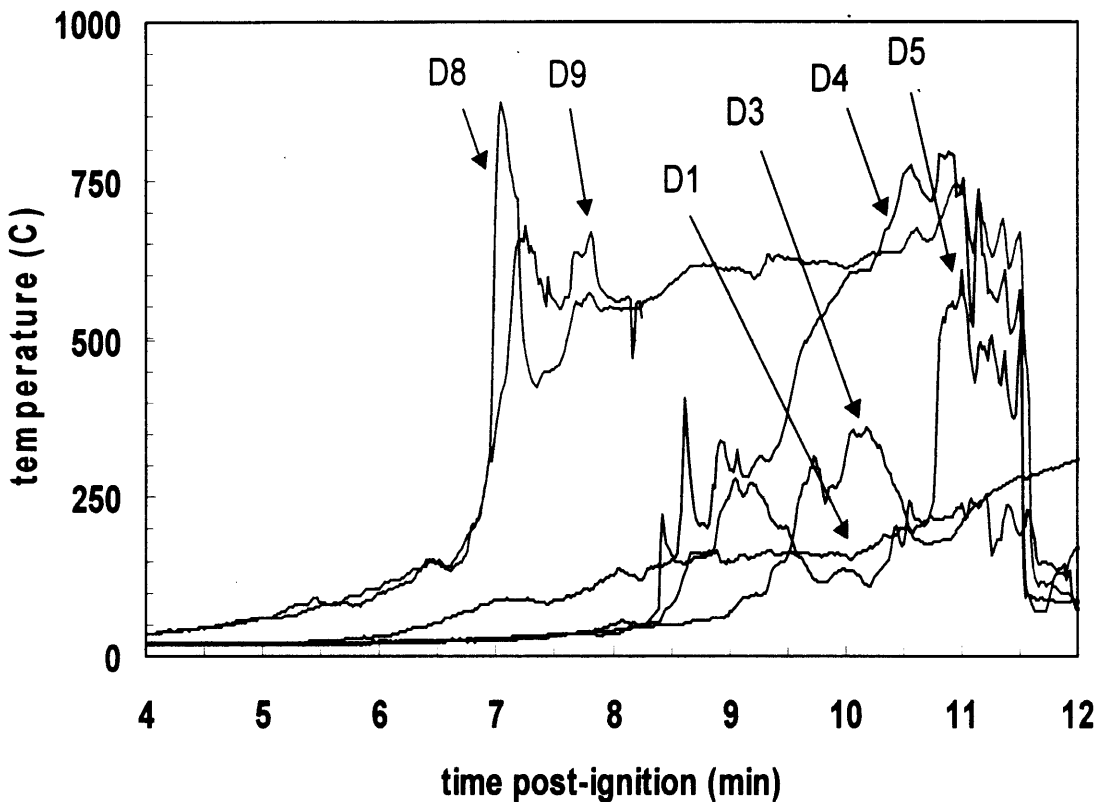


Figure 38. Fire Test F961115. Plots of temperatures recorded by thermocouples on the center of the instrument panel top cover (D8 and D9), in the left (D5), center (D4), and right (D3) of the distribution ducts, and in the upper section of the distribution housing (D1). See Figures C3 through C5 in **APPENDIX C** for the approximate locations of the D thermocouples in the test vehicle.

Hot gas and flames started to penetrate the center of the distribution duct assembly between 8 and 9 minutes post-ignition (Thermocouple D4, Fig. 38), which was burning by 10 minutes post-ignition. The distribution ducts extending to the left and right were not fully in flames when the

instrument panel was extinguished about 11½ minutes post-ignition (Thermocouples D3 and D5, Fig. 38). The temperature in the top of the distribution housing remained below 250°C throughout the test (Thermocouple D1, Fig. 38), indicating that the fire was extinguished before flames had spread to the bottom of the distribution housing. If there had been fire damage to the lower exterior surfaces of the distribution duct assembly and to the lower section of the distribution housing, it would have been nearly impossible to determine the direction of flame-spread in the center of the instrument panel. The absence of flame damage to the lower section of the distribution housing allowed unambiguous determination of flame-spread through the dash panel into the HVAC module (see **SECTION 6**).

Physical inspection of the test vehicle showed that fire damage was greatest to components in the upper section of the instrument panel – the top cover and distribution ducts, which suggests that flames spread downward into the center of the instrument panel from the instrument panel top cover. The instrument panel top cover was almost completely consumed by the fire (Fig. 39), but there was little fire damage to the front of the instrument panel (Fig. 40). A large section of the deployed passenger airbag was consumed by fire. The edge of the remaining fabric was melted, forming a brittle, charred, and inflexible solid. The vinyl covering on the passenger airbag door in the instrument panel was melted and charred. There was no apparent thermal or fire damage to the lower steering column cover, the knee bolster reinforcement, the steering column, or the lower

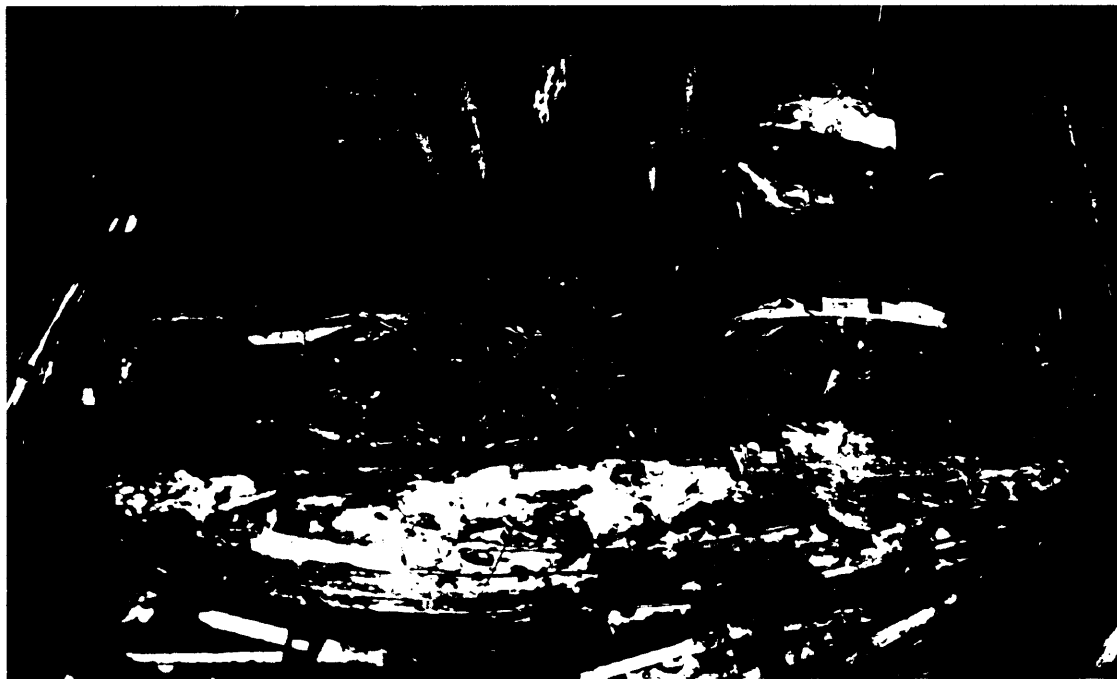


Figure 39. Fire Test F961115. Photograph showing fire damage to the instrument panel top cover.

face of the instrument panel.

The carpet was burned in several areas in front of the driver's seat, in front of the front passenger's seat, and between the driver's and front passenger's seats. Fragments of broken glass were found in all of these burned areas (Fig. 40). Pieces of the HVAC module, which fractured during the crash test and had fallen onto the carpet in front of the passenger's seat, were partially melted and charred (Fig. 40).

The lower right side of the center storage bin in the instrument panel was charred and melted. Small fragments of the windshield were embedded in the melted plastic. There was no evidence of flame-spread through the gap between the driver's door and the hinge pillar (Fig. 40). Nor was there evidence of thermal damage to the interior silencer pad, carpet pad, or carpet from conductive heating through the lower dash panel and floor pan.

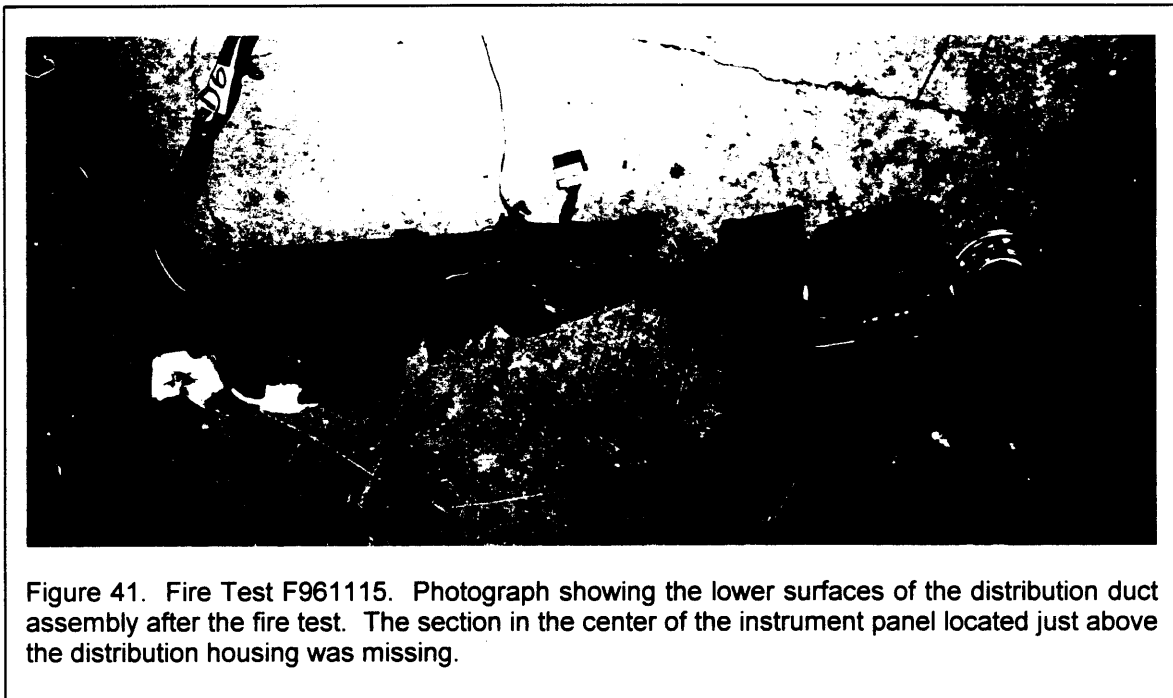


Figure 40. Fire Test F961115. Photograph showing fire damage to the front of the instrument panel and front carpet.

The extent of fire damage to the interior of the instrument panel was not clearly visible without disassembling the instrument panel. Components were removed sequentially to reveal fire damage to the interior of the instrument panel. The HVAC demister ducts, which were located just below the IP top cover and spanned almost the entire width of the dash, were melted, burned,

and charred. The instrument cluster and associated wiring harnesses, and the passenger air bag module, the HVAC vent nozzles, the HVAC distribution housing and the dash panel steering column mounting bracket and the body control module contained no evidence of fire damage. The carpeting and carpet pad were removed from the front of the passenger compartment, to approximately the rear mounting bolts for the front seats. Except for areas that were ignited by the windshield, the carpet, carpet pad, and mastic coating on the interior surface of the floor pan showed no evidence of thermal damage from conductive heat transfer through the floor pan.

The distribution duct assembly was burned through only in the center where it attached to the distribution housing (Fig. 41). The upper surfaces of the distribution ducts (not shown in Fig. 41) extending to the right and left were melted and charred along the entire width of the instrument panel. The plastic on the lower exterior surfaces of the ducts contained soot deposits, and had melted and flowed in several areas, but were not burned or charred (Fig. 41).



Most of the thermoplastic material in the upper section of the HVAC distribution housing was melted and charred. The lower exterior surfaces of the HVAC distribution housing showed no evidence of fire damage (Fig. 42).



Figure 42. Fire Test F961115. Photographs showing fire damage to the top (upper photograph) and lack of fire damage to the bottom (lower photograph) of the HVAC distribution housing.

#### 5.4 Flame-spread to the Front Seats

Fire damage to the driver's seat was greatest on the integral head restraint, where a large area of the fabric covering was melted exposing the underlying polyurethane foam (Fig. 43).



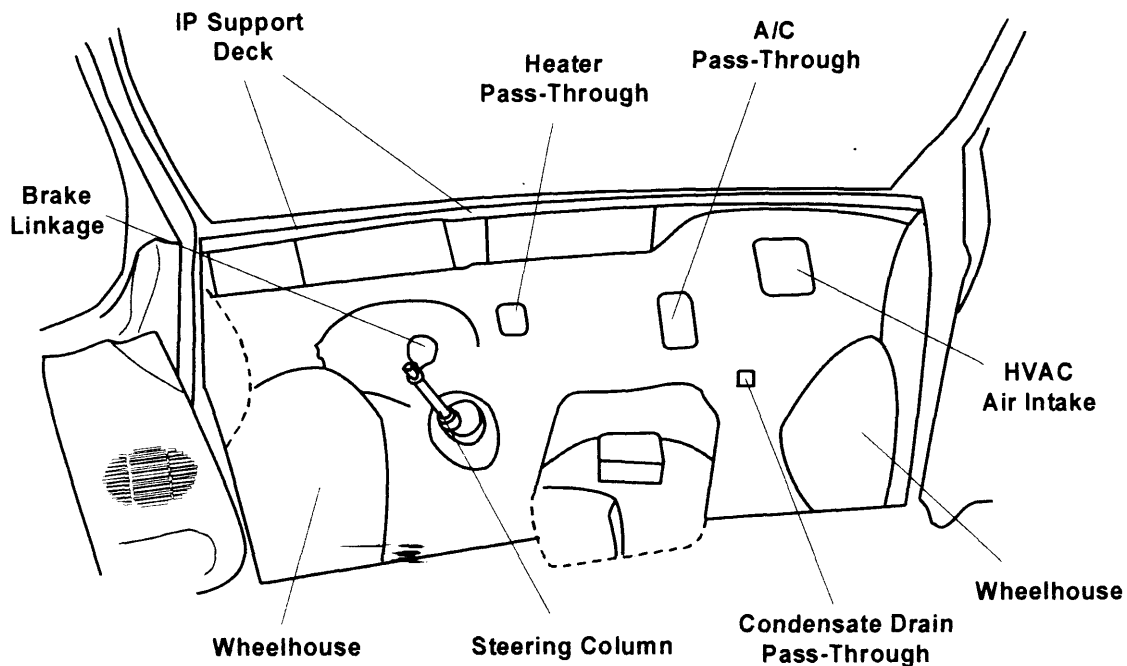
Figure 43. Fire Test F961115. Photograph showing fire damage to driver's (right photograph) and front passenger's (left photograph) seats.

The fabric was burned-through along the right (inboard) edge of the seat cushion, exposing the underlying foam. The fabric also was charred in the center of the seat cushion. The underside of the armrest (which was in the raised-position during the fire test) was charred. On the passenger's seat, the fabric was melted and charred on the head restraint, most of the seat back, and almost the entire upper surface of the seat cushion. Portions of the vinyl covering on the underside of the armrest (which was in the raised-position during the fire test) and on the front edge of the seat cushion also were melted and charred. The inboard corner of the storage bin under the seat was melted and charred. The pattern of melted and charred material on the seats indicates that thermal damage to the head restraints, seat backs, and armrests appears to have

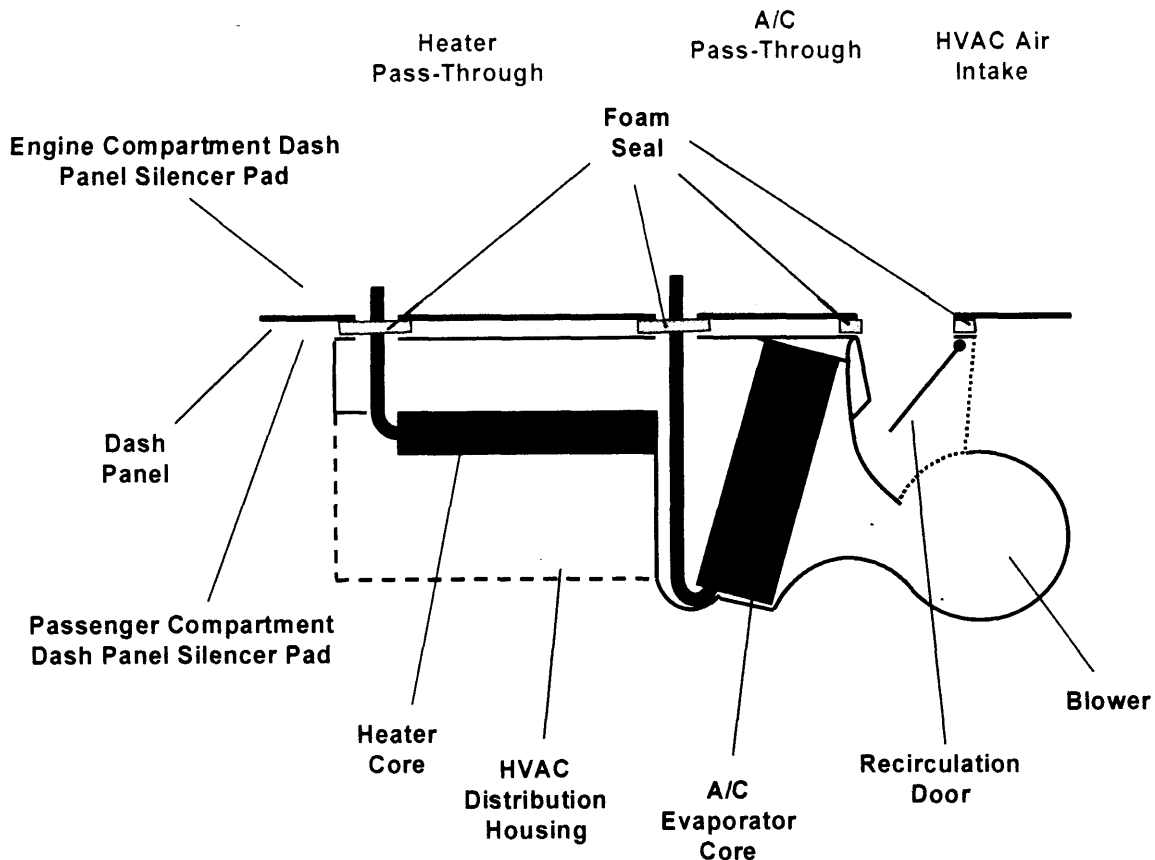
been caused by heat transfer from the burning passenger airbag and headliner. The seat cushions on both front seats, and the storage bin under the passenger's seat were ignited by pieces of the burning windshield that fell into the passenger compartment.

## 6 Flame-spread into the Passenger Compartment through the Dash Panel

The dash panel in the test vehicle contained a number of openings that could provide a path for flames to spread from the engine compartment into the passenger compartment. These potential fire paths included the HVAC air intake, the heater pass-through, A/C pass-through, the HVAC condensate drain pass-through, the brake linkage pass-through, and the steering column pass-through (see diagram below).



As stated in the **INTRODUCTION**, the residual crush to the front left corner of the test vehicle was 585 mm. The engine was displaced to the right and rearward against the dash panel, causing the right side of the dash panel to buckle inward where it was loaded by the displaced engine. The master cylinder power booster was crushed against the dash panel, blocking the brake-linkage pass-through. The steering-column pass-through was low in the dash panel and covered by a rubber boot, which remained intact after the crash test. The heater pass-through, the A/C pass-through, the condensate drain pass-through, and the HVAC air intake open into the HVAC module, which mounts to the interior face of the dash panel. The diagram below shows a top-view of the HVAC module mounted to the dash panel as it appeared in the test vehicle before the crash test. As a result of the deformation to the right side of the dash panel, the HVAC module broke in several places, and was dislodged rearward from its mounts to the dash panel.



The foam seals around the heater pass-through (see **SECTION 6.2**) and the A/C pass-through (see **SECTION 6.3**) were no longer compressed against the dash panel, creating gaps between the HVAC module and the dash panel in these areas. The HVAC in the test vehicle was set to the A/C recirculation mode before the crash test, causing the recirculation door to close completely. The recirculation door was dislodged from the closed position during the crash test (see **SECTION 6.4**), creating an opening from the HVAC air intake cowl into the instrument panel.

These crash-induced openings in the dash panel were obscured from view during the fire test. The engine and other components that were pushed to the rear of the engine compartment during the crash test obscured the exterior surface of the dash panel from video cameras located outside the vehicle. The instrument panel covered these openings, and obscured the interior surface of the dash panel from cameras located inside the vehicle. Data from the temperature and heat flux data suggested that flames spread through one or more of the crash-induced openings in the dash panel during this test. However, the number of thermocouples around these openings was not adequate to determine unambiguously all of the flame-spread pathways from the engine compartment into the passenger compartment through the dash panel or the exact timing of flame-spread through each of these openings. The pattern of fire and heat damage to

components in the instrument panel was important information in reconstructing the fire paths through the dash panel. Evidence of heat and flame spread into the instrument panel, which included deposits of soot and tar, melted and charred plastic, and paint discoloration, was obtained when the vehicle was systematically disassembled after the fire test. Much of this evidence was preserved because the fire was extinguished shortly after the upper layer had ignited, just as flames were penetrating the dash panel. In addition, the water mist used to extinguish the fire cooled the molten plastic rapidly, preserving the geometric shape of the plastic at that instant while avoiding damage that can be caused by a high-pressure water stream.

Fire consumed or melted most of the combustible material in the front of the vehicle and in the upper part of the engine compartment (Fig. 44). The front fascia, the front bumper energy absorber, plastic components around the radiator and cooling fan, and the coolant and refrigerant hoses were consumed, as were the upper sections of the washer fluid and engine coolant reservoirs. Residual fluid prevented the lower sections of each container from burning. A large solidified mass of charred plastic, the remains of the battery case, PDC, and air cleaner housing, was on top of the left frame rail and wheelhouse after the battery plates were removed. The polymer resin in the HVAC air intake cowl was consumed by the fire, leaving only the fiberglass



Figure 44. Fire Test F961115. Photograph showing fire damage to the front of the test vehicle after the fire test.

reinforcement.

The burn-pattern observed on the engine compartment dash panel silencer pad suggested that only its upper section was exposed to flames. The polymeric binder had burned away, leaving only the glass fiber mat containing a carbonaceous residue. The scrims on both faces were gone. The plastic clips holding the silencer pad to the exterior face of the dash panel had melted and presumably burned, allowing the glass fiber mat to fall onto the engine air intake manifold. The lower section of the dash panel silencer pad did not show signs of fire damage. There was no apparent physical evidence of fire damage to components around the brake linkage pass-through, the steering column pass-through, or the HVAC condensate drain pass-through. The temperature and heat flux data from transducers at both faces of the dash panel also did not indicate the presence of flames at the dash panel in these locations (**APPENDICIES C AND E**).

A general observation from the video records was the lack of any significant ground fires under the engine compartment that might have spread into the passenger compartment, which explains the lack of fire damage around openings through the lower portion of the dash panel. These areas were not exposed to flame. The thermocouple and heat flux transducer data (**APPENDICIES C AND E**) indicate that a strong vertical temperature gradient existed along the external face of the dash panel during the latter stages of this test.

### **6.1 Development of a Pressure Gradient Across the Dash Panel**

The thermocouple and heat-flux transducer data indicated that the timing of flame spread through the crash-induced openings in the dash panel correlated with the timing of the development of a pressure gradient across the dash panel. Several factors contributed to the development of positive pressure in the engine compartment. One factor was the growth of the fire in the engine compartment. This was reflected by the monotonically increasing heat- and gas-release rates before the fire spread into the passenger compartment (**APPENDIX H**). Another factor was the progressive settling of the hood during the fire. This was most evident on the right side of the vehicle. As combustible material supporting the hood was consumed in the fire, the hood settled and the area of the gap between the rear edge of the hood and the top of the air intake cowl decreased by a factor of four by the end of the test. Combined with the increasing rate of heat and gas generation, this would have forced flames and hot gases against the upper right side of the dash panel. Finally, a metal duct running along the top of the dash panel would have impeded the naturally upward buoyant flow of the fire plume. The metal duct was part of the HVAC air intake, and formed the instrument panel support deck that extended forward of the dash panel into the engine compartment. The cause of the pressure decrease in the passenger

compartment is not as evident. It may have been related to a decrease in static pressure caused by increasing gas temperatures, but this cannot be confirmed from the data collected in this test.

Pressure measurements at the exterior and the interior faces of the dash panel in the area of the heater and A/C pass-throughs indicated that there was no difference in pressure until about 5½ minutes post-ignition (Fig. 45).

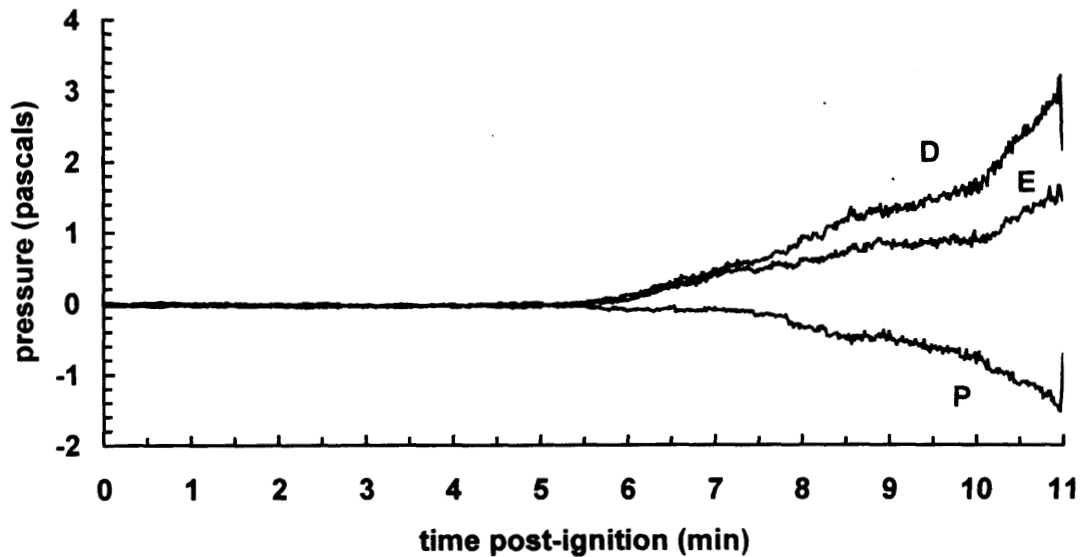


Figure 45. Fire Test F961115. Plots of pressures measured at the dash panel. Pressure taps were located in the approximate center of the dash panel. Curve P is the pressure in the passenger compartment relative to atmosphere; Curve E is the pressure in the engine compartment relative to atmosphere; and Curve D is the differential pressure across the dash panel ( $P_D = P_E - P_P$ ). A positive value indicates the pressure was greater in the engine compartment than in the passenger compartment.

During the first several minutes after ignition, flames spread from the battery and PDC to the hood liner and HVAC air intake cowl. These components were located high in the engine compartment, allowing the flames and hot gas to escape unimpeded from the engine compartment through the gaps along the sides and rear of the deformed hood (**SECTION 4**). The development of a pressure difference across the dash panel appears to have been caused by two factors. The first was a monotonic increase in the heat- and product-release rates of the fire (**APPENDIX H**) that correlated roughly with growth of the fire in the engine compartment. The second was a decrease in pressure in the passenger compartment that appeared to have been the result of entrainment

of air from the passenger compartment through holes in the windshield into the fire plume rising from the engine compartment.

The pressure difference between the engine compartment and the passenger compartment grew monotonically until the end of the test, with the pressure in the engine compartment being higher than the pressure in the passenger compartment. The pressure differential across the dash panel reached a maximum of 3 Pascals by the end of the test (11 minutes post-ignition). The flow rate through each crash-induced opening in the dash panel could not be determined from the data acquired during this test. A simple orifice calculation shows that the induced gas flow rate through a 1 cm<sup>2</sup> orifice at a pressure difference of 3 Pascals would be between 100 and 200 cm<sup>3</sup>/s. The flow rate through an orifice is proportional to the square root of the pressure differential across the orifice. Thus, the gas flow rate through a 1 cm<sup>2</sup> orifice with a 1 Pascal pressure difference would have been between 60 and 120 cm<sup>3</sup>/s. The heater and AC pass-throughs were partially obstructed and inaccessible once the instrument panel had been reassembled. The area open to airflow in these pass-throughs was estimated to be a few square centimeters. As indicated by the thermocouple data and by heat and fire damage to components in the instrument panel, this was sufficient to allow penetration of hot gas and flames through these openings in the dash panel a few minutes before the end of the test. The HVAC air intake was located at the rear of the HVAC air intake cowl in the upper right-hand side of the dash panel. To reach the HVAC air intake from the engine compartment, a portion of the fire plume escaping from the rear edge of the hood had to travel through a combination of composite and metal ducts that comprised the HVAC air intake cowl. Therefore, the estimate of gas flow through openings in the dash panel based on the pressure difference measured across the dash panel may not apply to the entry of hot gas and flames through the HVAC air intake.

## **6.2 The Heater Pass-through**

The pattern of fire damage to components in the instrument panel suggested that flames and hot gas entered the passenger compartment through three openings in the dash panel: the heater pass-through, the A/C pass-through, and the HVAC air intake. Figure 46 shows the locations of thermocouples and the heat flux transducer/radiometer assembly around the heater pass-through. The data from thermocouple B5 (Fig. 47) indicates that the outer surfaces of the air intake cowl above the heater pass-through was burning by about 4 minutes post-ignition. The temperature at the exterior surface of the engine compartment dash panel silencer pad above the heater pass-through started to increase about 4 minutes post-ignition, but remained less than 600°C until approximately 6½ minutes post-ignition (Thermocouple C5, Fig. 47). The measured heat flux to the exterior surface of the silencer pad at this location increased from 2 to 4 kW/m<sup>2</sup> at 4 minutes

post-ignition to about 20 kW/m<sup>2</sup> at this time (HFT2, Fig. 47). These results indicate that flames were contacting the exterior surface of the silencer pad above the heater pass-through between 6 and 7 minutes post-ignition. The timing of flame-contact with the silencer pad in this location was coincident with the development of a pressure gradient of approximately 1 Pa across the dash panel (Fig. 45).

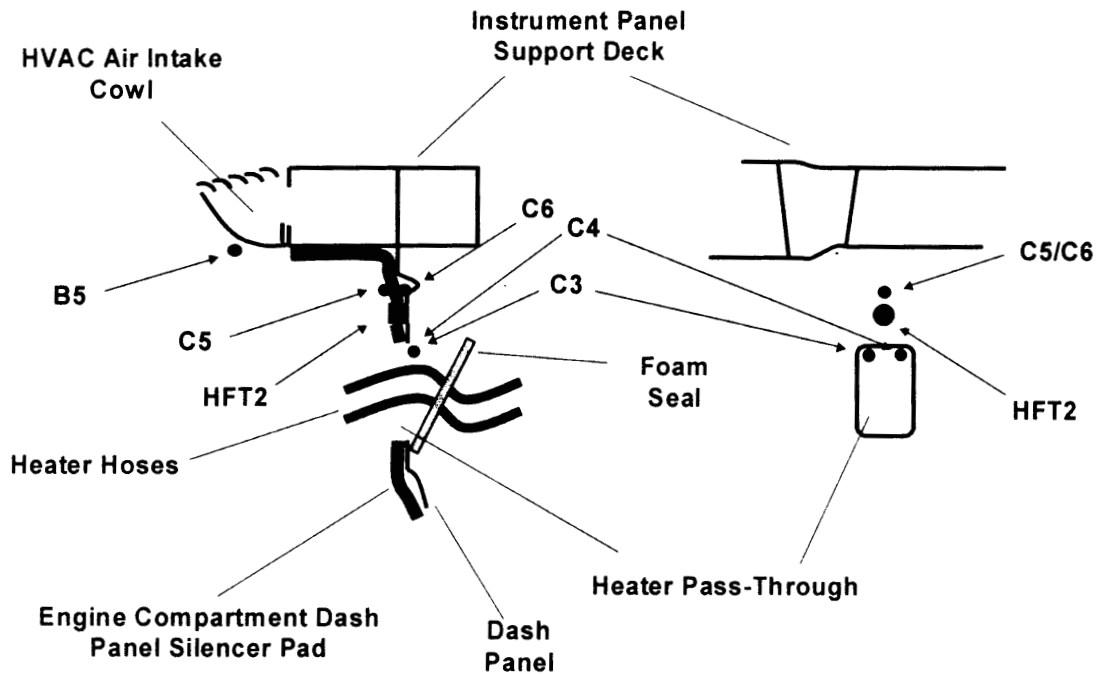


Figure 46. Fire Test F961115. Diagrams of the instrumentation in the dash panel around the heater pass-through. The diagram at the left is a schematic cross-section of the dash panel through the center of the heater pass-through. The diagram at the right is a schematic view of the interior face of the dash panel showing the heater pass-through. Thermocouple B5 was attached to the lower exterior surface of the HVAC air intake cowl above the heater pass-through. Heat-flux transducer 2 (HFT2) was inserted through the dash panel and engine-compartment-dash-panel-silencer pad just above the heater-hose pass-through. Thermocouples C3 and C4 were positioned in the gap between the dash panel and the dislodged foam seal. Thermocouple C5 was located above HFT2 approximately 1 cm in front of the silencer pad. Thermocouple C6 was located above HFT2 between the silencer pad and dash panel.

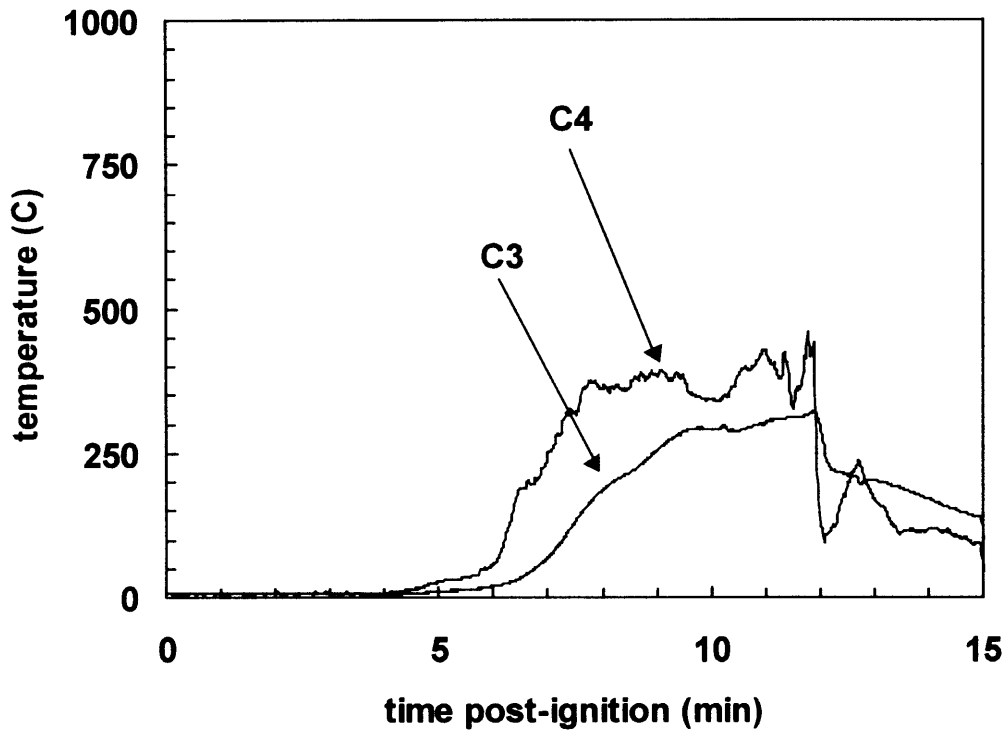
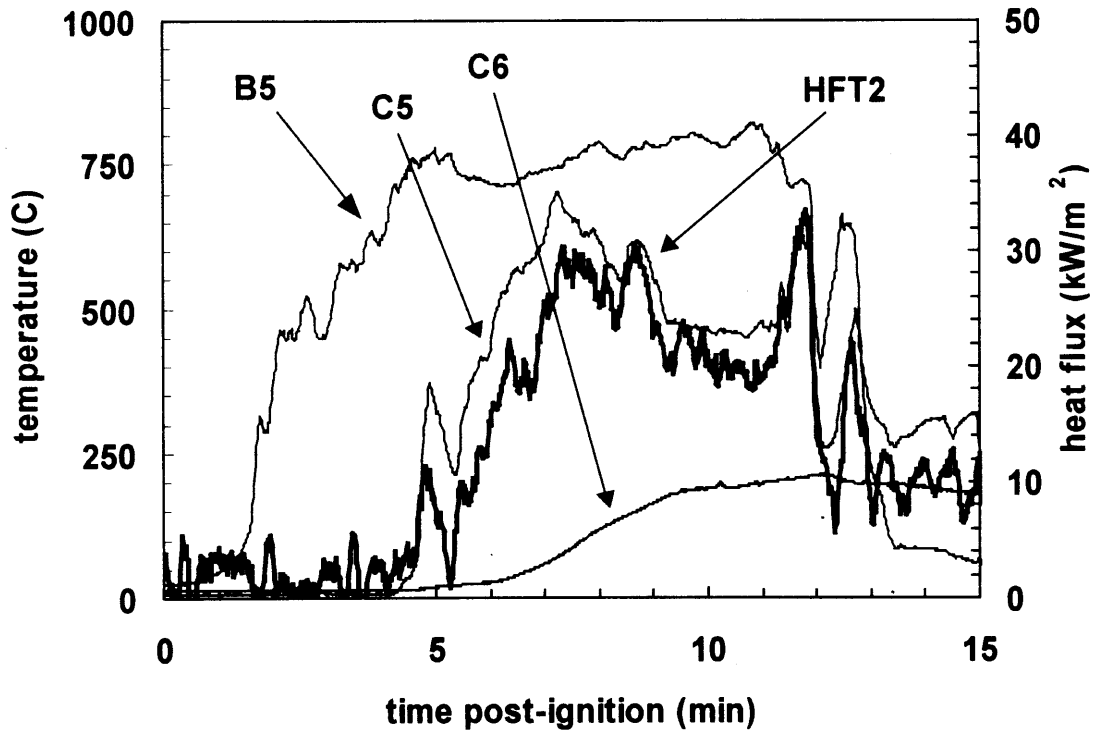


Figure 47. Fire Test F961115. Plots of temperatures recorded by Thermocouples B5, C5, and C6, and the heat-flux measured by HFT2 (upper panel), and temperatures recorded by Thermocouples C3 and C4 (lower panel).





Figure 49. Fire Test F961115. Photographs showing lack of fire damage to the passenger-compartment-dash-panel silencer pad (upper photograph) and dash panel (lower photograph) around the heater pass-through.

42, upper panel) was caused by flame spreading downward in the center of the instrument panel and not flame spread through the heater pass-through.

The upper edge of the passenger compartment dash panel silencer pad above the heater pass-through was melted and charred where flames had penetrated deepest into the center of the instrument panel, but the material around the heater was not charred, melted nor discolored (Fig. 49). The interior surface of the dash panel contained a light coating of soot, but did not contain heavy deposits of tar which are typically produced by thermal decomposition of thermoplastic material (Fig. 49). Soot was deposited on the exterior face of the flexible foam seal around the heater tubes. Hot gas flowing into the heater pass-through apparently caused the cellular structure to collapse in the upper right corner of the seal, but the polymer did not melt and flow. Gas flow through this opening appeared to have been at least partially obstructed by the engine air intake manifold, which was displaced rearward against the center of the dash panel in the crash test.

### **6.3 The A/C Pass-Through**

Flames also began to contact the exterior surface of the engine-compartment-dash-panel silencer pad around the A/C pass-through between 6 and 7 minutes post-ignition. Figure 50 shows the locations of the thermocouples and the heat flux transducer/radiometer assembly around the A/C pass-through. The temperature recorded at the surface of the silencer pad (C7, Fig. 51) increased rapidly from ambient to approximately 600°C between 5 and 6 ½ minutes post-ignition. The heat flux to the exterior surface of the silencer pad increased from less than 5 to approximately 30 kW/m<sup>2</sup> at this time (HFT3, Fig. 51). The temperature recorded by thermocouple C8 remained less than 150°C throughout the test. As before, the start of flame contact with the silencer pad correlated closely with the development of a pressure gradient across the dash panel (Fig. 45), and not the presence of flames on the HVAC air intake cowl above this area (B6, Fig. 51).

Flames penetrated the dash panel through the upper right corner of the A/C pass-through. Temperatures recorded by the thermocouple in the upper left corner of the A/C pass-through were less than 300°C throughout the test (C9, Fig. 51). In contrast, temperatures recorded by the thermocouple in the upper right corner (C10, Fig. 51) exceeded the flame-threshold of 600°C from approximately 6½ to 9 minutes post-ignition (C7, Fig. 51). The passenger-compartment dash-panel silencer pad was melted and burned-through in this area (Fig. 52, upper photograph). The flexible foam backing was eroded and charred above the A/C pass-through, and a thick layer of

tar was deposited on the dash panel and instrument panel support deck above the A/C pass-through (Fig. 52, lower photograph).

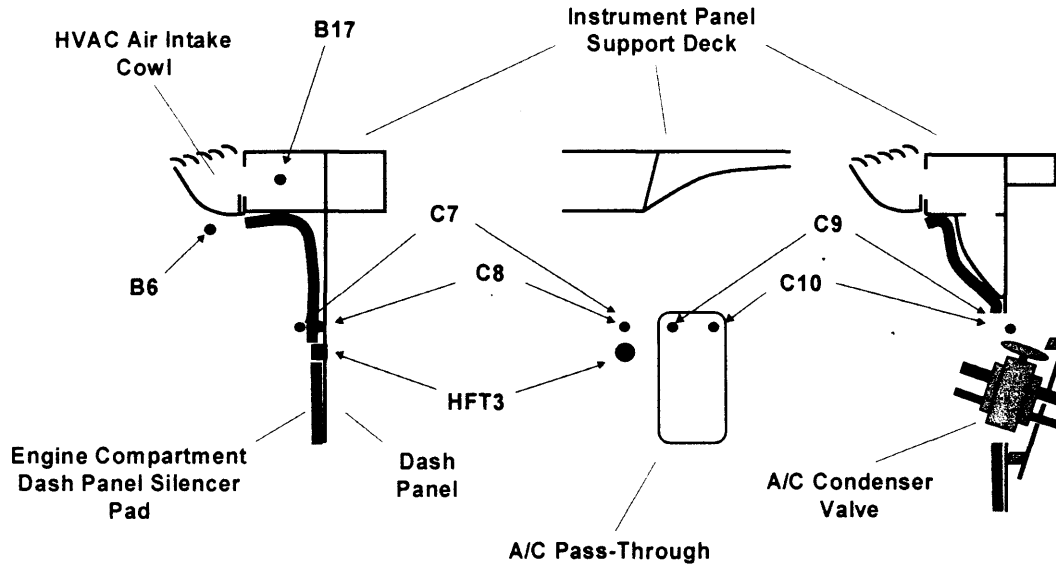


Figure 50. Fire Test F961115. Diagrams showing the location of instrumentation in the dash panel around the A/C pass-through. The diagram at the left is a schematic cross-section of the dash panel to the left of the A/C refrigerant line pass-through. The diagram in the center is a view of the interior face of the dash panel. The diagram at the right is a schematic cross-section of the dash panel through the A/C refrigerant line pass-through. Thermocouples B6 and B17 were located on the lower exterior surface of the HVAC air intake cowl and inside the metal duct behind the intake cowl, respectively. Heat-flux Transducer 3 (HFT3) was inserted through the dash panel and engine-compartment-dash-panel-silencer pad to the left of the A/C pass-through. Thermocouple C7 was located above HFT2 approximately 1 cm in front of the silencer pad. Thermocouple C8 was located above HFT2 between the silencer pad and dash panel. Thermocouples C9 and C10 were positioned in the gap between the dash panel and the dislodged condenser valve/sealing plate assembly.

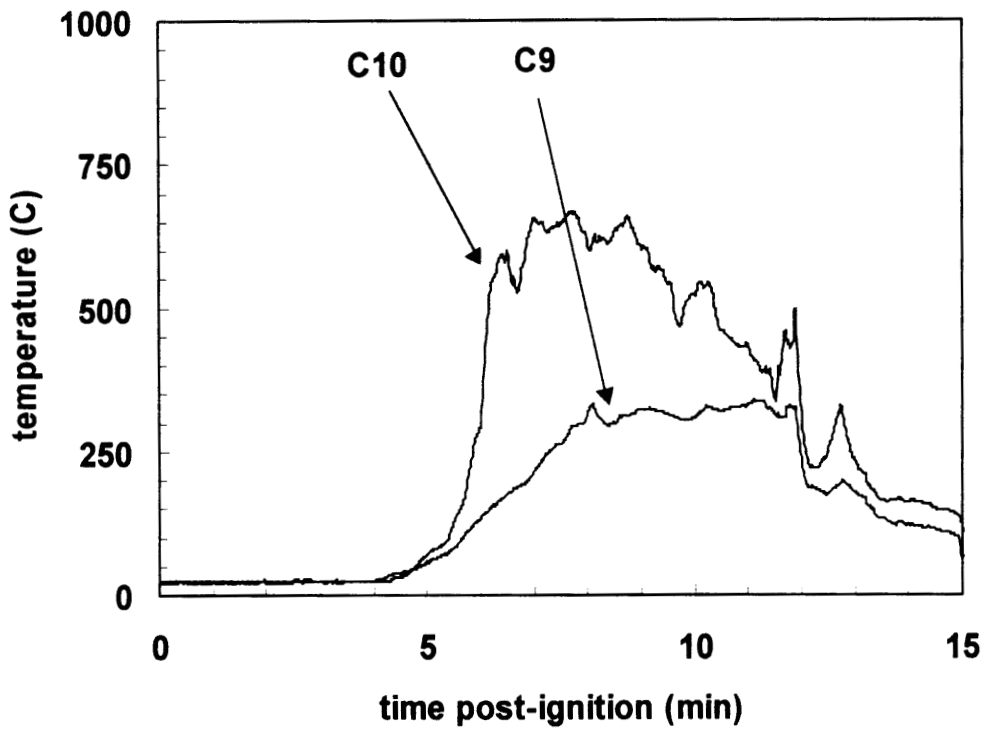
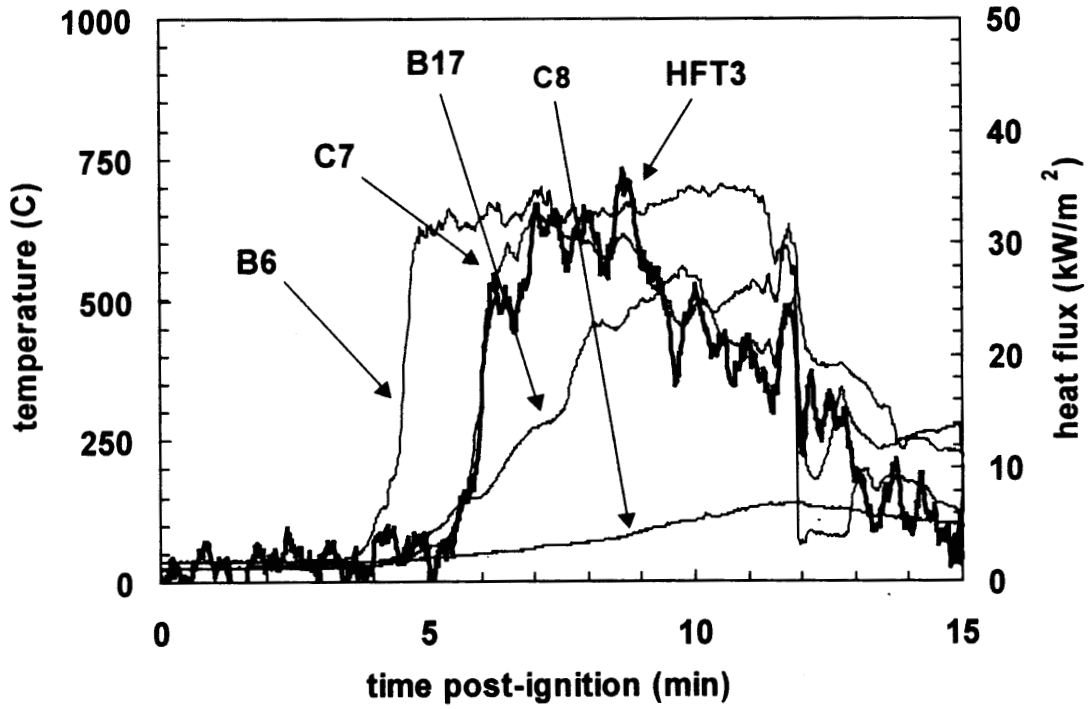


Figure 51. Fire Test F961115. Plots of temperatures recorded by Thermocouples C7 and C8 (upper panel, heat-flux measured by HFT3 (upper panel), and temperatures recorded by thermocouples C9 and C10 (lower panel).

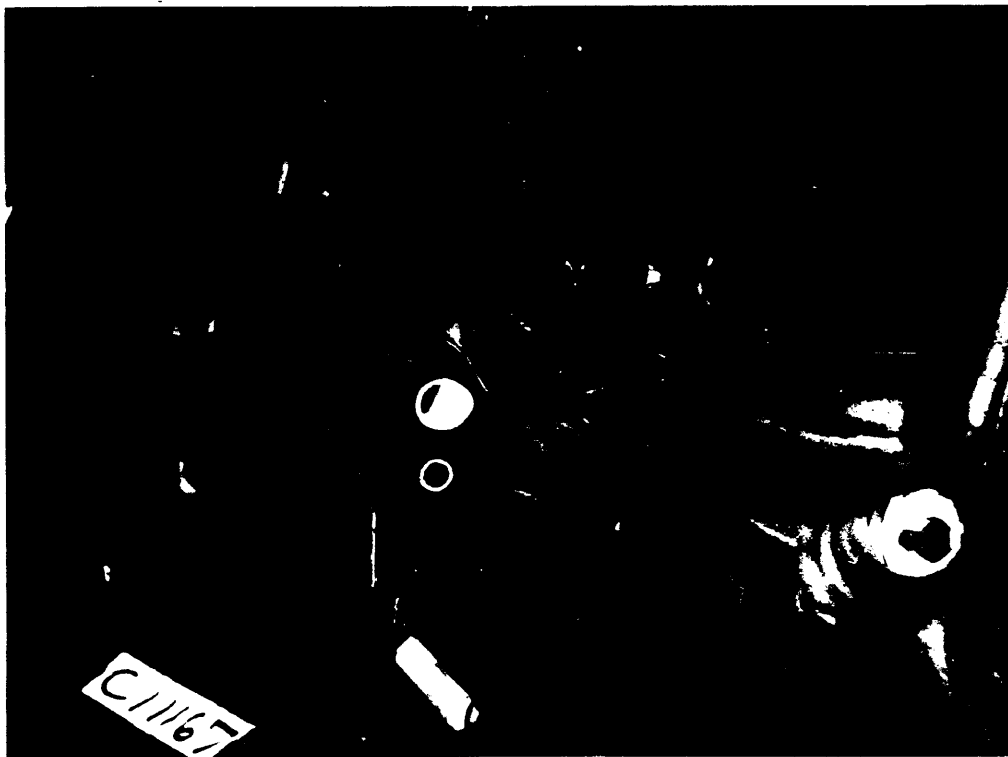


Figure 52. Fire Test F961115. Photographs showing heat and fire damage to the passenger compartment dash panel silencer pad (upper photograph) and the dash panel (lower photograph) around the A/C pass-through.

#### 6.4 The HVAC Air Intake

Evidence of flame-spread through the HVAC air intake from the thermocouple data is ambiguous. Figure 53 shows the locations of thermocouples around the HVAC air intake. Thermocouples B8 and B12 indicated flames below and in the air intake cowl above the HVAC air intake from 5 minutes post-ignition to the end of the test (Fig. 54). Although the temperatures recorded by thermocouples B18, and C11 and C12 increased sharply between 5 and 6 minutes post-ignition, they remained less than 600°C throughout the test. These thermocouples were in the path from the cowl to the HVAC air intake, suggesting that flames did not reach the air intake.

Fire damage to the recirculation door (Fig. 55) and the passenger-compartment-dash-panel silencer pad suggest direct exposure to flames (Fig. 56, upper photograph). In addition, thermocouple D2 measured several temperature-spikes exceeding 850°C in the HVAC blower housing from 10 minutes post-ignition to the end of the test, clearly indicating the presence of flames inside the HVAC module. A fire plume entering the center of the HVAC air intake may have missed thermocouples C11 and C12, which were positioned close to the upper-left and upper-right corners of the opening (Fig. 53).

The passenger-compartment-dash-panel silencer pad was charred and melted above the HVAC air intake (Fig. 56, upper photograph). The foam backing was eroded and charred above this area. The interior surface of the dash panel was coated with a layer of tar to the right and left of the HVAC air intake (Fig. 56, lower photograph). The lower surface of the instrument panel support deck contained a layer of tar and smoke above the A/C line feed-through.

The recirculation door was a metal plate with flexible foam covering both faces. The foam layer on the outer face was melted and charred, and contained a thick layer of soot. Flame damage was localized to the center of the door, with soot deposited above the charred area (Fig. 55). The blower housing was melted where it sealed to the forward bulkhead around the air intake. The upper interior surface of the blower housing, directly below thermocouple D2, contained smoke deposits, and was melted and charred in areas (Fig. 57).

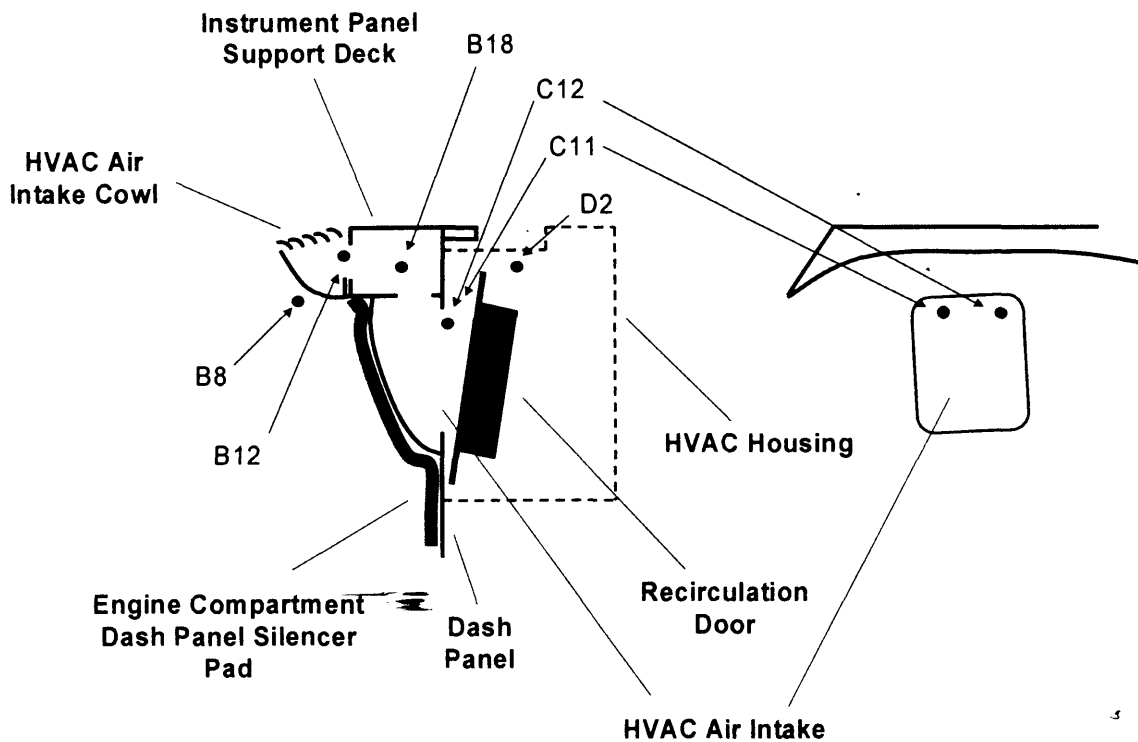


Figure 53. Fire Test F961115. Diagrams showing the locations of thermocouples in the dash panel and HVAC module around the HVAC air intake. The diagram at the left is a schematic cross-section of the dash panel through the HVAC air intake. The diagram at the right is a view of the interior face of the dash panel. The dashed line indicates the approximate outline of the HVAC module. Thermocouples B8, B12, and B18 were located on the lower exterior surface of the HVAC air intake cowl, inside the HVAC air intake cowl, and inside the metal duct behind the intake cowl, respectively. Thermocouples C11 and C12 were positioned in the gap between the air intake and the recirculation door. Thermocouple D2 was in the HVAC module between the recirculation door and blower.

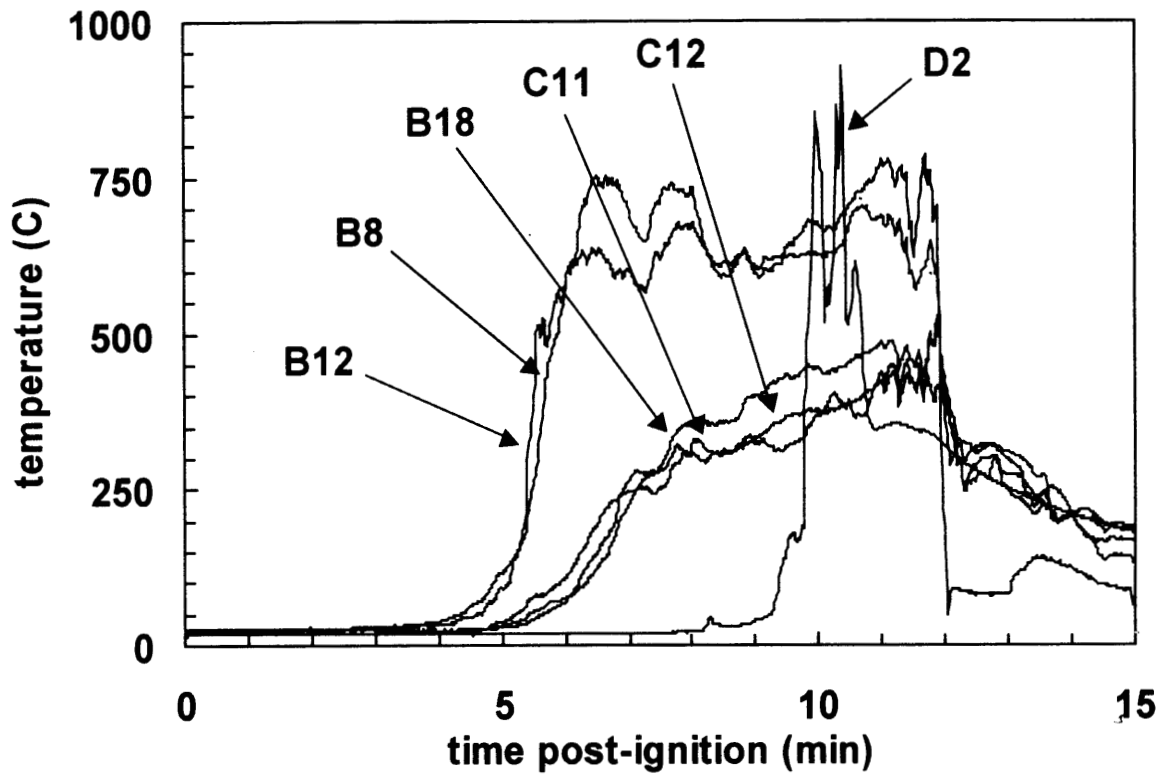


Figure 54. Fire Test F961115. Plots of the data recorded by the thermocouples in the dash panel and HVAC module around the HVAC air intake.



Figure 55. Fire Test F961115. Photograph showing fire damage to the exterior face of the HVAC recirculation door.



Figure 56. Fire Test F961115. Photographs showing heat and fire damage to the passenger compartment dash panel silencer pad (upper photograph) and the dash panel (lower photograph) around the HVAC air intake.



Figure 57. Fire Test F961115. Photograph of the HVAC module showing soot deposits and melted plastic on the interior surface of the HVAC blower housing.

## 7 Combustion Conditions

The output of combustion products from a fire depends on the material burning and on the supply of air to the flame. A well-ventilated fire is one in which the air supplied to the flames is sufficient for complete combustion. In partially enclosed spaces, such as an engine compartment or passenger compartment, airflow to the flames may be inadequate for complete combustion. In this case, called a ventilation-controlled or under-ventilated fire, the supply of air limits both the heat released by the fire and oxidation (combustion) of the gaseous fuel in the fire zone. As ventilation decreases, the output of carbon monoxide, hydrocarbons, smoke, and other products of incomplete combustion increase. The chemical composition of these gases depends on the chemical compositions of the materials burning and on the burning conditions, primarily ventilation. Accumulation of partially oxidized gases and gaseous unburned thermal decomposition products in an enclosed space can create a hazardous condition. In most cases, these gases are heated relative to the surrounding air and, because of their buoyancy, typically accumulate below the ceiling or roof of the enclosed space, forming what is called the upper layer. The upper layer can be ignited by flames from burning objects (piloted ignition) or can ignite spontaneously (autoignition) when the temperature of the gases exceeds a minimum threshold temperature (autoignition temperature), which depends on the chemical composition and the fuel/oxygen ratio of the gaseous upper layer. Once ignited, radiation from the burning upper layer transfers heat downward, and may ignite combustible materials below the burning upper layer. Some of the partially oxidized gases and unburned thermal decomposition products may be toxic (see **SECTION 8**). Ventilation has a significant effect on the chemical composition of the gases produced in a fire.

The equivalence ratio is a quantitative measure of ventilation:

$$\Phi = \frac{\left[ \text{fuel} / \text{O}_2 \right]_{\text{fire}}}{\left[ \text{fuel} / \text{O}_2 \right]_{\text{stoichiometric}}}$$

where  $\Phi$  is the equivalence ratio,  $[\text{fuel}/\text{O}_2]_{\text{fire}}$  is the fuel-to-oxygen ratio in the fire, and  $[\text{fuel}/\text{O}_2]_{\text{stoichiometric}}$  is the fuel-to-oxygen ratio required for complete combustion. In most instances, the equivalence ratio cannot be measured directly in a large-scale test such as this. Different materials burned at different times and in different environments. Ventilation, and thus the equivalency ratio is not uniform in situations where objects are burning in different physical environments, such as burning motor vehicle. It was impossible to isolate and measure the fire

products produced by each of the materials burning, and to measure airflow into each of the unique environments that existed during this test. Estimates of the average ventilation was obtained from the data acquired during this test.

Heat and combustion gases produced by all burning objects in the test vehicle rose into the Fire Products Collector at the test facility. Thus, data from the Fire Products Collector can be used to estimate an average ventilation for the burning vehicle. A similar approach can be used to estimate an average ventilation for the passenger compartment from the gas concentration measurements from the FTIR gas analyzer and the air temperature data from the aspirated thermocouples. Estimation of ventilation from these data is done by comparison to the results obtained from testing individual materials in small-scale flammability tests,<sup>15</sup> where the equivalence ratio can be measured precisely [6].

Five derived parameters were used in this comparison. Values of these parameters for polymeric materials similar to those used in the test vehicle are shown in Table 1.

Table 1  
Fire Products for Well-ventilated Fires<sup>1,2</sup>

material	Y(CO)/Y(CO <sub>2</sub> ) (g/g)	Y(HC)/Y(CO <sub>2</sub> ) (g/g)	Y(CO <sub>2</sub> )/ΔH <sub>CON</sub> (g/kJ)	Y(CO)/ΔH <sub>CON</sub> (g/kJ)	Y(HC)/ΔH <sub>CON</sub> (g/kJ)
poly(ethylene)	0.0087	0.0025	0.13	0.0011	0.00032
poly(propylene)	0.0086	0.0022	0.12	0.0011	0.00027
poly(styrene)	0.026	0.0060	0.21	0.0054	0.00127
polyester	0.05	0.019	0.15	0.0065	0.00185
Nylon	0.018	0.0078	0.13	0.0035	0.00098
Flexible urethane foams	0.006 - 0.027	0.0013 - 0.0033	0.15 - 0.21	0.0012 - 0.0055	0.00023 - 0.00069
Rigid urethane foams	0.015 - 0.046	0.006 - 0.036	0.17 - 0.23	0.0028 - 0.0081	0.00011 - 0.00070

<sup>1</sup>Values reported in Table 1 were calculated from data reported in Table 3-4.11 in reference 6.

<sup>2</sup>Y(CO) is the mass-yield of carbon monoxide (g). Y(CO<sub>2</sub>) is the mass-yield of carbon dioxide (g). Y(HC) is the mass-yield of gaseous hydrocarbons (g).  $Y(CO_2)/\Delta H_{con} = (C_{CO_2}/c_p\Delta T)(\rho_{CO_2}/\rho_{air})$ ,  $Y(CO)/\Delta H_{con} = (C_{CO}/c_p\Delta T)(\rho_{CO}/\rho_{air})$ , and  $Y(HC)/\Delta H_{con} = (C_{HC}/c_p\Delta T)(\rho_{HC}/\rho_{air})$ . ΔH<sub>CON</sub> is the convective heat of combustion per unit fuel vaporized (kJ/g). The C<sub>i</sub> are the gas-phase concentrations (volume fraction) of carbon dioxide, carbon monoxide, and total hydrocarbons. The ρ<sub>i</sub> are the gas-phase densities (g/m<sup>3</sup>) of carbon dioxide, carbon monoxide, total hydrocarbons, and air. c<sub>p</sub> is the heat capacity of air (kJ/g-K). ΔT is the difference between the gas temperature and the temperature of the ambient air (K).

<sup>15</sup> Small-scale flammability tests to determine combustion properties of materials were conducted in the Factory Mutual Research Corporation Flammability Apparatus is a small-scale test apparatus (see reference 6).

These parameters include  $Y(\text{CO})/Y(\text{CO}_2)$ ,  $Y(\text{HC})/Y(\text{CO}_2)$ ,  $Y(\text{CO}_2)/\Delta H_{\text{CON}}$ ,  $Y(\text{CO})/\Delta H_{\text{CON}}$ ,  $Y(\text{HC})/\Delta H_{\text{CON}}$ . The values of these parameters in Table 1 were determined for the well-ventilated combustion of a poly(ethylene), a poly(propylene), a poly(styrene), a polyester, a Nylon, a group of flexible urethane foams, and a group of rigid urethane foams.<sup>16</sup>

Analysis of the data from the Fire Products Collector suggests that initially, the production of carbon monoxide relative to carbon dioxide was greater than expected for well-ventilated combustion of materials typical of those used in the test vehicle. Figure 58 shows a plot of  $[G_{\text{CO}}]/[G_{\text{CO}_2}]$  versus time post-ignition, where  $G_{\text{CO}}$  and  $G_{\text{CO}_2}$  are the carbon monoxide- and carbon dioxide-release rates measured using the Fire Products Collector (**APPENDIX H**).

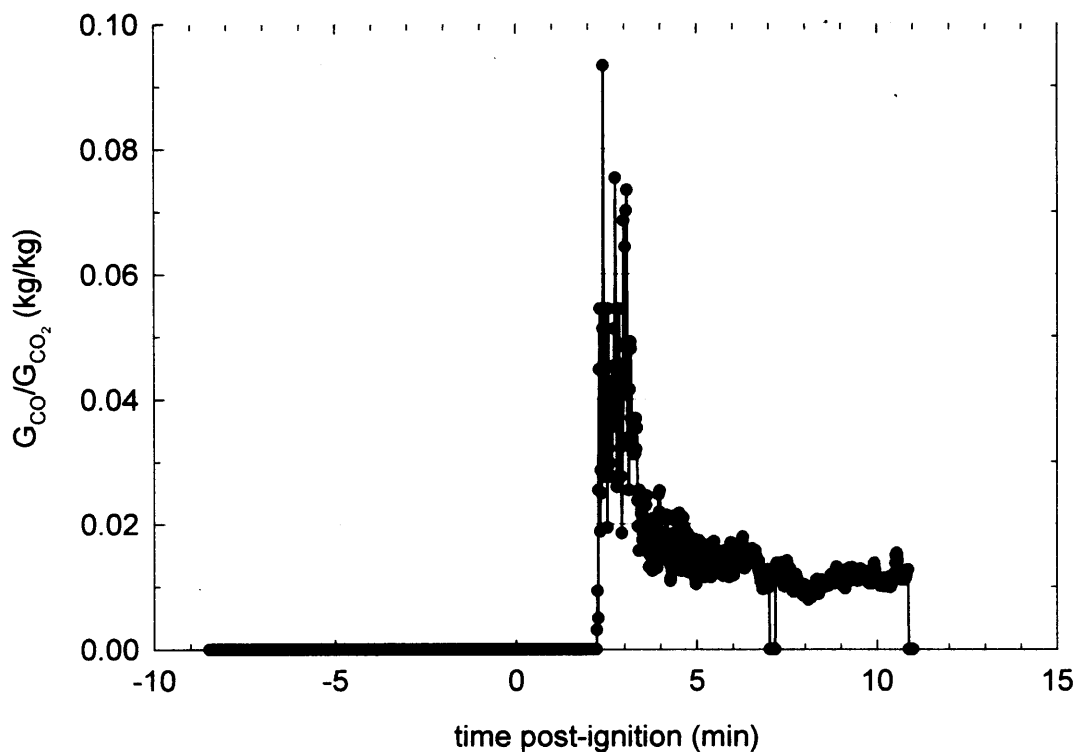


Figure 58. Fire Test F961115. Plot of  $[G_{\text{CO}}]/[G_{\text{CO}_2}]$  versus time post-ignition determined from the carbon monoxide and carbon dioxide release rates measured by the Fire Products Collector.

The ratio  $[G_{\text{CO}}]/[G_{\text{CO}_2}]$  is equivalent to the ratio  $[Y(\text{CO})]/[Y(\text{CO}_2)]$  determined for individual materials listed in Table 1. Before ignition,  $[G_{\text{CO}}]/[G_{\text{CO}_2}]$  was undefined because  $G_{\text{CO}} = G_{\text{CO}_2} = 0$ . The value of  $[G_{\text{CO}}]/[G_{\text{CO}_2}]$  increased rapidly starting at approximately  $\frac{1}{2}$  minute post-ignition,

<sup>16</sup> The compositions and physical properties such as density, thermal conductivity, and heat capacity of these materials were not specified.

reaching a maximum of almost 0.1 at approximately 1 minute post-ignition. In contrast, the value of  $[Y(\text{CO})]/[Y(\text{CO}_2)]$  determined for well-ventilated combustion of representative materials was in the range of 0.06 to 0.05 (Table 1). The cause of the initial peak in  $[G_{\text{CO}}]/[G_{\text{CO}_2}]$  is unclear; the initial burning did not appear to have been under-ventilated.

As the heat release rate increased, the relative production of carbon monoxide decreased. The value of  $[G_{\text{CO}}]/[G_{\text{CO}_2}]$  decreased so that between 3 and 9 minutes post-ignition it was in the range expected for well-ventilated combustion of materials typical of those used in the engine and passenger compartments of the test vehicle ( $0.01 < [G_{\text{CO}}]/[G_{\text{CO}_2}] < 0.02$ ).

A similar analysis of the air temperature data and the concentrations of gaseous combustion products in the passenger compartment suggests that the combustion efficiency was low when objects in the passenger compartment started to burn. The data were used to determine the following ratios:  $[C_{\text{CO}} \times d_{\text{CO}}]/[C_{\text{CO}_2} \times d_{\text{CO}_2}]$ ,  $[C_{\text{HC}} \times d_{\text{HC}}]/[C_{\text{CO}_2} \times d_{\text{CO}_2}]$ ,  $[C_{\text{CO}_2} \times d_{\text{CO}_2}]/[t_{\text{air}} \times C_p]$ ,  $[C_{\text{CO}} \times d_{\text{CO}}]/[t_{\text{air}} \times C_p]$ , and  $[C_{\text{CO}_2} \times d_{\text{CO}_2}]/[t_{\text{air}} \times C_p]$  (Fig.'s 59 through 63), where  $C_j$  is the gas-phase concentration of species  $j$ ,  $d_j$  is the density of species  $j$ ,  $t_{\text{air}}$  is the air temperature, and  $C_p$  is the heat capacity of air. The product  $[C_j \times d_j]$  equals the mass-concentration of species  $j$  in passenger compartment. The concentrations of the gaseous combustion products ( $C_j$ ) were determined by Fourier Transform Infrared Spectrometry (**APPENDIX I**). Temperature data from the aspirated thermocouple assembly in the passenger compartment (**APPENDIX D**) was used to determine the vertical air temperature ( $t_{\text{air}}$ ) gradient in the passenger compartment.

The values of the ratios shown in Figures 59 through 63 were within the ranges expected for well-ventilated combustion from between 7 and 8 minutes post-ignition until flames in the passenger compartment were extinguished at approximately 11 minutes post-ignition:  $0.01 < [C_{\text{CO}} \times d_{\text{CO}}]/[C_{\text{CO}_2} \times d_{\text{CO}_2}] < 0.024$ ;  $0.001 < [C_{\text{HC}} \times d_{\text{HC}}]/[C_{\text{CO}_2} \times d_{\text{CO}_2}] < 0.012$ ;  $0.1 < [C_{\text{CO}_2} \times d_{\text{CO}_2}]/[t_{\text{air}} \times C_p] < 0.3$ ;  $0.025 < [C_{\text{CO}} \times d_{\text{CO}}]/[t_{\text{air}} \times C_p] < 0.005$ ;  $0.0001 < [C_{\text{CO}_2} \times d_{\text{CO}_2}]/[t_{\text{air}} \times C_p] < 0.00075$ . This was coincident with flame-spread to objects in the passenger compartment rearward of the instrument panel. Gaseous combustion products started to accumulate in the passenger compartment between 6 and 8 minutes post-ignition. Initially the fire was localized to the top of the instrument panel, and most of the fire plume escaped through the large hole in the center of the windshield. Several large pieces of the burning windshield fell onto the seat cushion in the front passenger seat and the carpet in forward of the front the passenger seat at about 7½ minutes post-ignition.<sup>17</sup> A greater portion of the fire plume was trapped below the headliner, resulting in an increase in the

---

<sup>17</sup> Objects burning at this time included the instrument panel top cover (vinyl covered flexible urethane foam), parts of the HVAC module (poly(propylene)), the passenger air bag (poly(ethylene terphthalate)), the fabric (nylon-6) and cushion (flexible urethane foam) on the front seats, and the carpet (nylon-6).

air temperature (see Fig. 36) and concentrations of carbon monoxide, carbon dioxide, and the light hydrocarbons (**APPENDIX I**) in the upper gas layer between 10 and 11 minutes post-ignition.

The air temperature and concentrations of all combustion gases decreased rapidly when the fire in the passenger compartment was extinguished. The ratios shown in Figures 58 through 63 increased approximately 10 fold at this time, but it is difficult to interpret the meaning of these increases. Although flaming combustion had ceased, several objects in the passenger compartment continued to thermally decompose. Thus, these increases in  $[C_{CO} \times d_{CO}]/[C_{CO_2} \times d_{CO_2}]$  and  $[C_{HC} \times d_{HC}]/[C_{CO_2} \times d_{CO_2}]$  may reflect the transition to non-flaming combustion.

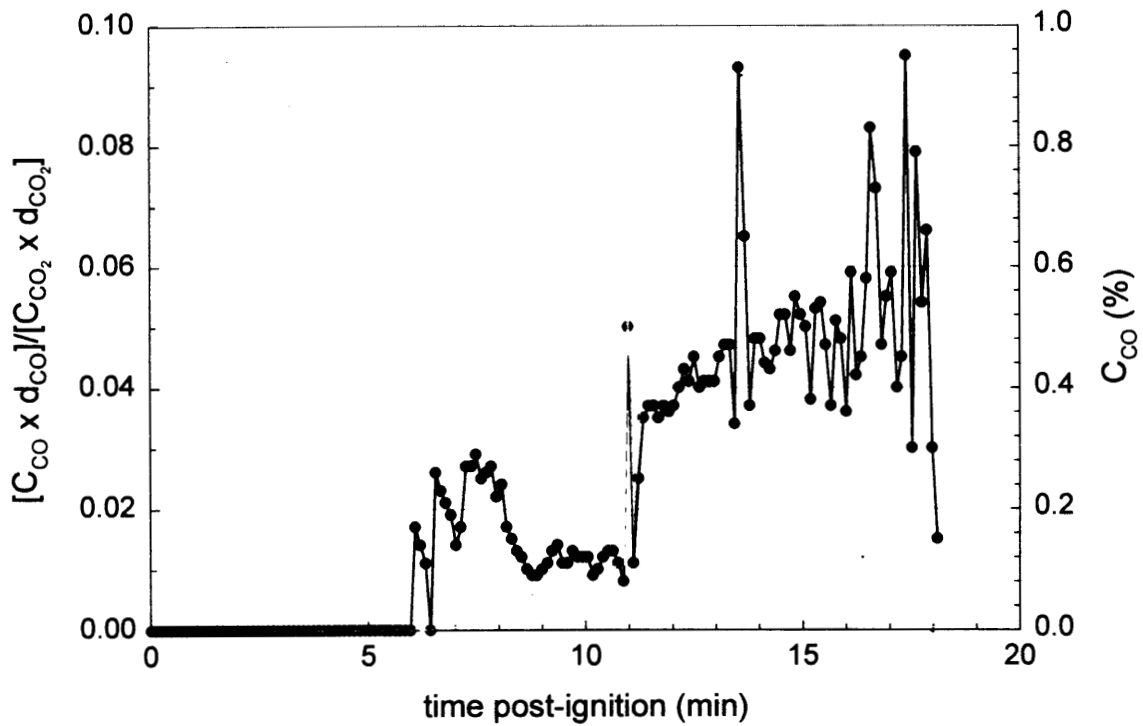


Figure 59. Fire Test F961115. Plots of  $[C_{CO} \times d_{CO}] / [C_{CO_2} \times d_{CO_2}]$  (—●—, left axis) and the concentration of carbon monoxide ( , right axis) in the passenger compartment.

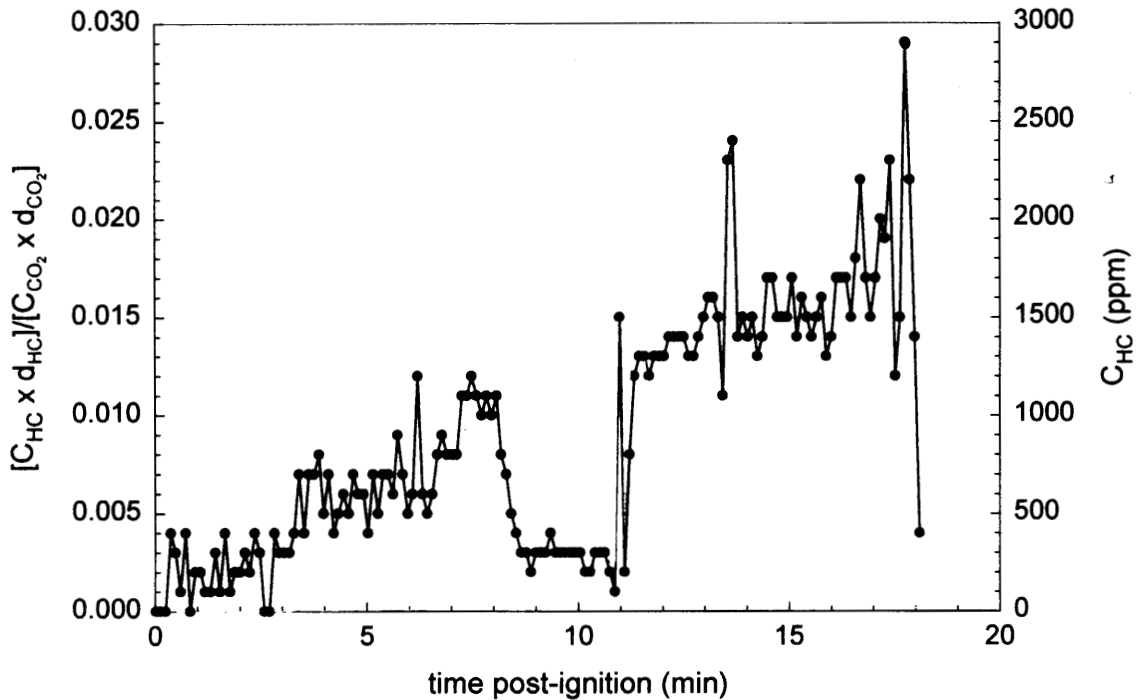


Figure 60. Fire Test F961115. Plots of  $[C_{HC} \times d_{HC}] / [C_{CO_2} \times d_{CO_2}]$  (—●—, left axis) and the concentration of total hydrocarbons ( , right axis) in the passenger compartment.

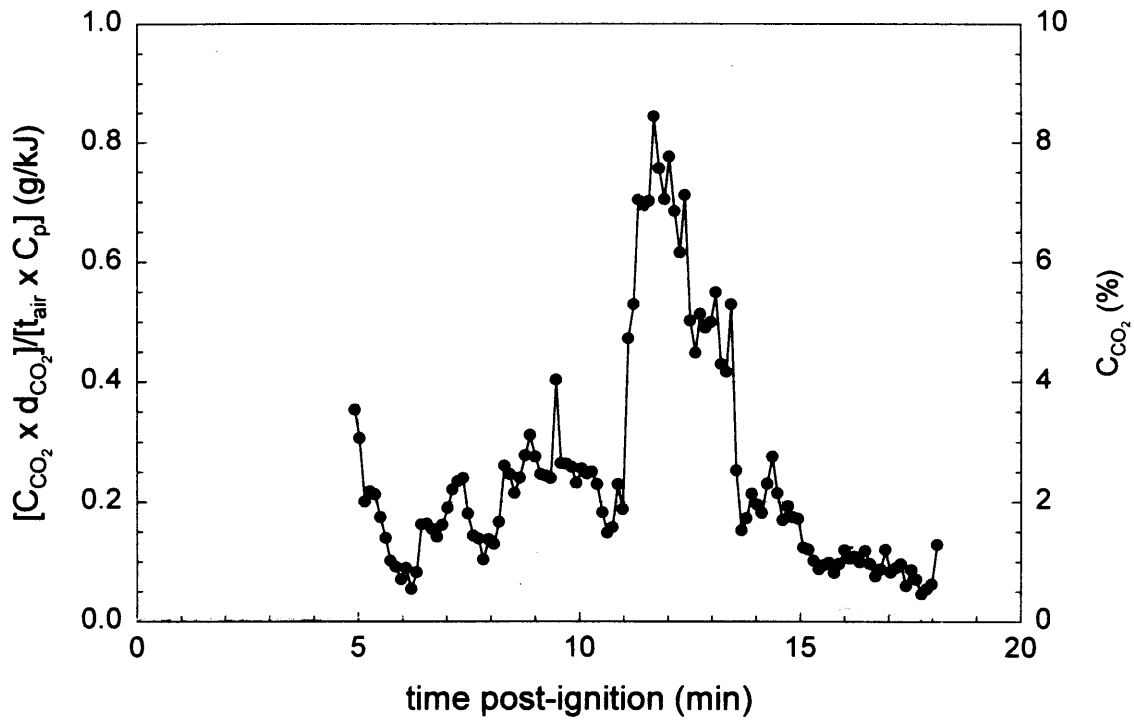


Figure 61. Fire Test F961115. Plots of  $[C_{CO_2} \times d_{CO_2}] / [t_{air} \times C_p]$  (—●—, left axis) and the concentration of carbon dioxide ( , right axis) in the passenger compartment.

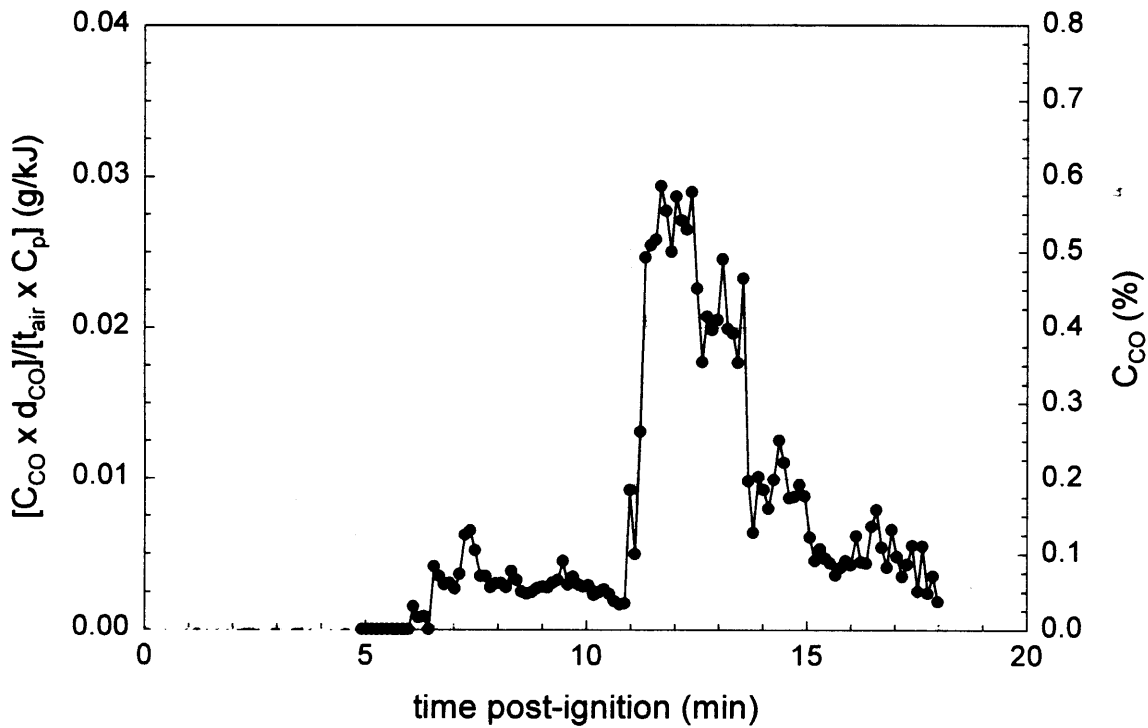


Figure 62. Fire Test F961115. Plots of  $[C_{CO} \times d_{CO}] / [t_{air} \times C_p]$  (—●—, left axis) and the concentration of carbon monoxide ( , right axis) in the passenger compartment.

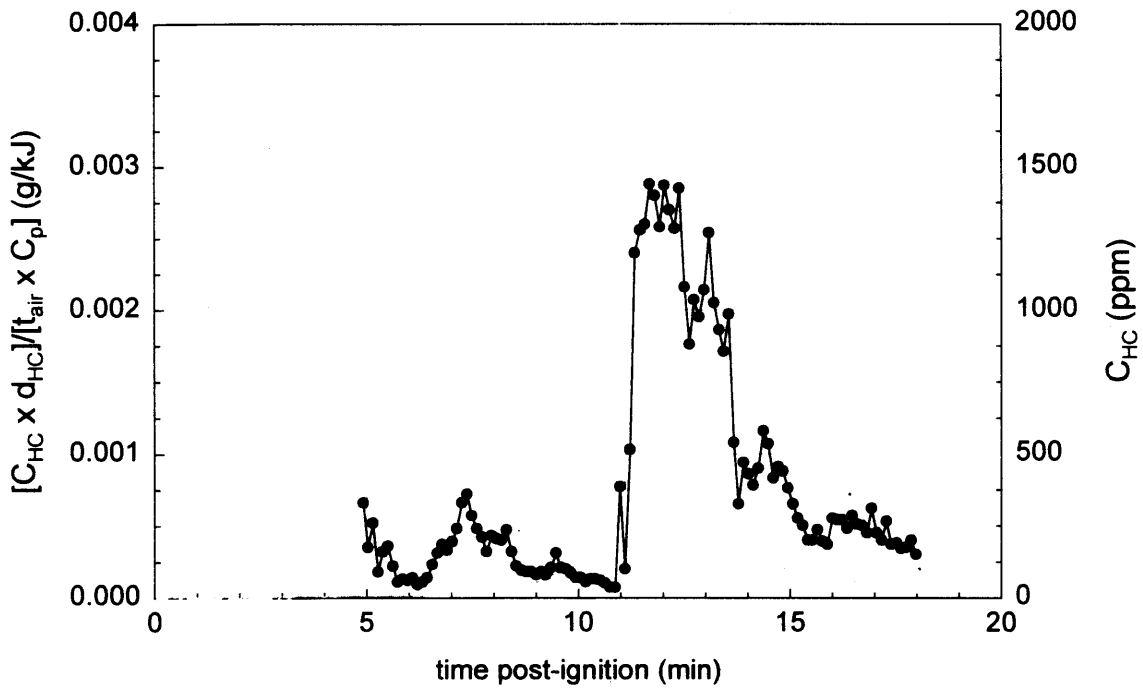


Figure 63. Fire Test F961115. Plots of  $[C_{HC} \times d_{HC}] / [t_{air} \times C_p]$  (—●—, left axis) and the concentration of hydrocarbons ( , right axis) in the passenger compartment.

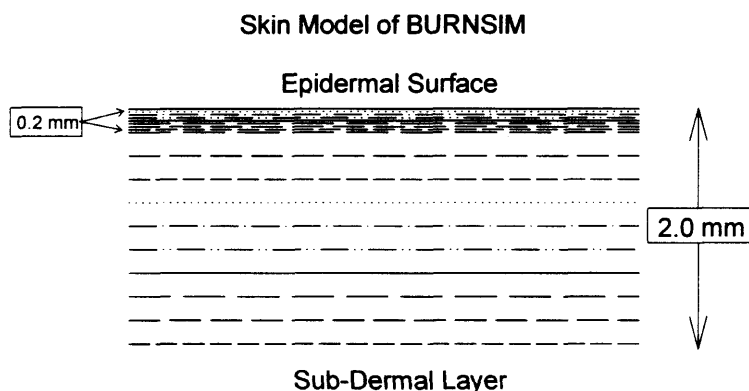
## 8 Estimation of Skin Temperature Profiles from Measured Heat Flux Data, Fractional Equivalent Dose Parameters from Measured Gas Concentration Data, and Thermal Damage to the Respiratory Tract from Measured Air Temperature Data

The mathematical model "BURNSIM: A Burn Hazard Assessment Model" [7] was used to estimate the time and depth of burns to exposed skin. The inputs to this model were heat fluxes derived from the directional flame thermometer measurements and air temperatures measured using the aspirated thermocouple probe.

Two models were used to estimate the potential for toxicity from exposure to the combustion gases measured in the passenger compartment. The Federal Aviation Administration (FAA) Combined Hazard Survival Model [8] was used to estimate the time to incapacitation and the time to lethality. A model described by Purser [9] also was used to estimate the time to incapacitation. Both models estimate the risk from exposure to hot air, reduced oxygen, carbon monoxide, carbon dioxide, hydrogen cyanide, hydrogen chloride, hydrogen fluoride, hydrogen bromide, acrolein, and nitrogen dioxide. Both models also account for the physiological effect of carbon dioxide-induced hyperventilation, which increases the respiratory uptake.

### 8.1 The BURNSIM Model

The computer model BURNSIM was the analytical tool chosen to estimate skin temperature depth profiles from the heat flux data in **APPENDIX G**. The BURNSIM model divides the skin into a series of ten layers, with a uniform thickness of 0.2 mm per layer. The top layer was divided into 8 layers each with a uniform thickness of 0.025 mm to better account for the non-instantaneous heat transfer from the epidermal surface into the first layer.



The BURNSIM analysis used here incorporated the following assumptions to estimate skin temperature profiles. The absorbtivity of exposed skin was assumed to be 0.60 (i.e., the skin absorbs 60% of the radiation incident upon the epidermal surface). The absorbtivity of surface

hair was assumed to be 0.05 (i.e., surface hair absorbs 5% of the incident radiation before it reached the skin). Exposed skin was assumed to absorb 100% of the measured convective heat flux to its surface. The temperature of each layer was estimated as a function of the time of exposure to an external heat flux. A portion of the absorbed heat is removed from the skin by the circulatory system. Thermal damage to a layer of skin exceeds the capacity of the physiological repair processes when the temperature of that layer exceeds 45°C.

In estimating skin temperature, the analysis presented in this paper using BURNSIM did not account for the presence of facial or head hair, or clothing covering the skin, all of which may block direct heat transfer to the skin. This analysis also did not account for variations in skin thickness among individuals, or variations in skin thickness at different parts of the body on the same individual. For example, skin thickness can vary from 1 to 5 mm with body location. This analysis also did not account for effect of skin pigmentation on absorbtivity. In using the radiative and convective heat flux estimates shown in **APPENDIX G** to estimate skin temperature profiles, this analysis assumed that the location and orientation of the skin was identical to that of the transducers used to measure heat flux. Small changes in position or angle of the surface of the skin relative to the DFT's in this test can lead to large differences between in the actual incident heat flux to exposed surfaces and that measured by the DFT (see below). Based on the currently available information and data, the accuracy of the estimated skin temperature depth profiles in humans exposed to heat flux levels from fire such as measured in this test obtained using BURNSIM has not been determined.

### **8.1.1 Estimation of Skin Temperature Profiles using BURNSIM**

Figures 62 through 67 show skin temperature profile estimated for exposed skin at five locations in the passenger compartment of the test vehicle. These include head-level above the driver's seat, knee-level on the driver's seat, head-level above the front passenger's seat, knee level on the front passenger's seat, and head level between the driver's and front passenger's seats.

The timing of the estimated increases in skin temperature at head-level generally correlated with the timing of flame-spread across the headliner (Fig.'s 64, 66, and 68). Analysis of the data from the DFT's and the aspirated thermocouples indicated that radiation from the burning headliner accounted for between 80 and 85% of the total heat flux to the DFT's at head level in the front of the test vehicle. The orientation of the DFT affected the view angle and thus the incident radiant heat flux to these transducers. For example, the DFT's above the front seats were facing forward and were perpendicular to the roof of the test.

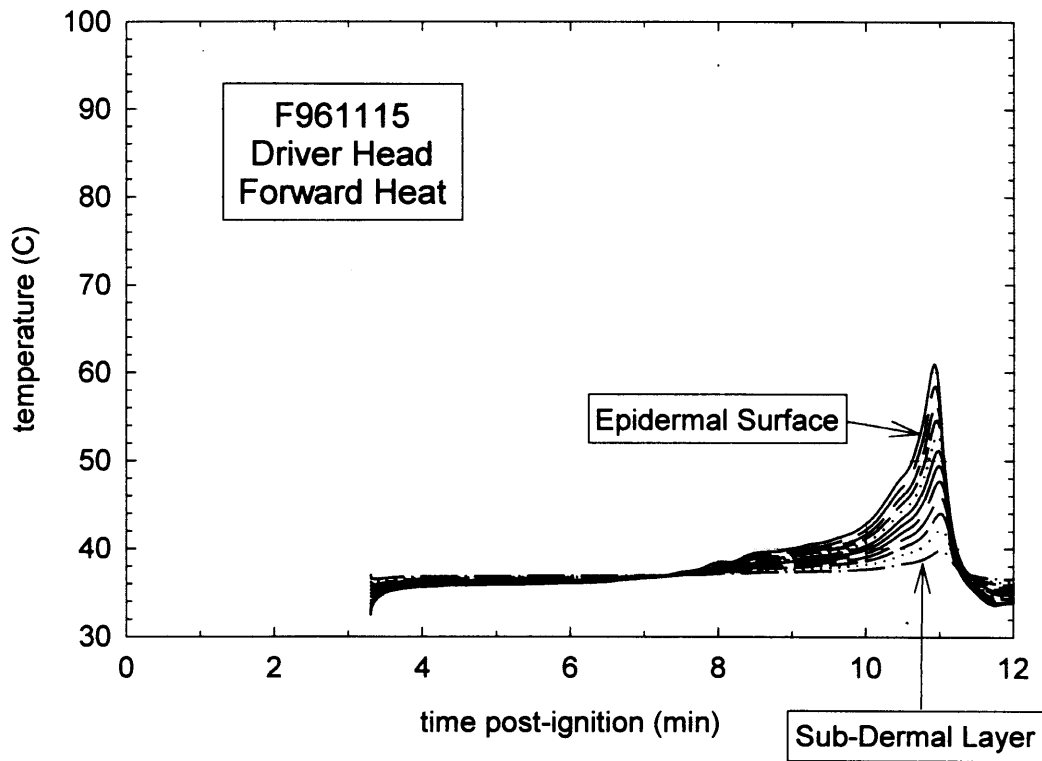


Figure 64. Fire Test F961115. Skin temperature profile estimated from heat flux to a forward-facing vertical surface at the drivers head level (APPENDIX G, Plot G6).

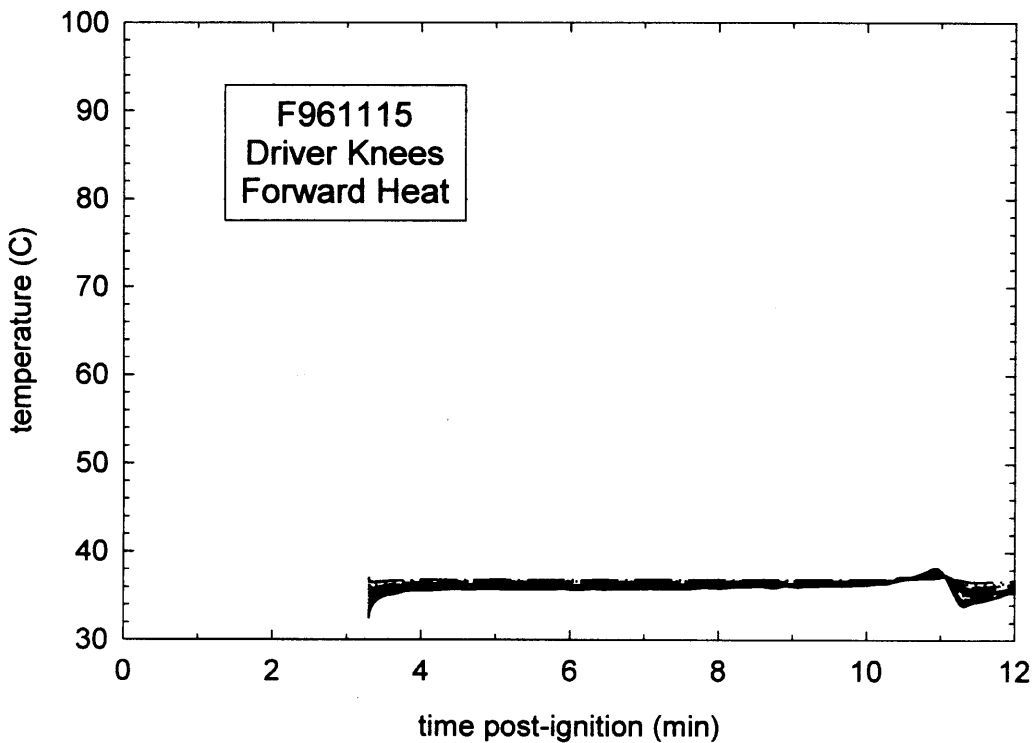


Figure 65. Fire Test F961115. Skin temperature profile estimated from heat flux to a forward-facing vertical surface at the drivers knee level (APPENDIX G, Plot G8).

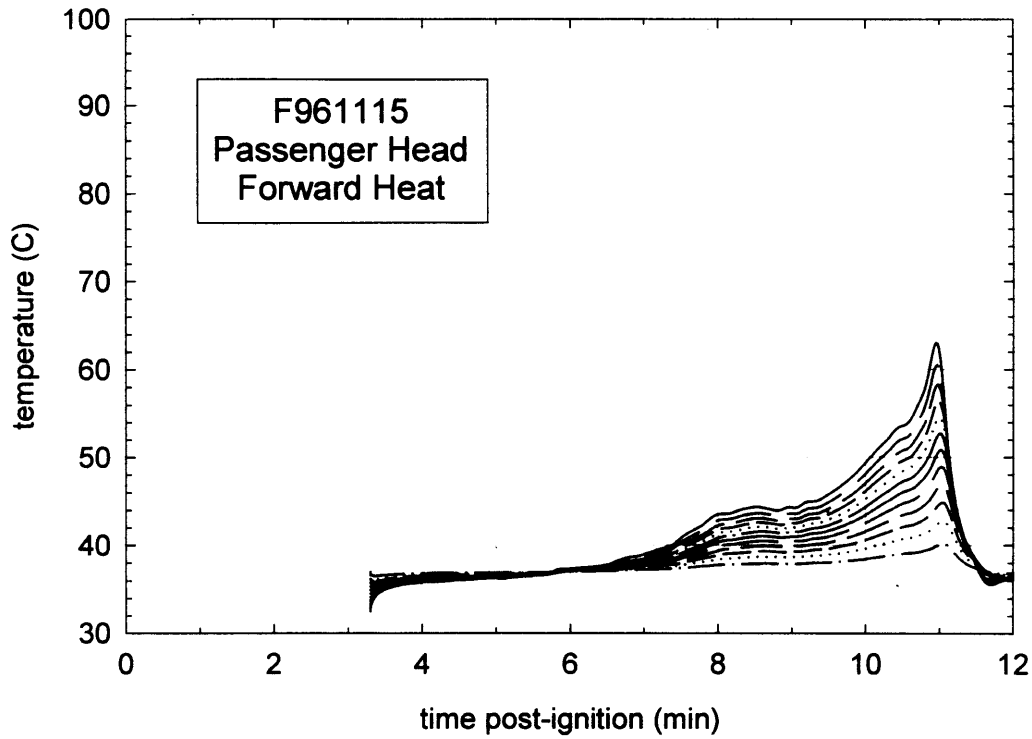


Figure 66. Fire Test F961115. Skin temperature profile estimated from heat flux to a forward-facing vertical surface at the passenger head level (**APPENDIX G**, Plot G2).

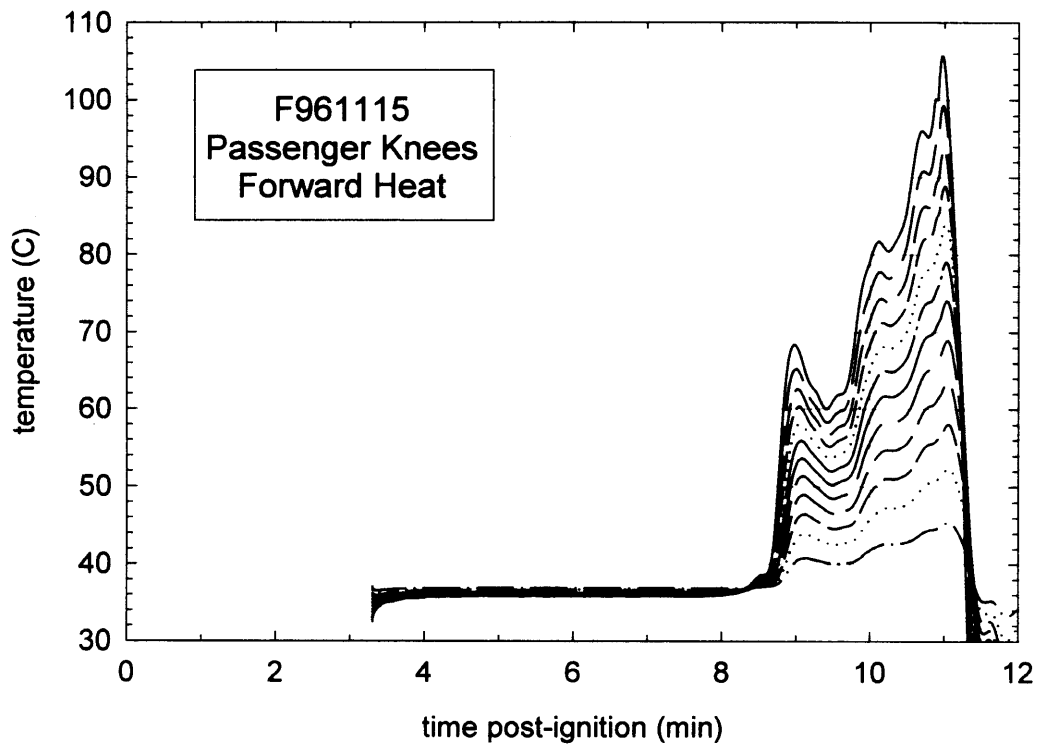


Figure 67. Fire Test F961115. Skin temperature profile estimated from heat flux to a forward-facing vertical surface at the passenger knee level (**APPENDIX G**, Plot G4).

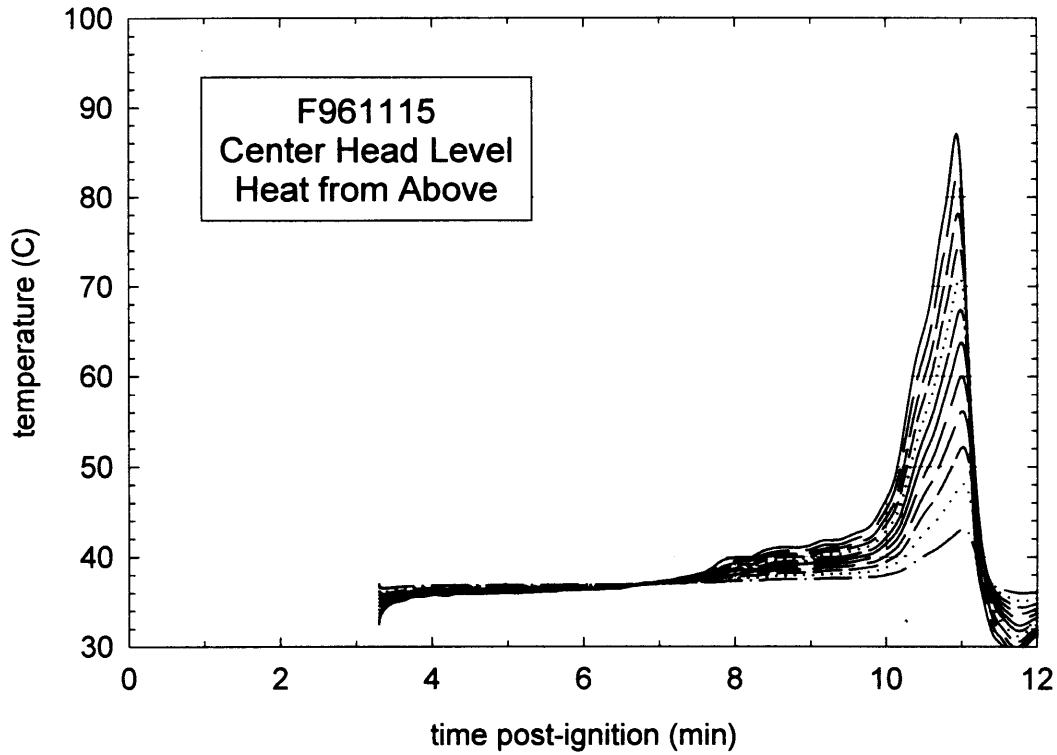


Figure 68. Fire Test F961115. Skin temperature profile estimated from heat flux to a upward-facing horizontal surface at the passenger head level (APPENDIX G, Plot G10).

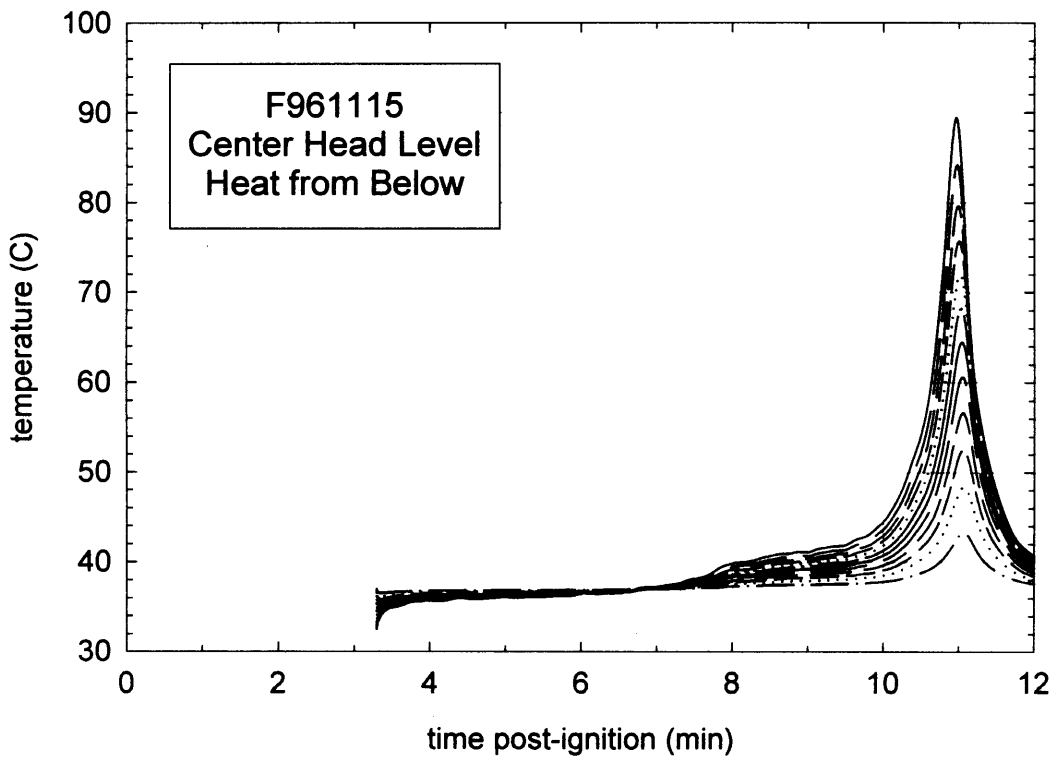


Figure 69. Fire Test F961115. Skin temperature profile estimated from heat flux to a downward-facing horizontal surface at the passenger head level (APPENDIX G, Plot G12).

The estimated radiant heat fluxes to these DFT's reached maximum values of approximately 10 kW/m<sup>2</sup> at approximately 11 minutes post-ignition (Plots F2 and F6, **APPENDIX F**). The DFT between the front seats was facing upward and was parallel to the roof of the test vehicle. The estimated radiant heat flux to this DFT reached a maximum value of approximately 22 kW/m<sup>2</sup> at this time (Plot G10, **APPENDIX G**). These results emphasize that the angle of the surface of the skin relative to the flames can lead to large differences in the incident heat flux.

The orientation of the DFT also effected the estimated skin temperature profile. For example, the maximum estimated skin temperatures for exposed skin at head level in the front of the test vehicle were 87°C for heating from above (Fig. 68) and 89°C for heating from below (Fig.69). The estimated maximum skin temperature of exposed skin at head level facing forward was between 61 and 63.°C (Fig.'s 64 and 66).

This analysis indicated that the estimated heat flux to the DFT at knee-level on the driver's seat was low throughout this test (Plot G8, **APPENDIX G**). The maximum estimated temperature of exposed skin at this location was approximately 38°C (Fig. 65).

The maximum estimated radiative heat flux to the DTF located at knee level on the front passenger's seat was just under 40 kW/m<sup>2</sup> at 11 minutes post-ignition (Plot G4, **APPENDIX G**), resulting in a maximum estimated skin temperature of approximately 106°C (Fig. 67). The convective heat flux to this transducer was not estimated because air temperature was not measured at this level in the test vehicle. In the estimation of the skin temperature profiles of exposed skin at this location (Fig. 67), it was assumed that the sole mechanism of heat transfer was radiation from the burning passenger air bag just in front of the passenger's seat.

## **8.2 The FAA Combined Hazard Survival Model and Purser's Model of Combustion Gas Toxicity**

The FAA Combined Hazard Survival Model and Purser's model utilize the concept of a Fractional Effective Dose [FED] to estimate the cumulative effects of exposure to a mixture of gases produced by burning materials. For exposure to a single gas with an unchanging concentration in air, the Fractional Effective Dose for Incapacitation [FED(I)] is defined as the product of the gas-phase concentration and the time of exposure ( $C \times t$ ) normalized to the concentration-time product that results in incapacitation of 50% of an exposed population [8, 9]. Similarly, the Fractional Effective Dose for lethality [FED(L)] is defined as the product of the gas-phase concentration and the time of exposure normalized to the concentration-time product that results in the death of 50% of an exposed population [see references in 8 and 9]. The estimates of

FED(I) and FED(L) obtained using the FAA Combined Hazard Survival Model or Purser's model of combustion gas toxicity and presented in this report cannot be used to predict precisely when the gas concentrations measured in this test would have resulted in incapacitating narcosis or death for a vehicle occupant. Whether exposure to these gases results in toxicity depends on a number of complex physical and physiological variables.

Some of the physical variables include the exact chemical composition of the gaseous mixture, the concentration of each component of the gaseous mixture, and the time of exposure. Exposure to these gases in a burning vehicle can be highly variable, and depend on factors such as elevation in the passenger compartment and airflow through the passenger compartment. As mentioned in the previous section, combustion gases are hotter than the ambient air and form an upper layer. The air temperature data from the aspirated thermocouples indicated that a steep air-temperature gradient developed in the front of the passenger compartment during this test (see **SECTION 8.3**). Since both heat and mass are conserved in a fire, the existence of a steep vertical air-temperature gradient implies the existence of similarly steep vertical concentration gradients for gaseous combustion products accumulating in the passenger compartment. The location of the head and nose in the passenger compartment will effect the exposure concentration. An occupant whose head was located below the level where gases were measured, such as an occupant bent over in the seat, would have been exposed to lower concentrations of combustion gases than those shown in **APPENDIX I** and in Figures 62 through 65. Airflow through the passenger compartment will dilute or remove these gases.

Uncertainties in the responses of humans exposed to these gases also complicated the determination of when and whether toxicity occurs. The mathematical equations for the calculation of FED(I) and FED(L) were derived by analysis of data from controlled experiments in which different species of laboratory animals were exposed to a range of concentrations of each gas. In using data from these laboratory animal experiments to define FED(I) and FED(L), both models implicitly assume that humans respond the same as laboratory animals to exposure to these gases – an assumption that is largely untested and may not be accurate. For example, except for incapacitation from exposure to carbon dioxide, none of the model predictions using either the FAA Combined Hazard Survival Model or Purser's model have been validated for humans. That is, the accuracy of FED(I) and FED(L) in predicting human responses to exposure to the combustion gases measured in this test has not been determined. Consequently, there is a high degree of uncertainty as to the effect exposure to these levels of combustion gases would actually have on a human vehicle occupant. In addition, neither of these models accounts for variation in individual responses to these gases nor the effect of trauma suffered during the crash on an occupant's response to these gases.

The equations presented in both the FAA Combined Hazard Survival Model and in Purser's model divide the exposure into one-minute intervals when the concentration of the gaseous species changes with time. In this test, Fourier Transform Infrared spectra were obtained at seven-second intervals to characterize the changing gas concentrations observed in the passenger compartment. The equations presented in the FAA Combined Hazard Survival Model and in Purser's model were modified to account for the faster sampling times used in this test. These modified equations are shown below and were used to derive the estimated of FED(I) and FED(L) shown in **SECTION 8.2.1**.

Carbon dioxide-induced hyperventilation can increase the respiratory uptake of airborne combustion products. The FAA Combined Hazard Survival Model uses a multiplication factor to account for the increased respiratory uptake of gaseous combustion products because of exposure to elevated levels of carbon dioxide [ $V_{CO_2}$ ]:

$$V_{CO_2} = \frac{\exp(1.9086 + 0.2496 \times C_{CO_2})}{6.8} \quad (1)$$

where the units of  $C_{CO_2}$  are %. This equation was not modified for the analysis presented in **SECTION 8.2.1**.

The Fractional Effective Doses for Incapacitation from exposure to carbon dioxide, carbon monoxide, hydrogen chloride, hydrogen cyanide and decreased oxygen were calculated using the following equations modified to account for sampling intervals of less than 1 minute:

$$FED(I)_{CO_2} = \left(\frac{t}{60}\right) \times \sum \left\{ \frac{1}{2193.8 - (311.6 \times C_{CO_2})} \right\} \quad (2)$$

when  $5.5 \leq C_{CO_2} \leq 7.0\%$ ,

$$FED(I)_{CO_2} = \left(\frac{t}{60}\right) \times \sum \left\{ \frac{1}{\exp(6.1623 - (0.5189 \times C_{CO_2}))} \right\} \quad (3)$$

when  $C_{CO_2} > 7.0\%$ ,

$$FED(I)_{CO} = \left(\frac{t}{60}\right) \times \left(\frac{1}{3.4250}\right) \times \sum \{V_{CO_2} \times C_{CO}\} \quad (4)$$

when  $V_{CO_2} \times C_{CO} > 0.01\%$ ,

$$FED(I)_{HCl} = \left(\frac{t}{60}\right) \times \sum \left\{ \frac{1}{3 + \frac{336,000}{(V_{CO_2} \times C_{HCl}) - 300}} \right\} \quad (5)$$

when  $V_{CO_2} \times C_{HCl} > 300$  ppm;

$$FED(I)_{HCN} = \left(\frac{t}{60}\right) \times \left(\frac{1}{564}\right) \times \sum \{(V_{CO_2} \times C_{HCN}) - 63\} \quad (6)$$

when  $V_{CO_2} \times C_{HCN} > 63$  ppm; and

$$FED(I)_{O_2} = \left(\frac{t}{60}\right) \times \sum \left\{ \frac{1}{\exp(8.55 - (0.511 \times (20.9 - C_{O_2})))} \right\} \quad (7)$$

when  $C_{O_2} < 11\%$ . The value of  $t$  in these equations was the time in seconds between acquisition of FTIR spectra. The overall Fractional Effective Dose for Incapacitation was calculated by summing the terms in equations 2 through 7:

$$FED(I)_{TOTAL} = FED(I)_{CO_2} + FED(I)_{CO} + FED(I)_{HCl} + FED(I)_{HCN} + FED(I)_{O_2} \quad (8)$$

The Fractional Effective Doses for Lethality from exposure to carbon monoxide and hydrogen cyanide were calculated using the following equations modified to account for sampling intervals of less than 1 minute:

$$FED(L)_{CO} = \left(\frac{t}{60}\right) \times \sum \left\{ \frac{1}{\exp(5.85 - (0.00037 \times V_{CO_2} \times C_{CO}))} \right\} \quad (9)$$

when  $2000 \leq V_{CO_2} \times C_{CO} \leq 9000$  ppm,

$$FED(L)_{CO} = \left(\frac{t}{60}\right) \times \sum \left\{ \frac{1}{0.4 + \left(\frac{58,000}{V_{CO_2} \times C_{CO}}\right)} \right\} \quad (10)$$

when  $V_{CO_2} \times C_{CO} > 9000$  ppm, and

$$FED(L)_{HCN} = \left(\frac{t}{60}\right) \times \left(\frac{1}{2586}\right) \times \sum \{(V_{CO_2} \times C_{HCN}) - 43.2\} \quad (11)$$

when  $V_{CO_2} \times C_{HCN} > 43.2$  ppm;

The overall Fractional Effective Dose for Lethality was calculated by summing the terms in equations 8 through 10:

$$FED(L)_{TOTAL} = FED(L)_{CO} + FED(L)_{HCN} \quad (12)$$

The model described by Purser also uses a multiplication factor to account for the enhanced respiratory uptake of toxic gases because of exposure to elevated levels of carbon dioxide:

$$V_{CO_2} = \frac{\exp(1.9086 + (0.2496 \times C_{CO_2}))}{6.8} \quad (13)$$

The Fractional Effective Doses for Incapacitation from exposure to carbon monoxide and hydrogen cyanide were calculated using the following equations modified to account for sampling intervals of less than 1 minute:

$$FED(I)_{CO_2} = \left(\frac{t}{60}\right) \times \sum \left\{ \frac{1}{\exp(6.1623 - (0.5189 \times C_{CO_2}))} \right\} \quad (14)$$

when  $C_{CO_2} > 5\%$ ,

$$FED(I)_{CO} = \left(\frac{t}{60}\right) \times V_{CO_2} \times \sum \left\{ \frac{0.00082925 \times C_{CO}}{30} \right\} \quad (15)$$

where the units of  $C_{CO}$  are ppm,

$$FED(I)_{HCN} = \left(\frac{t}{60}\right) \times V_{CO_2} \times \sum \left\{ \frac{4.4}{185 - C_{HCN}} \right\} \quad (16)$$

when  $80 \leq C_{HCN} \leq 180$  ppm,

$$FED(I)_{HCN} = \left(\frac{t}{60}\right) \times V_{CO_2} \times \sum \left\{ \frac{1}{\exp(5.396 - (0.023 \times C_{HCN}))} \right\} \quad (17)$$

when  $C_{HCN} > 180$  ppm; and

$$FED(I)_{O_2} = \left(\frac{t}{60}\right) \times \sum \left\{ \frac{1}{\exp(8.13 - (0.54 \times (20.9 - C_{O_2})))} \right\} \quad (18)$$

when  $C_{O_2} < 11.3\%$ .

As in the FAA model, the value of  $t$  in these equations was the time in seconds between acquisition of FTIR spectra. The overall Fractional Effective Dose for Incapacitation was calculated by summing the terms in equations 14 through 18:

$$FED(I)_{TOTAL} = FED(I)_{CO_2} + FED(I)_{CO} + FED(I)_{HCN} + FED(I)_{O_2} \quad (19)$$

Both the FAA Combined Hazard Survival model and Purser's model predict that 50% of an exposed population would experience incapacitating narcosis (*i.e.*, an occupant loses consciousness and would be unable to exit a vehicle without assistance) when  $FED(I)_{TOTAL} = 1.0$ . Similarly, both of these models predict that 50% of an exposed population would die when  $FED(L)_{TOTAL} \geq 1.0$ .

### 8.2.1 Estimation of Fractional Equivalent Dose Parameters

The analysis presented in this report included estimates of FED(I) and FED(L) for carbon dioxide, carbon monoxide, hydrogen cyanide, hydrogen chloride and oxygen using the FAA Combined Hazard Survival Model and Purser's model for assessment of the toxicity of combustion products. The other gaseous species included in the FAA Combined Hazard Model and Purser's model were not measured during this test; therefore, values of FED(I) or FED(L) were not estimated for these gases. The arrows in these plots indicate the approximate times of the following events: ignition of the instrument panel top cover (**A**), ignition of the deployed passenger airbag (**B**), and the start of flame propagation forward across the head liner (**C**). Fire suppression began at approximately 11 minutes post-ignition.

Figures 70 through 72 show plots of  $FED(I)_{CO_2}$ ,  $FED(I)_{CO}$ , and  $FED(I)_{HCN}$  computed using the FAA Combined Hazard Survival Model and Purser's model for assessment of the toxicity of combustion products. The concentration of hydrogen chloride in the passenger compartment never exceeded the lower limit of detection of the chemical analysis (see **APPENDIX H**), and the concentration of oxygen in the passenger compartment was not during this test. Therefore, neither  $FED(I)_{HCl}$  or  $FED(I)_{O_2}$  were calculated.

Plots of the  $FED(I)_{CO_2}$  parameters estimated using the FAA Combined Hazard Model and Purser's model are shown in Figure 70. Both models yielded estimates of  $FED(I)_{TOTAL} > 0$  starting at about 10 ½ minutes post-ignition, when  $C_{CO_2} > 5\%$ . And both models yielded estimated of  $FED(I)_{TOTAL} < 1$  from the time of ignition until approximately 18 minutes post-ignition when this gas analysis was stopped.

Plots of the  $FED(I)_{CO}$  parameters estimated using both models are shown in Figure 71. The equations presented in the Purser model for computation of  $FED(I)_{CO}$  include a term for respiratory minute volume. Minute volumes corresponding to respiration during rest (8.5 L/min) and light activity (25 L/min) were used in these calculations [9]. Purser's model also accounts for the effect of exposure to carbon dioxide on respiratory rate. The FAA Combined Survival Hazard Model computes only one estimate of  $FED(I)_{CO}$ , which accounts for the effect of exposure to carbon dioxide on respiratory rate [8]. The estimates of  $FED(I)_{CO}$  using these different models differed substantially. For example, calculations using the FAA model yielded estimates of  $FED(I)_{TOTAL} > 0$  starting between 7 and 7½ minutes post-ignition. These estimates of  $FED(I)_{TOTAL} < 1$  throughout this test. Calculations using Purser's model using a respiratory minute volume of 8.5 L/min yielded estimates of  $FED(I)_{TOTAL} > 0$  between 6½ and 7 minutes post-ignition. These estimates of  $FED(I)_{TOTAL} < 1$  throughout this test. Calculations using Purser's model using a respiratory minute volume of 25 L/min yielded estimates of  $FED(I)_{TOTAL} > 0$  between 2 and 2 ½ minutes post-ignition. These estimates of  $FED(I)_{TOTAL}$  asymptotically approached a value of 1 during the final few minutes of data acquisition. At 15 minutes post-ignition, a value of  $FED(I)_{CO} = 0.785$  was computed using the FAA Combined Hazard Survival Model. In contrast, values of  $FED(I)_{CO} = 0.215$  and  $FED(I)_{CO} = 0.983$  were computed using the Purser model with respiratory minute volumes of 8.5 and 25 L/min, respectively.

Plots of the  $FED(I)_{HCN}$  parameters estimated using both models are shown in Figure 72. Both the FAA Combined Survival Hazard Model and Purser's model employ a threshold concentrations to determine when to start computing  $FED(I)_{HCN}$  (refer to equations 6 and 14, respectively).

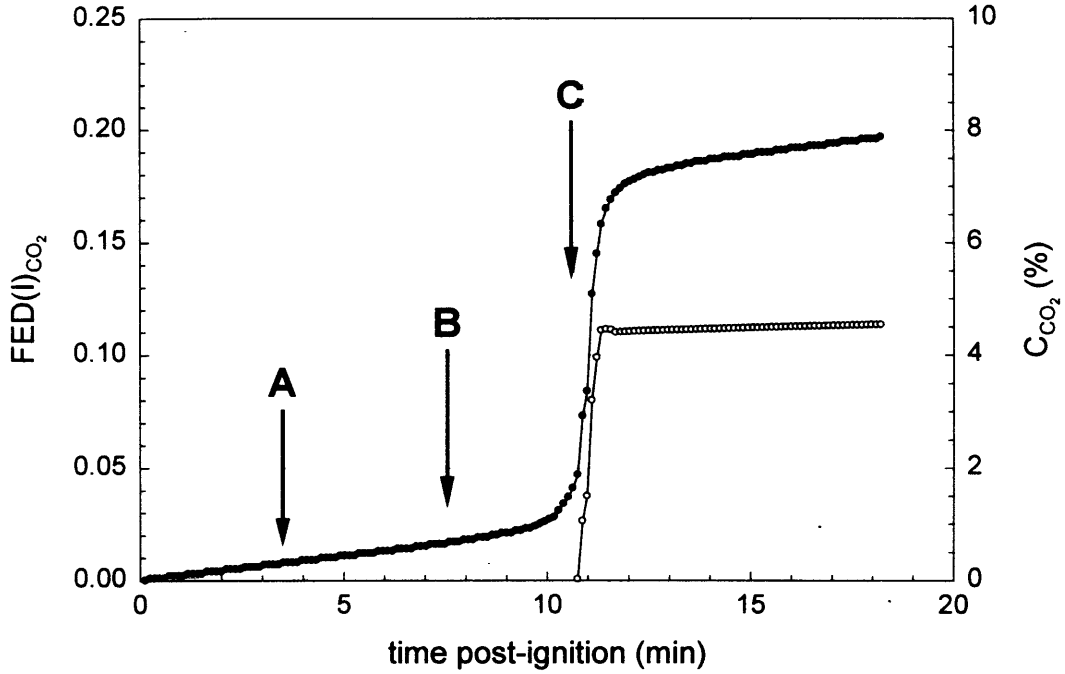


Figure 70. Fire Test F961115. Plots of  $FED(I)_{CO_2}$  versus time post-ignition: FAA Combined Hazard Survival Model ( $-O-$ ); and Purser's model ( $-●-$ ). A plot of  $C_{CO_2}$  ( $-$ ) is included for reference.

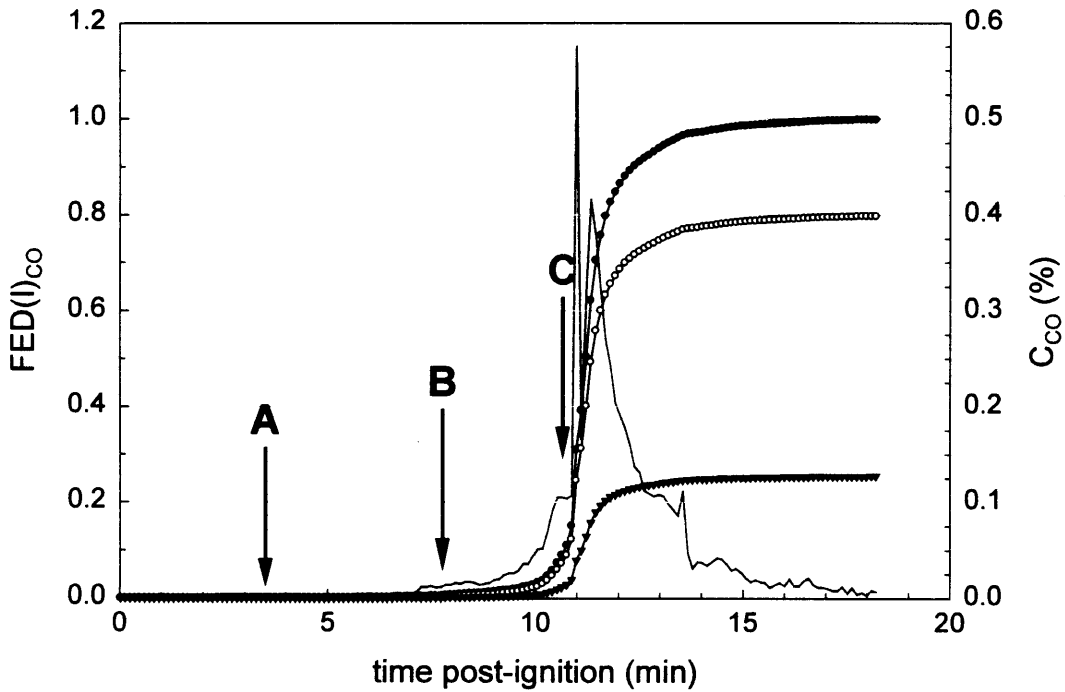


Figure 71. Fire Test F961115. Plots of estimates of  $FED(I)_{CO}$  versus time post-ignition computed using the FAA Combined Hazard Survival Model ( $-O-$ ), the Purser model with a respiratory minute volume of 8.5 L/min ( $-▼-$ ), and the Purser model with a respiratory minute volume of 25 L/min ( $-●-$ ). A plot of  $C_{CO}$  ( $-$ ) is included for reference.

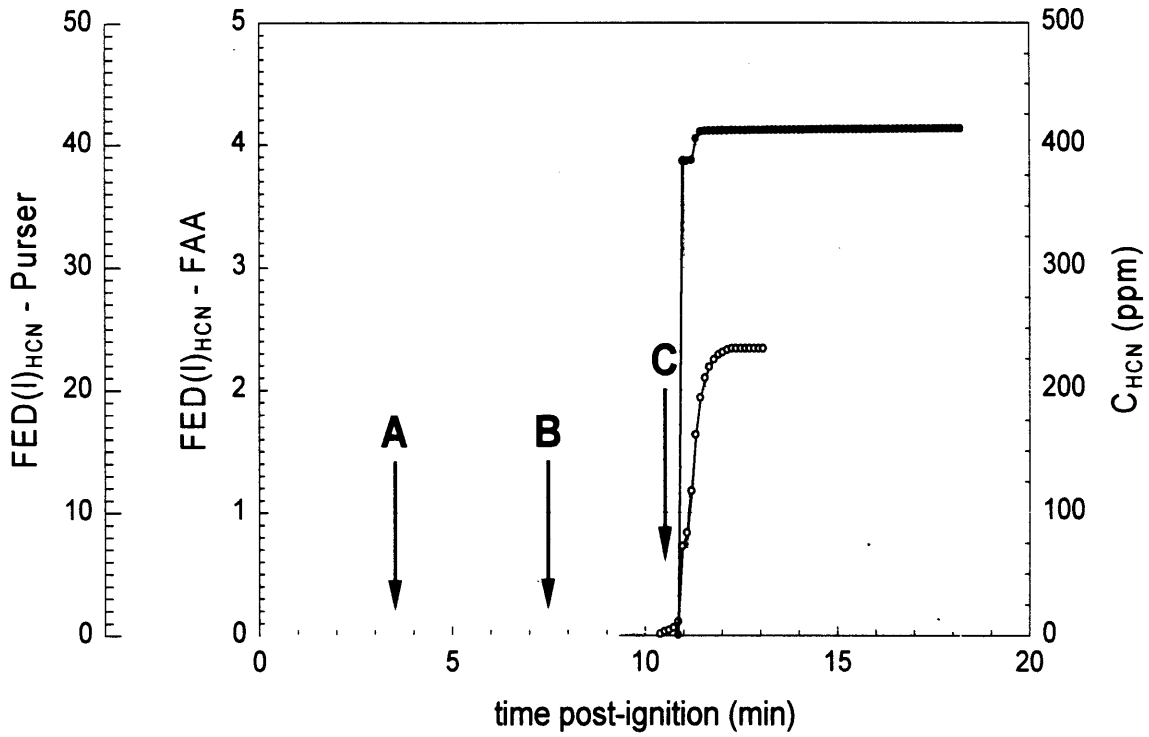


Figure 72. Fire Test F961115. Plots of  $FED(I)_{HCN}$  versus time post-ignition: FAA Combined Hazard Survival Model ( $\circ$ ); and Purser's model ( $\bullet$ ). A plot of  $C_{HCN}$  (—) is included for reference.

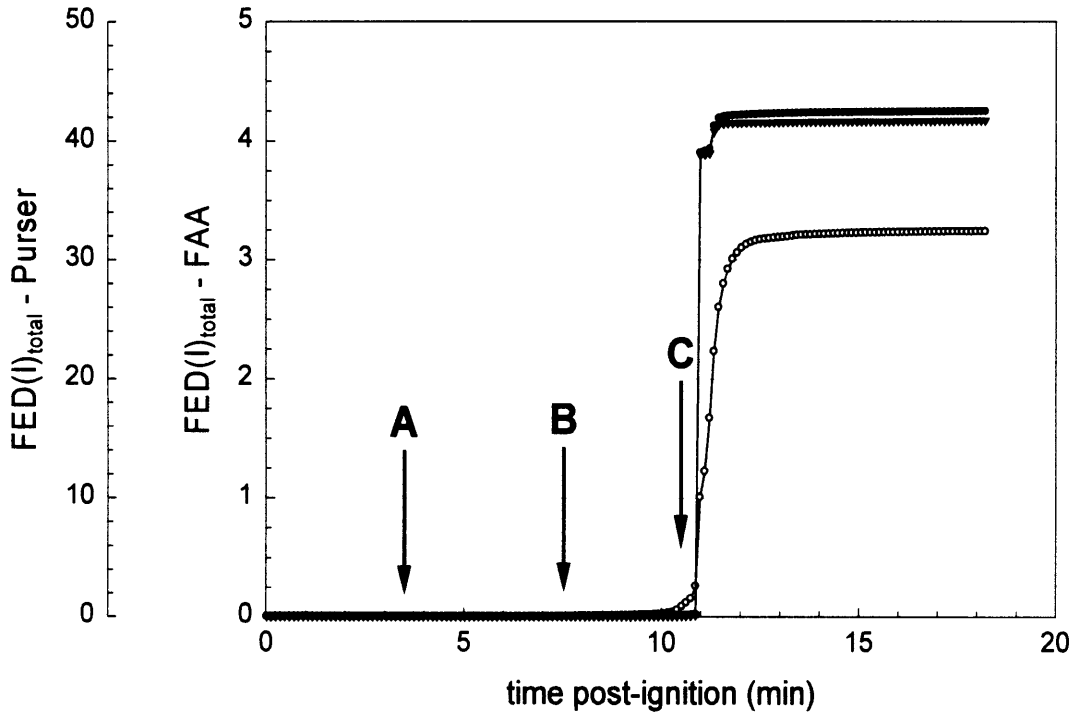


Figure 73. Fire Test F961115. Plots of  $FED(I)_{TOTAL}$  versus time post-ignition: FAA Combined Hazard Survival Model ( $\circ$ ); Purser's model with  $RMV = 8.5$  L/min ( $\blacktriangledown$ ); and Purser's model with  $RMV = 25$  L/min ( $\bullet$ ).

As in the estimation of  $FED(I)_{CO}$ , the estimates of  $FED(I)_{HCN}$  using these different models differed substantially. For example, calculations using the FAA model yielded  $FED(I)_{HCN} > 1$  starting between 11 and 11 ½ minutes post-ignition, and these estimates reached values of approximately 2.3 by about 12 minutes post-ignition. Calculations using Purser's model yielded  $FED(I)_{HCN} > 11$  starting between 10½ and 11 minutes post-ignition, and these estimates reached values approximately 41 by 12 minutes post-ignition. That is, the numerical values of the two estimates of  $FED(I)_{HCN}$  differed 18-fold.

Plots of the  $FED(I)_{TOTAL}$  parameters estimated using both models are shown in Figure 73. The FAA Combined Survival Hazard Model yielded  $FED(I)_{TOTAL} > 1$  at about 11 minutes post-ignition, where  $FED(I)_{HCN}$  accounted for 70% of  $FED(I)_{TOTAL}$ ,  $FED(I)_{CO}$  accounted for approximately 25% of  $FED(I)_{TOTAL}$ , and  $FED(I)_{CO_2}$  accounted for approximately 5% of  $FED(I)_{TOTAL}$ . The estimated  $FED(I)_{TOTAL}$  reached a value of approximately 3.2 between 13 and 13 ½ minutes post-ignition. Purser's model yielded  $FED(I)_{TOTAL} > 1$  starting between 10½ and 11 post-ignition using a respiratory minute volumes of 8.5 L/min and 25 L/min in the calculations. The relative contributions of  $FED(I)_{CO_2}$ ,  $FED(I)_{CO}$ , and  $FED(I)_{TOTAL}$  did not differ substantially with respiratory minute volume:  $FED(I)_{HCN}$  accounted for  $> 97\%$  of  $FED(I)_{TOTAL}$ ;  $FED(I)_{CO}$  accounted for approximately 2.5% of  $FED(I)_{TOTAL}$ ; and  $FED(I)_{CO_2}$  accounted for  $< 1\%$  of  $FED(I)_{TOTAL}$ .

Figure 74 shows plots of  $FED(L)_{CO}$ ,  $FED(L)_{HCN}$ , and  $FED(L)_{TOTAL}$  computed using the FAA Combined Survival Hazard Model. These calculations yielded  $FED(L)_{CO} = 0.38$ ,  $FED(L)_{HCN} = 0.52$ , and  $FED(L)_{TOTAL} = 0.90$  at 15 minutes post-ignition. None of these indices exceeded values of 1 from the time of ignition until this gas analysis was stopped at about 18 minutes post-ignition.

As stated previously, the estimates of  $FED(I)$  and  $FED(L)$  obtained using the FAA Combined Hazard Survival Model and Purser's model of combustion gas toxicity can not predict precisely when the gas concentrations measured in this test would have resulted in incapacitating narcosis or death. This is especially true for prediction of lethality, where the mathematical relationships in these models were derived from experiments using laboratory animals or accidental, uncontrolled human exposures [8, 9]. Variation in the susceptibility to these hazards among the human population also will contribute to the uncertainty in these predictions. In addition, the effect of trauma suffered during the crash on an occupant's tolerance to these toxic gases is impossible to quantify.

Another variable that may affect an occupant's susceptibility to the combustion products is the location of the head. The data from the aspirated thermocouples indicated that a steep air-temperature gradient developed in the front of the passenger compartment during this test. Since

both heat and mass are conserved in a fire, the existence of a steep vertical air-temperature gradient implies the existence of a similarly steep vertical concentration gradient for combustion products accumulating in the passenger compartment. The inlet to the gas sampling tube in the passenger compartment was in the breathing zone of that of a six-foot tall adult male sitting upright in either the driver's or front passenger's seat. An occupant whose head was located below the level where gases were sampled would have been exposed to lower concentrations of combustion gases that those shown in **APPENDIX I**. And the estimated values of FED(I) and FED(L) for this occupant would have been lower than those shown in Figures 70 through 74.

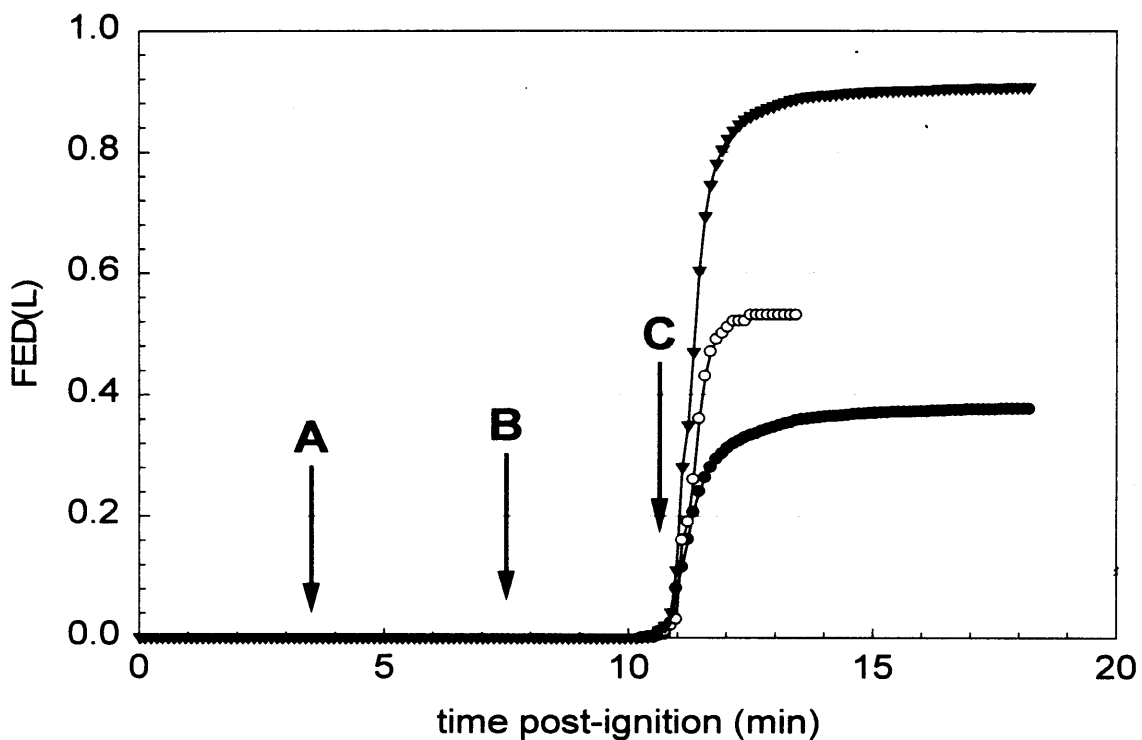


Figure 74. Fire Test F961115. Plots of  $FED(L)_{CO}$  (●),  $FED(L)_{HCN}$  (○), and  $FED(L)_{TOTAL}$  (▼) versus time post-ignition computed using the FAA Combined Hazard Survival Model. Fire. The arrows indicate ignition of the instrument panel top cover (A), ignition of the deployed passenger airbag (B), and the start of flame propagation forward across the head liner (C). Fire suppression began at approximately 11 minutes post-ignition.

### 8.3 Estimation of Burn-Injury to the Respiratory Tract

Figure 75 shows plots of the air temperature measured at 1, 4, 7, 10, 13, and 16 inches below the lower surface of the headliner versus time post-exposure. These plots show that the temperature

of the air in the front of the passenger compartment increased between 9½ and 10½ minutes post-ignition. By the end of the test, the air temperature measured 1 inch below the headliner exceeded 750°C, while the air temperature measured 16 inches below the headliner was approximately 250°C.

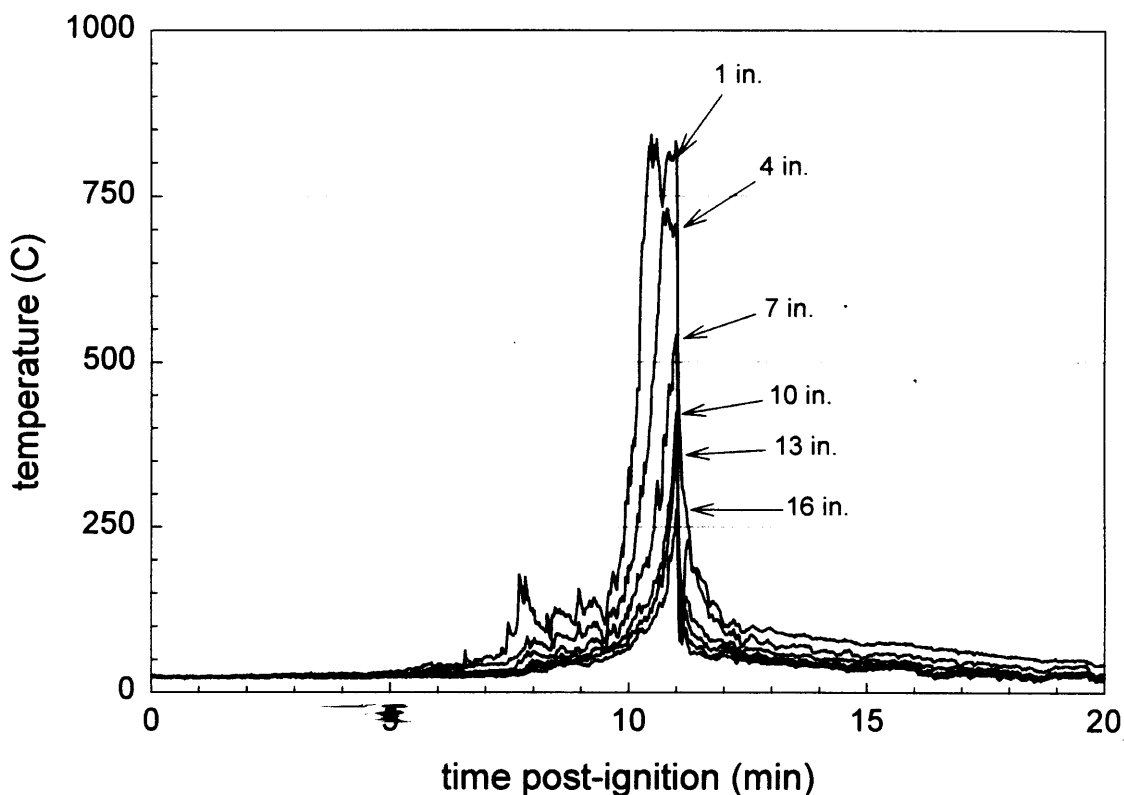


Figure 75. Fire Test F961116. Plots of air temperature at 1, 4, 7, 10, 13, and 16 inches below the lower surface of the headliner versus time post-ignition.

As the data in Figure 75 clearly shows, the temperature of the air inhaled by an occupant in the front of the test vehicle at this time would have depended on the height of the occupant's head. It is impossible to estimate the potential for burn injury to the respiratory tract caused by inhalation of hot air from air temperature data alone. Water and particulate produced by the fire increase the heat capacity of the air. The concentrations of these species in the inhaled air may affect both the severity and depth of burn injury in the respiratory system. Neither the water- nor the particulate-concentrations in the passenger compartment were measured in this test. Additionally, a robust quantitative relationship between temperature, water content, and particulate concentration of inhaled air and subsequent burn injury to respiratory airways caused by inhaling such a mixture has not been established [9]. A few controlled animal studies indicate that inhalation of steam at 100°C caused burns to the larynx and trachea similar to those

produced by inhalation of dry air at 350°C or flames at 500°C [9]. In these controlled animal studies, death was not immediate, but occurred a few to twenty-four hours after the exposure and resulted from obstructive edema in the burned airways. Given these uncertainties, it is impossible to assess whether and when burn injury to the respiratory airways would occur from the data shown in Figure 75.

## **ACKNOWLEDGEMENTS**

Dr. Thomas Ohlemiller and Thomas Cleary of the Building and Fire Research Laboratory, National Institute of Standards and Technology were responsible for video taping this fire test, and provided an initial analysis of the test data for fire propagation. Dr. Kenneth Strom of the General Motors Corporation provided the analysis of the pressure and flow data, and the BURNSIM analysis for this report. Dr. Archibald Tewarson of Factory Mutual Research Corporation provided the data from the Fire Products Collector at the test facility that was collected during this test.

## REFERENCES

1. Jack L. Jensen and Jeffrey Santrock. Evaluation of Motor Vehicle Fire Initiation and Propagation. Part 1: Vehicle Crash Test and Fire Propagation Test Program. Submitted to the National Highway Transportation Safety Administration pursuant to the Settlement Agreement between General Motors and the Department of Transportation. Submitted July 31, 1997.
2. Jack L. Jensen and Jeffrey Santrock. Evaluation of Motor Vehicle Fire Initiation and Propagation. Part 2: Crash Tests on a Passenger Van. Submitted to the National Highway Transportation Safety Administration pursuant to the Settlement Agreement between General Motors and the Department of Transportation. Submitted September 1, 1998.
3. Federal Safety Standards. Motor Vehicle Safety Standard No. 214 Side Impact Protection - Passenger Cars, Trucks, Buses & Multipurpose Passenger Vehicles with GVWR of 10,000 Pounds or Less. 60FR57838-39 (November 22, 1995).
4. Thomas J. Ohlemiller and John R. Shields. Burning Behavior of Selected Automotive Parts from a Minivan. National Institute of Standards and Technology Internal Report NISTIR 6143. August 1998. Submitted to the National Highway Transportation Safety Administration pursuant to the Settlement Agreement between General Motors and the Department of Transportation. Submitted September 9, 1998.
5. Yuji Hasemi, Masashi Yoshida, Shuichi Takushima, Ryoichi Kikuchi, and Yutaka Yokobayashi. "Flame Length and Flame Heat Transfer Correlations in Corner-wall and Corner-Wall Ceiling Configurations". In Proceedings of Interflam '96. Interscience Communications, LTD., London, 1996.
6. Archibald Tewarson. "Generation of Heat and Chemical Compounds in Fires" Section 3/Chapter 4, SFPE Handbook of Fire Protection Engineering, 2nd Edition, 1995, pp. 3:53-124.
7. F. S. Knox III, Dena Bonetti, and Chris Perry. User's Manual for BRNSIM/BURNSIM: A Burn Hazard Assessment Model. United States Army Aeromedical Research Laboratory Report No. 93-13. Fort Rucker, Alabama 36362-5292. February 1993.
8. L. C. Speitel. Toxicity Assessment of Combined Gases and Development of a Survival Model. DOT/FAA/AR-95-5. July 1995.
9. David A. Purser. "Toxicity Assessment of Combustion Products" Section 2/Chapter 8, SFPE Handbook of Fire Protection Engineering, 2nd Edition, 1995, pp. 2:85-146

**APPENDIX A  
VIDEO CAMERA SET-UP**

Scientific and technical personnel from the Building and Fire Research Laboratory, National Institute of Standards and Technology were primarily responsible for obtaining a video record of this test. Seven video cameras were used in this test. Figure A1 shows the approximate locations of the video cameras relative to the test vehicle during this test.

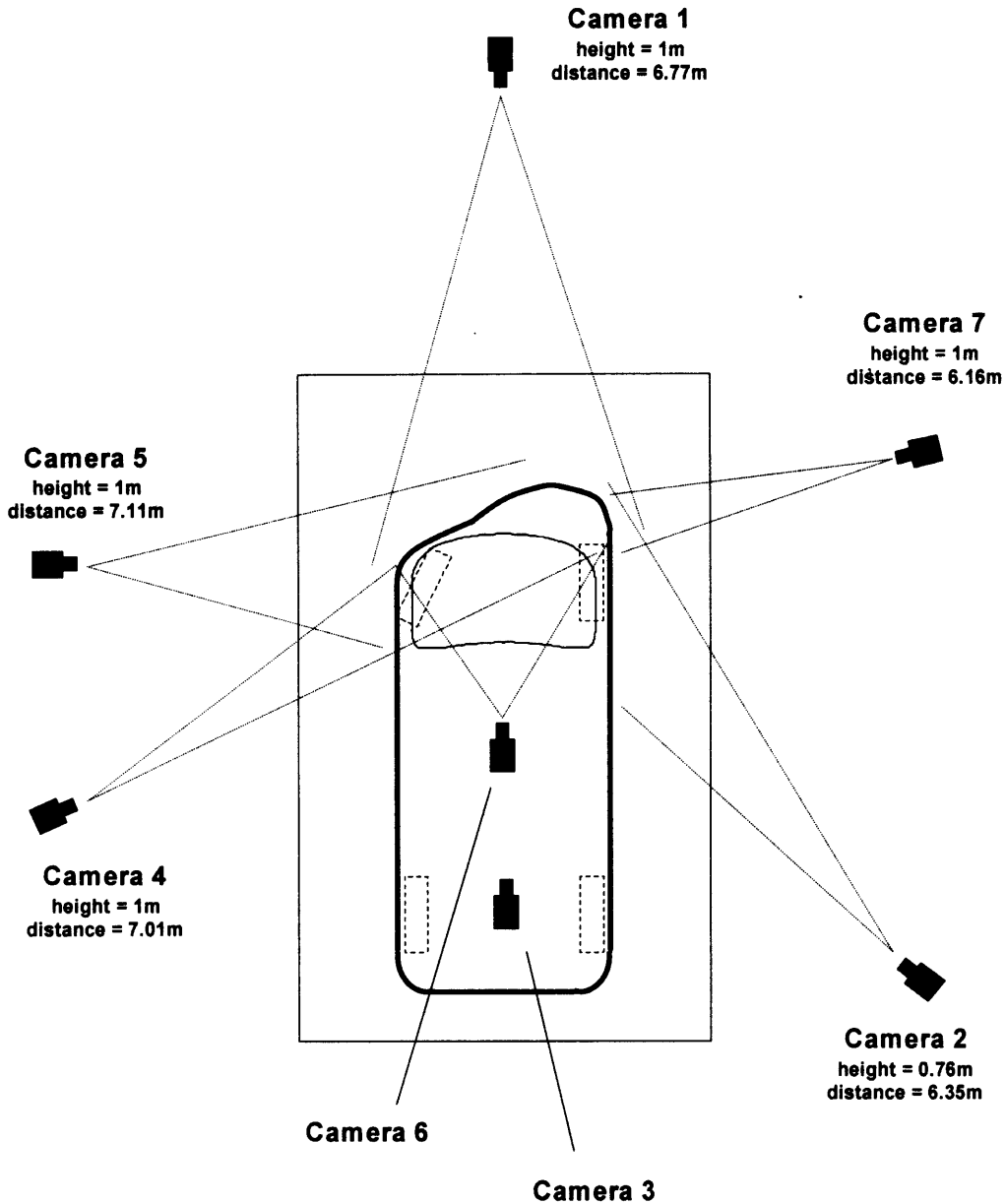


Figure A1. Fire Test F961115. Diagram showing the approximate locations of the video cameras during this test. Distances in this figure are not to scale in this diagram.

Cameras 1, 2, 4, 5, and 7 were Hi-8 camcorders mounted on tripods. Camera 1 had a field-of-view that included the full height and width of the front of the test vehicle, and the surface of the

fluid containment pan under the front bumper. Camera 2 had a field-of-view that included the lower half of the test vehicle from the right front door to the front bumper fascia, and the surface of the fluid containment pan under the engine compartment. Camera 4 was focused on the top of the instrument panel through the left front window. Its field-of-view included the windshield, the instrument panel top cover, the upper portion of the instrument panel, the steering wheel, and the deployed driver and passenger airbags. Camera 5 had a field-of-view that included the full height of the test vehicle from the rear edge of the left front door to the front bumper fascia. A water pipe for the extinguishing system on the fire products collector obscured a section of the test vehicle around the left A-pillar. Camera 7 was focused on the engine compartment through a gap between the left side of the hood and the left fender. Its field-of-view included the windshield, the hood, the HVAC air intake cowl and cowl cover, the battery and PDC, and the air intake manifold on top of the engine.

Camera 3 was a Hi-8 camcorder mounted on a sled, which was placed on the ground just ahead of the rear axle. Its field-of-view included the area under the engine compartment between the front tires. Cameras 2 and 3 provided two intersecting views of the area below the engine compartment to help locate the position of any fluid-spill or melt/drip-fires on the ground.

Camera 6 was a black-and-white CCD device mounted on a tripod located inside the vehicle between the front seats. Its field-of-view included the full width of the lower section of the instrument panel.

All video cameras were started before the test. A microphone on each camera recorded the air horn, which signaled the start and end of the test.

Quartz-halogen floodlights were used to illuminate the exterior of the vehicle. The level of illumination provided by these lamps was insufficient to balance the intensity of light reflecting from the vehicle surfaces with the brightness of the flames. To compensate for this imbalance, the light sensitivity adjustments on the Hi-8 camcorders were set to the manual position so that the apparent brightness of the vehicle surfaces did not change as the fire developed. As a result, the flames were overexposed, causing them to appear more opaque than they actually were.

**APPENDIX B**  
**INFRARED THERMOGRAPHY**

Infrared thermal imaging radiometers were used to help determine fire propagation, flame, and surface temperatures during this test. These imaging systems measure thermal radiation within a definite waveband, over a variable field of view. The data obtained from these measurements can be analyzed to produce a two-dimensional map of apparent temperature called a thermogram.

Thermal imaging systems produce a spatially resolved map of surface temperatures from the radiant energy emitted in the field of view. The response time of these systems is nanoseconds, giving them the capability to acquire over 1 million discrete measurements per second. The capability of high-speed data acquisition is advantageous in that it can provide a tremendous amount of thermal data during a vehicle fire test, which can be over in only a few minutes. Thermal imaging radiometers can be used concurrently as a vision system and a measurement system. However, the thermal sensitivity, scan speed, and spatial resolution must be optimized for a particular application.

### **B.1 Infrared Camera Location**

Four thermal imaging systems were used in this test. Figure B1 shows the approximate locations of the infrared cameras relative to the test vehicle during this test. IR1, IR2, and IR3 were mounted on tripods positioned outside the test vehicle. IR1 was an Inframetrics Model SC1000 ThermoCam (Inframetrics Inc, Billerica, MA) with an optical window of 3 to 5  $\mu\text{m}$ , and was fitted with a 3.9  $\mu\text{m}$  cut-off filter. Its field-of-view included the full height and width of the front of the test vehicle, and the surface of the fluid containment pan under the front bumper. IR 2 was an Inframetrics 740 thermal imaging radiometer with an optical window of 8 to 12 $\mu\text{m}$ . Its field-of-view included the full height of the test vehicle from the rear edge of the left front door to the front bumper fascia. IR 3 was an Inframetrics Model 760 thermal imaging radiometer with an optical window of 3 to 12  $\mu\text{m}$ , and was fitted with a 3.9  $\mu\text{m}$  cut-off filter. It was focused on the center of the instrument panel through the left front window. Its field-of-view included the windshield, the instrument panel top cover, the upper portion of the instrument panel, the steering wheel, and the deployed driver and passenger airbags.

IR4 was a Flir Model 7300 thermal imaging radiometer (Flir Systems, Inc., Portland, OR) with an optical window of 3 to 5  $\mu\text{m}$ . This system was mounted to a bracket suspended from the roof of the vehicle over the middle bench seat. The thermal imaging radiometer was wrapped with aluminized silica cloth to protect it from flames. The 3.9  $\mu\text{m}$  cut-off filters were used on IR1 and IR3 to eliminate or significantly reduce infrared radiation from flames, and thus allow more accurate measurement of surface temperatures. Emission from soot in the flames still interfered with the determination of temperature when flames were in the direct line of sight of a surface.

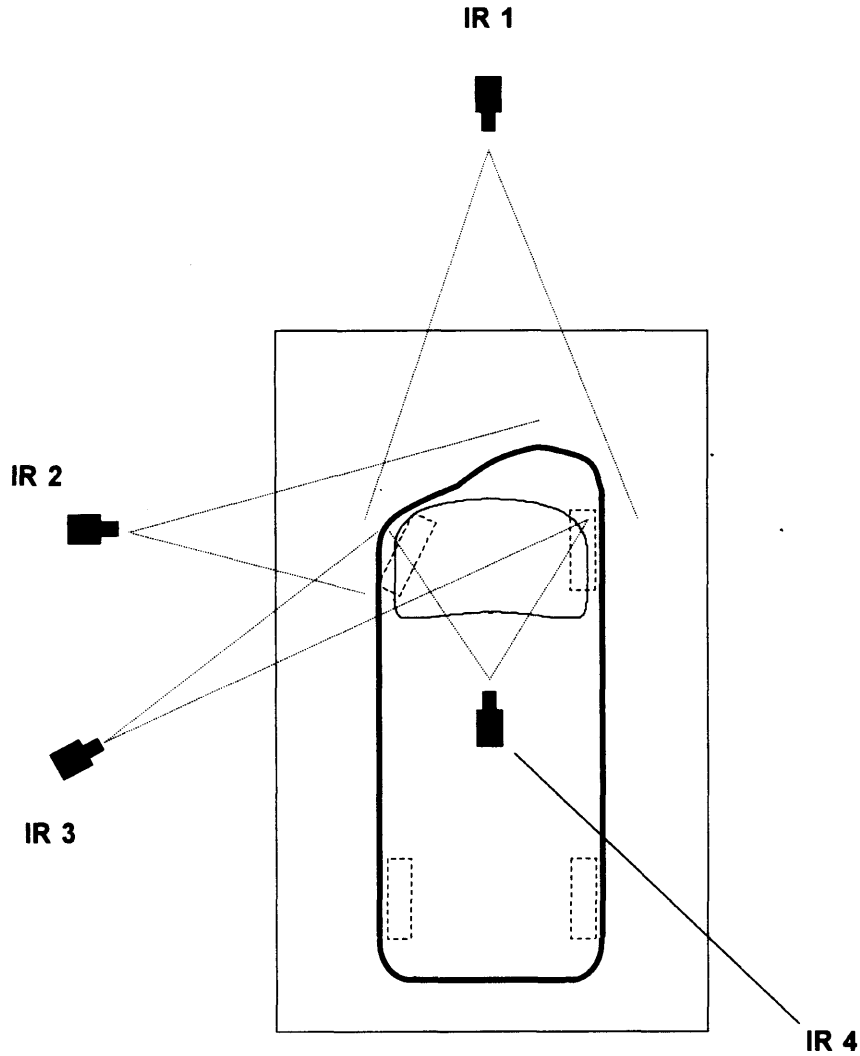


Figure B1. Layout of infrared thermal imaging systems during Fire Test F961115. Distances are not to scale in this diagram.

## B.2 Data Systems

The analog output signals from the Inframetrics Models 740 and 760 radiometers were recorded to videotape during the fire test. The thermal images stored on the tapes were converted to an 8-bit digital format and stored to a computer hard drive. The Inframetrics Model SC1000 ThermaCam output an 8-bit digital signal, which was stored directly to a computer hard drive during the fire test. In both cases, the data acquisition software (*ThermaGram Pro version 1.3*) was configured to sample data at 5-sec. intervals. The computer data system used to process

the IR thermograms was a PC with a 90 MHz Pentium Processor, 64 MB of RAM, 2.0 GB hard drive, and a thermal A/D conversion card (*Inframetrics and ThermoTeknix Systems*).

### B.3 Data Analysis

Thermal imaging systems measure infrared radiation within a certain spectral band and must be calibrated to convert radiant intensity in that spectral band to temperature. Due to variations in system response, every system has to be calibrated. Calibration curves for the basic thermal imaging radiometers are measured at the factory and stored in read-only memory or in analysis software programs. Additional calibrations are needed for the optical filters. These calibrations are stored in the analysis software programs. Since thermal imaging radiometers are AC coupled devices, they measure differences in thermal radiation. To get absolute temperatures, there must be a reference to provide DC restoration. In these instruments, the reference is an internal blackbody reference source that is viewed periodically by the detector.

The general radiometric equation was used to convert radiant energy to temperature:

$$\hat{I} = [E_t \times F(T_t)] + [(1 - E_t) \times F(T_b)] - [E_r \times F(T_r)] - [(1 - E_r) \times F(T_b)] \quad (B1)$$

Where  $\hat{I}$  is the difference in radiance between the target and a reference surface;  $E_t$  is the emittance of the target surface, generally unknown;  $E_r$  is the emittance of the reference surface,  $T_t$  is the temperature of the target surface;  $T_b$  is the temperature of background surfaces (i.e., ambient temperature), or other emitters such as flames reflected from the target;  $T_r$  is the temperature of the reference surface;  $F(T_t)$  is the radiance from an ideal emitting surface (i.e., black body) at the temperature of the target surface ( $T_t$ );  $F(T_r)$  is the radiance from an ideal emitting surface at the temperature of the reference ( $T_r$ ); and  $F(T_b)$  is the radiance from the background relative to the radiance value from the reference surface when  $E_r = 1$ . Factors other than temperature determine the emittance of an object. These factors include the type of material, the texture of the surface, the wavelength of the detector, and the view-angle. In determining temperatures from the radiant energy from an object, the operator can set the emittance of an unknown target surface to a value of between .01 and 1.0.

Radiant intensity measured by the thermal imaging system is converted to a gray-scale value. An 8 bit system provides gray scale values from 0 to 255 for the radiant energy at each pixel in the instantaneous field of view. A 12 bit system provides gray scale values from 0 to 4095. As the radiometer scans the image, each pixel is assigned a gray scale value, and the gray scale image is stored either in a computer memory or onto videotape. When stored in computer memory, a

single frame (1 thermogram) can contain up to 68,000 pixels (discrete measurements) with an assigned 8 bit or 12 bit value. Videotape provides a temporal resolution of 30 frames per second. Depending on the thermal range of the thermal imaging radiometer, a temperature value was assigned to each pixel using either the factory calibration curves accompanying each instrument, or calibration curves stored in IR analysis software.

Separation of the apparent temperatures of various surfaces on and inside a burning vehicle from the captured data is not a trivial task. The data represent a complex combination of emitted infrared energy from those surfaces as well as reflected infrared energy from the flames, and reflected infrared energy from high intensity lights used to illuminate the vehicle for visual data capture. In addition, the flames themselves were emitting infrared radiation due to their sooty content, some part of which was captured by the infrared thermal imaging systems. Also, some of the infrared radiation being emitted by the vehicle surfaces had to pass through flames containing soot from incomplete combustion of synthetic polymers or through clear (clean) flames where more complete combustion was occurring, and/or a combination of both types of flames. In all of these cases, gases in the flame absorbed some of the infrared radiation emitted by objects behind the flame.

The following steps were taken to minimize the impact of unwanted infrared radiation being captured by the thermal imaging systems.

- Anti-reflection tapes, paint, and glazes were applied to highly reflective surfaces on the test vehicle.
- The thermal imaging systems were located in the shadows of the vehicle to block the video lights from shining directly into the radiometer.
- Two of the thermal imaging systems were fitted with flame filters (3.9  $\mu\text{m}$ ) to screen out a portion of the infrared radiation from both sooty and clear flames.

Despite these precautions, accurate surface temperatures could not be determined for areas of the vehicle blocked by intense flame. As a result, only surface temperatures determined to be reliable by the IR analysts are reported here. In some cases, specialized data analysis techniques were used to obtain reliable surface temperatures from areas in close proximity to, but not shielded by flame. Where possible, temperature data were reported from areas that lie in the shadow of the flames, which comes from highly emissive surfaces not affected by the flame radiation, and/or is deemed reliable based on the experience of the analysts. Data from nearby thermocouples were compared to IR temperature readings for a more comprehensive analysis.

During the data analysis, the videotapes were reviewed frame-by-frame to observe the burn sequence. The analyst captured images from selected frames on a video board. The image was processed to produce a digitized gray scale value for each element in the pixel matrix utilizing the camera settings automatically documented between video frames on the videotape during data acquisition. Thermograms were produced from the digitized image matrix using a commercial software package (Thermogram Pro V1.3, sold by Inframetrics, Inc., Billerica, MA). This software utilized the NIST traceable calibration tables supplied by the manufacturer with each thermal imaging system.

**APPENDIX C  
THERMOCOUPLE DATA**

Type-N thermocouples were fabricated by Medtherm Corporation (Huntsville, AL). They consisted of an enclosed, grounded thermocouple junction (30 AWG thermocouple wire) in an Inconel 600 sheath with magnesium oxide insulation (o.d. = 0.040 in. (1 mm), length = 50 ft. (15.2 m)). A transition to a duplex thermocouple extension cable (24 AWG) with fiberglass insulation and a stainless steel over-braid (length = 50 ft. (15.2 m)) was made through a stress-relief bushing. The thermocouple extension cables were connected directly to the multiplex thermocouple input cards in the data acquisition system (see below).

Type-K thermocouples with exposed, bead-type junctions were prepared from thermocouple duplex wire with glass fiber insulation (26 AGW, length = 10 ft (3.04 m). Each thermocouple was connected to a Type-K thermocouple extension cable using compensated ceramic thermocouple connectors. The extension cables consisted of Type-K thermocouple wire (24 AWG) with fiberglass insulation and a Teflon-jacketed stainless steel over-braid (length = 25 m (15.2 m)). The extension cables were connected directly to the multiplex thermocouple input cards in the data acquisition system (see below).

A PC-based data system was used for data acquisition from the thermocouples. The PC contained a 75 MHz Pentium Processor, 16 MB RAM, an 814 MB hard disk, and a 16-bit (Model BG45-AP5CP, ACER Inc., Taiwan R. O. C.). A 100 kHz I/O board with 16 analog input channels (DaqBoard 200A, IOTech, Inc., Cleveland, OH) was installed in one of the expansion slots in the PC. Thermocouple multiplex expansion cards (DBK-19, IOTech, Inc., Cleveland, OH) were used for data acquisition from the Type-N and Type-K thermocouples. The electrical shields on the thermocouple cables were connected to the electronic chassis grounds on the thermocouple multiplex extension cards. The vehicle chassis was connected to the electronic chassis ground by a large-gauge cable. The data acquisition software (DASYLab, Daten System Technik GmbH, Mönchengladbach, Germany) was configured to sample each channel at a rate of 10 Hz and store the data in 10-point block averages.

Figures C1 through C6 show the approximate locations of thermocouples installed in the test vehicle for this test. Plots C1 through C77 show that temperature data recorded from these thermocouples.

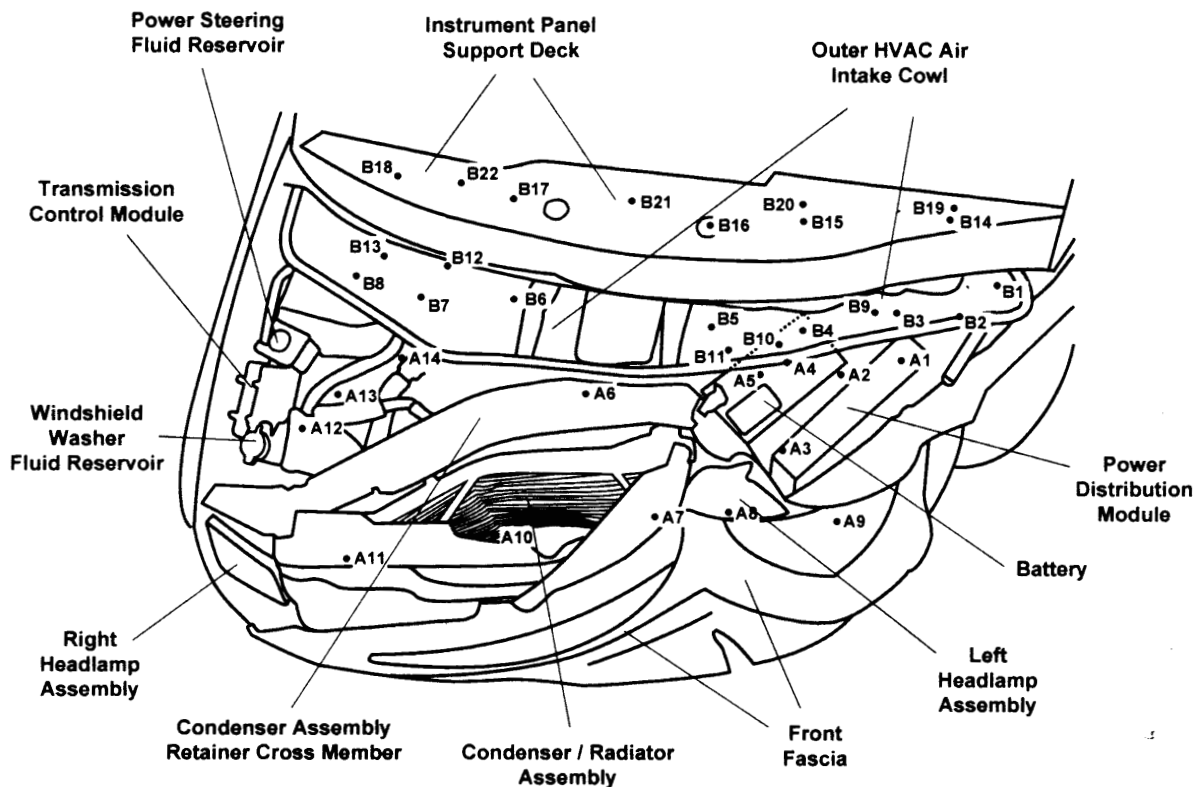


Figure C1. Fire Test F961115. Top view of the front of the test vehicle showing the approximate locations of thermocouples in the engine compartment, in the HVAC air intake cowl, and on the instrument panel support deck. Thermocouples A1 through A14 were located in the engine compartment. Thermocouple A6 was located below the Radiator Assembly Retainer Cross-Member. Thermocouples B1, B2, B3, B4, B5, B6, B7, B8, and B10 were located approximately 1 cm below the lower face of the HVAC air intake cowl. Thermocouples B9, B11, B12, and B13 were located inside the HVAC air intake cowl. Thermocouples B14, B15, B16, B17, and B18 were located inside the HVAC air intake ducts, approximately 5 cm below the lower surface of the instrument panel support deck. Thermocouples B19, B20, B21, and B22 were located on the upper surface of the instrument panel support deck.

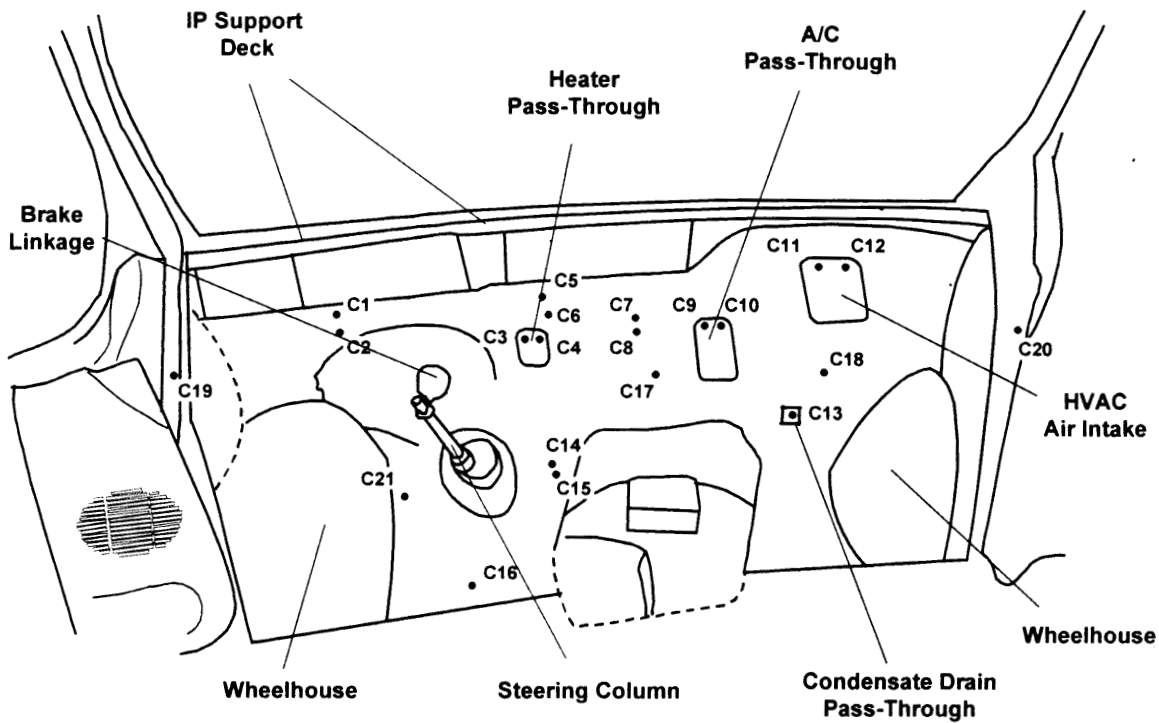


Figure C2. Fire Test F961115. Interior view of the front of the test vehicle showing the approximate locations of thermocouples on the dash panel. Thermocouples C1, C5, C7, and C14 were located on the interior surface of the dash panel. Thermocouples C2, C6, C8, C15, C16, C18, and C21 extended through the dash panel and engine compartment dash panel silencer pad so that the thermocouple junction was in the engine compartment approximately 1 cm forward of the exterior face of the engine compartment dash panel silencer pad. Thermocouples C3 and C4 were located in the upper left and right, respectively, of the heater feed-through. Thermocouples C9 and C10 were located in the upper left and right, respectively, of the A/C feed-through. Thermocouples C11 and C12 were located in the upper left and right, respectively, of the HVAC air intake. Thermocouple C13 was located in the A/C condensate drain feed-through. Thermocouples C19 and C20 were located on polymer covers in the left and right hinge-pillars.

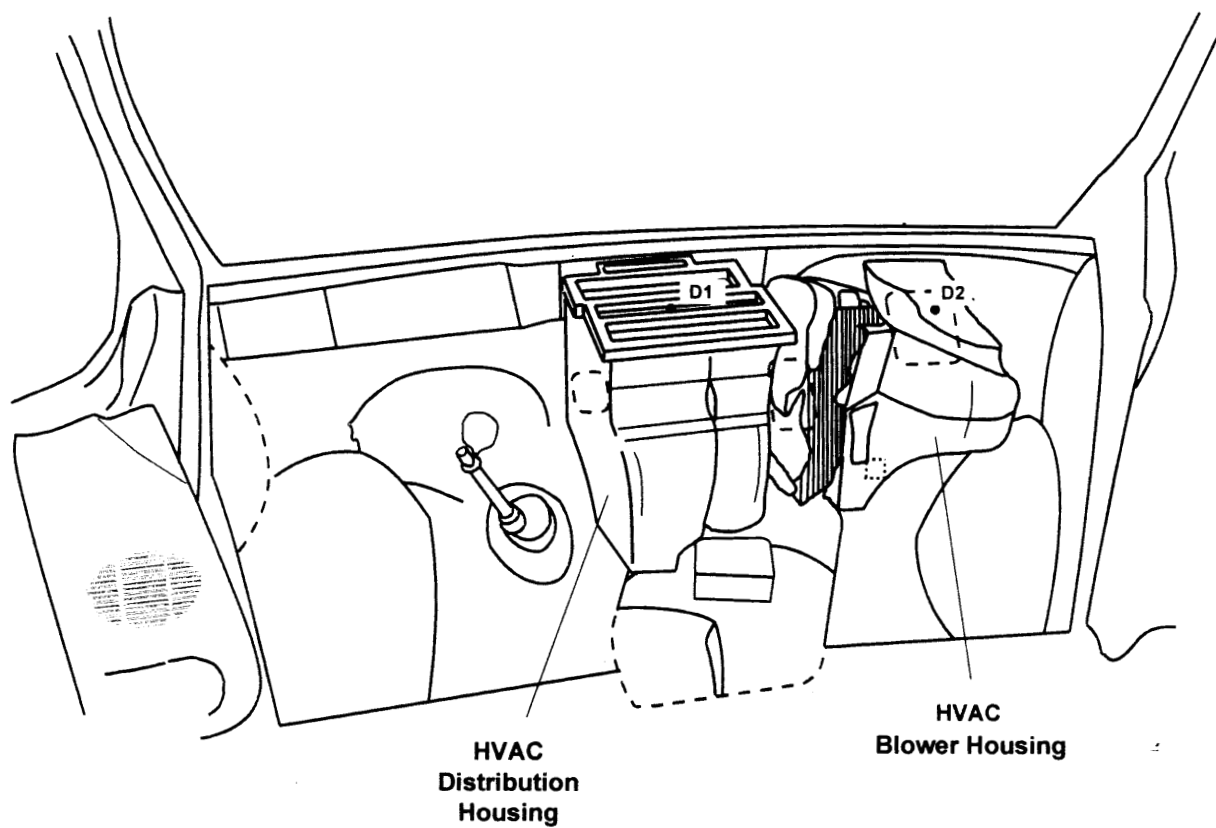


Figure C3. Fire Test F961115. Diagram showing the locations of thermocouples (shown in pink) in the HVAC blower and distribution housings. Thermocouple D1 was located in the lumen at the top of the HVAC distribution housing. Thermocouple D2 extended through the top of the HVAC blower housing into the air space between the damper door and the blower. The section of the HVAC module housing the A/C evaporator core was broken in the crash test, exposing the evaporator core as shown in this diagram. The feed-through openings in the dash panel were covered by the HVAC blower and distribution housings. For reference, these openings are shown as dashed lines in this diagram.

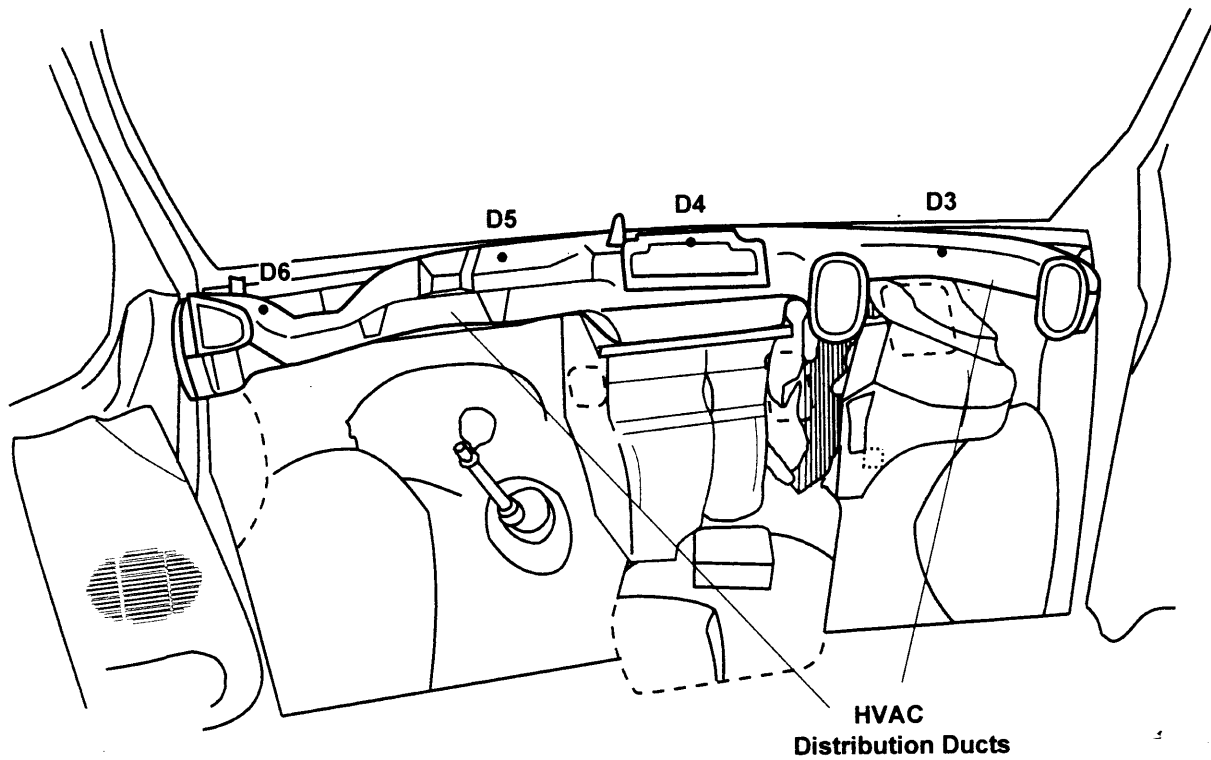


Figure C4. Fire Test F961115. Diagram showing the locations of thermocouples in the HVAC distribution ducts. Thermocouple D3 through D6 were located in the lumen of the HVAC distribution duct assembly approximately 1 cm below the upper internal surface of the duct.

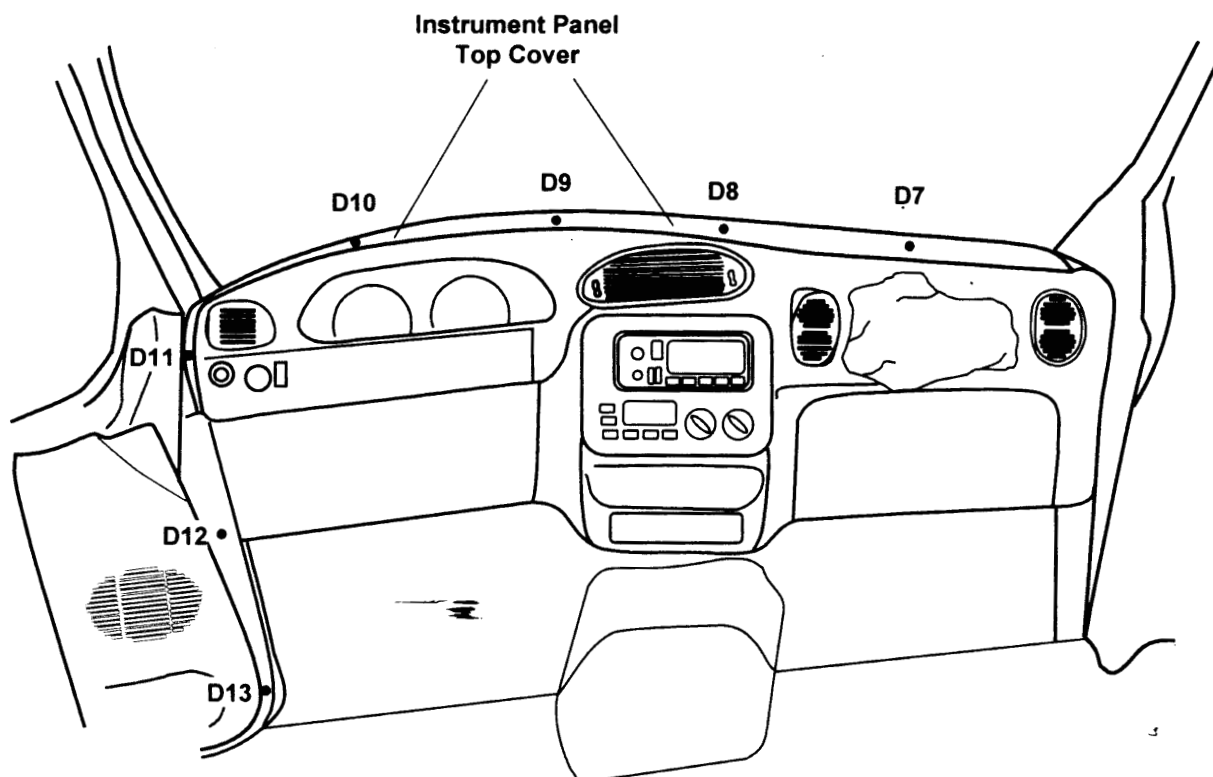


Figure C5. Fire Test F961115. Diagram showing the locations of thermocouples on the instrument panel top cover and the gap along the forward edge of the driver's door. Thermocouples D7 through D10 were located on the upper surface of the instrument panel top cover. Thermocouples D11 through D13 were located in the gap between the forward edge of the driver's door and the front left hinge pillar.

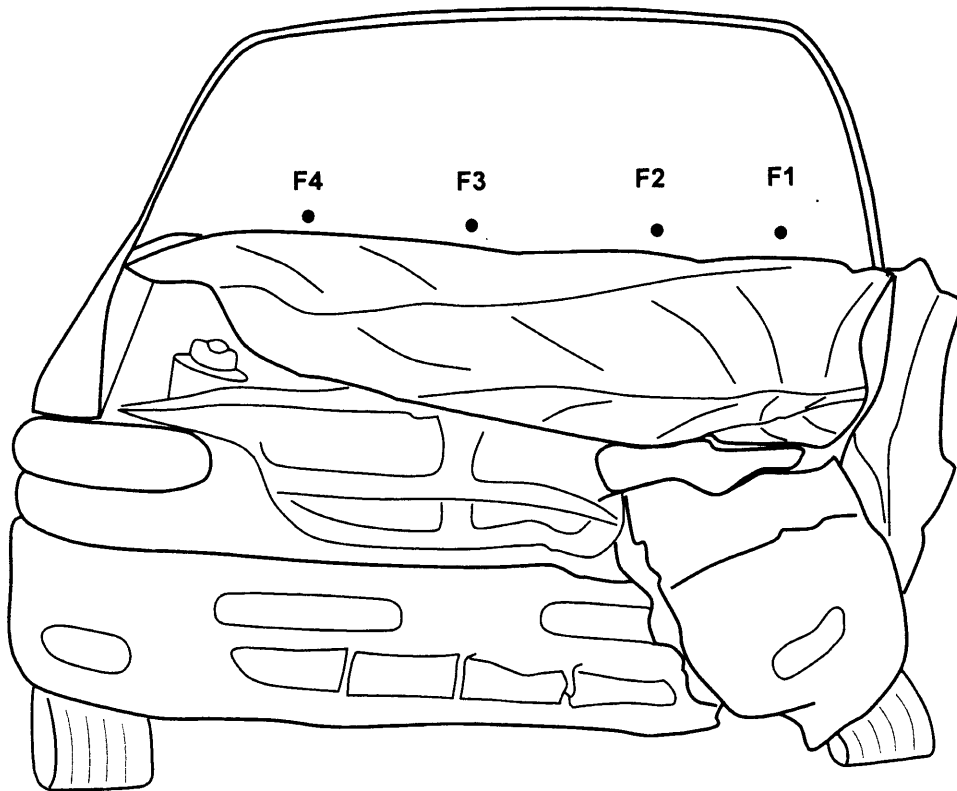
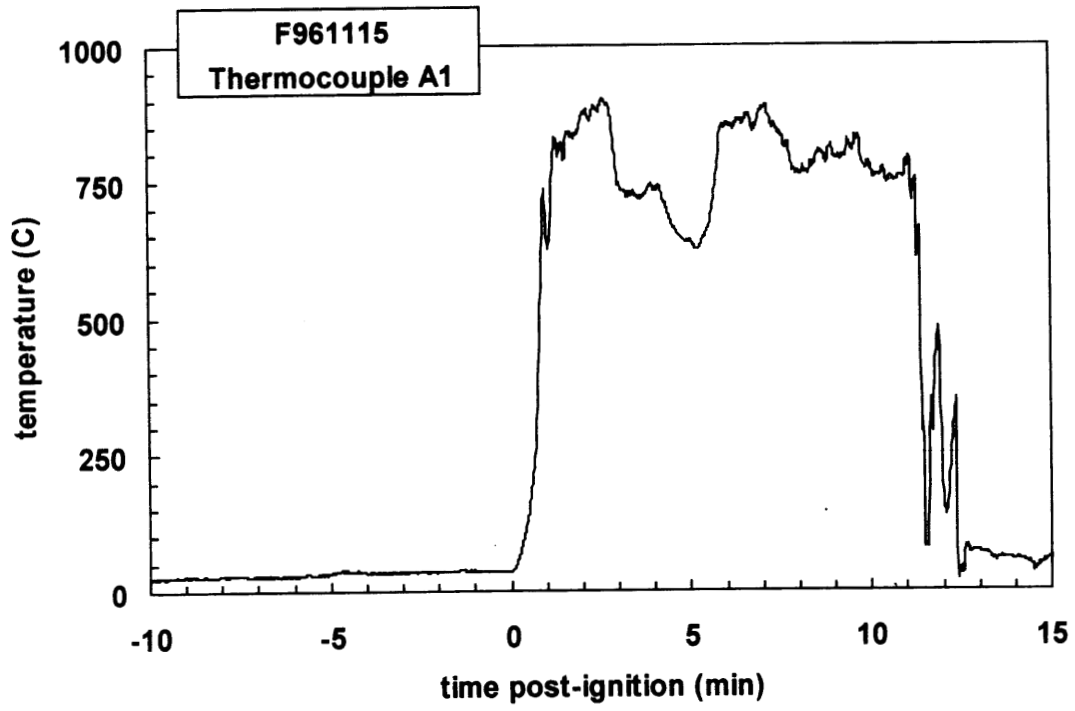
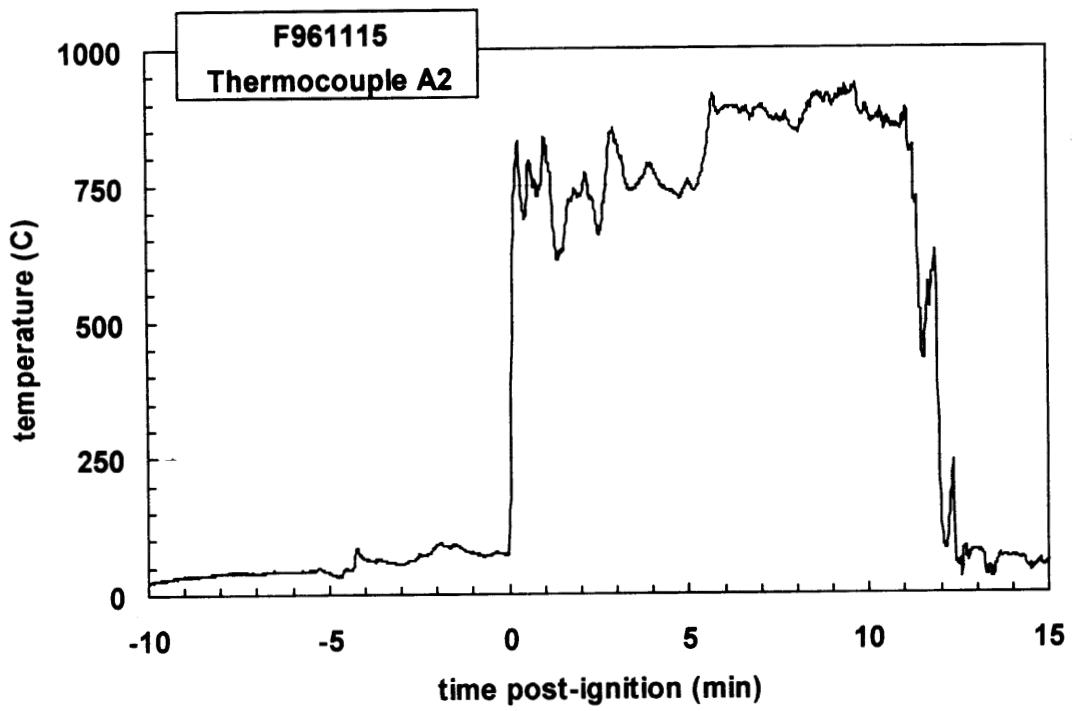


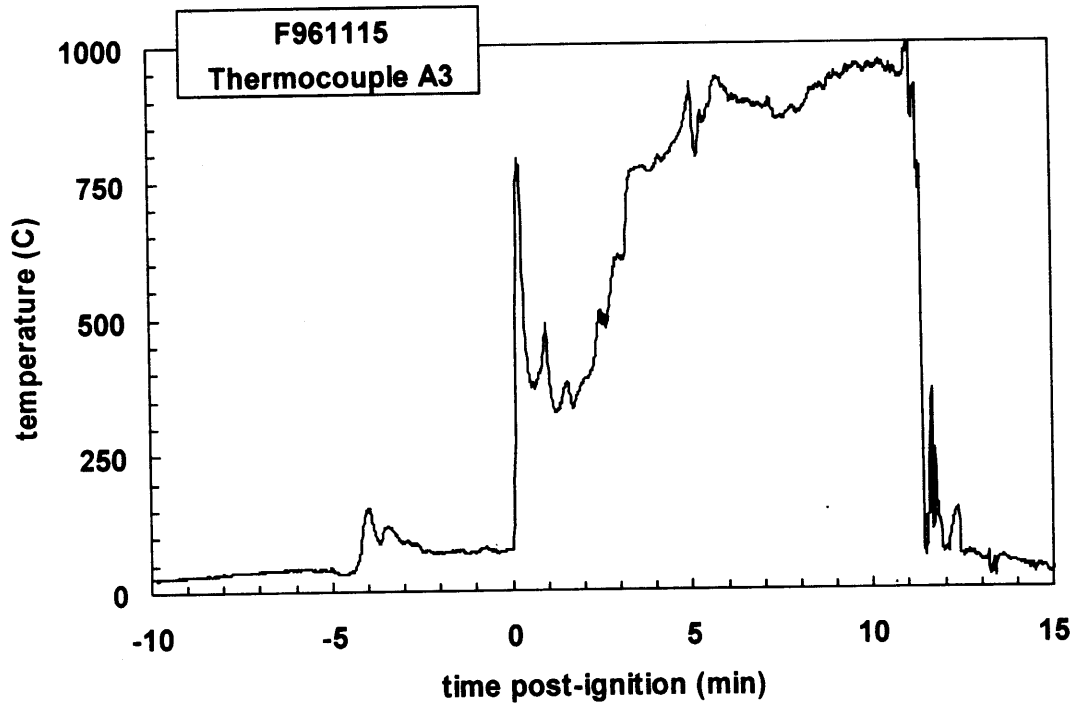
Figure C6. Fire Test F961115. Diagram showing the locations of thermocouples on the exterior surface of the windshield. Thermocouples F1 through F4 were located on the exterior surface of the windshield.



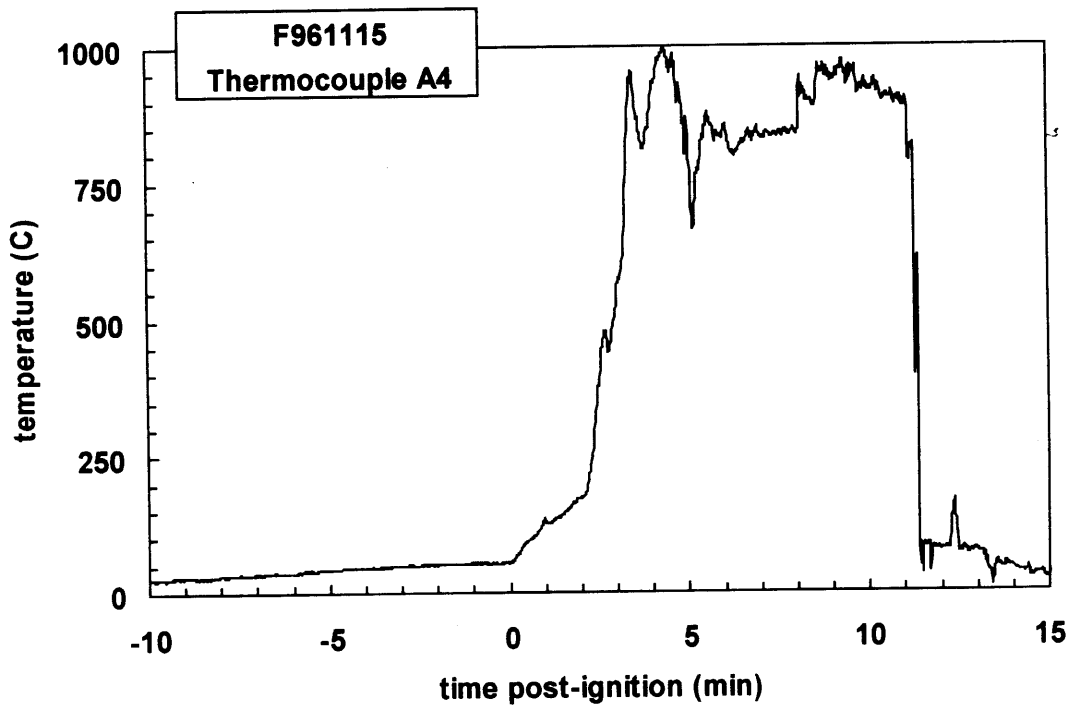
Plot C1. Fire Test F961115. Data plot from thermocouple A1.



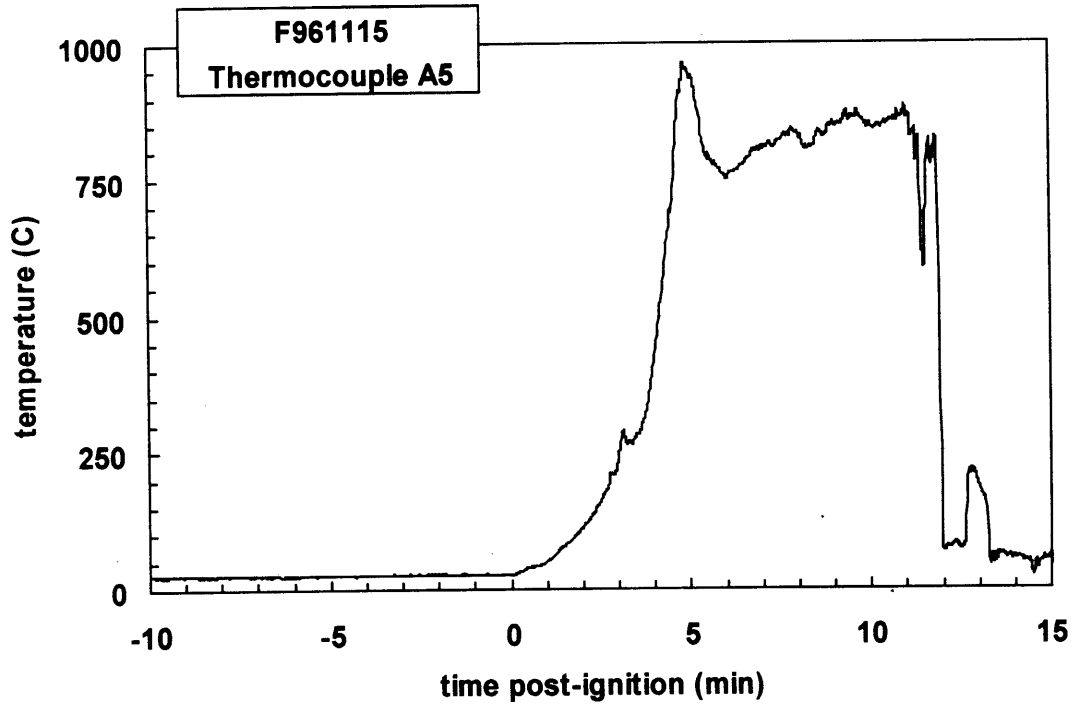
Plot C2. Fire Test F961115. Data plot from thermocouple A2.



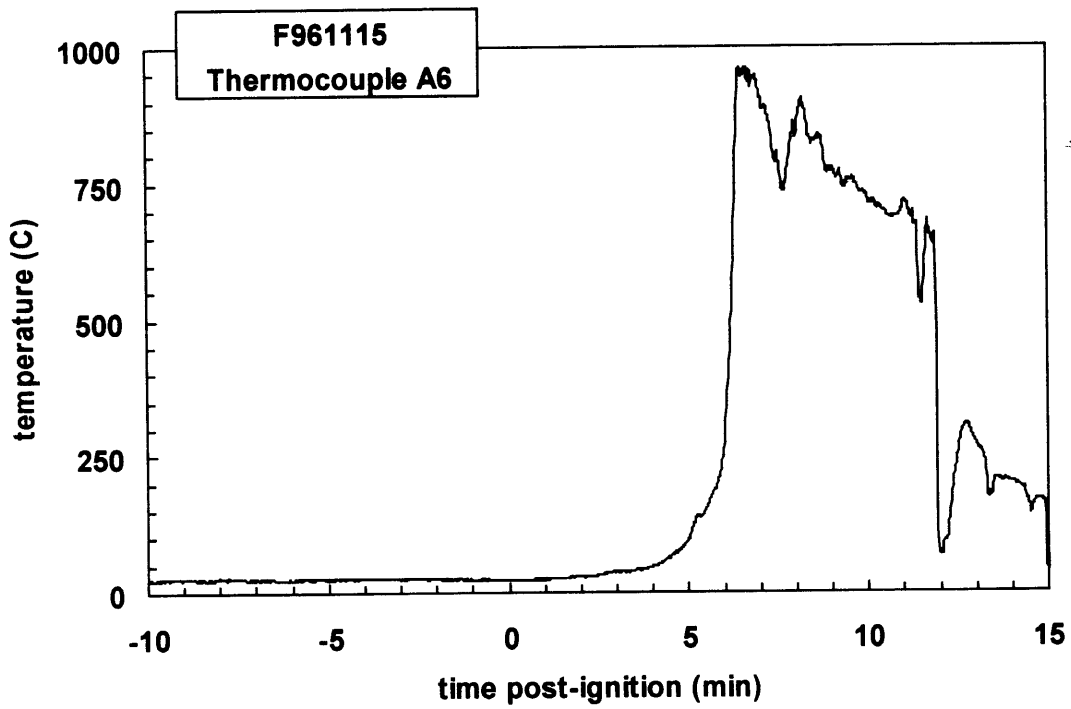
Plot C3. Fire Test F961115. Data plot from thermocouple A3.



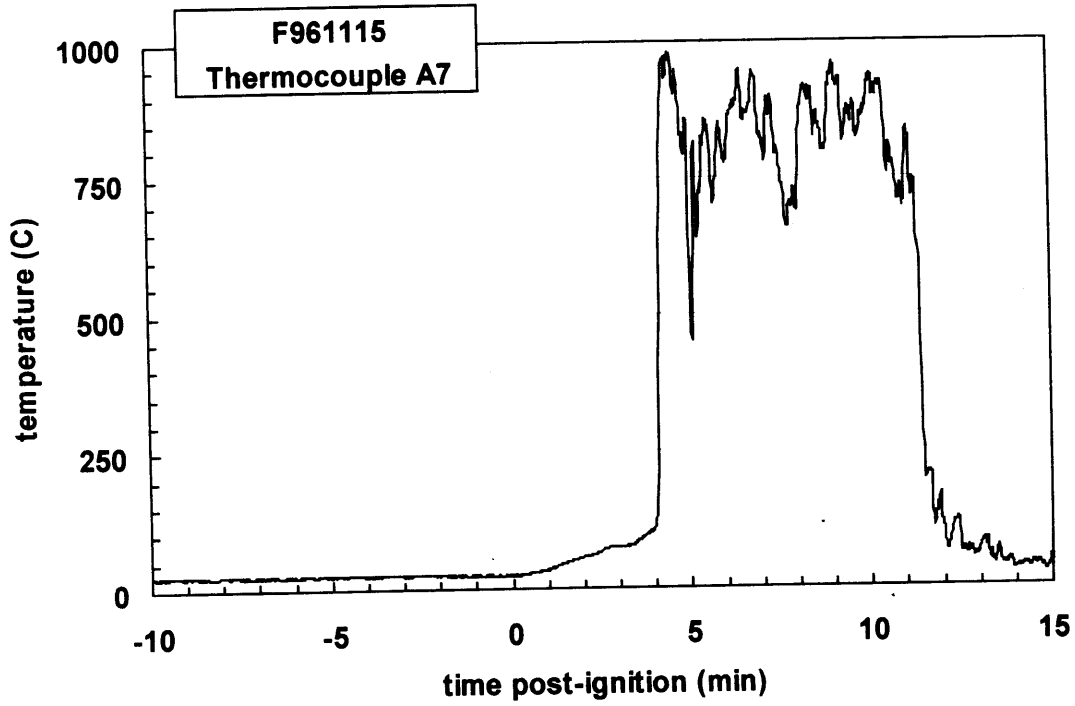
Plot C4. Fire Test F961115. Data plot from thermocouple A4.



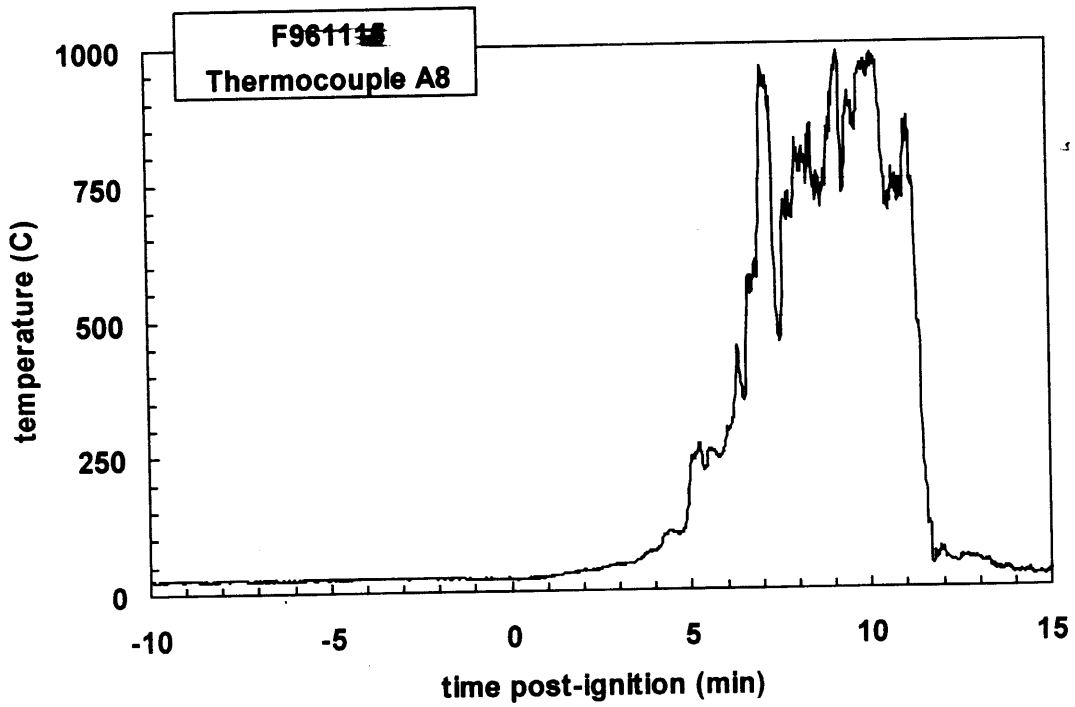
Plot C5. Fire Test F961115. Data plot from thermocouple A5.



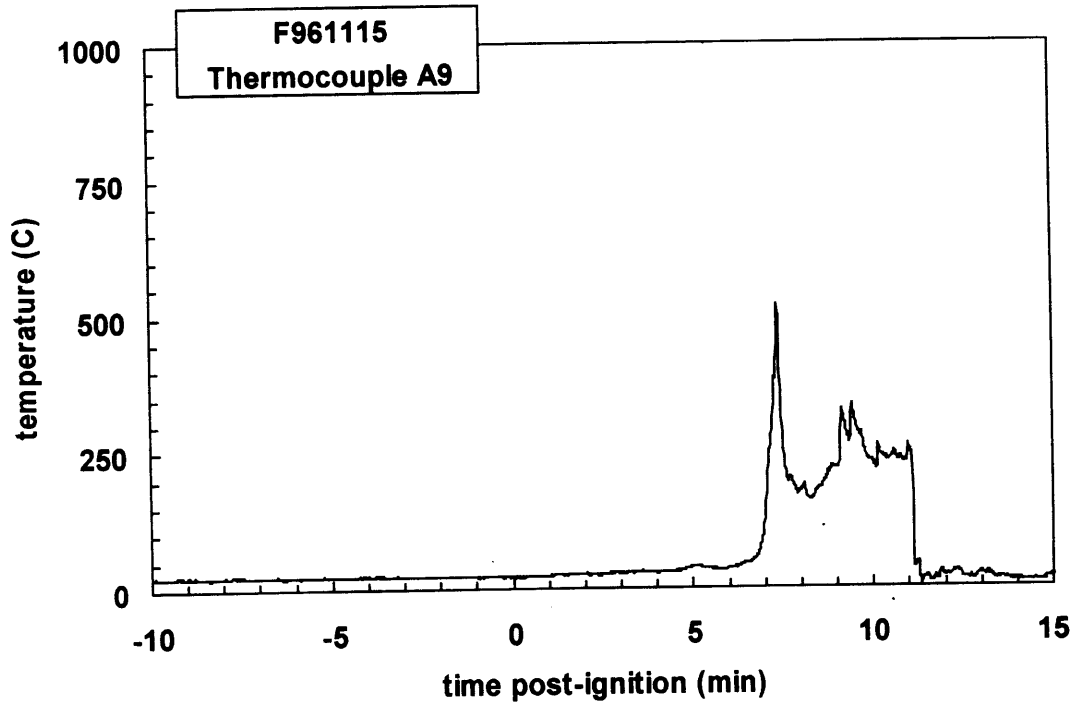
Plot C6. Fire Test F961115. Data plot from thermocouple A6.



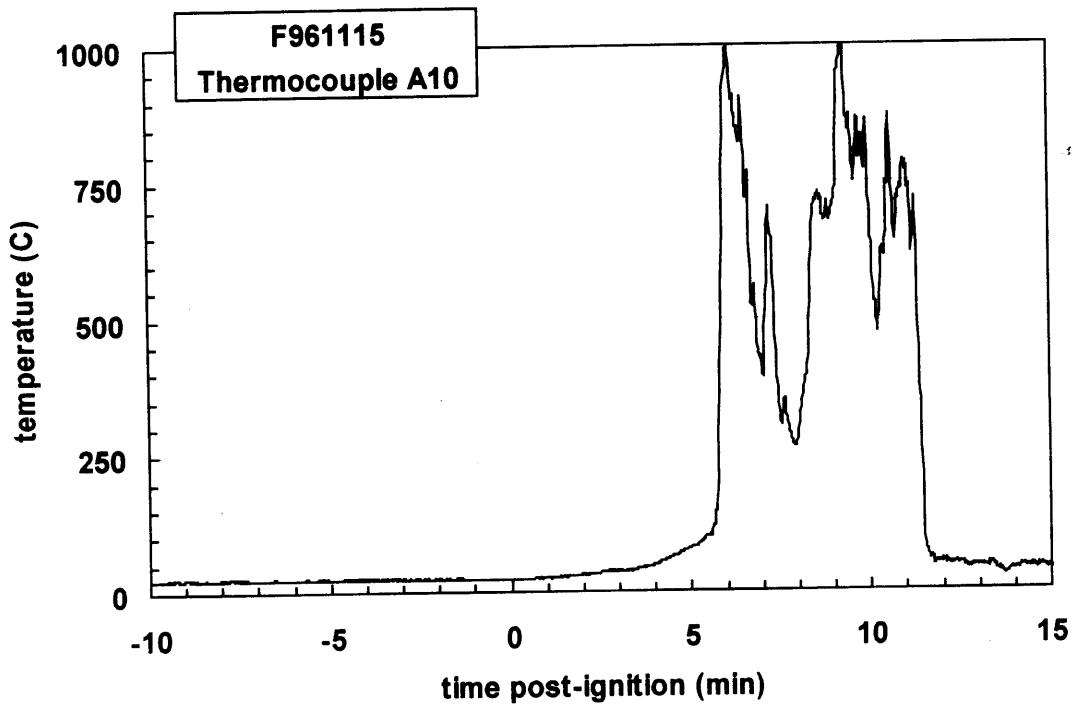
Plot C7. Fire Test F961115. Data plot from thermocouple A7.



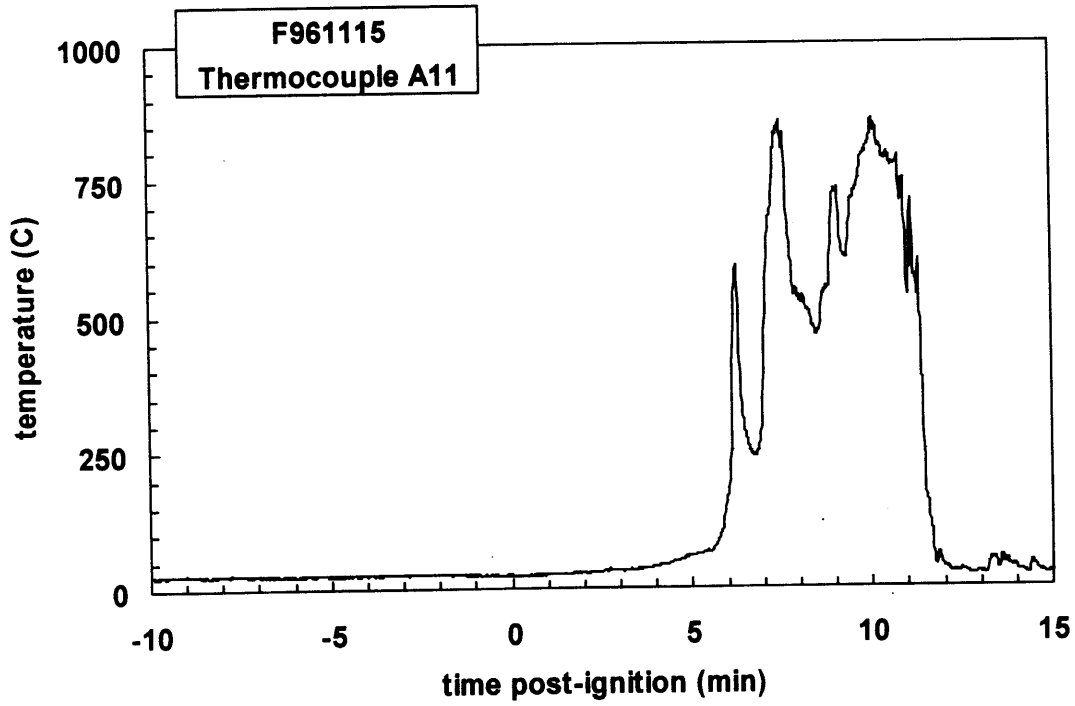
Plot C8. Fire Test F961115. Data plot from thermocouple A8.



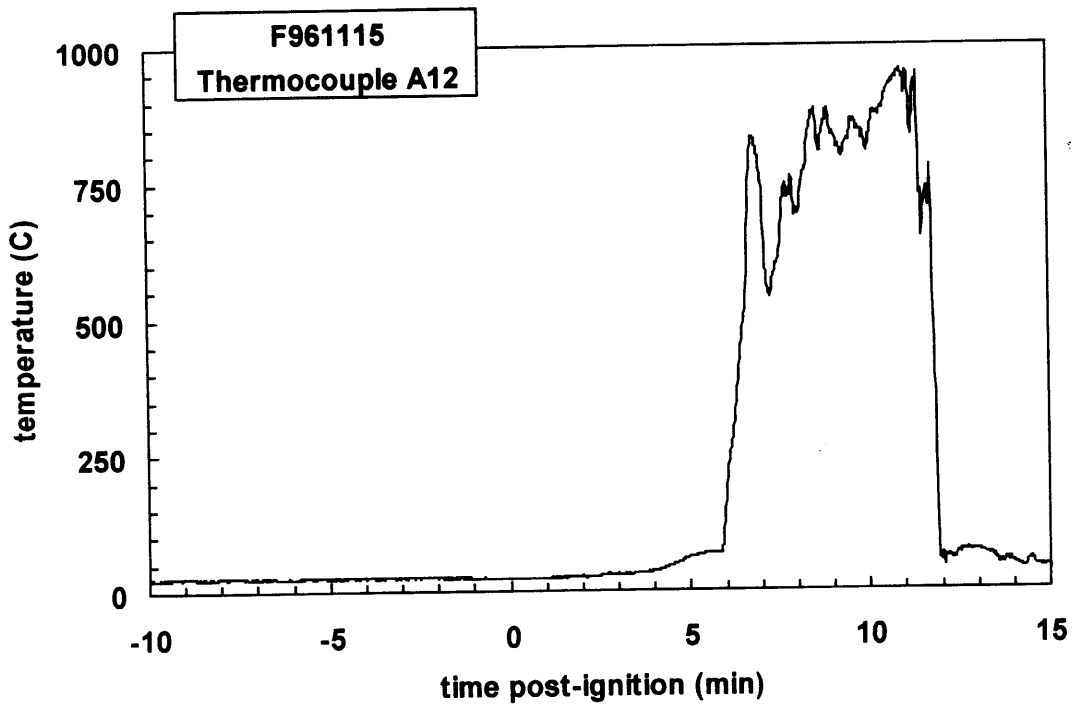
Plot C9. Fire Test F961115. Data plot from thermocouple A9.



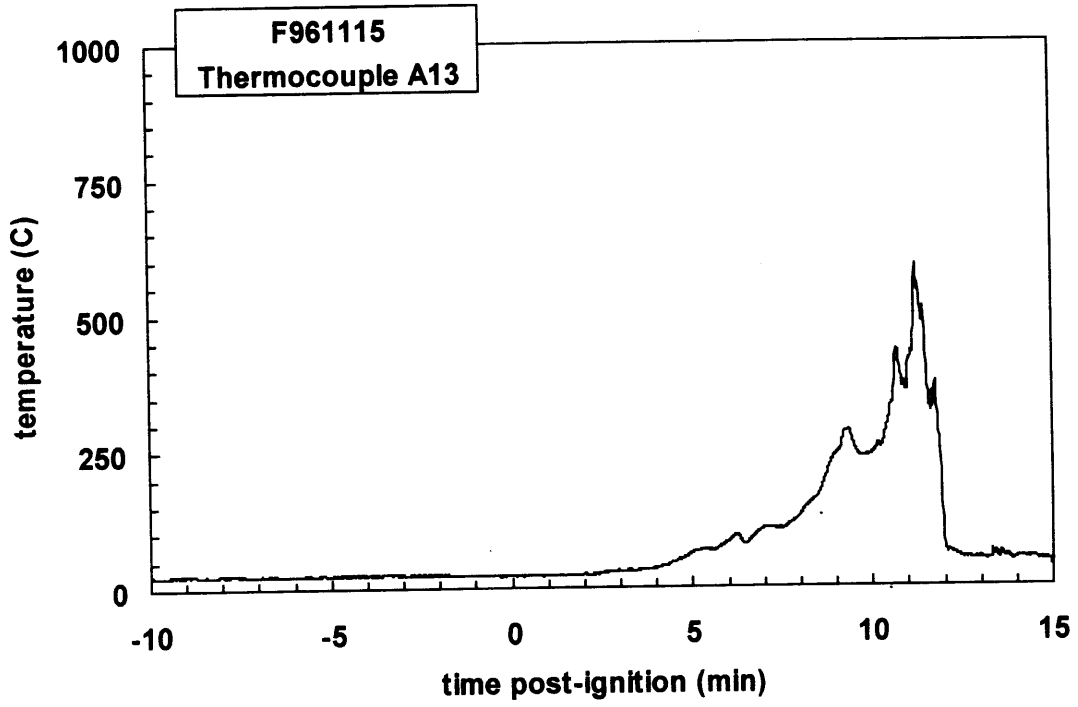
Plot C10. Fire Test F961115. Data plot from thermocouple A10.



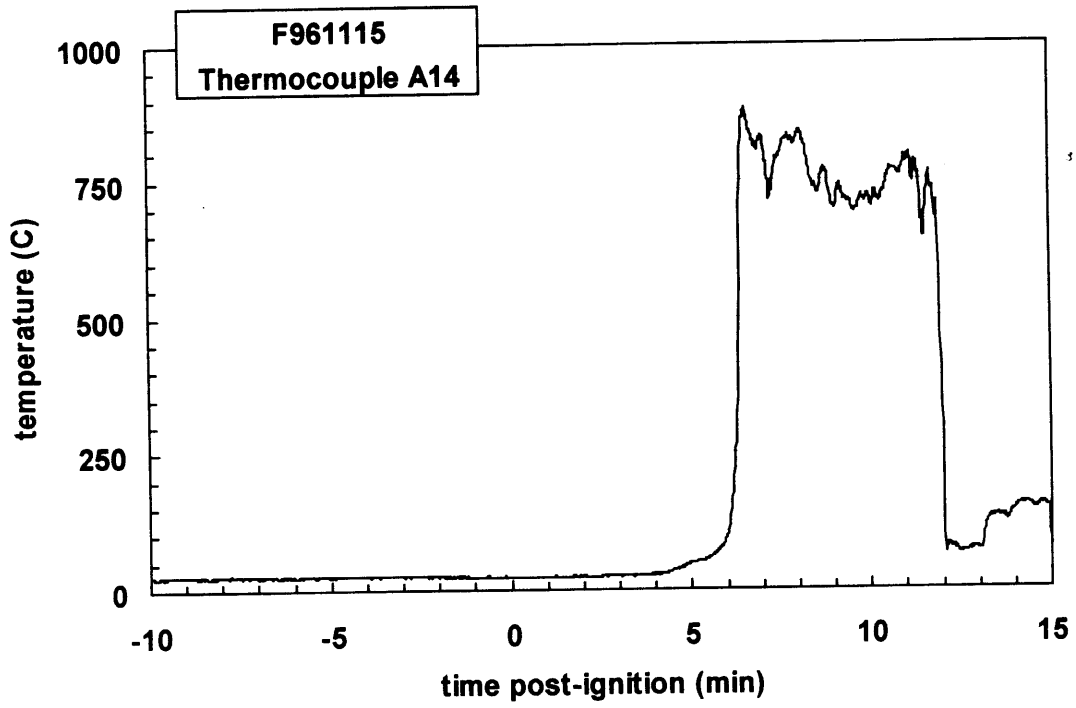
Plot C11. Fire Test F961115. Data plot from thermocouple A11.



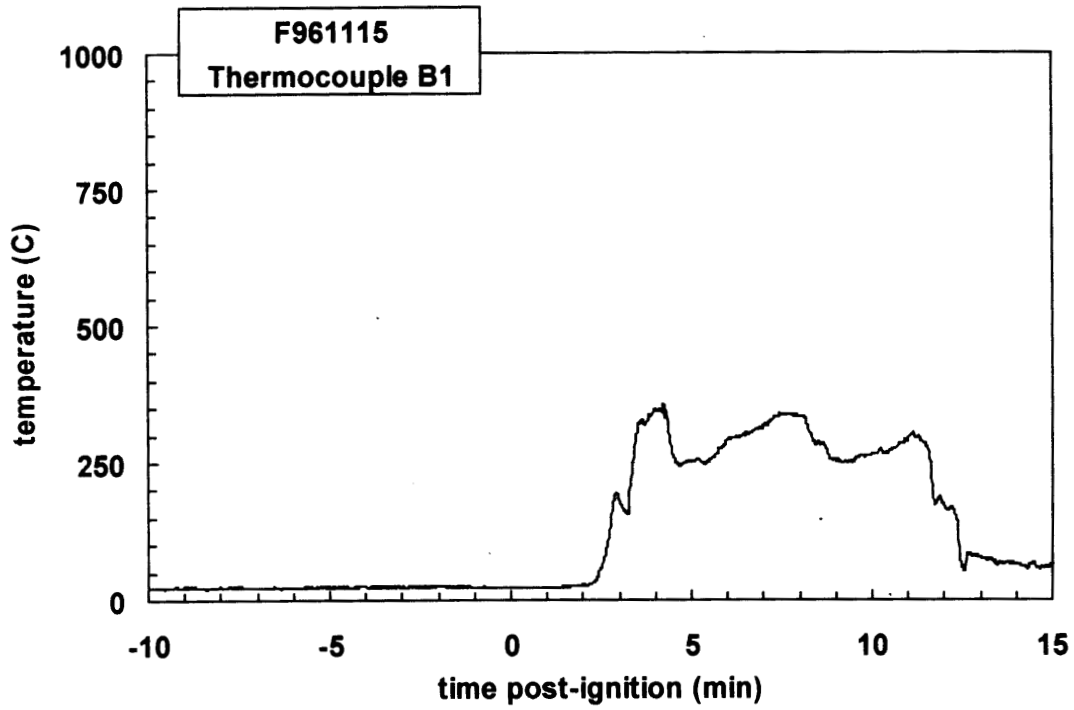
Plot C12. Fire Test F961115. Data plot from thermocouple A12.



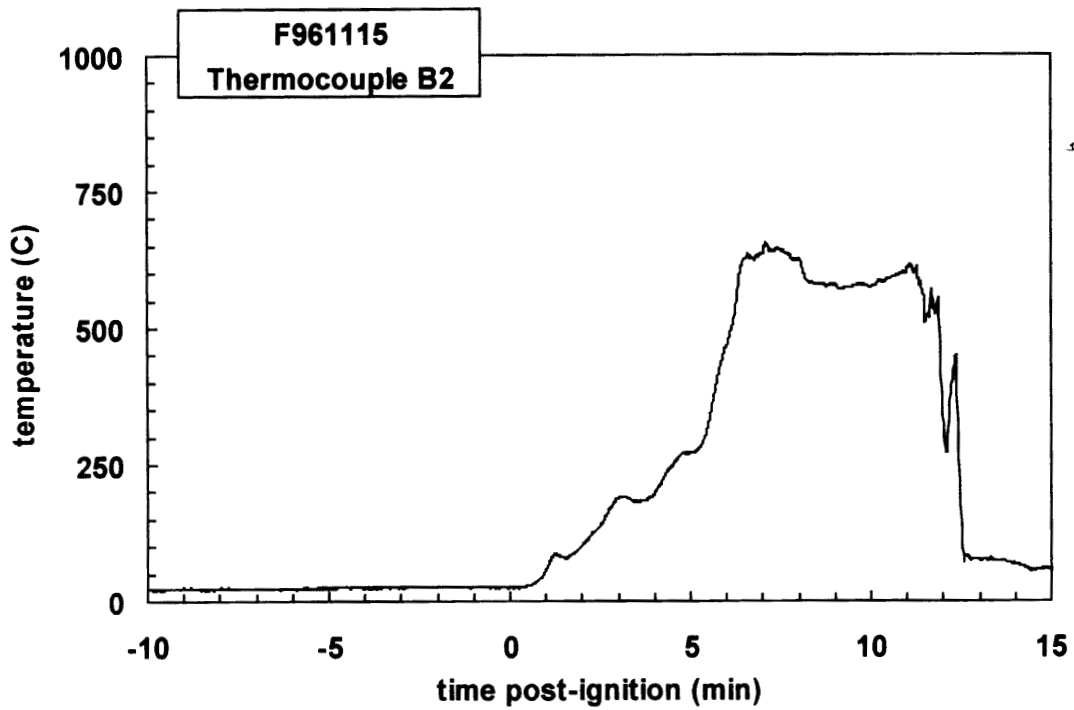
Plot C13. Fire Test F961115. Data plot from thermocouple A13.



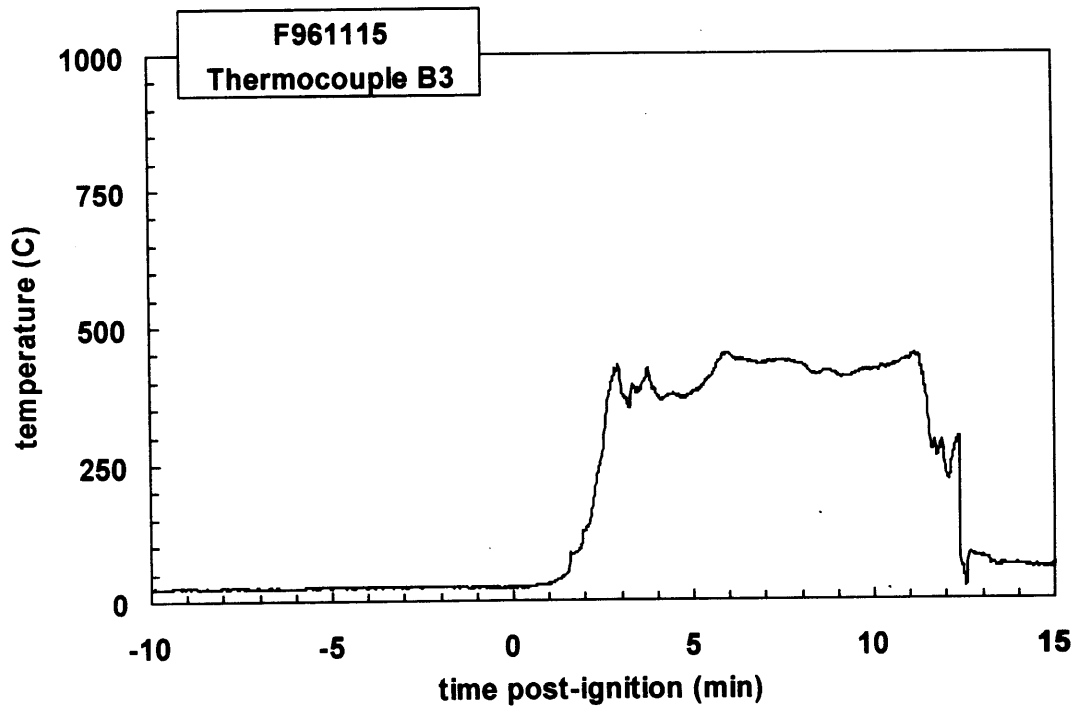
Plot C14. Fire Test F961115. Data plot from thermocouple A14.



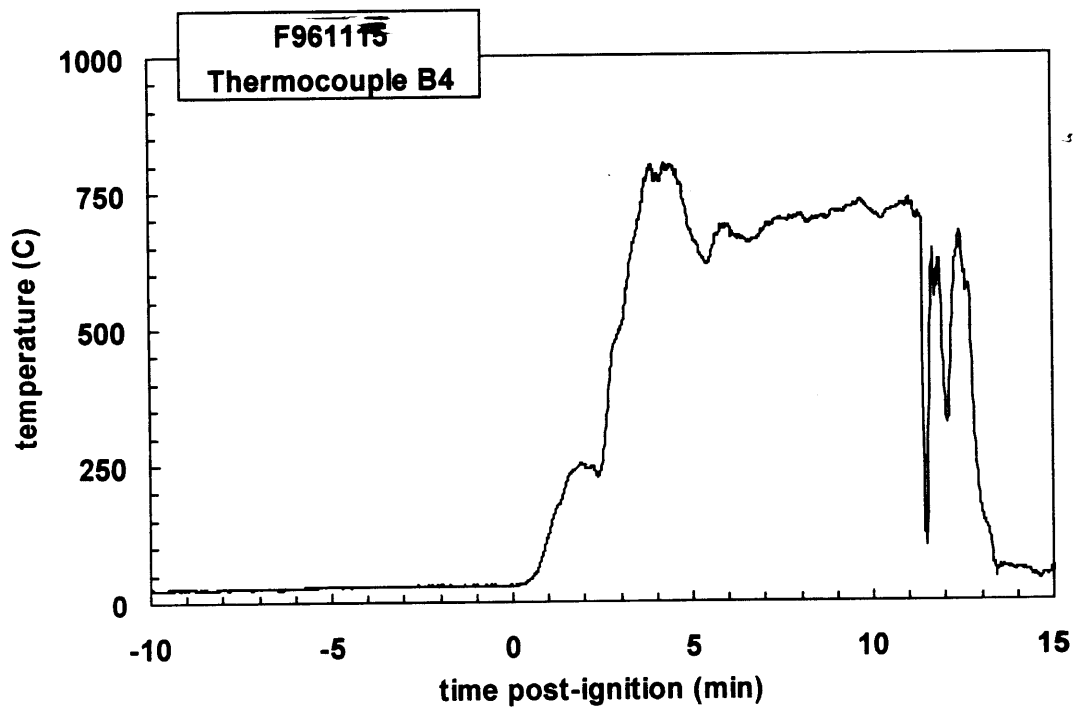
Plot C15. Fire Test F961115. Data plot from thermocouple B1.



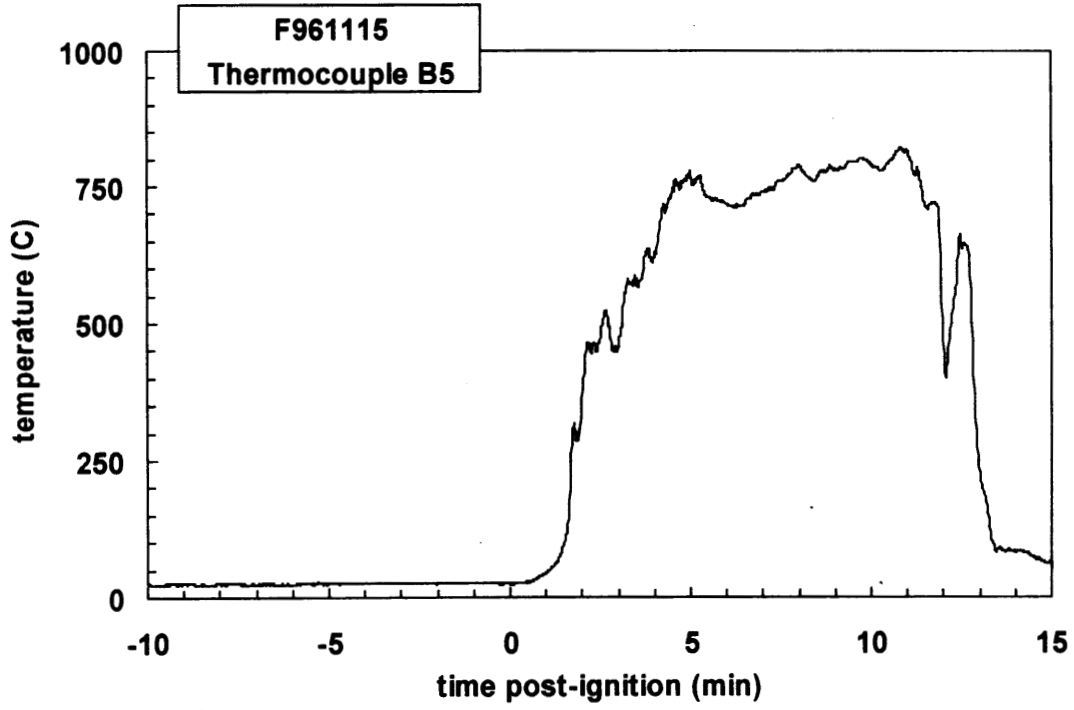
Plot C16. Fire Test F961115. Data plot from thermocouple B2.



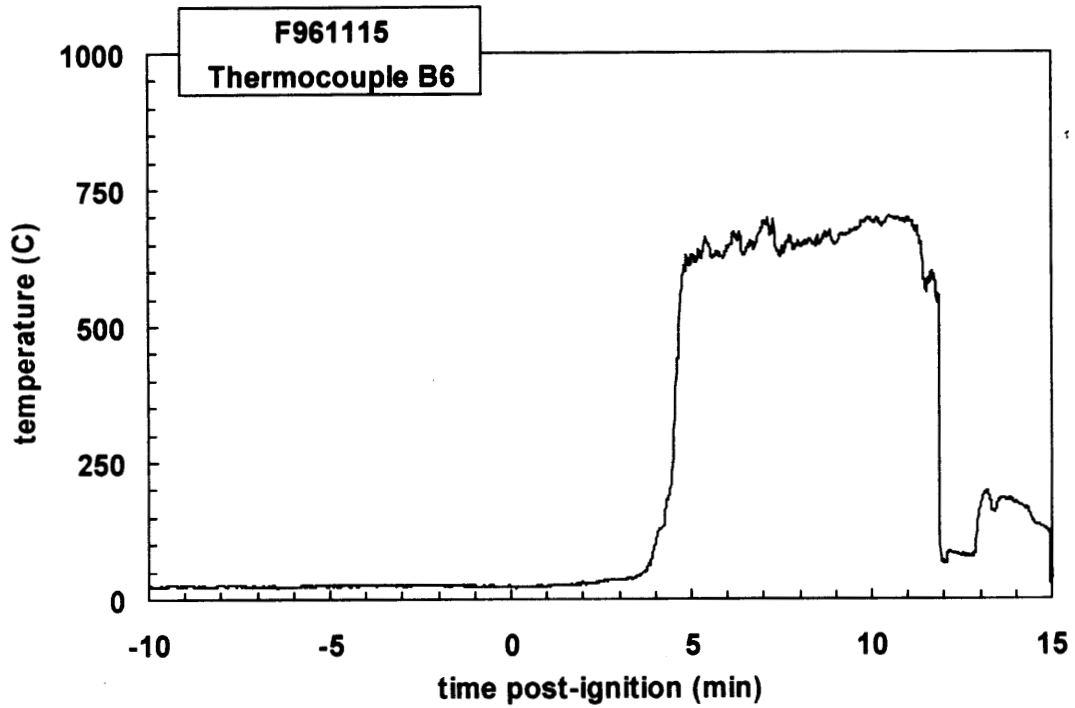
Plot C17. Fire Test F961115. Data plot from thermocouple B3.



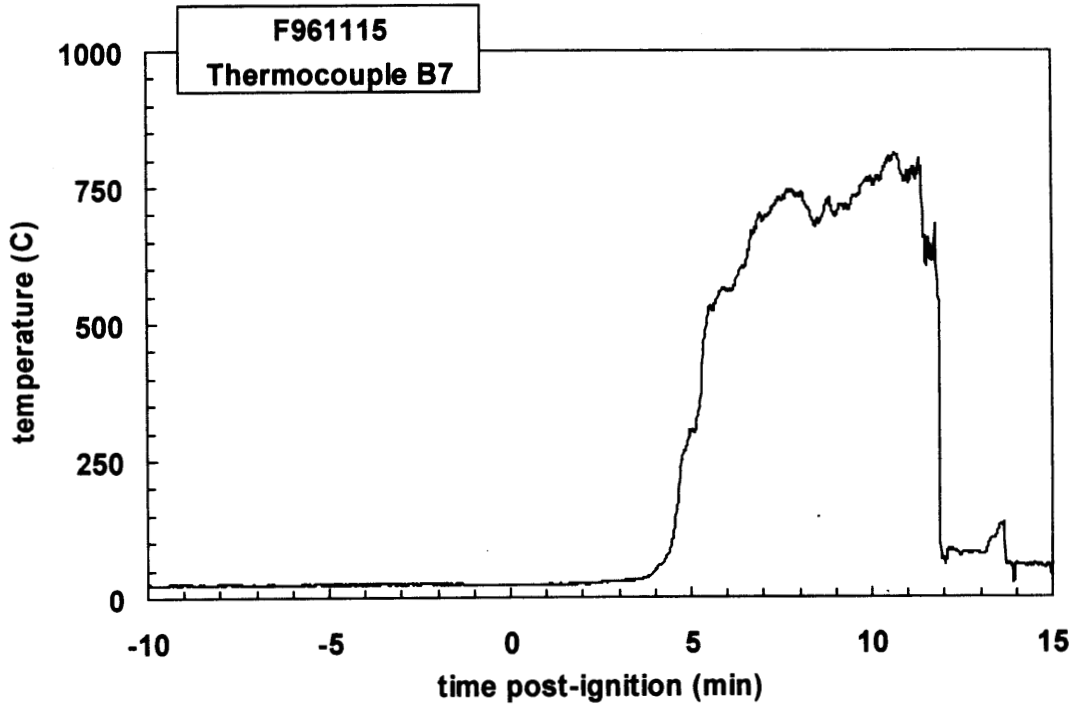
Plot C18. Fire Test F961115. Data plot from thermocouple B4.



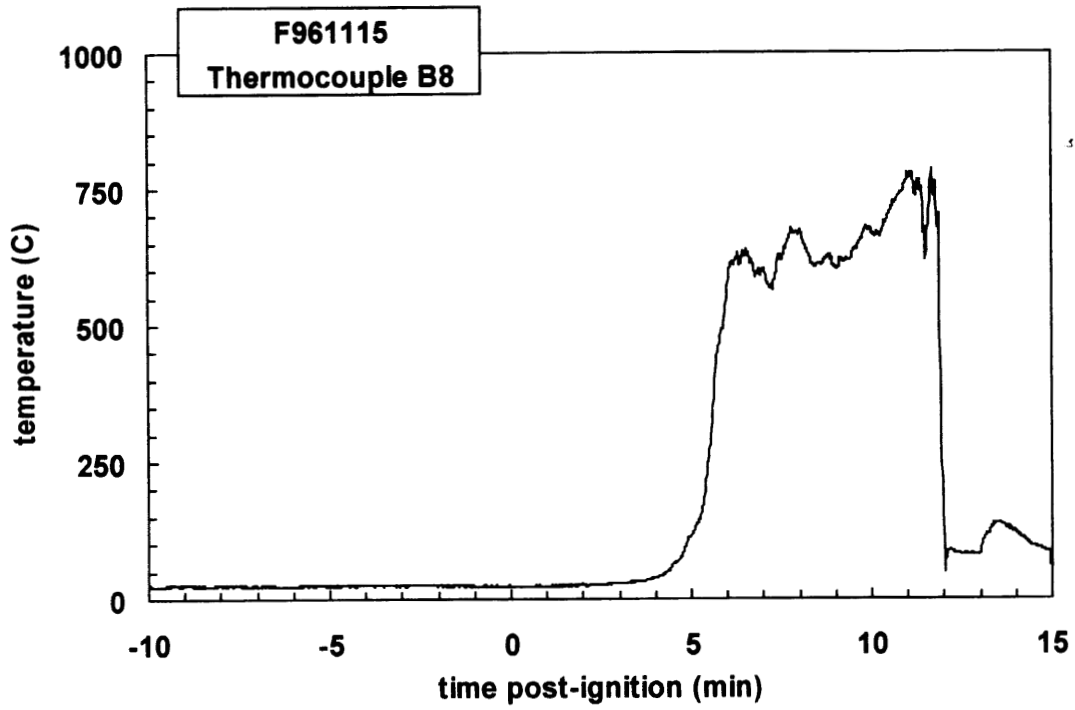
Plot C19. Fire Test F961115. Data plot from thermocouple B5.



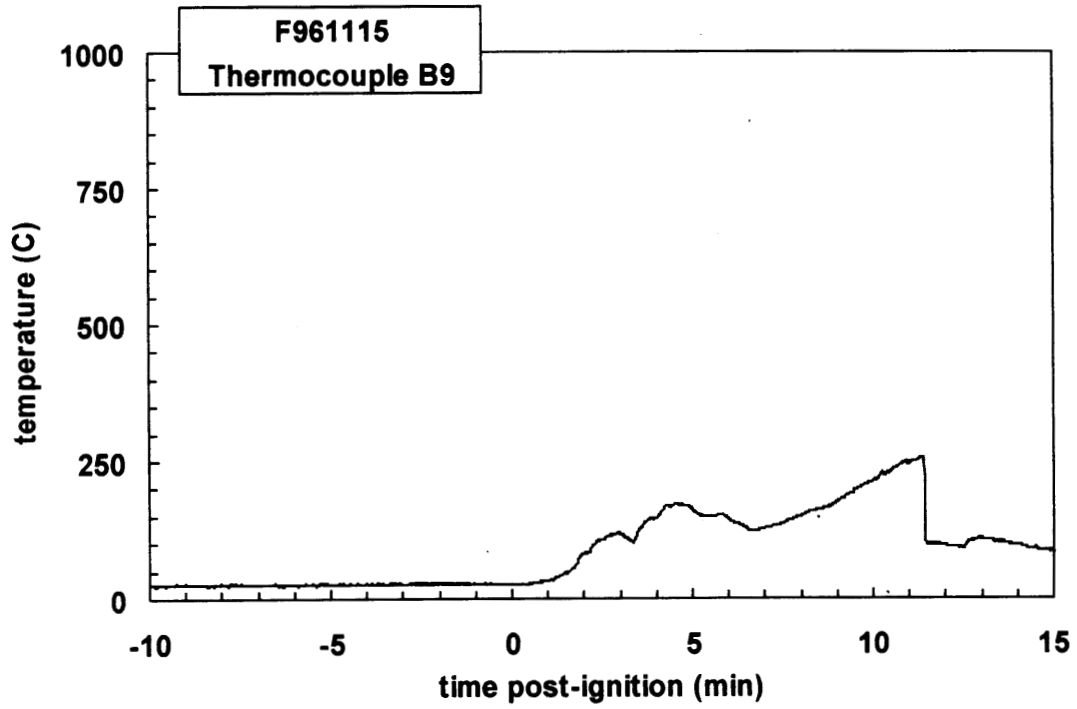
Plot C20. Fire Test F961115. Data plot from thermocouple B6.



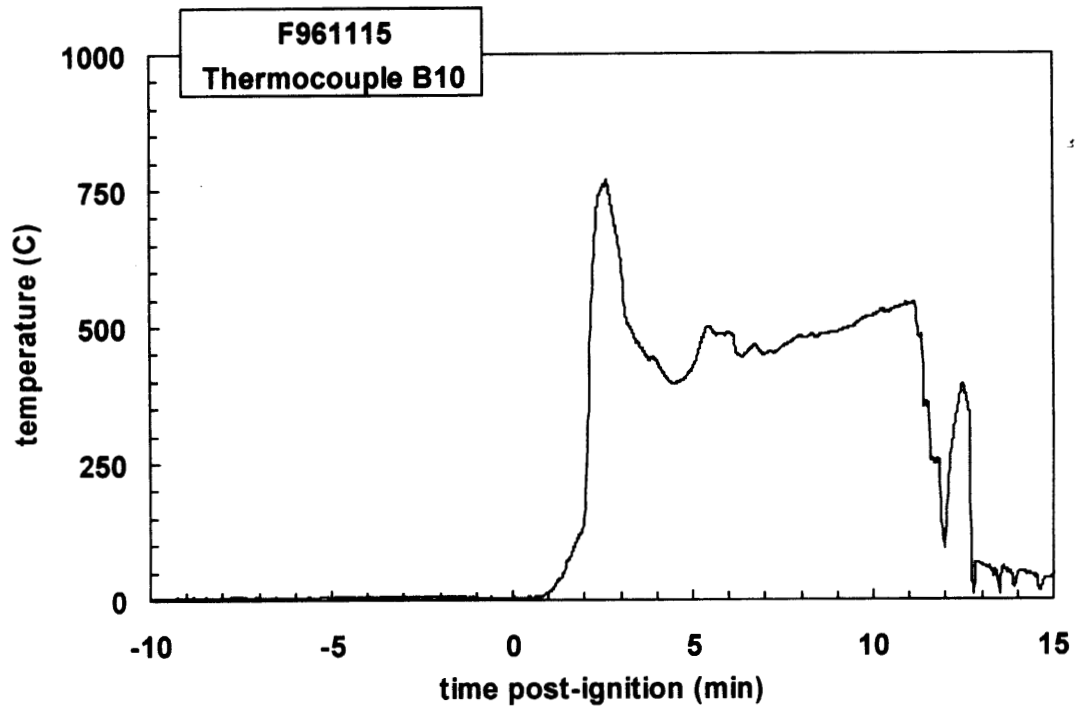
Plot C21. Fire Test F961115. Data plot from thermocouple B7.



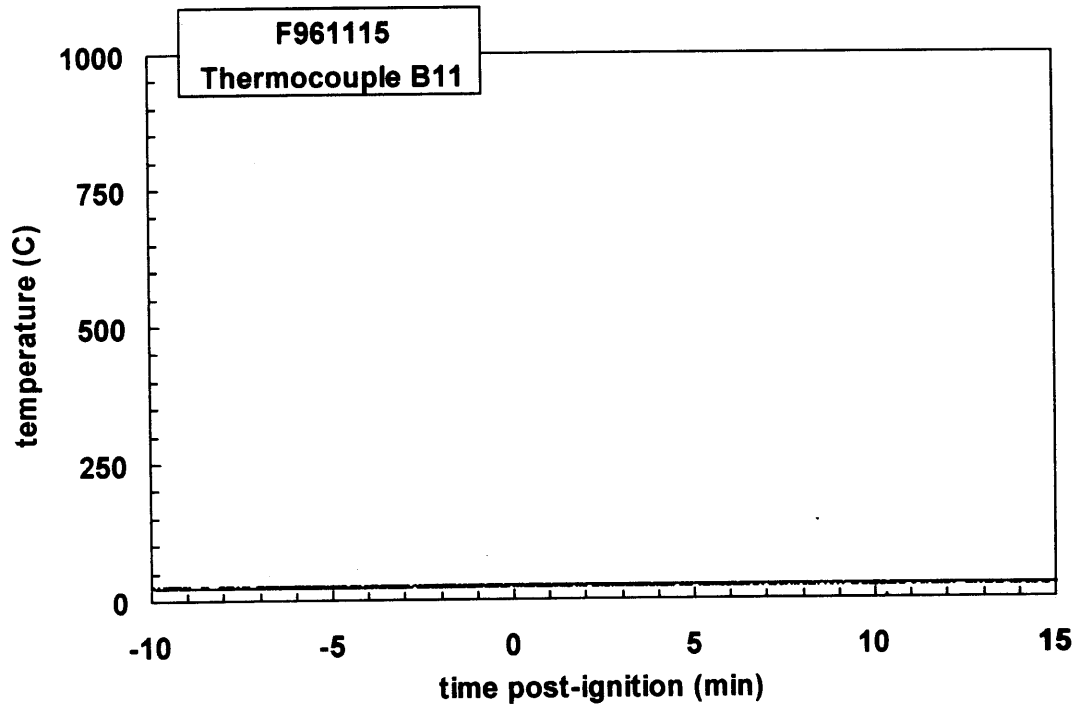
Plot C22. Fire Test F961115. Data plot from thermocouple B8.



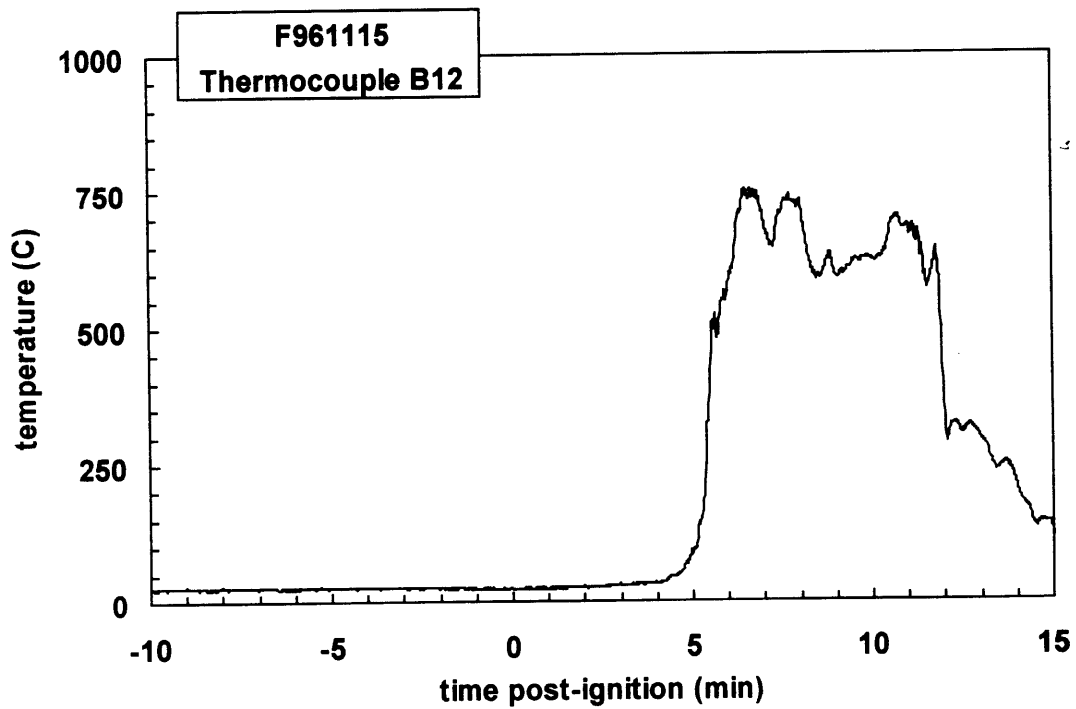
Plot C23. Fire Test F961115. Data plot from thermocouple B9.



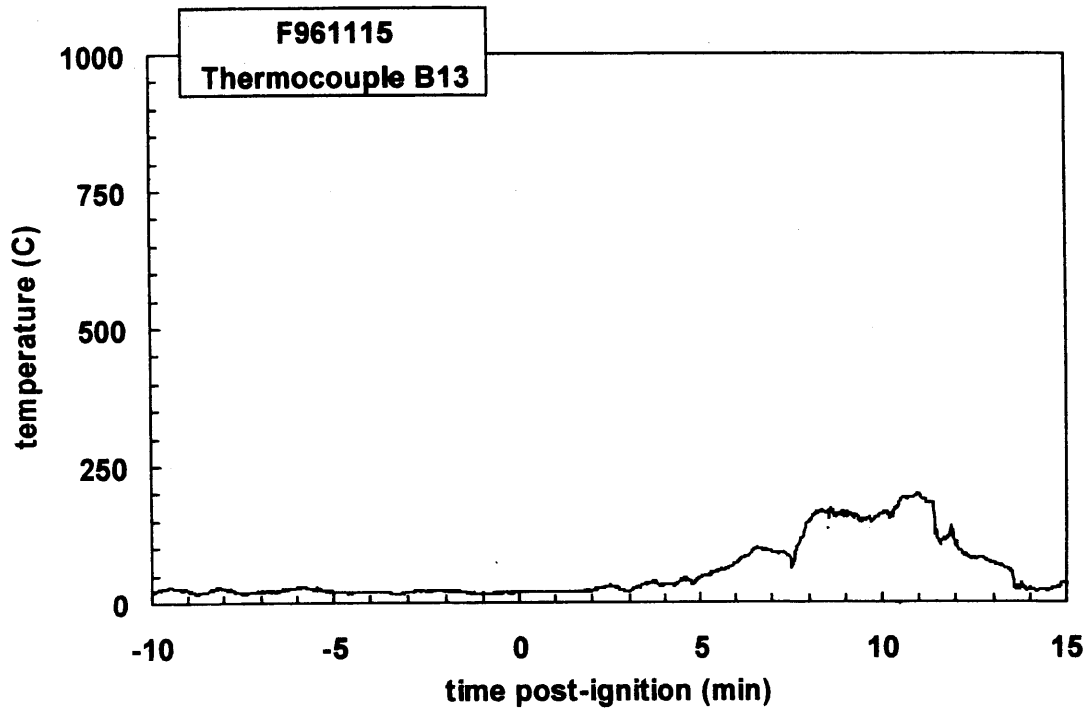
Plot C24. Fire Test F961115. Data plot from thermocouple B10.



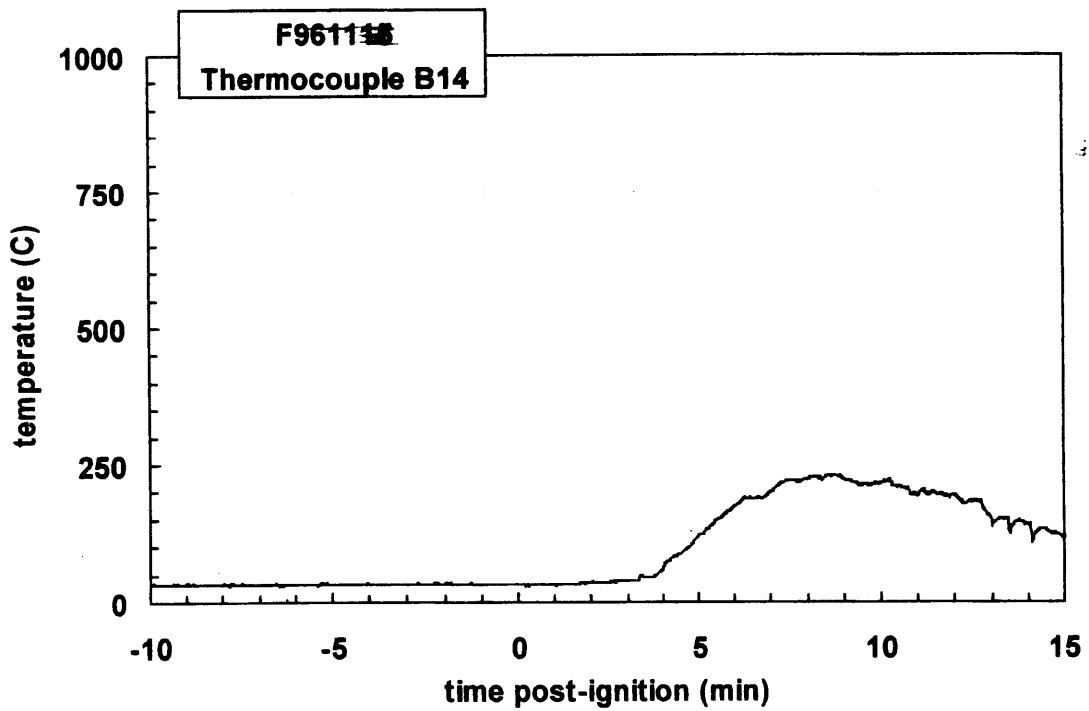
Plot C25. Fire Test F961115. Data plot from thermocouple B11.



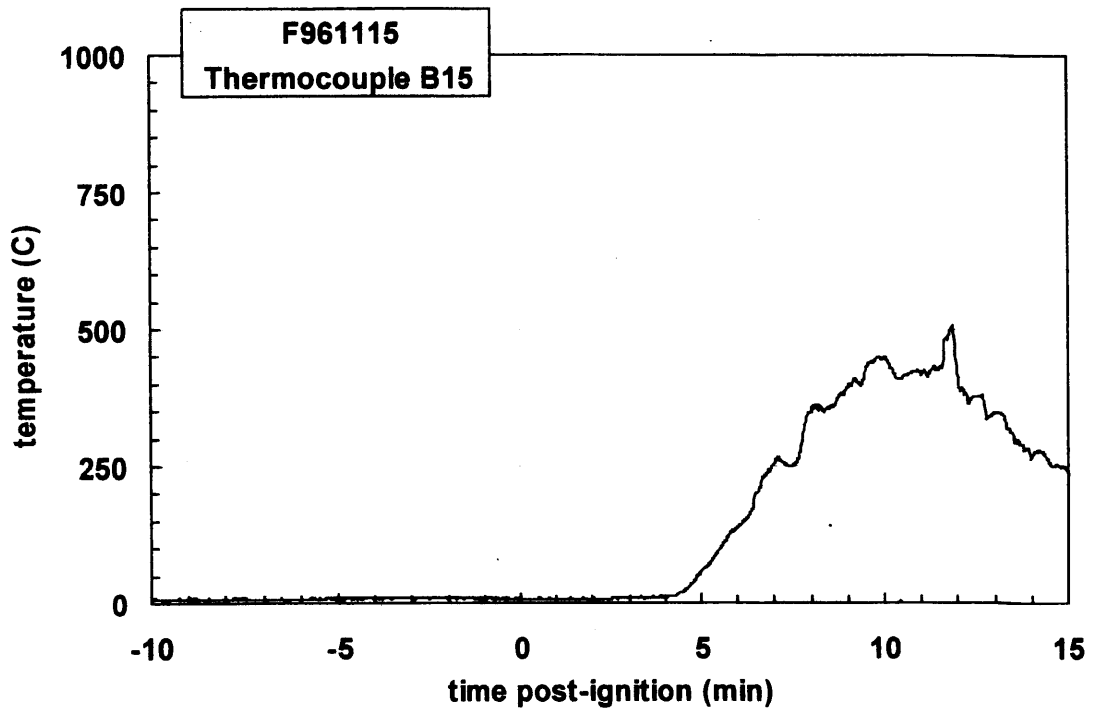
Plot C26. Fire Test F961115. Data plot from thermocouple B12.



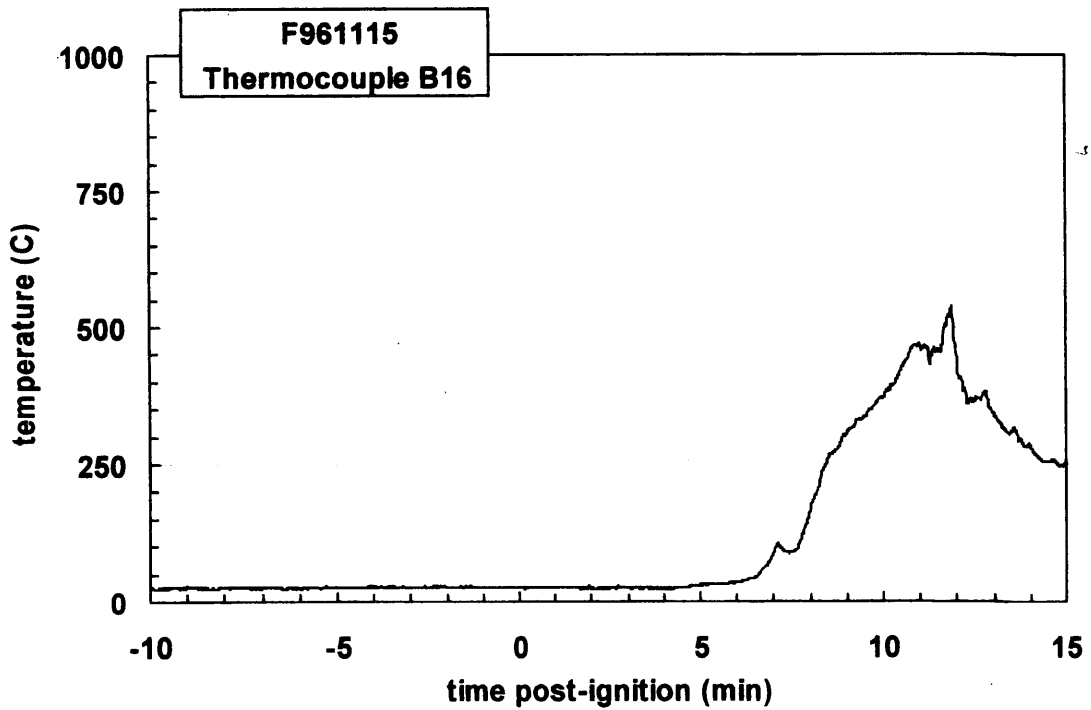
Plot C27. Fire Test F961115. Data plot from thermocouple B13.



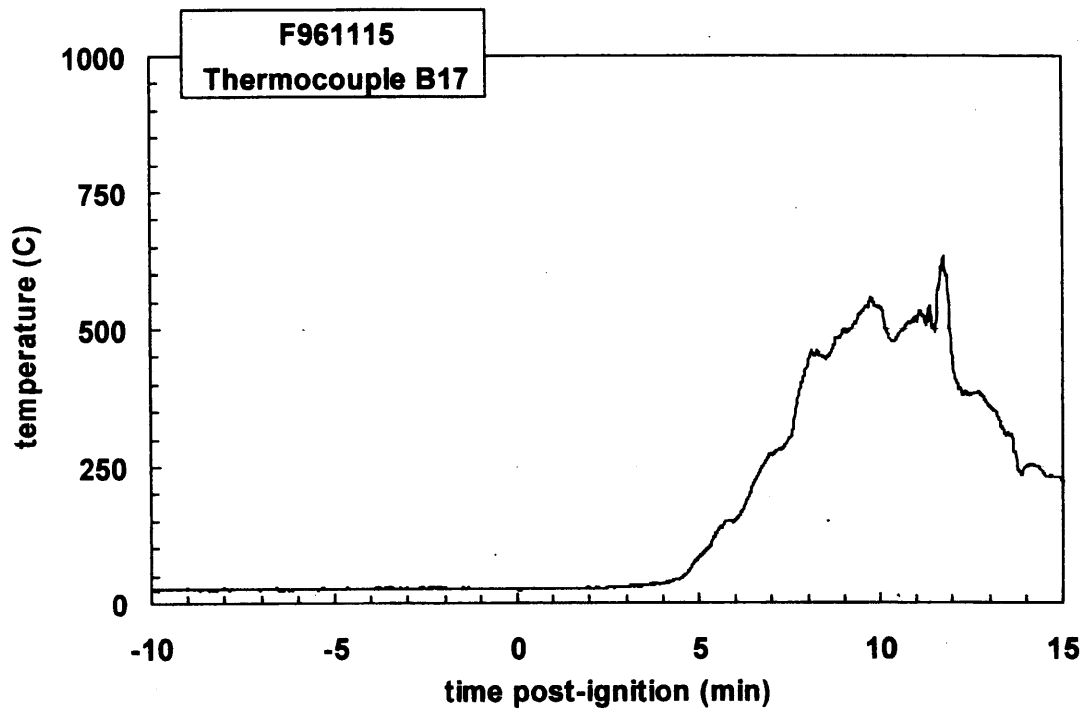
Plot C28. Fire Test F961115. Data plot from thermocouple B14.



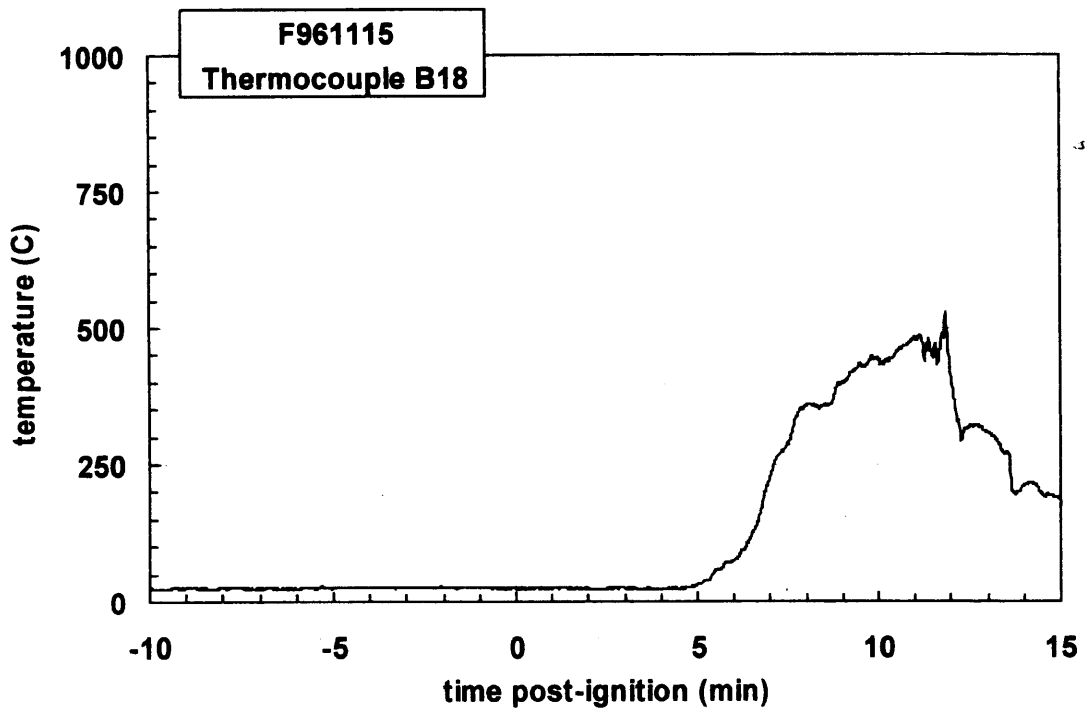
Plot C29. Fire Test F961115. Data plot from thermocouple B15.



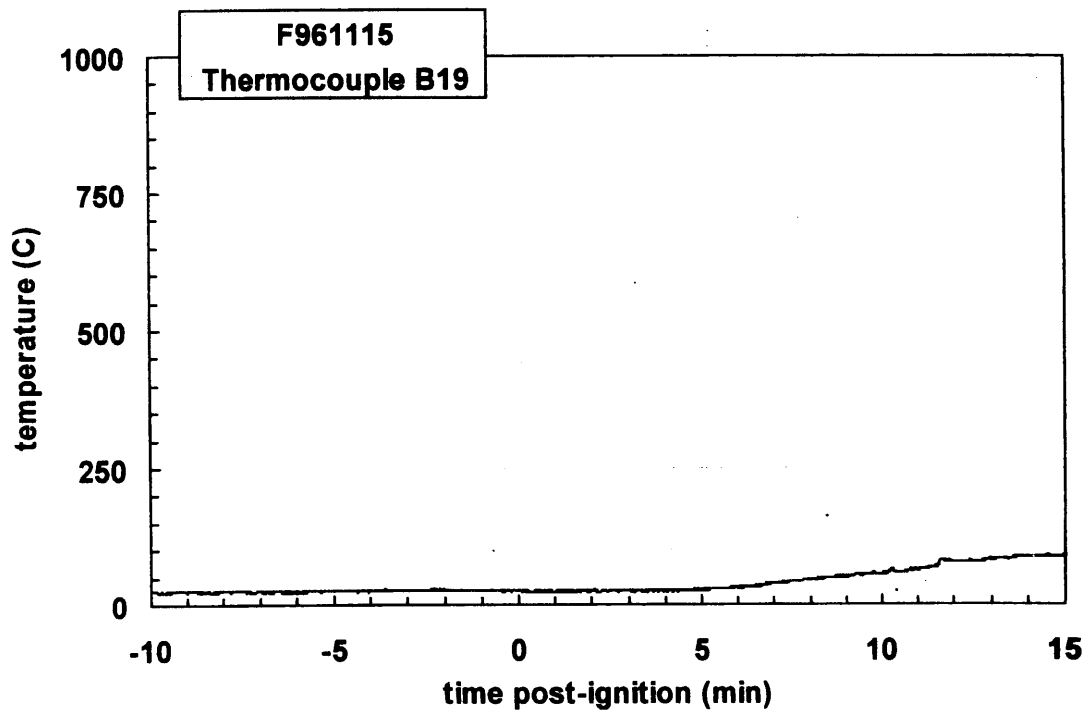
Plot C30. Fire Test F961115. Data plot from thermocouple B16.



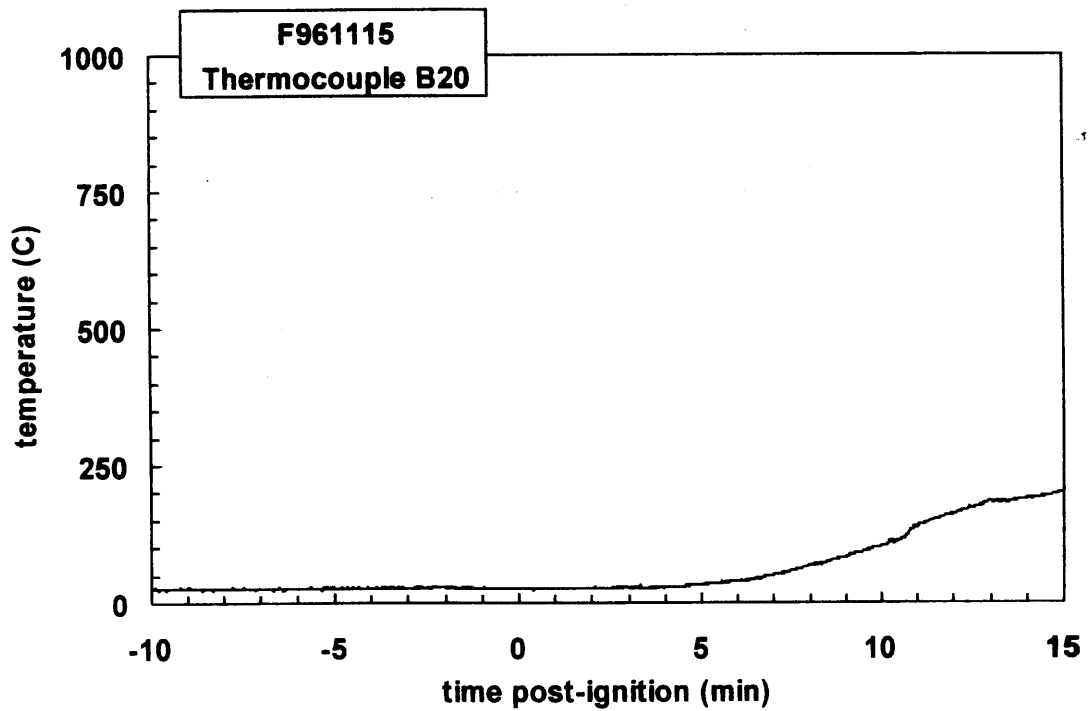
Plot C31. Fire Test F961115. Data plot from thermocouple B17.



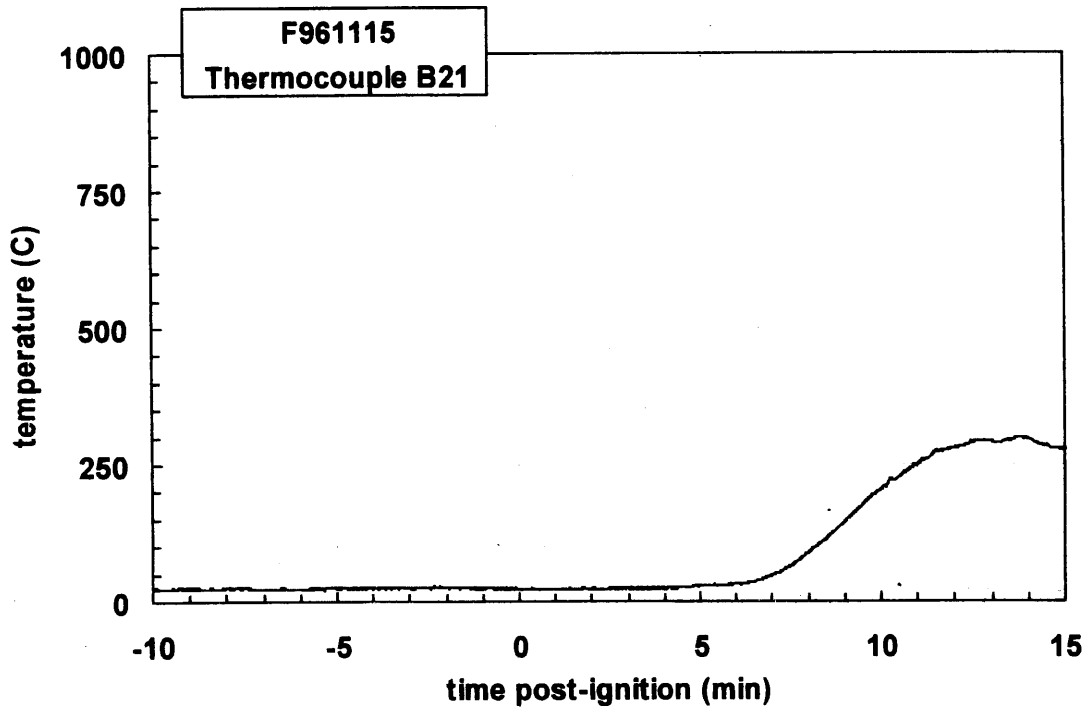
Plot C32. Fire Test F961115. Data plot from thermocouple B18.



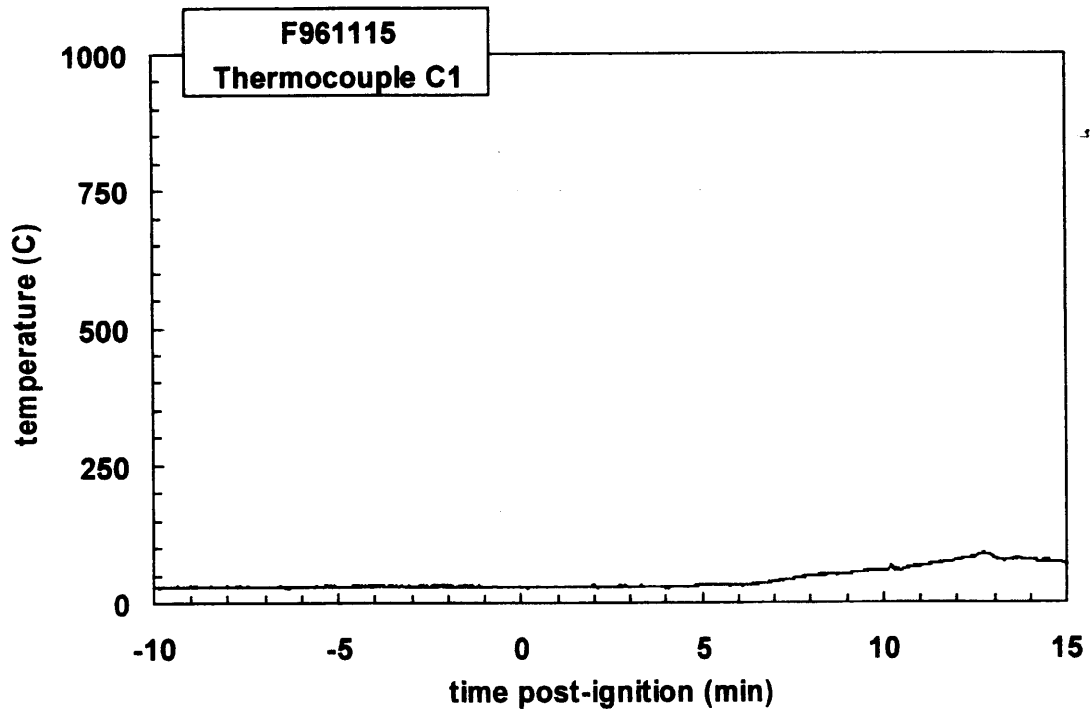
Plot C33. Fire Test F961115. Data plot from thermocouple B19.



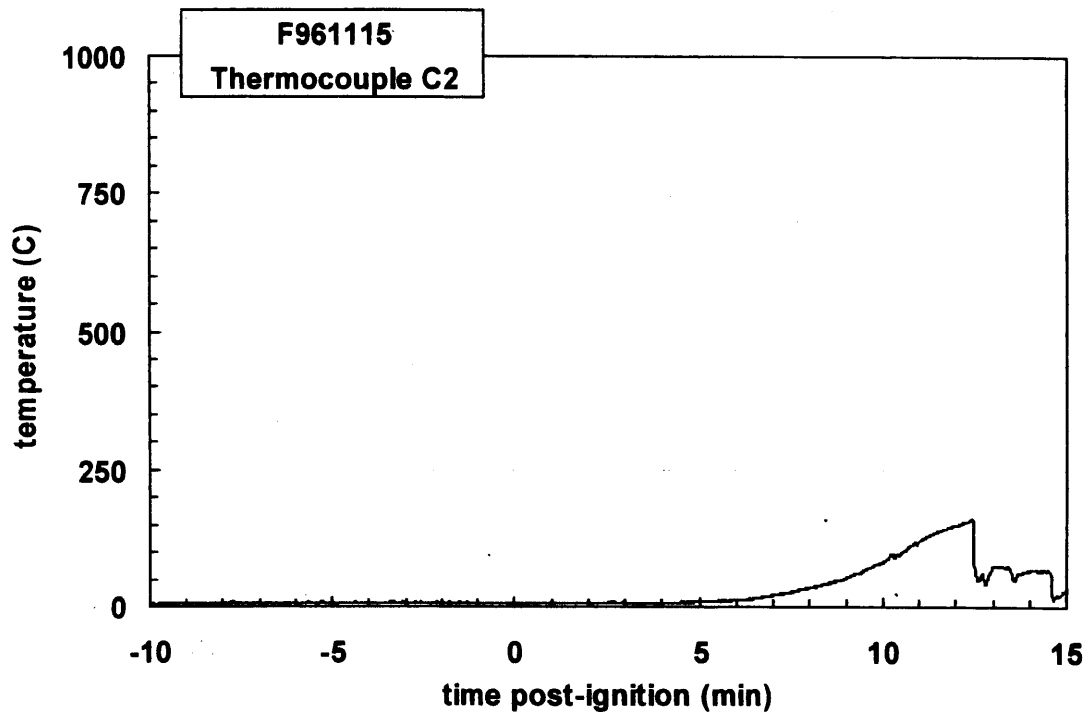
Plot C34. Fire Test F961115. Data plot from thermocouple B20.



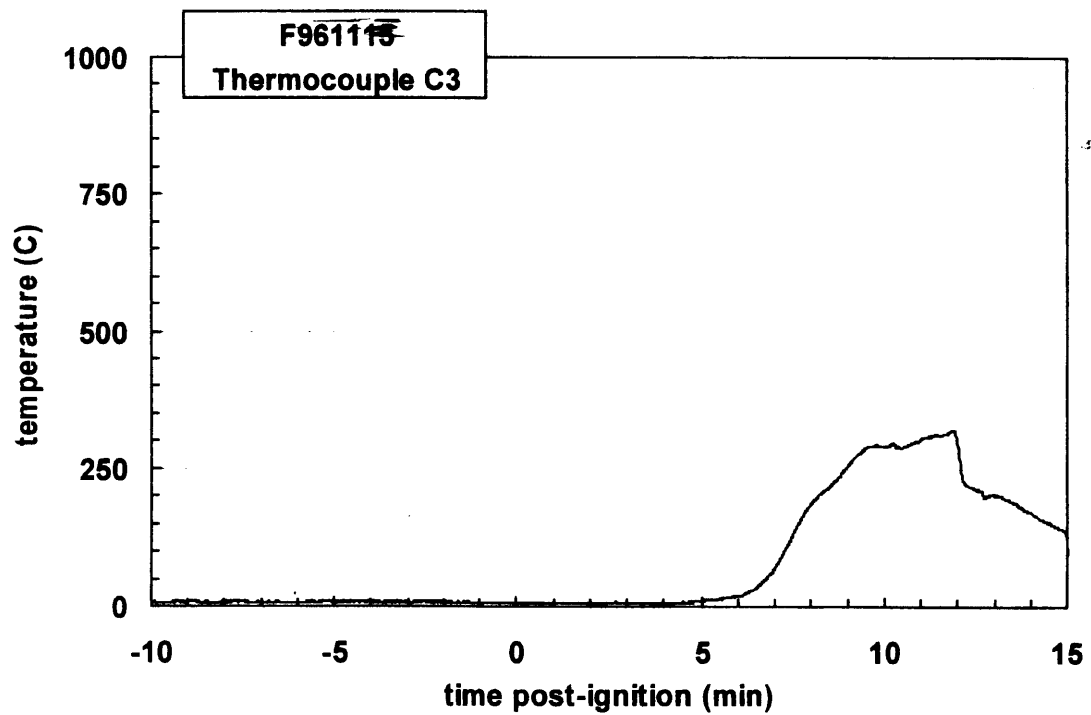
Plot C35. Fire Test F961115. Data plot from thermocouple B21.



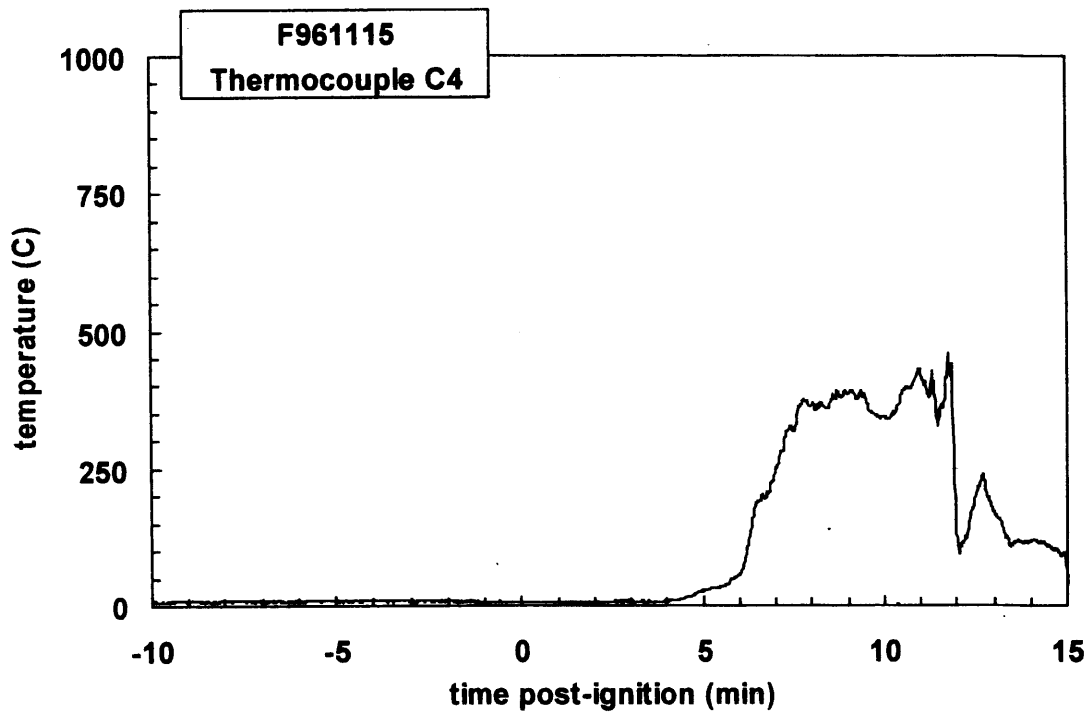
Plot C36. Fire Test F961115. Data plot from thermocouple C1.



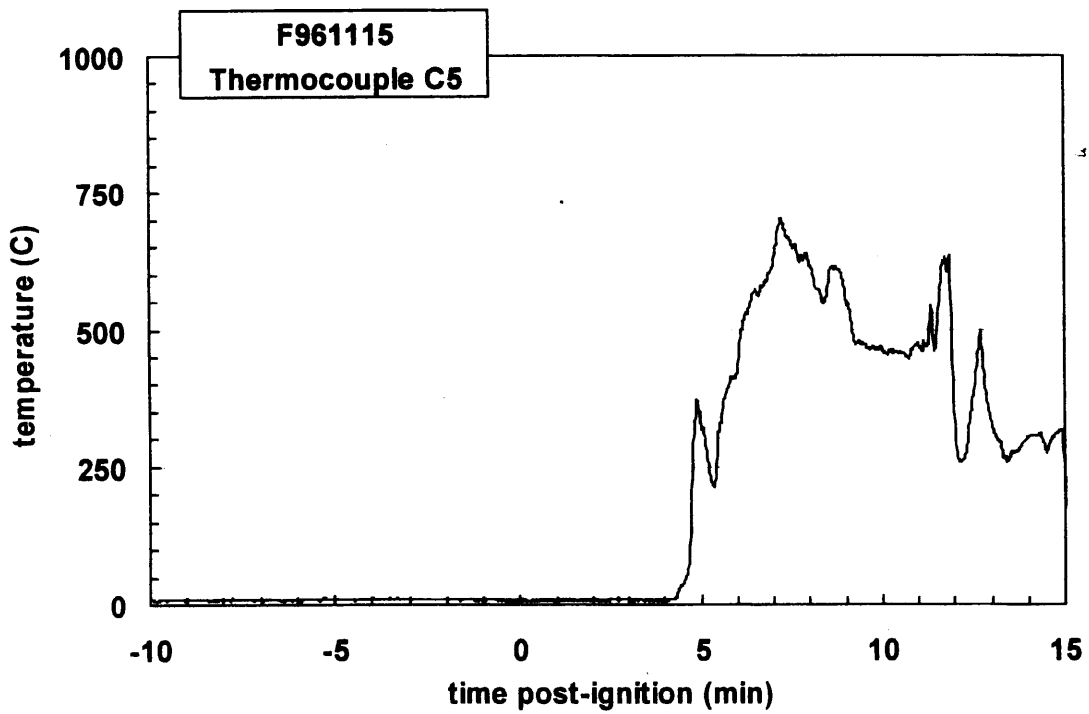
Plot C37. Fire Test F961115. Data plot from thermocouple C2.



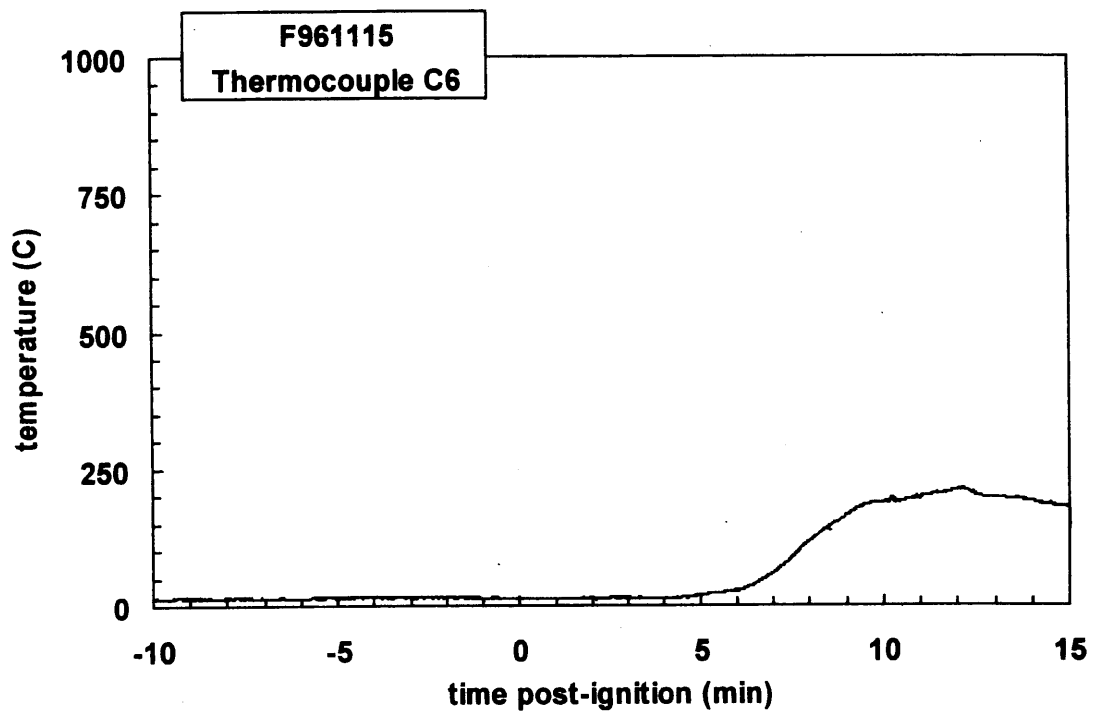
Plot C38. Fire Test F961115. Data plot from thermocouple C3.



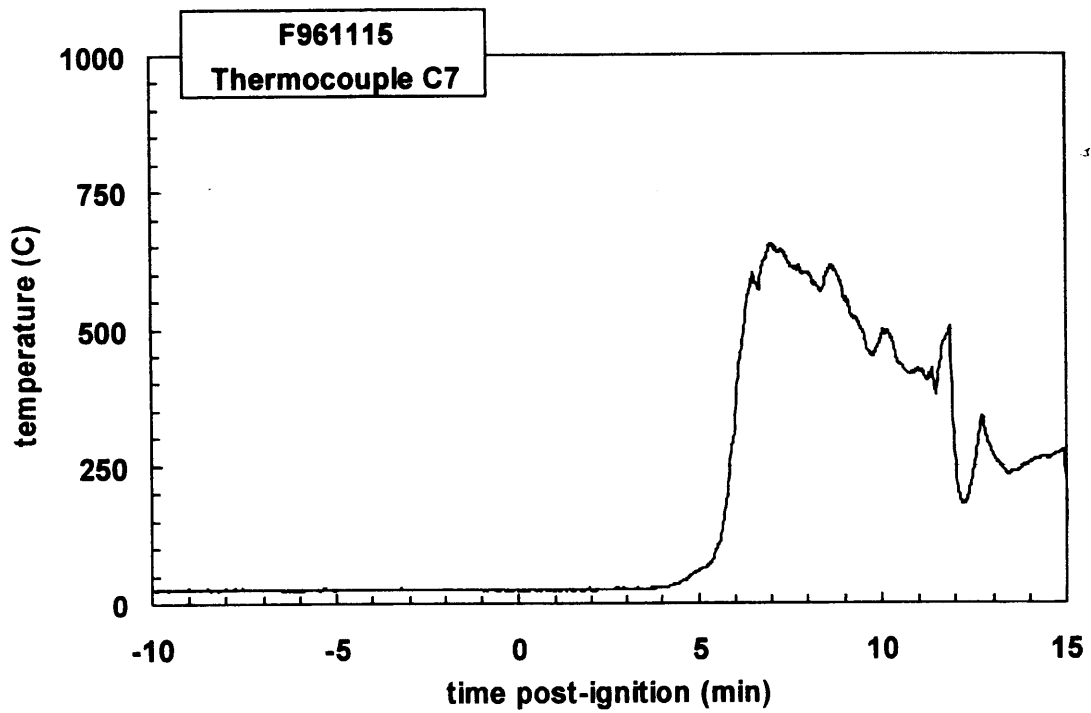
Plot C39. Fire Test F961115. Data plot from thermocouple C4.



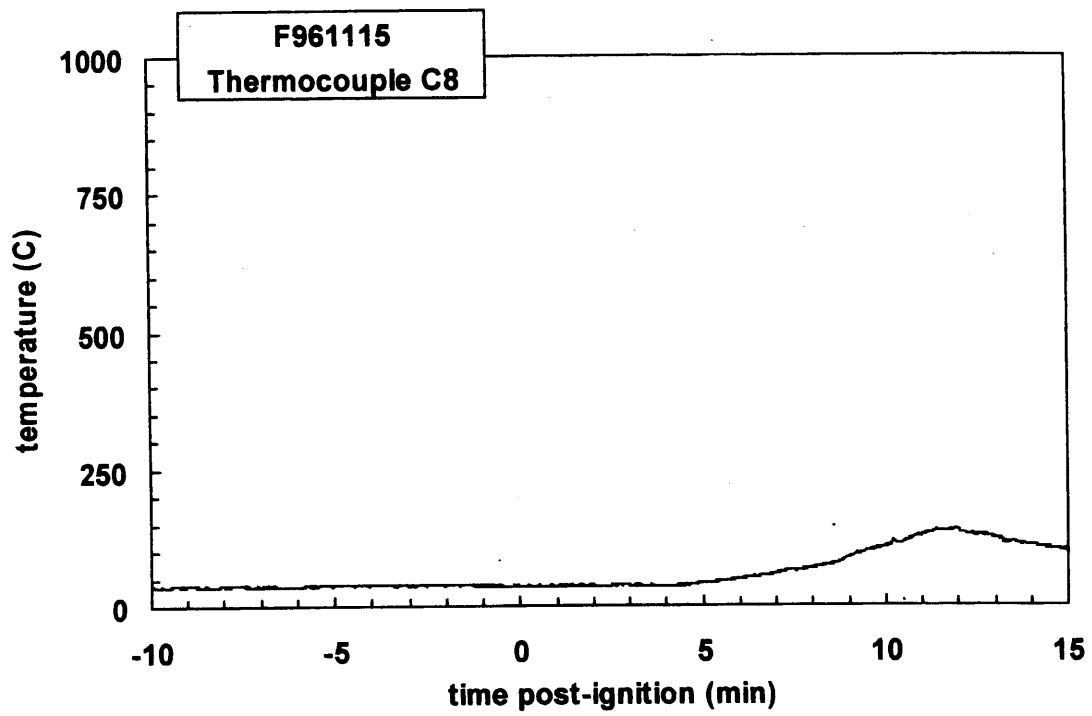
Plot C40. Fire Test F961115. Data plot from thermocouple C5.



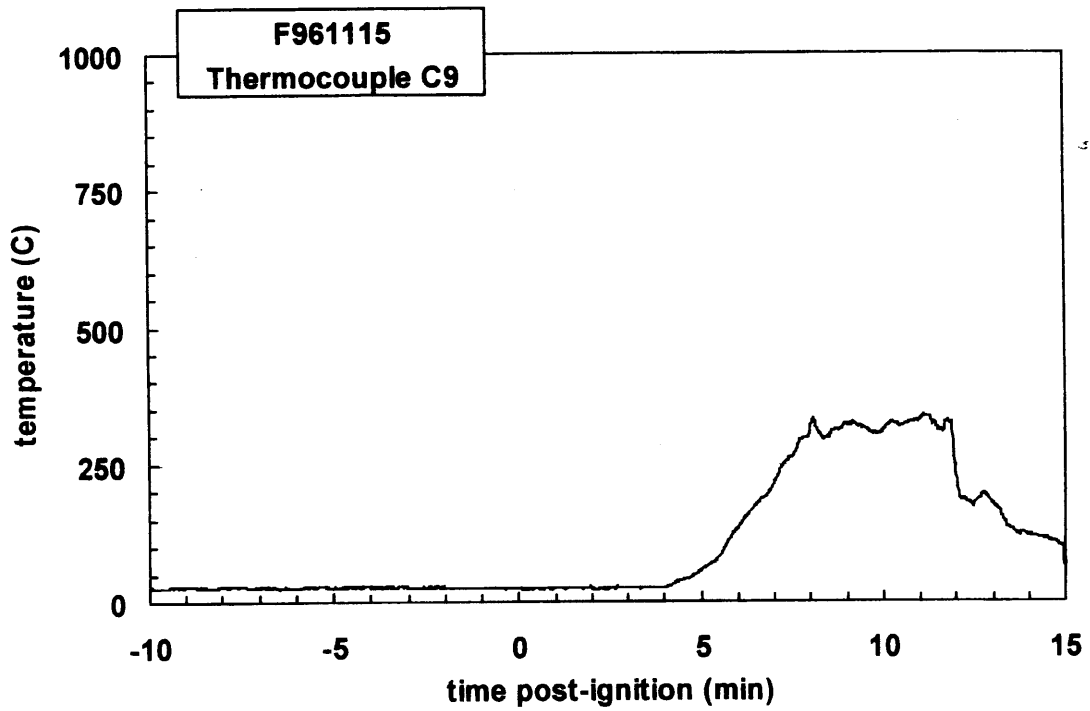
Plot C41. Fire Test F961115. Data plot from thermocouple C6.



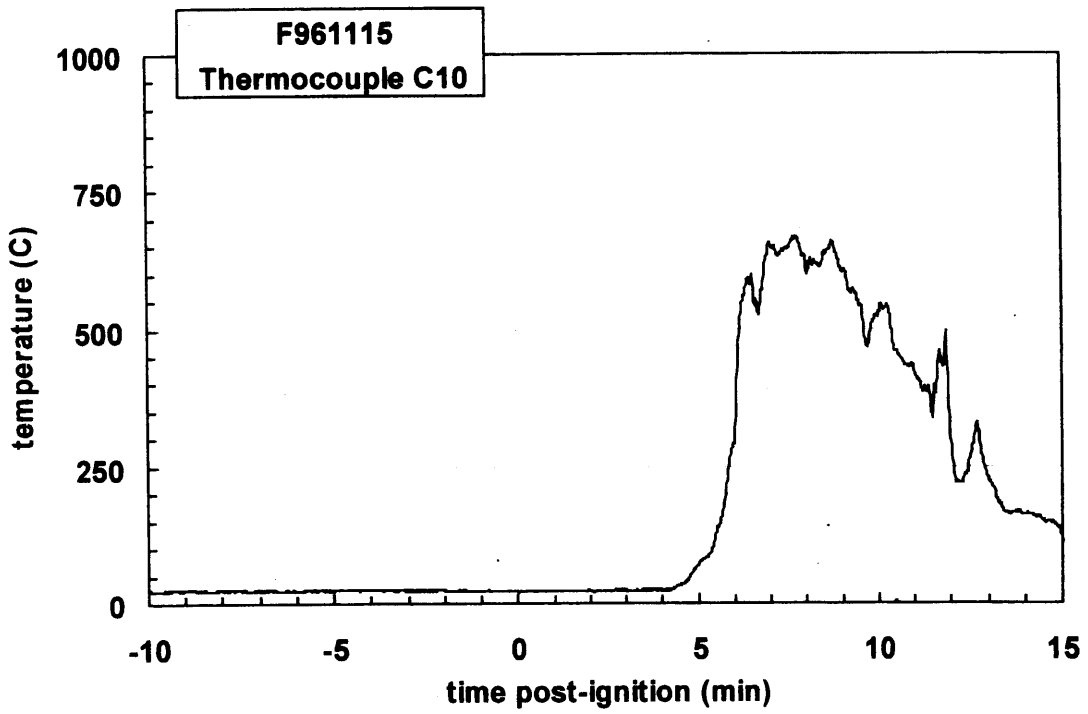
Plot C42. Fire Test F961115. Data plot from thermocouple C7.



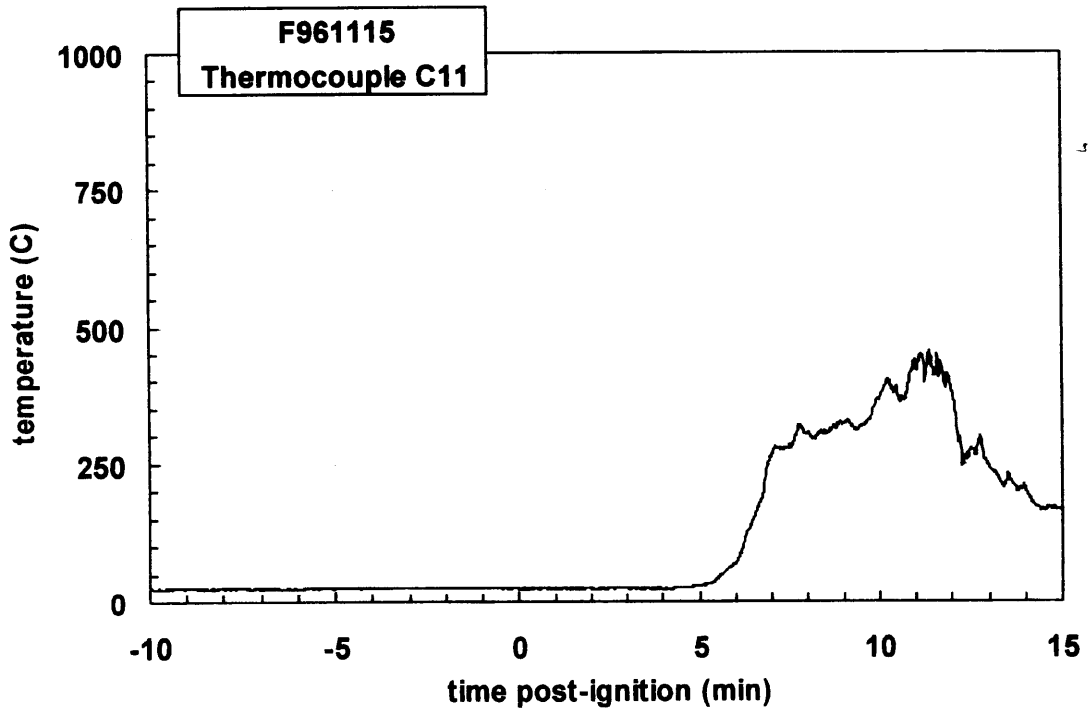
Plot C43. Fire Test F961115. Data plot from thermocouple C8.



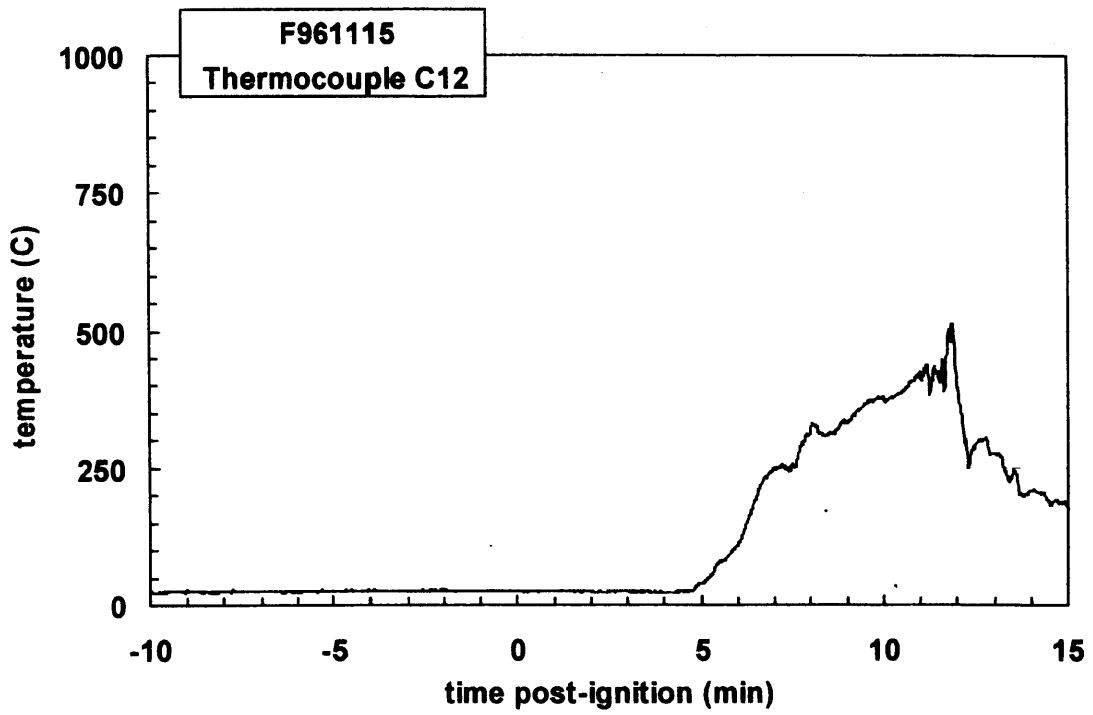
Plot C44. Fire Test F961115. Data plot from thermocouple C9.



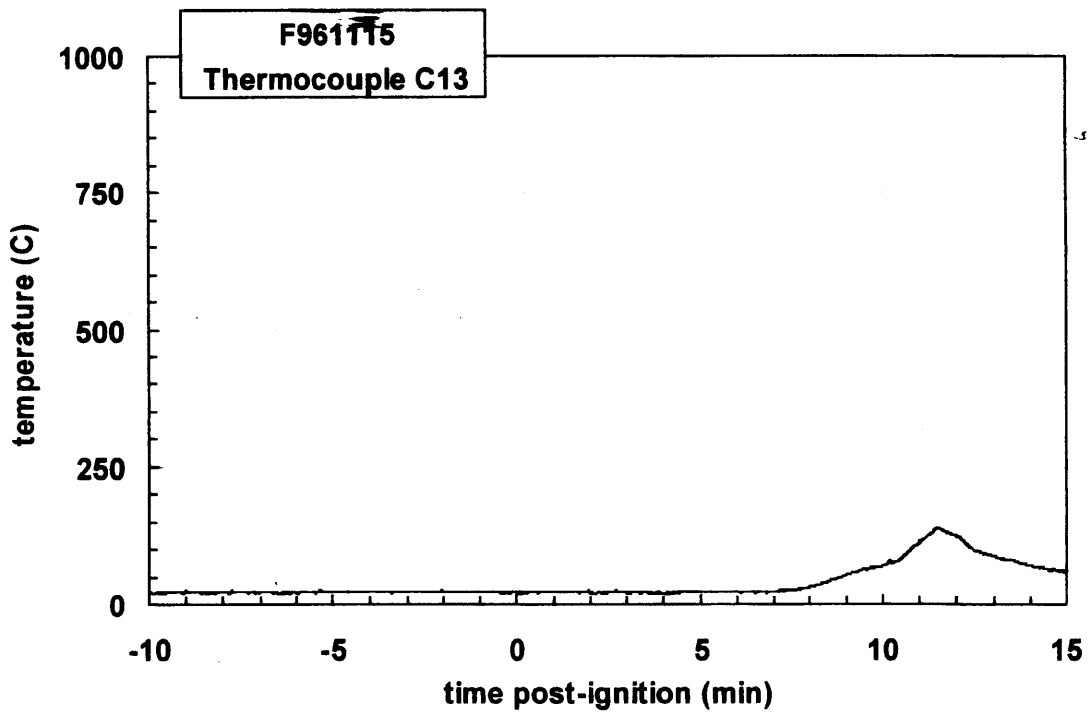
Plot C45. Fire Test F961115. Data plot from thermocouple C10.



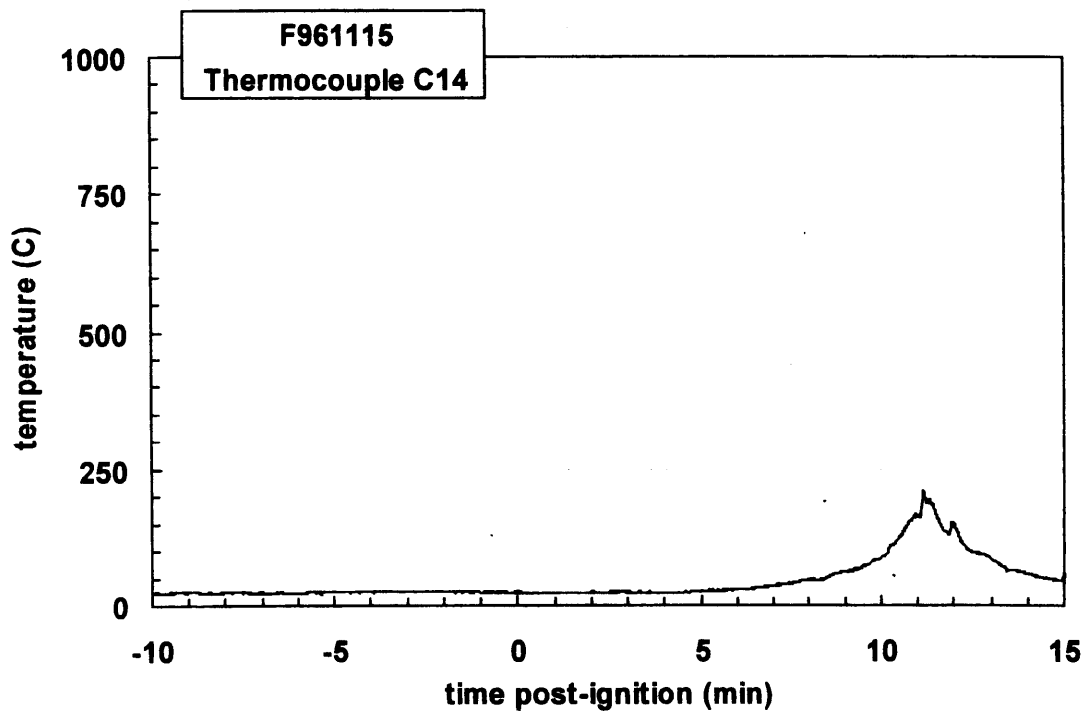
Plot C46. Fire Test F961115. Data plot from thermocouple C11.



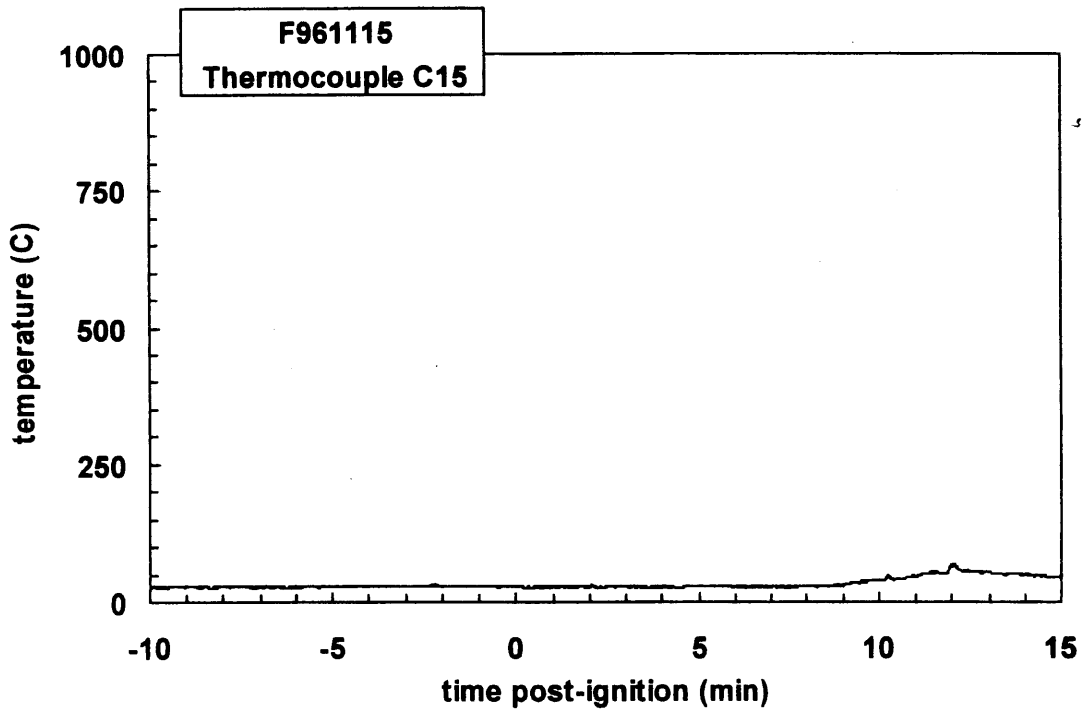
Plot C47. Fire Test F961115. Data plot from thermocouple C12.



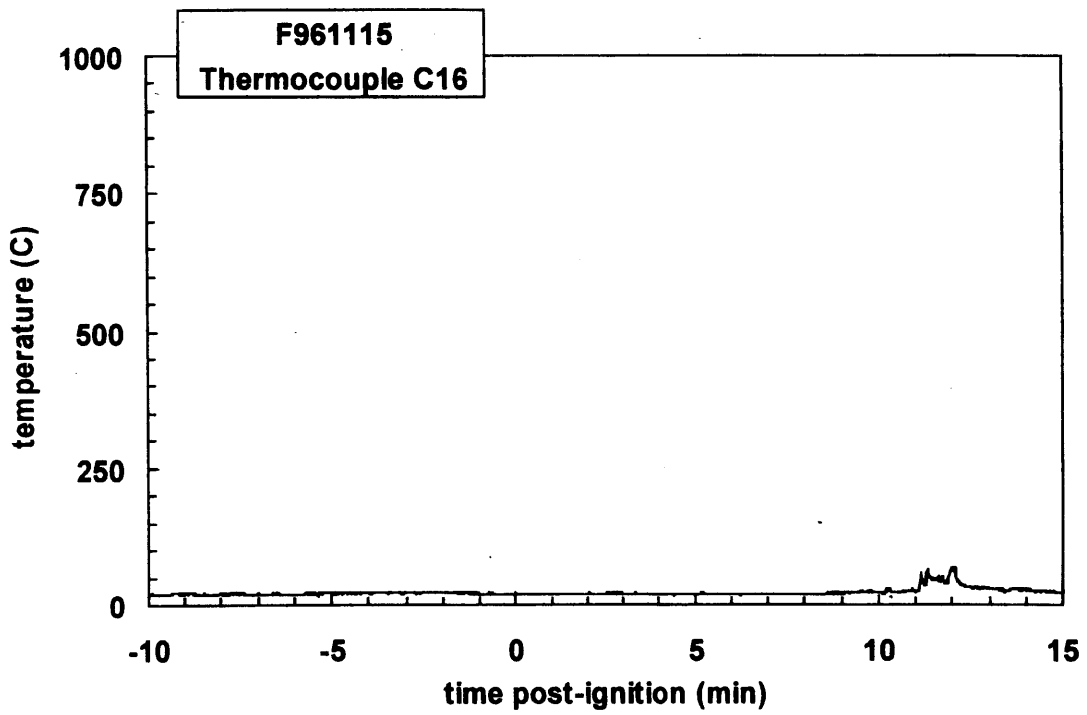
Plot C48. Fire Test F961115. Data plot from thermocouple C13.



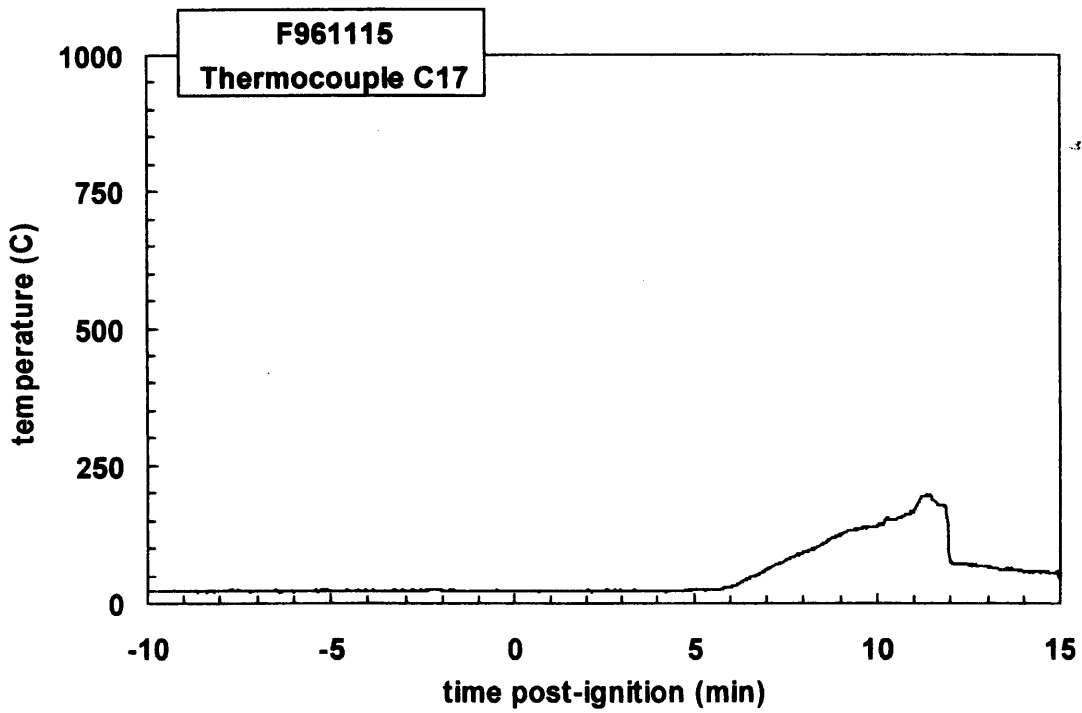
Plot C9. Fire Test F961115. Data plot from thermocouple C14.



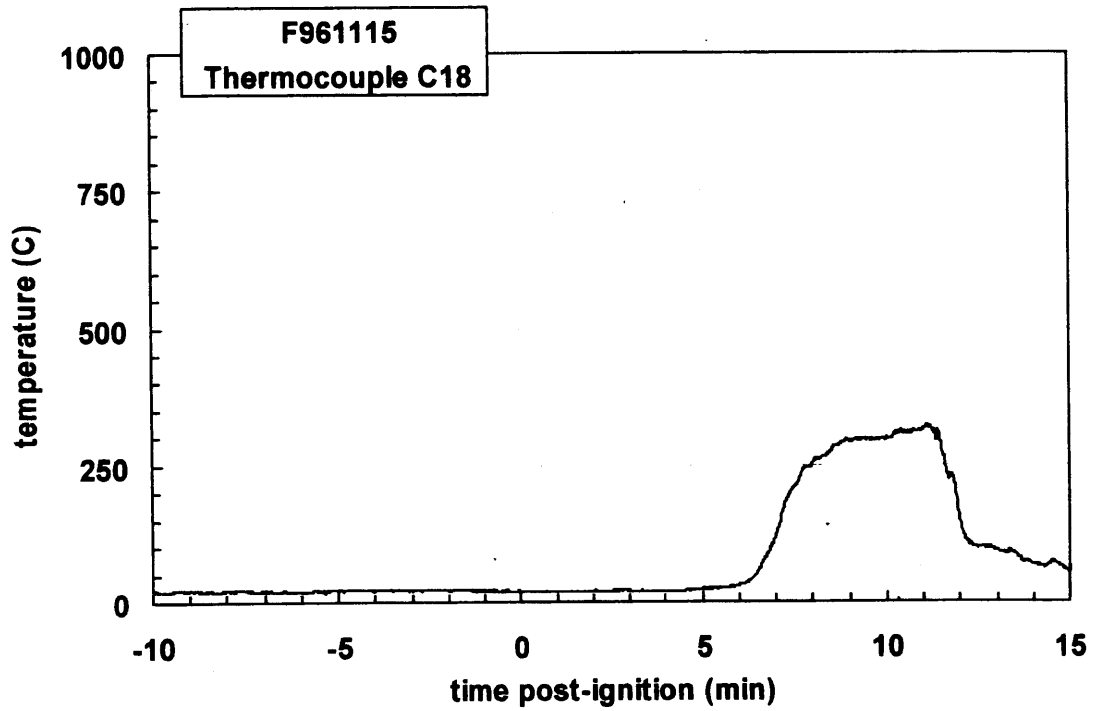
Plot C50. Fire Test F961115. Data plot from thermocouple C15.



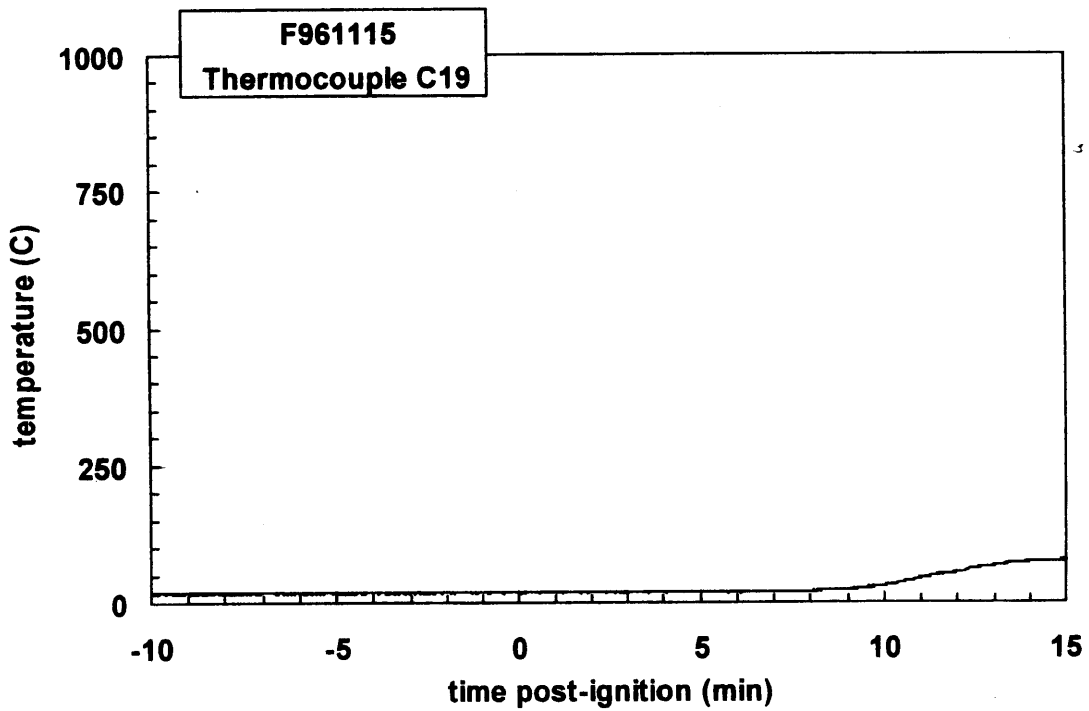
Plot C51. Fire Test F961115. Data plot from thermocouple C16.



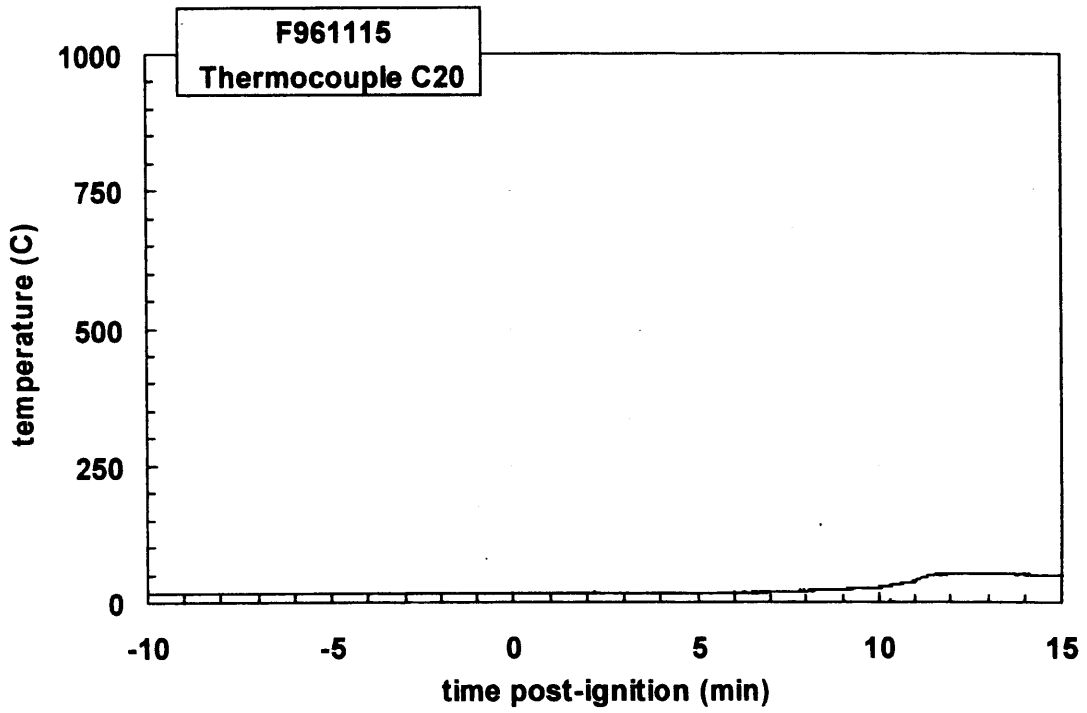
Plot C52. Fire Test F961115. Data plot from thermocouple C17.



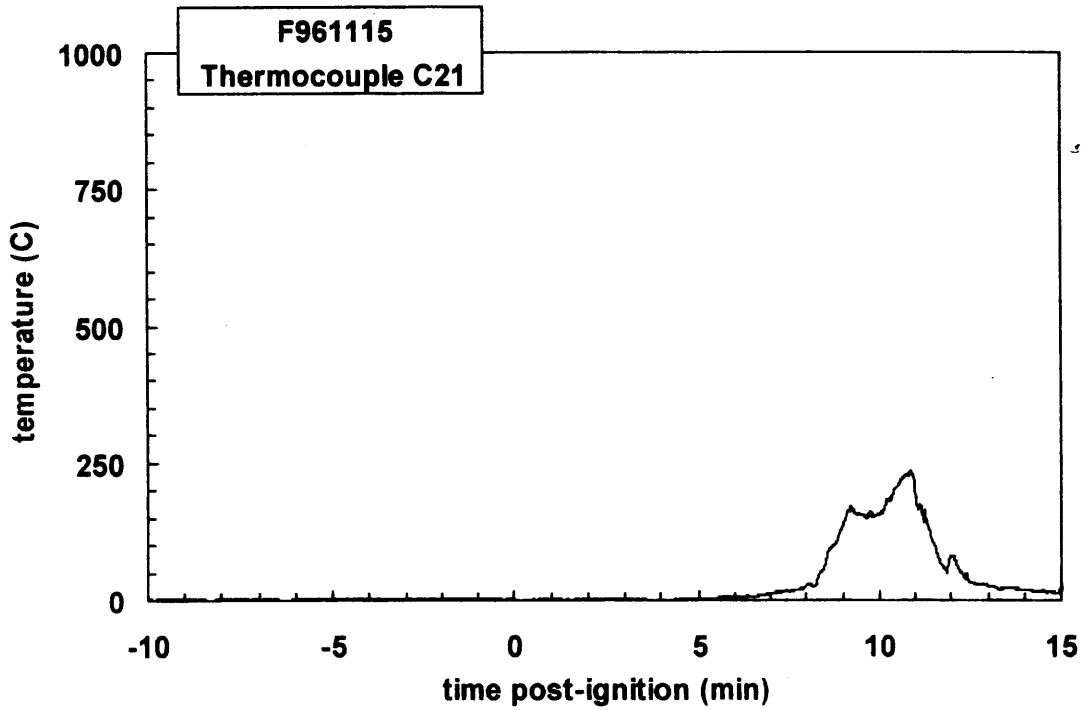
Plot C53. Fire Test F961115. Data plot from thermocouple C18.



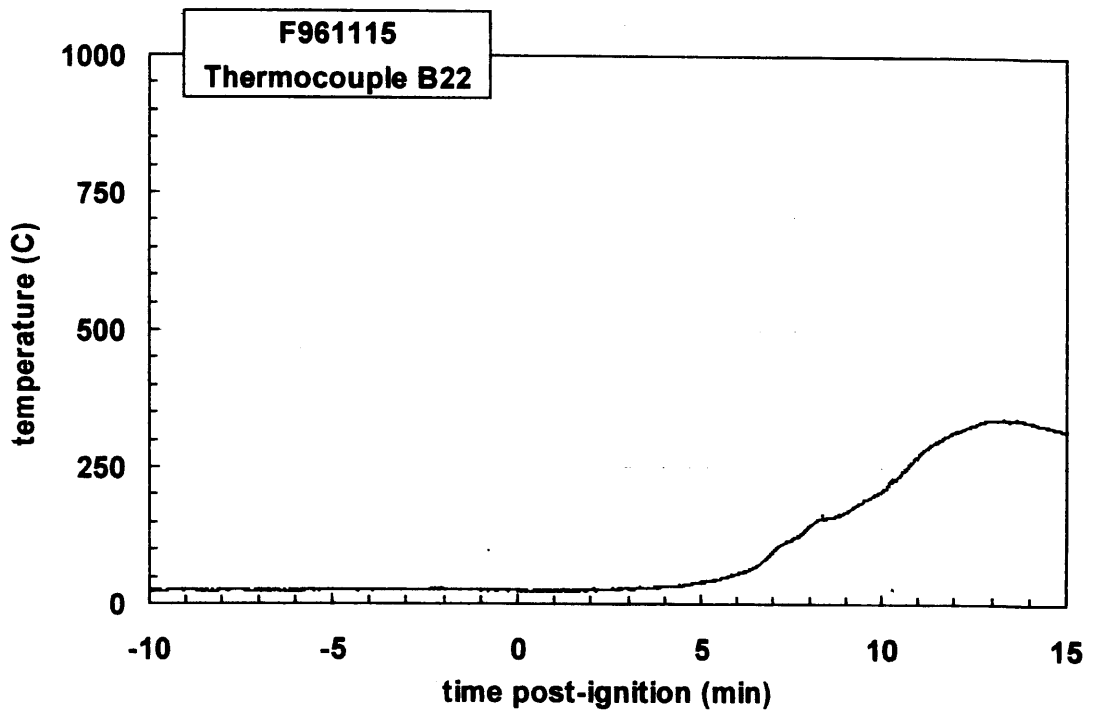
Plot C54. Fire Test F961115. Data plot from thermocouple C19.



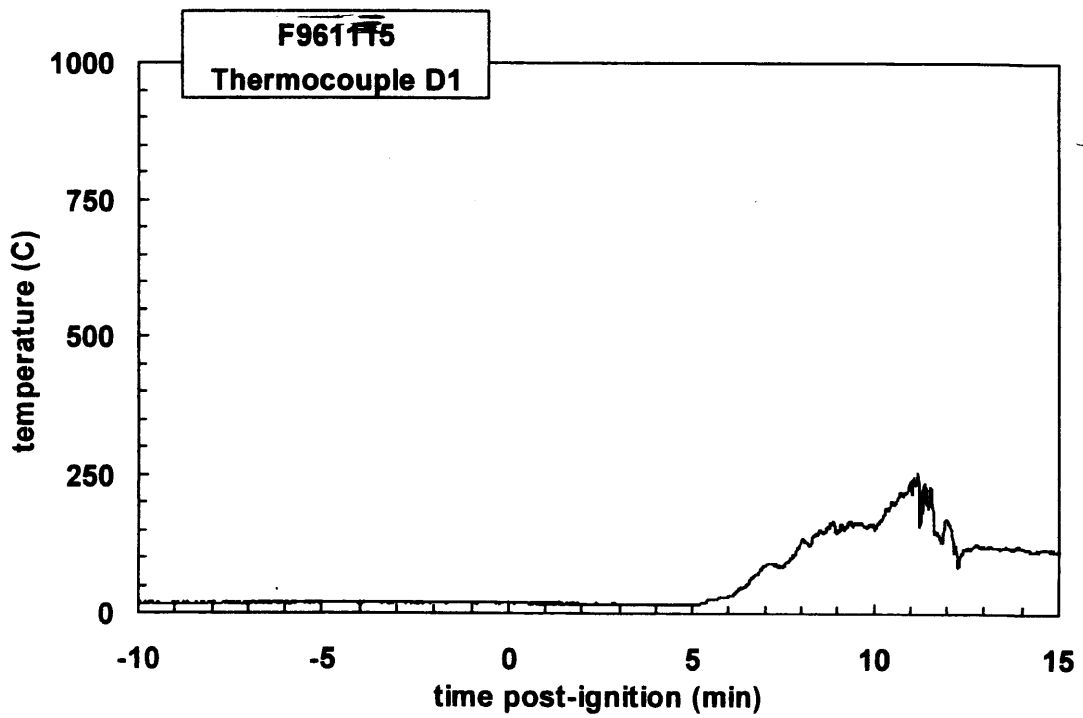
Plot C55. Fire Test F961115. Data plot from thermocouple C20.



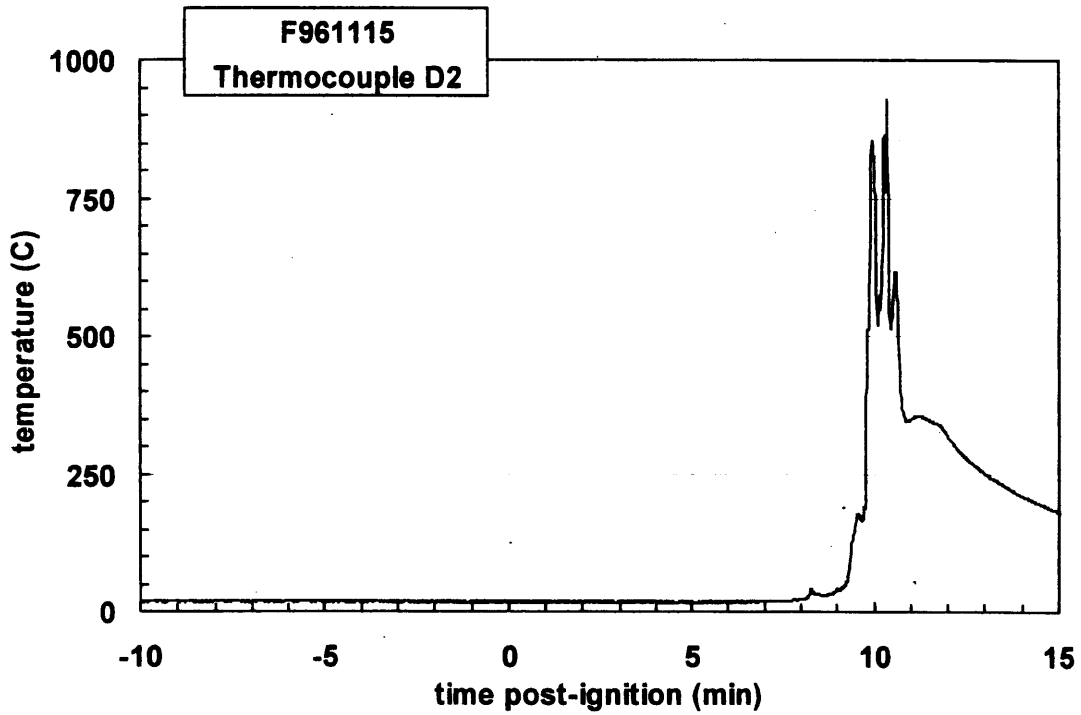
Plot C56. Fire Test F961115. Data plot from thermocouple C21.



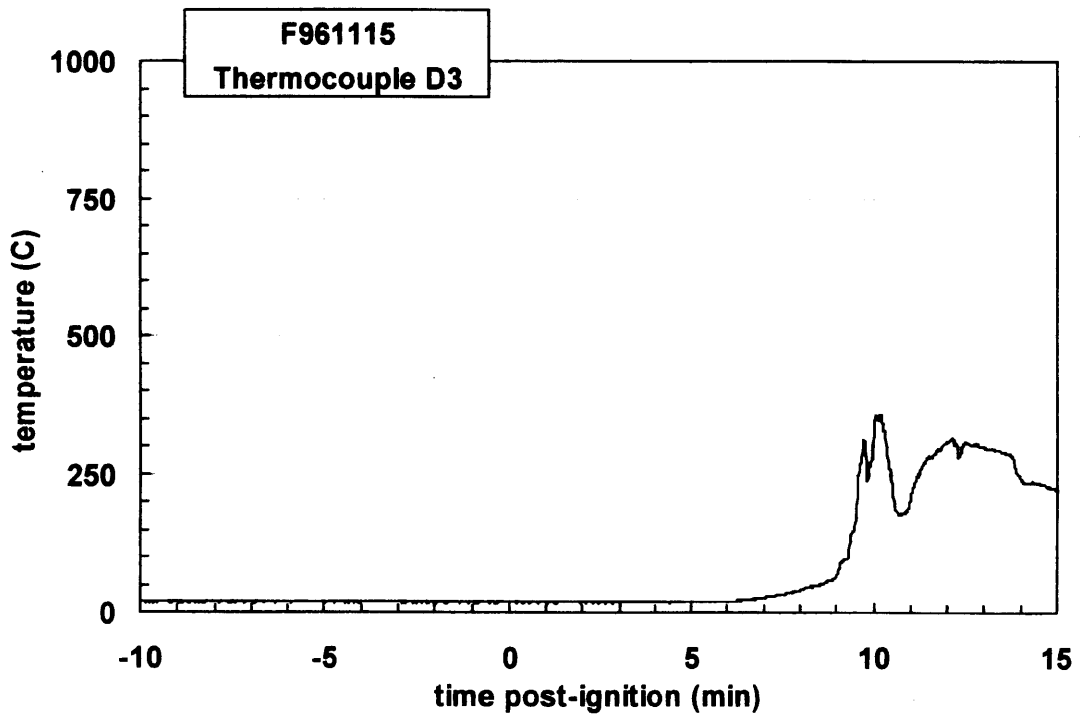
Plot C57. Fire Test F961115. Data plot from thermocouple C22.



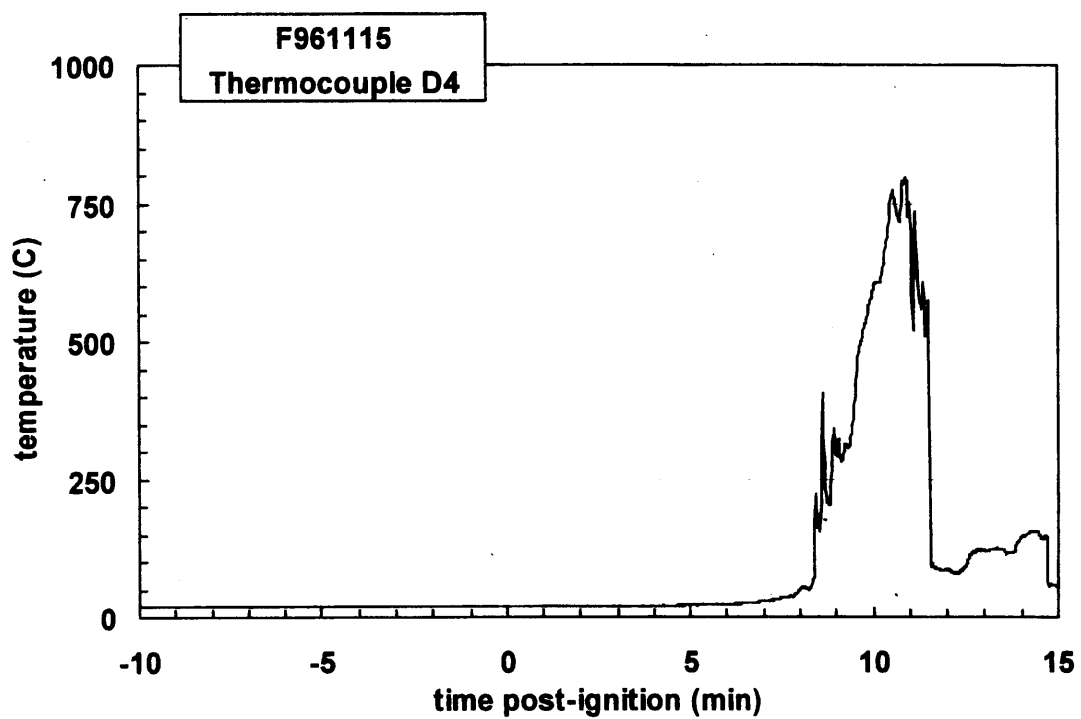
Plot C58. Fire Test F961115. Data plot from thermocouple D1.



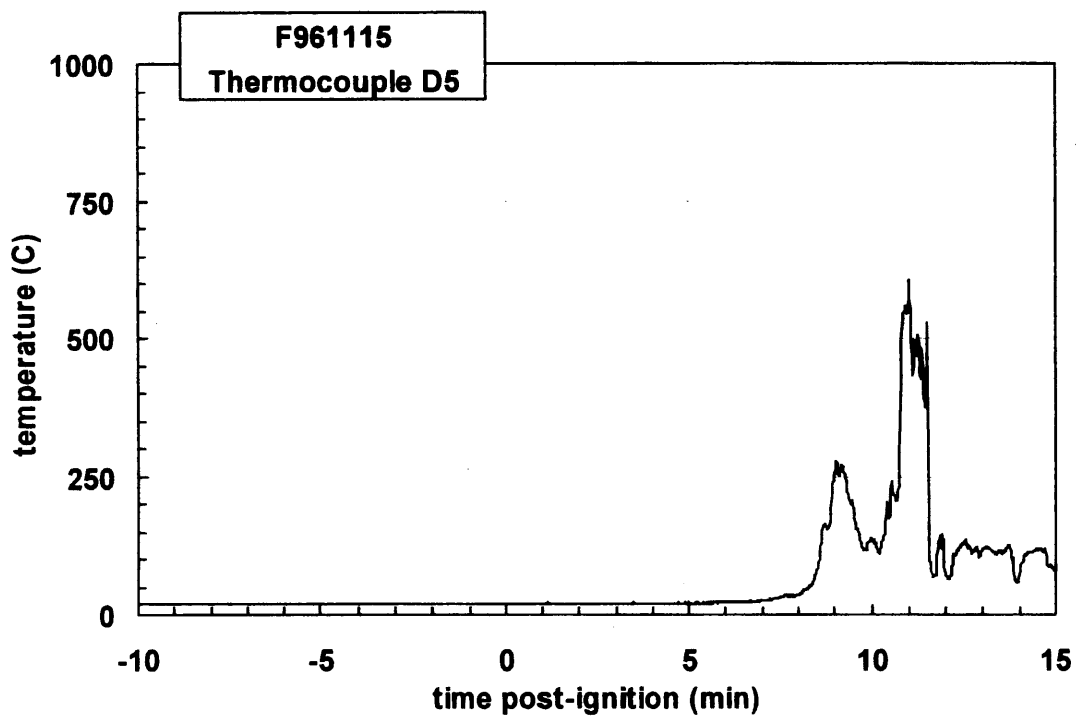
Plot C59. Fire Test F961115. Data plot from thermocouple D2.



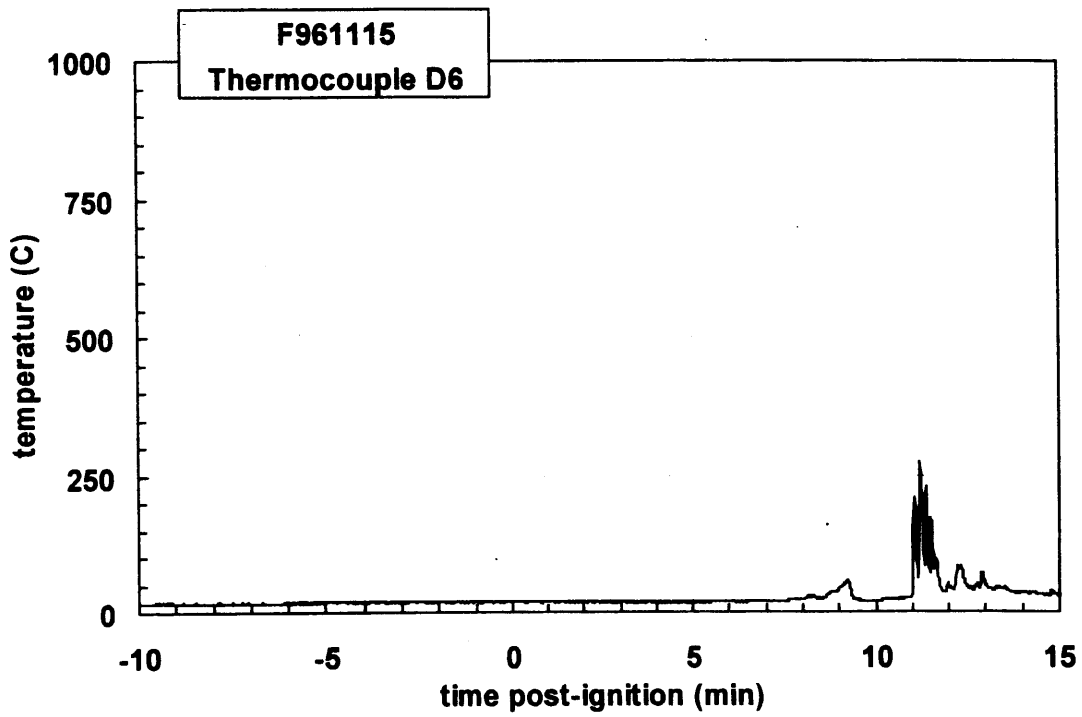
Plot C60. Fire Test F961115. Data plot from thermocouple D3.



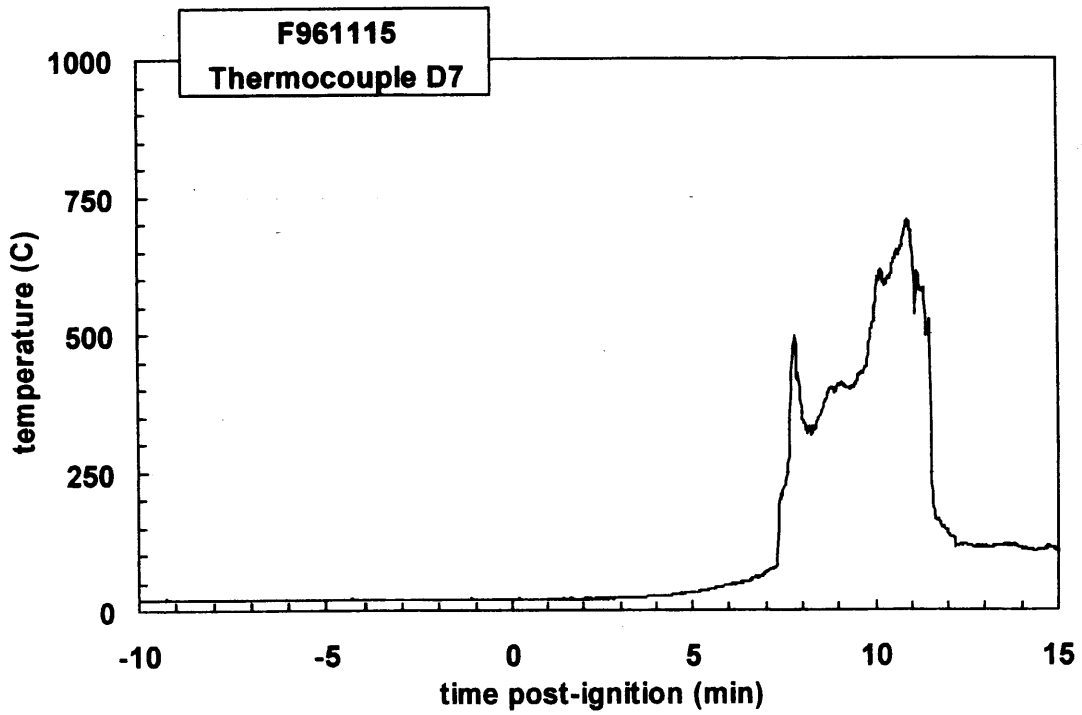
Plot C61. Fire Test F961115. Data plot from thermocouple D4.



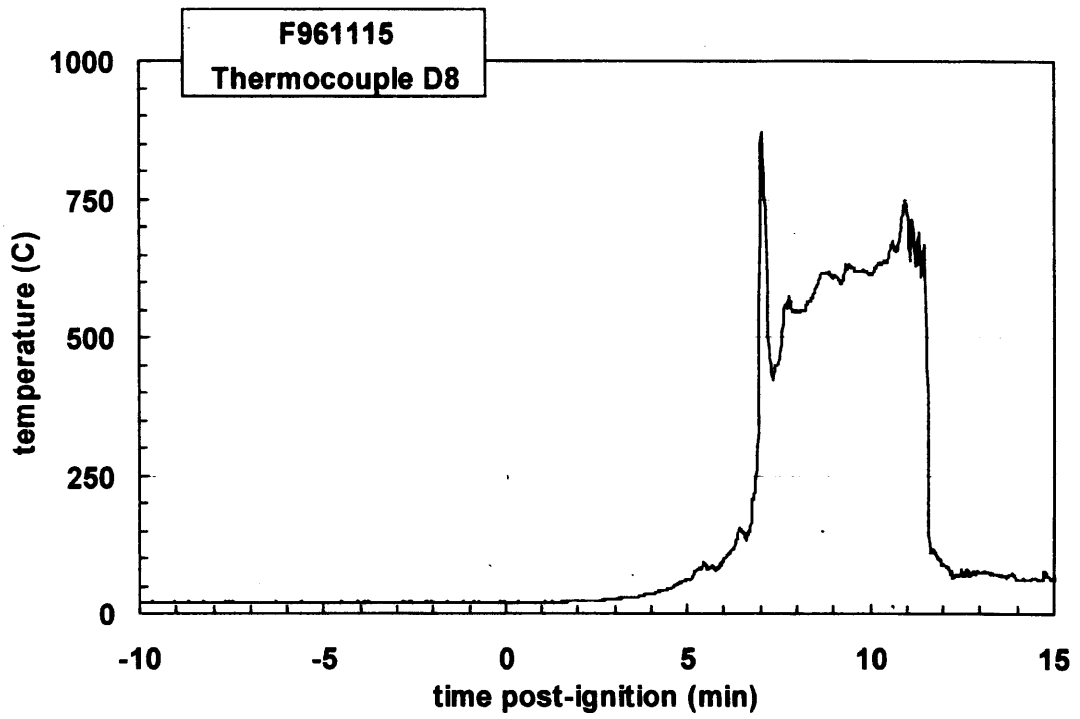
Plot C62. Fire Test F961115. Data plot from thermocouple D5.



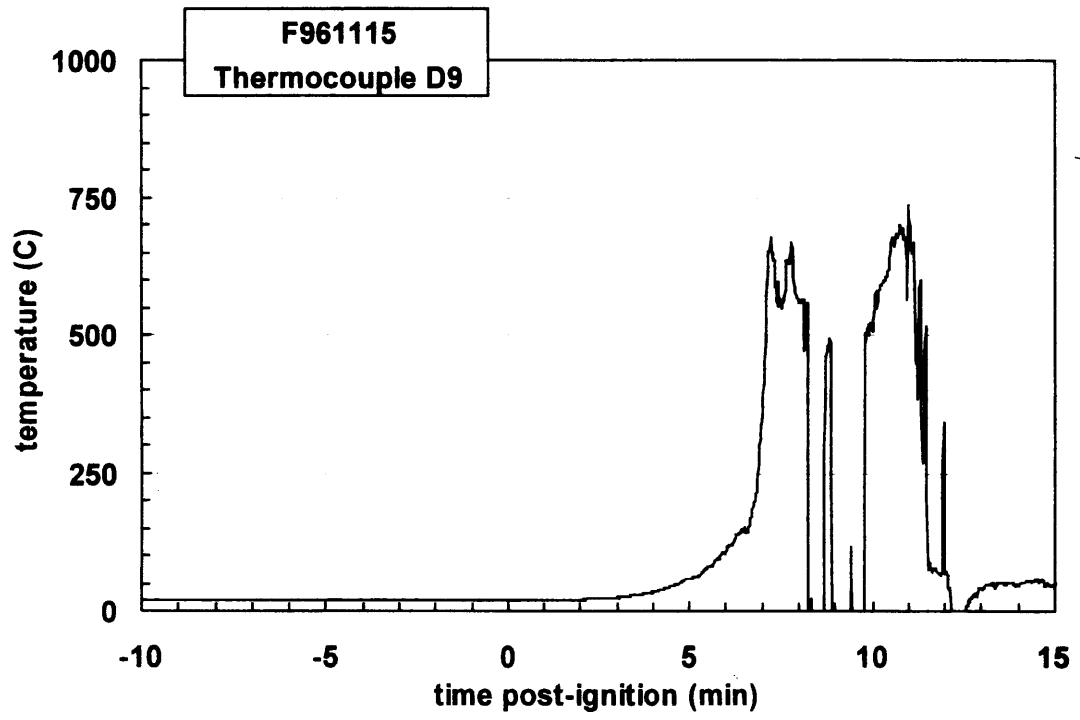
Plot C63. Fire Test F961115. Data plot from thermocouple D6.



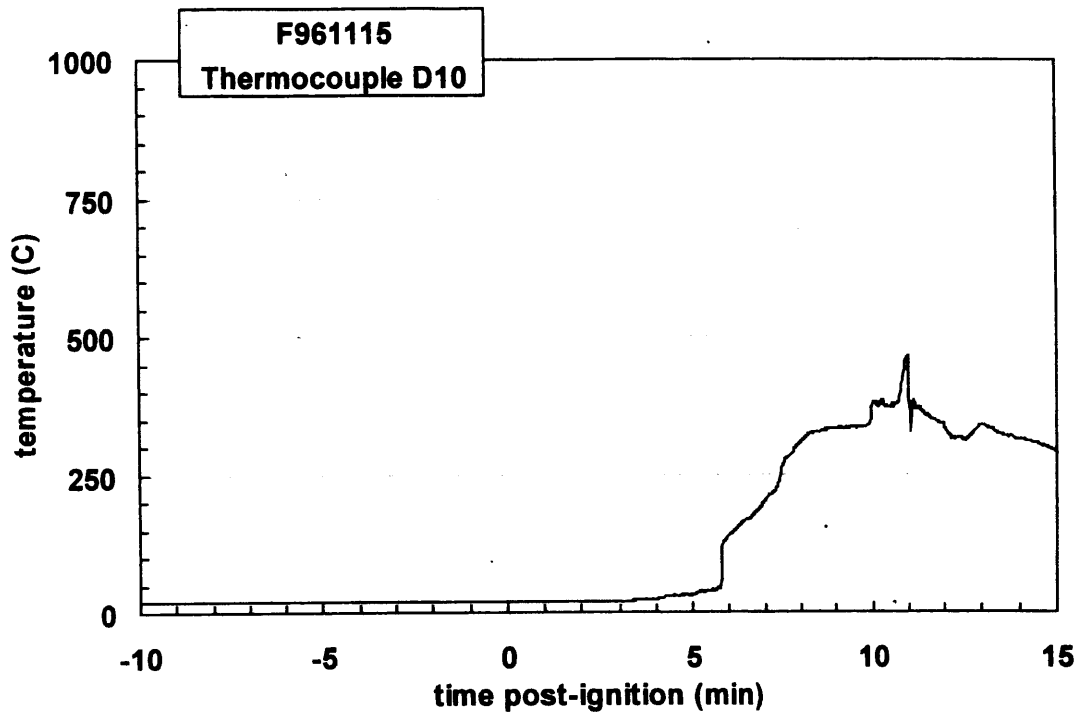
Plot C64. Fire Test F961115. Data plot from thermocouple D7.



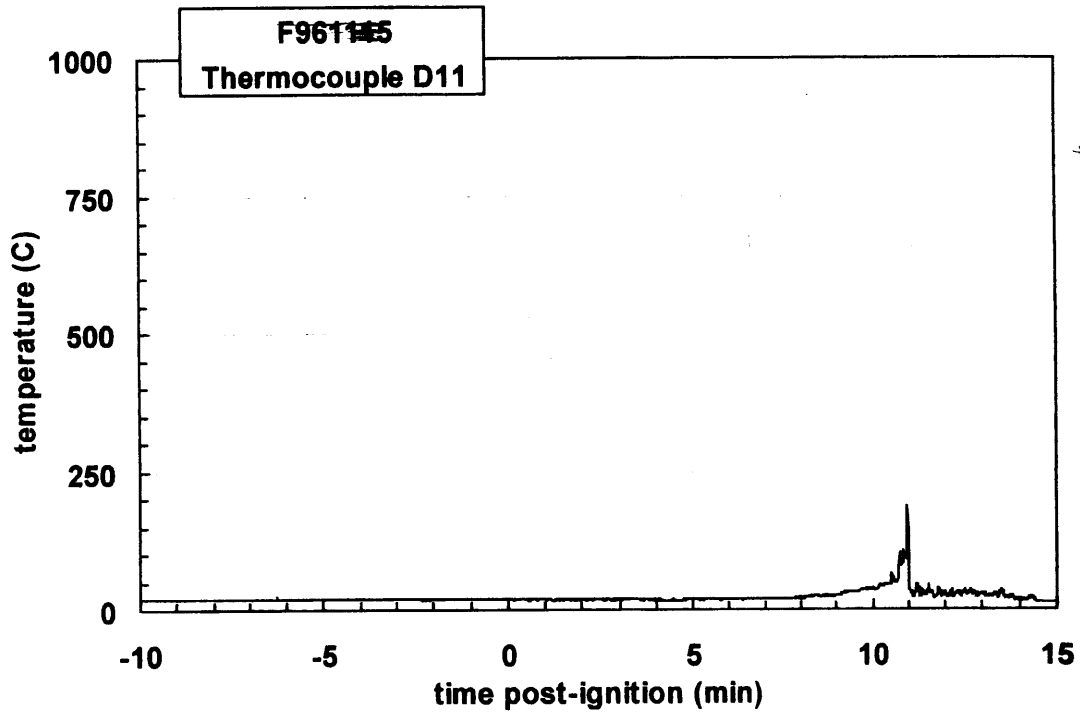
Plot C65. Fire Test F961115. Data plot from thermocouple D8.



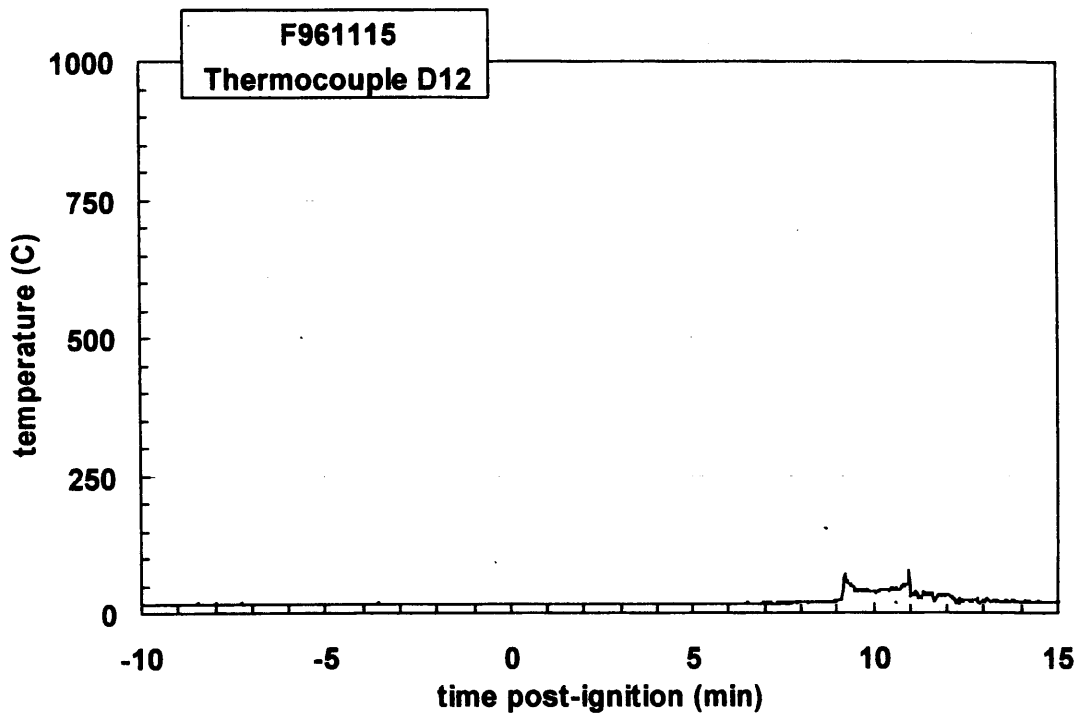
Plot C66. Fire Test F961115. Data plot from thermocouple D9.



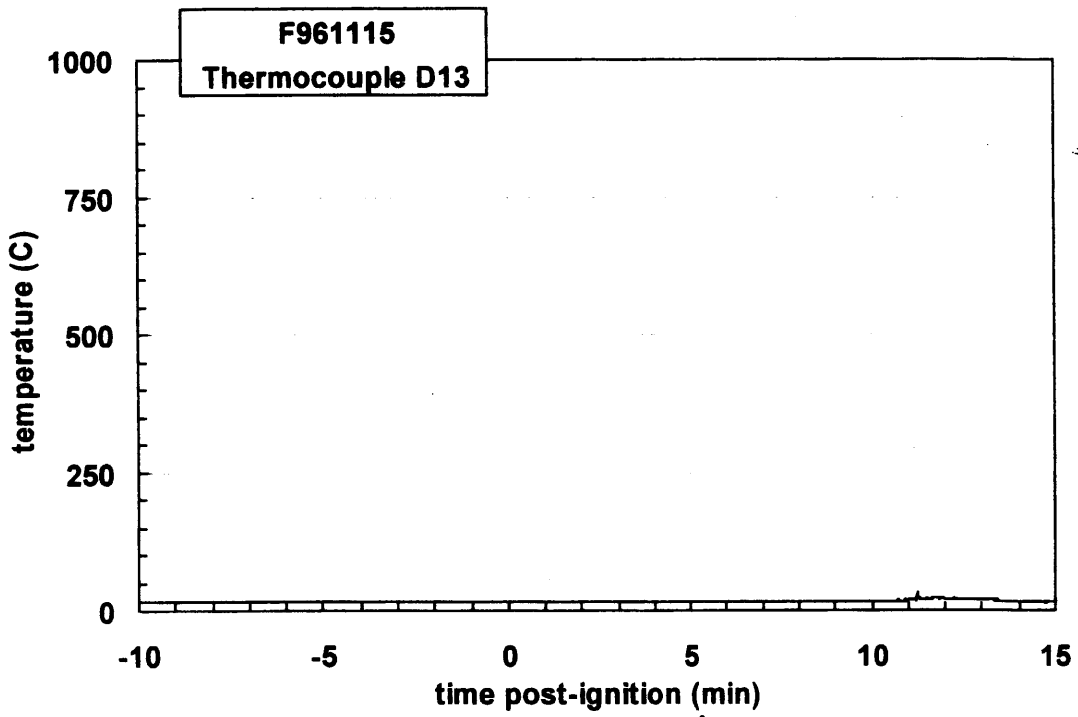
Plot C67. Fire Test F961115. Data plot from thermocouple D10.



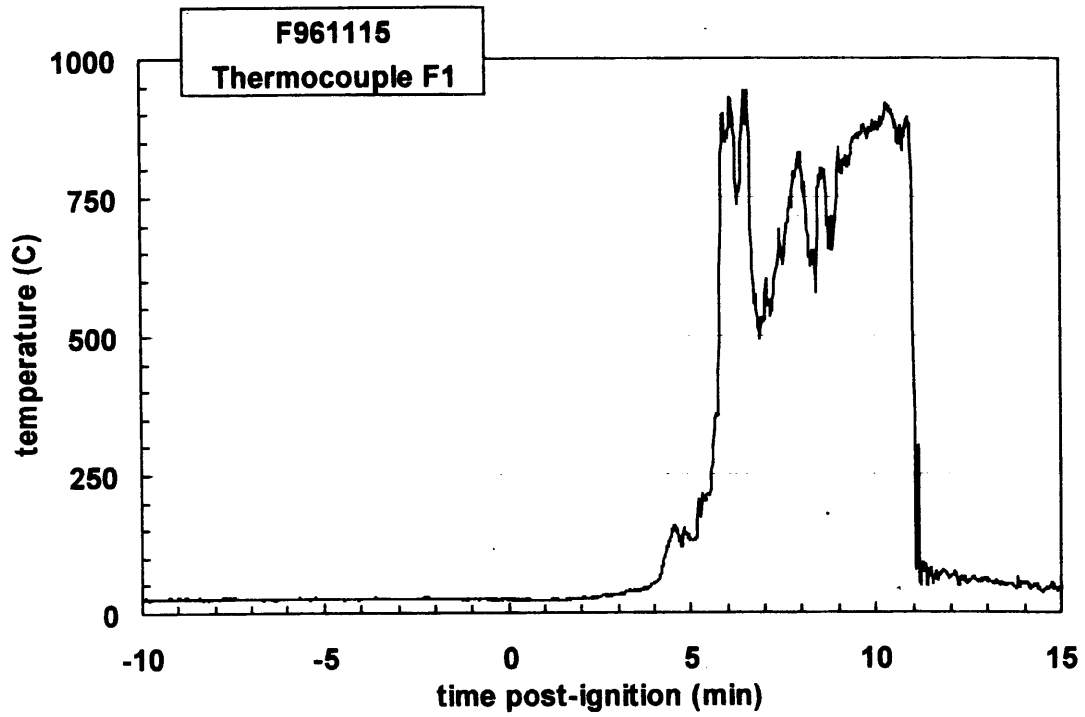
Plot C68. Fire Test F961115. Data plot from thermocouple D11.



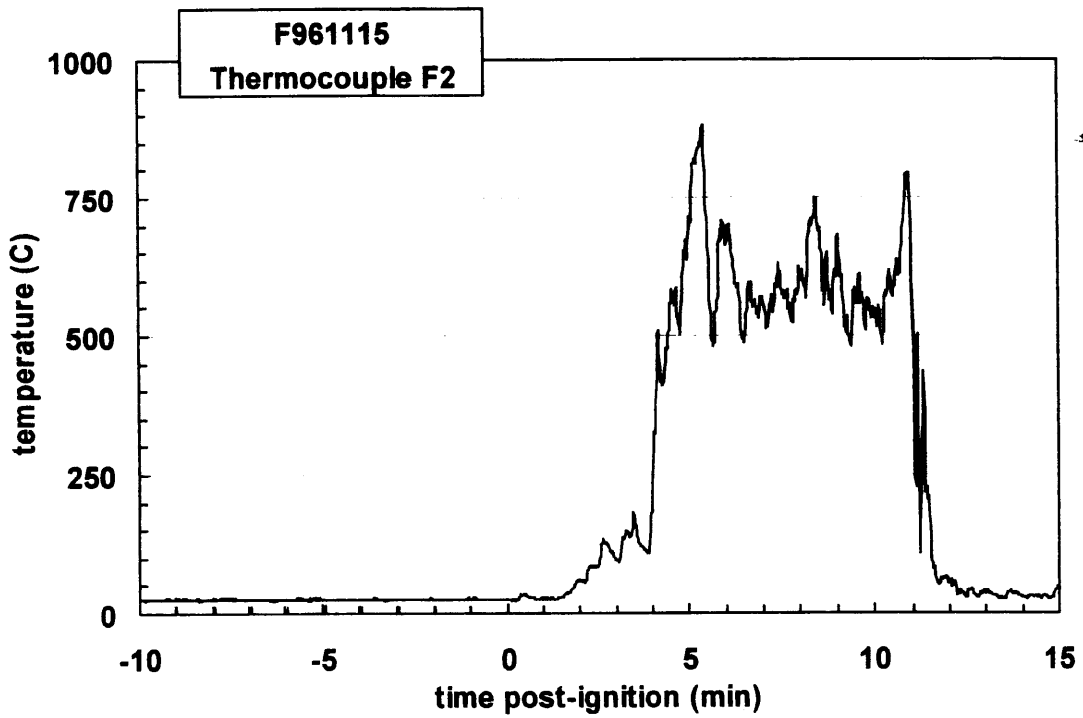
Plot C69. Fire Test F961115. Data plot from thermocouple D12.



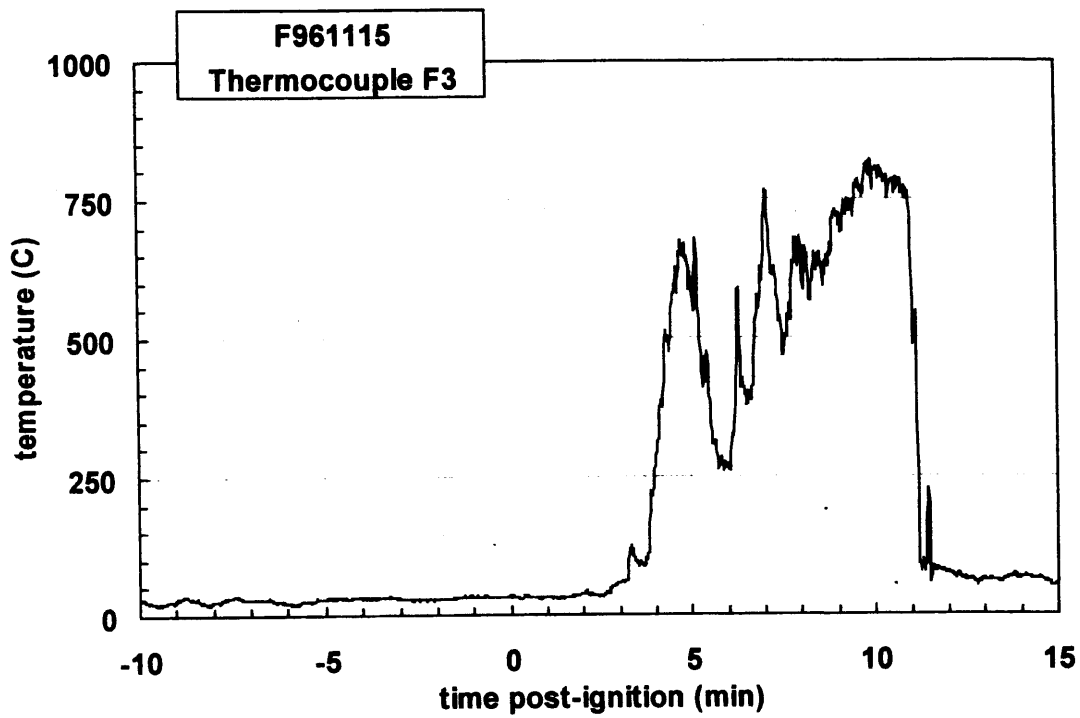
Plot C70. Fire Test F961115. Data plot from thermocouple D13.



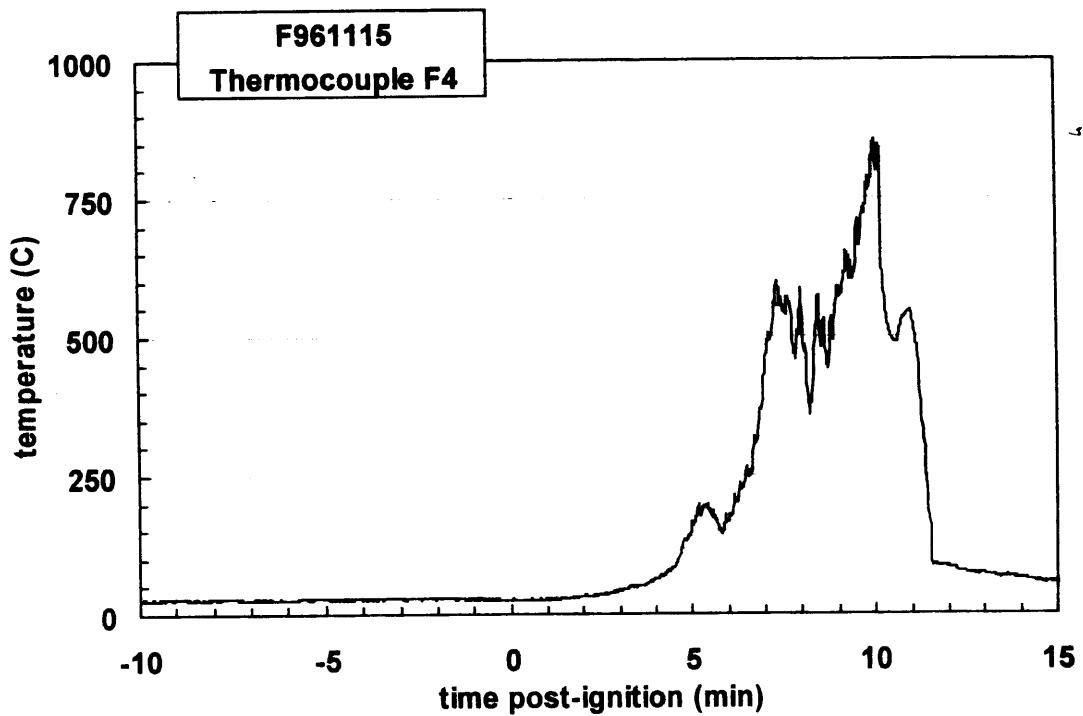
Plot C71. Fire Test F961115. Data plot from thermocouple F1.



Plot C72. Fire Test F961115. Data plot from thermocouple F2.



Plot C73. Fire Test F961115. Data plot from thermocouple F3.



Plot C74. Fire Test F961115. Data plot from thermocouple F4.

**APPENDIX D  
ASPIRATED THERMOCOUPLE DATA**

An aspirated thermocouple assembly (Medtherm Corporation) was installed in the test vehicle and used to measure air temperature at six elevations in the passenger compartment of the test vehicle during this test (Fig. D1). The aspirated thermocouple assembly was fabricated from Inconel 600 tubing. Each assembly consisted of a vertical manifold (o.d. = 0.375 in. (9.5 mm), i.d. = 0.25 in. (6.4 mm), length = 16 in. (406 mm)) with six horizontal radiation shields (o.d. = 0.25 in. (6.4 mm), i.d. = 0.19 in. (4.8 mm), length = 1.00 in. (25.4 mm)). The vertical spacing between the radiation shields along the manifold was 3 in. (75 mm). Three radial holes were drilled near the tip of each radiation shield. The holes were sized to approximately balance the airflow-rates over each thermocouple. A Type-N thermocouple inserted into each radiation shield so that the thermocouple junction was positioned approximately 0.2 in. (5.1 mm) down-stream from the inlet holes.

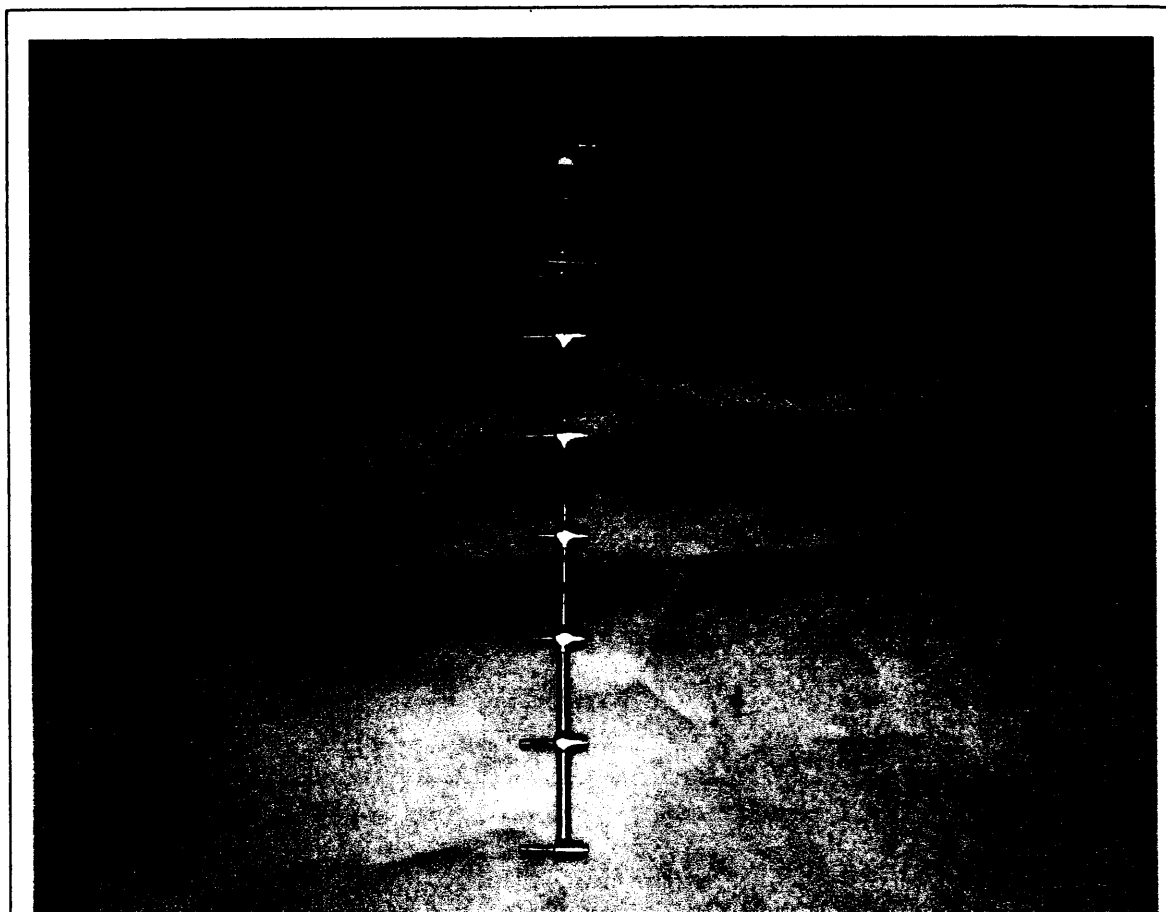


Figure D1. Fire Test F961115. Photograph of the aspirated thermocouple assembly used in the passenger compartment of the test vehicle.

The mounting flange of the aspirated thermocouple probe assembly was attached to the roof of the vehicle. The probe extended into the passenger compartment through a hole in the roof so that all 6 thermocouples were located below the headliner. The probe was vertical and located along the longitudinal mid-line of the vehicle approximately equidistant from the driver and passenger seats. The upper-most aspirated thermocouple was approximately 0.5 in. (12 mm) below the lower surface of the headliner. The manifold was connected to a rotary-vane pump with flexible copper tubing (o.d. = 0.5 in. (12 mm), length = 15 ft. (4.6 m)). The capacity of the pump was 50 L/min at atmospheric pressure. The flow rate of air into each radiation shield under these conditions was measured using a dry-gas meter. The linear velocity of the air flowing through each radiation shield was calculated from the flow rate measurements, and determined to be between 5 and 10 m/s.

The linear velocity of airflow over the thermocouple junction affects the accuracy of the air temperature measurement [D1]. The linear velocity of gas flowing through each radiation shield was sufficient to achieve a relative error of < 5% for gas temperature measurements in or close to a steady-state flame [D1]. However, the time-response of an aspirated thermocouple becomes a factor in the accuracy of the gas temperature measurement in environments where the heat release rate of the fire is changing or the flame is spreading relative to the aspirated probe. Both were the case in these tests. The time-delay in the response of the aspirated thermocouple probe used in these tests was estimated to be approximately 5 sec [D2].

Figures D2 and D3 show the approximate location of the aspirated thermocouple probe assembly in the test vehicle for this test.

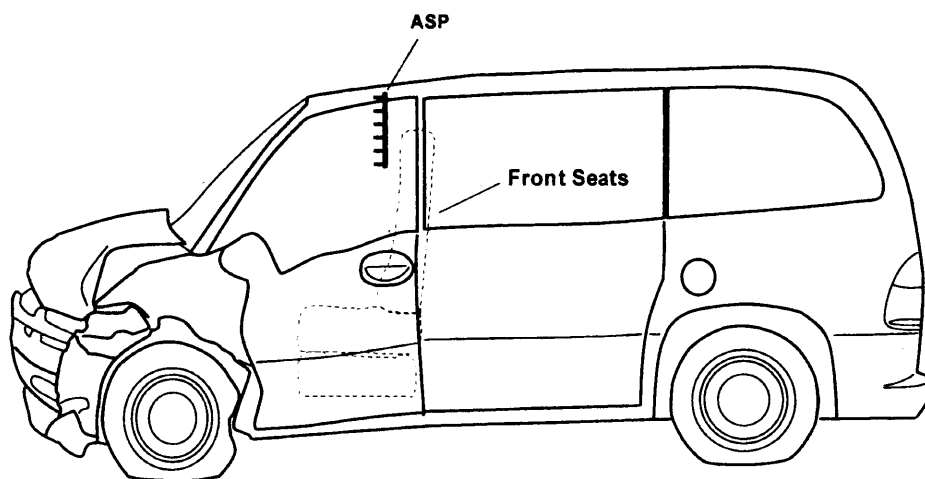


Figure D2. Fire Test F961115. Side view of the test vehicle showing the approximate location of the aspirated thermocouple probe assembly in the passenger compartment.



The mounting flange of the aspirated thermocouple probe assembly was attached to the roof of the vehicle. The probe extended into the passenger compartment through a hole in the roof so that all 6 thermocouples were located below the headliner. The probe was vertical and located along the longitudinal mid-line of the vehicle approximately equidistant from the driver and passenger seats. The upper-most aspirated thermocouple was approximately 0.5 in. (12 mm) below the lower surface of the headliner. The manifold was connected to a rotary-vane pump with flexible copper tubing (o.d. = 0.5 in. (12 mm), length = 15 ft. (4.6 m)). The capacity of the pump was 50 L/min at atmospheric pressure. The flow rate of air into each radiation shield under these conditions was measured using a dry-gas meter. The linear velocity of the air flowing through each radiation shield was calculated from the flow rate measurements, and determined to be between 5 and 10 m/s.

The linear velocity of airflow over the thermocouple junction affects the accuracy of the air temperature measurement [D1]. The linear velocity of gas flowing through each radiation shield was sufficient to achieve a relative error of < 5% for gas temperature measurements in or close to a steady-state flame [D1]. However, the time-response of an aspirated thermocouple becomes a factor in the accuracy of the gas temperature measurement in environments where the heat release rate of the fire is changing or the flame is spreading relative to the aspirated probe. Both were the case in these tests. The time-delay in the response of the aspirated thermocouple probe used in these tests was estimated to be approximately 5 sec [D2].

Figures D2 and D3 show the approximate location of the aspirated thermocouple probe assembly in the test vehicle for this test.

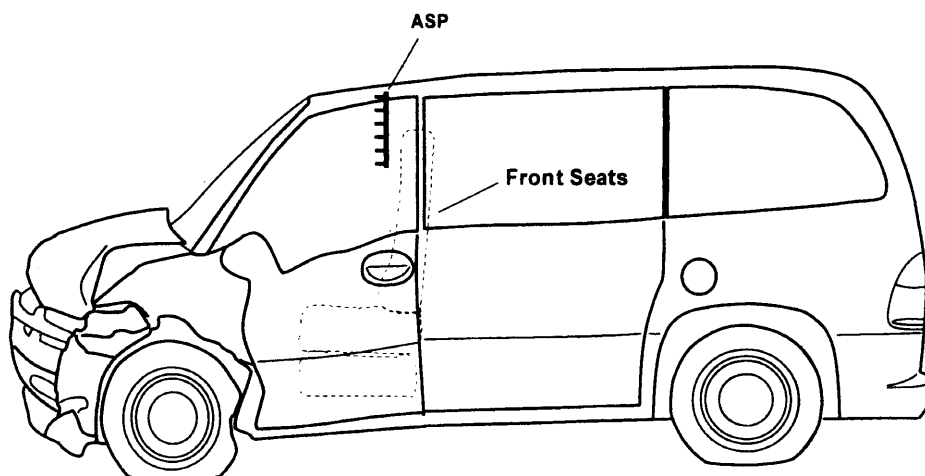


Figure D2. Fire Test F961115. Side view of the test vehicle showing the approximate location of the aspirated thermocouple probe assembly in the passenger compartment.

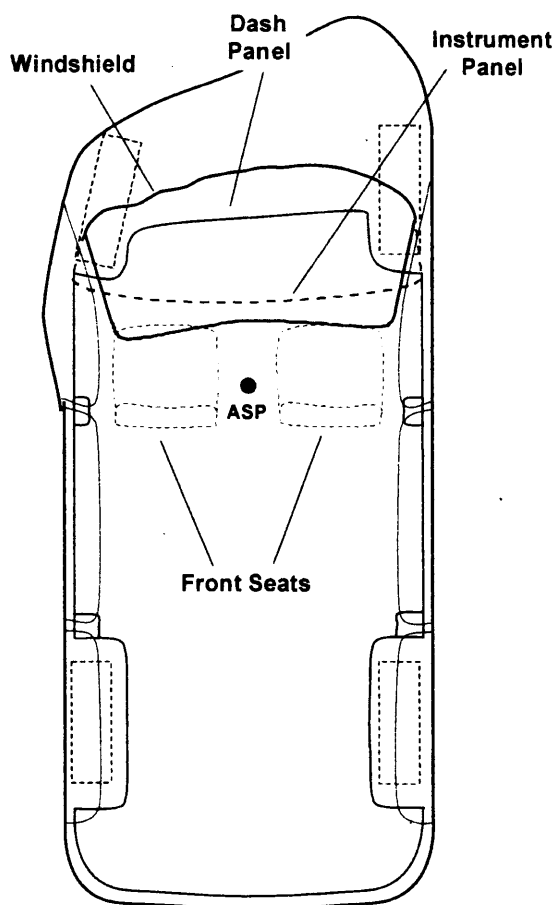
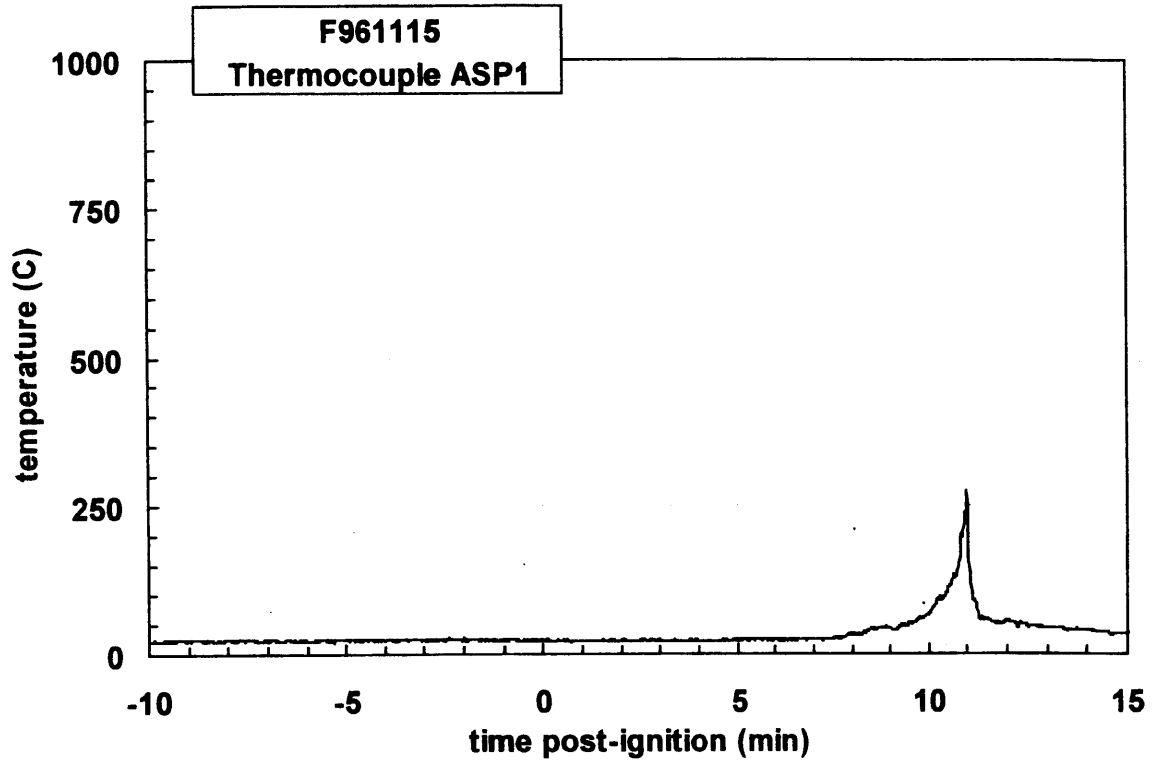


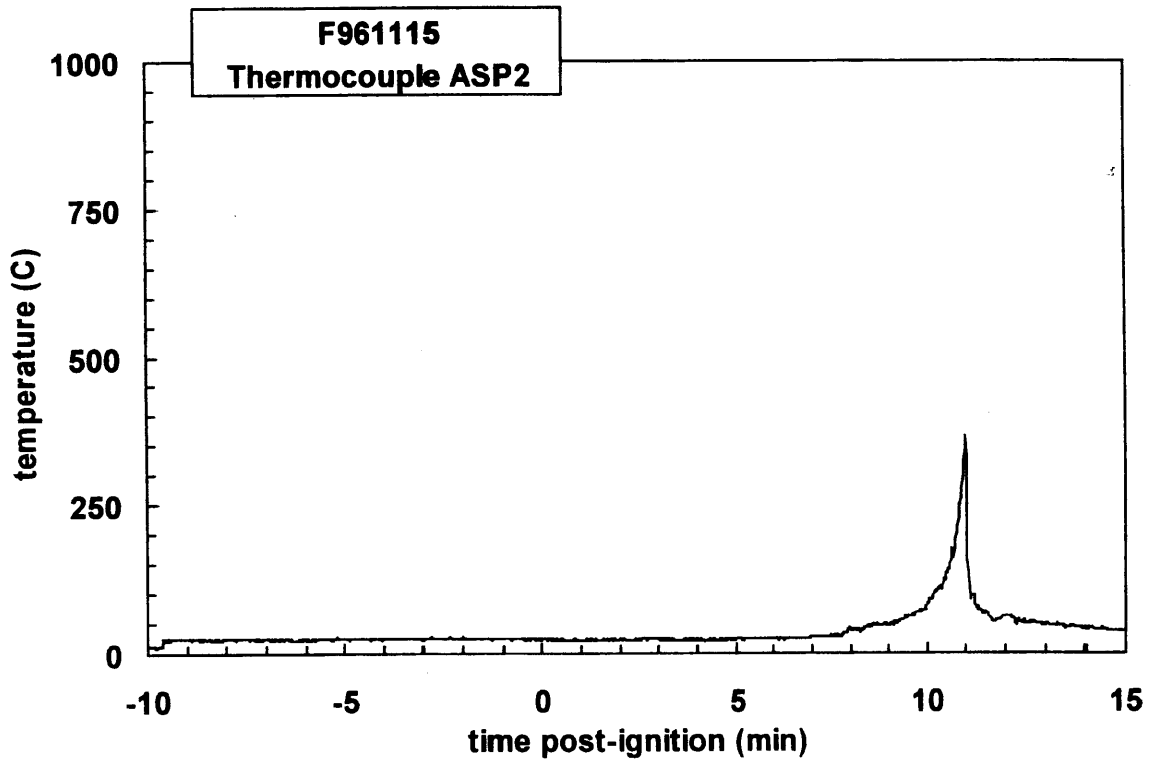
Figure D3. Fire Test F961115. Top view of the test vehicle showing the approximate location of the aspirated thermocouple probe assembly in the passenger compartment.

#### REFERENCES

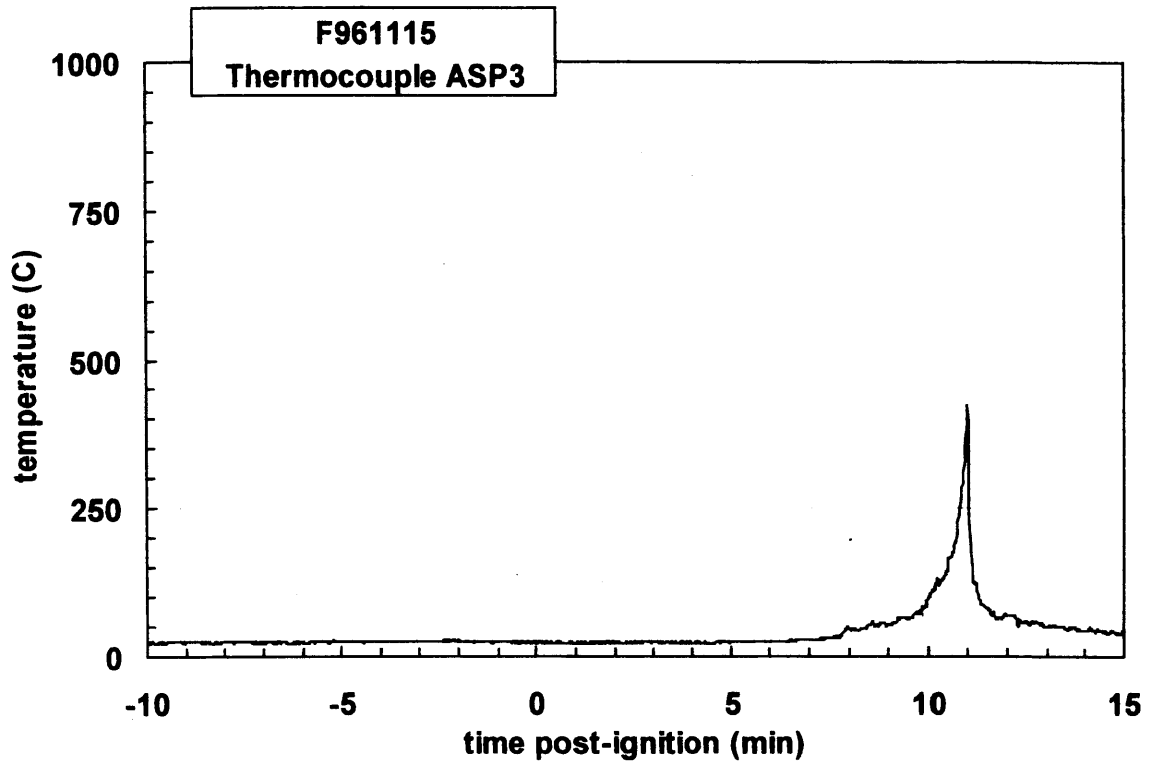
- D1. J. S. Newman and P. A. Croce. A simple aspirated thermocouple for use in fires. *J. Fire Flamm.* **10**:326-336 (1979).
- D2. N. R. Keltner and K. A. Strom. Thermal Measurement Uncertainty and Compensation. Paper in preparation.



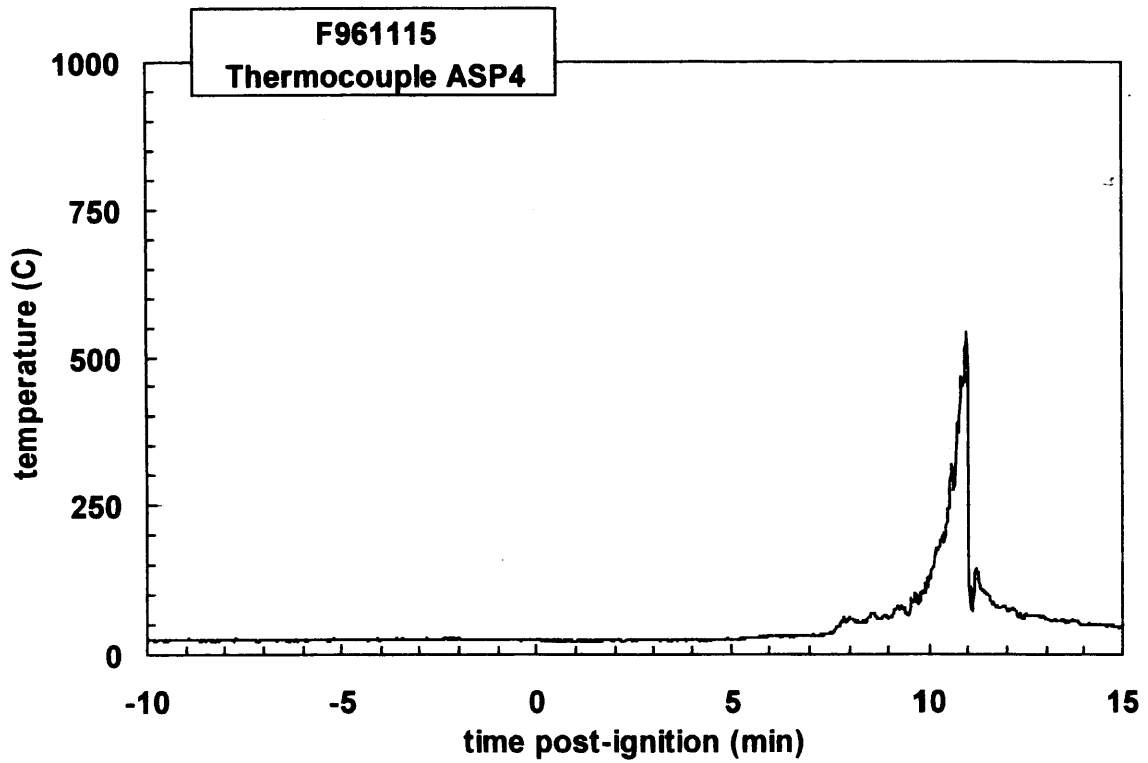
Plot D1. Fire Test F961115. Data plot from thermocouple ASP1.



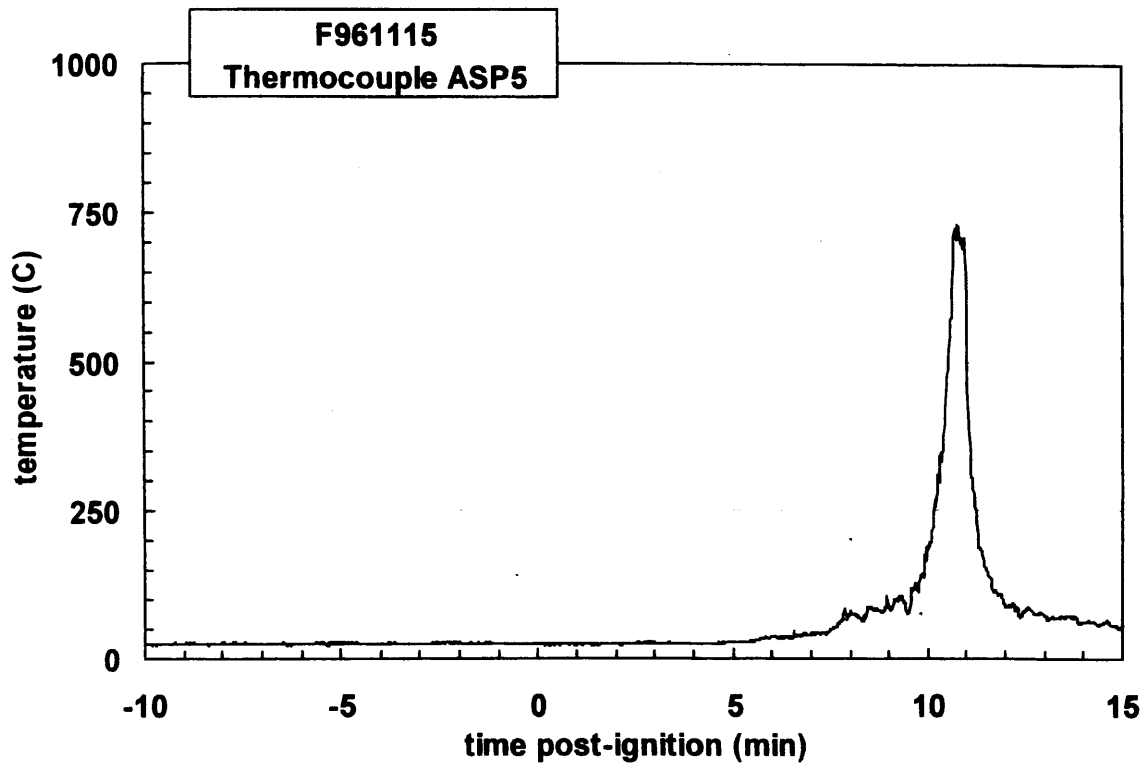
Plot D2. Fire Test F961115. Data plot from thermocouple ASP2.



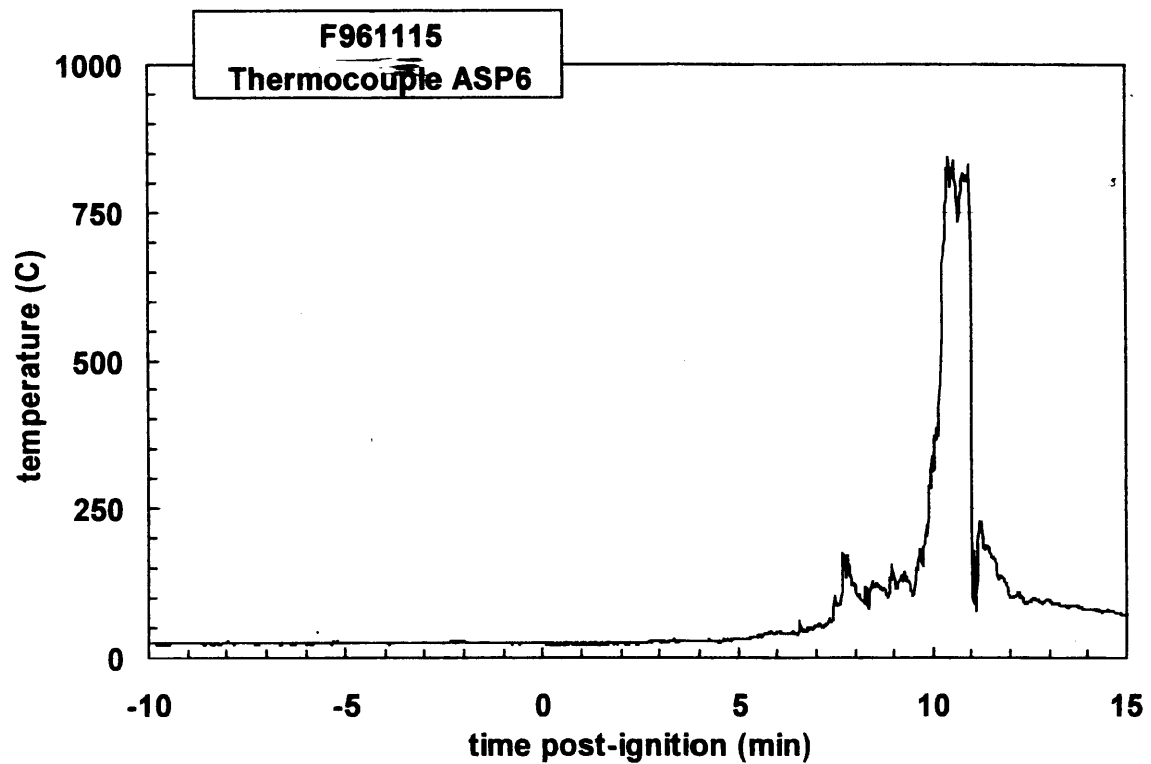
Plot D3. Fire Test F961115. Data plot from thermocouple ASP3.



Plot D4. Fire Test F961115. Data plot from thermocouple ASP4.



Plot D5. Fire Test F961115. Data plot from thermocouple ASP5.



Plot D6. Fire Test F961115. Data plot from thermocouple ASP6.

**APPENDIX E**  
**HEAT FLUX TRANSDUCER / RADIOMETER DATA**

Heat-flux transducer/radiometer assemblies (64 Series, Medtherm Corporation) were used to measure convective and radiative heat transfer to selected objects in the vehicle. Each assembly contained two Schmidt-Boelter thermopiles in a water-cooled copper body (diameter = 1 in. (25.4 mm), length = 1 in. (25.4 mm)). The faces of the heat flux transducers were coated with high-temperature optical black paint. The radiometers had permanent sapphire windows (view-angle = 150°; optical transmittance range 0.4 to 4.2  $\mu\text{m}$ ). Both transducers were calibrated to 100 kW/m<sup>2</sup> at a reference temperature of 25°C.

A PC-based data system was used for data acquisition from the heat flux transducers and radiometers. The PC contained a 75 MHz Pentium Processor, 16 MB RAM, an 814 MB hard disk, and a 16-bit (Model BG45-AP5CP, ACER Inc., Taiwan R. O. C.). A 100 kHz I/O board with 16 analog input channels (DaqBoard 200A, IOTech, Inc., Cleveland, OH) was installed in one of the expansion slots in the PC. An analog-input multiplex expansion card (DBK-12, IOTech, Inc., Cleveland, OH) was used for data acquisition from these transducers. The electrical shields on the signal cables were connected to the electronic chassis grounds on the analog-input expansion card. The vehicle chassis was connected to the electronic chassis ground by a large-gauge cable. The data acquisition software (DASYLab, Daten System Technik GmbH, Mönchengladbach, Germany) was configured to sample each channel at a rate of 10 Hz and store the data in 10-point block averages.

Figure E1 shows the approximate locations of heat flux transducer/radiometer assemblies in the dash panel of the test vehicle during this test. To install the of heat flux transducer/radiometer assemblies in the dash panel, a clearance-hole was drilled in the metal bulkhead and the transducer was mounted on stand-offs so that the face of the transducer was flush with the exterior metal surface. One Type-K thermocouple was attached to the back of each transducer with high-temperature ceramic cement. Copper tubing (o.d. = 0.25 in. (6.4 mm)) was used for the cooling water supply and waste lines. The temperature of the water supplied to the transducer assemblies was approximately 45°C, and the flow rate of water through each body was approximately 100 mL/min.

The data recorded from these transducers is shown in Plots E1 through E12.

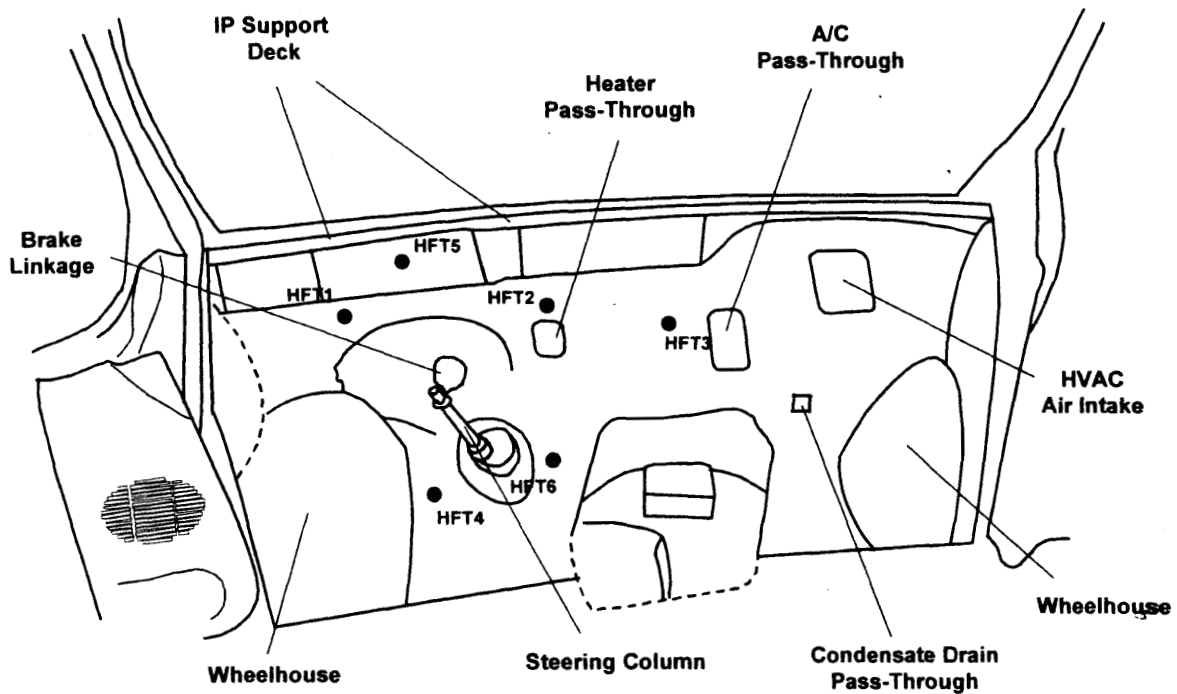
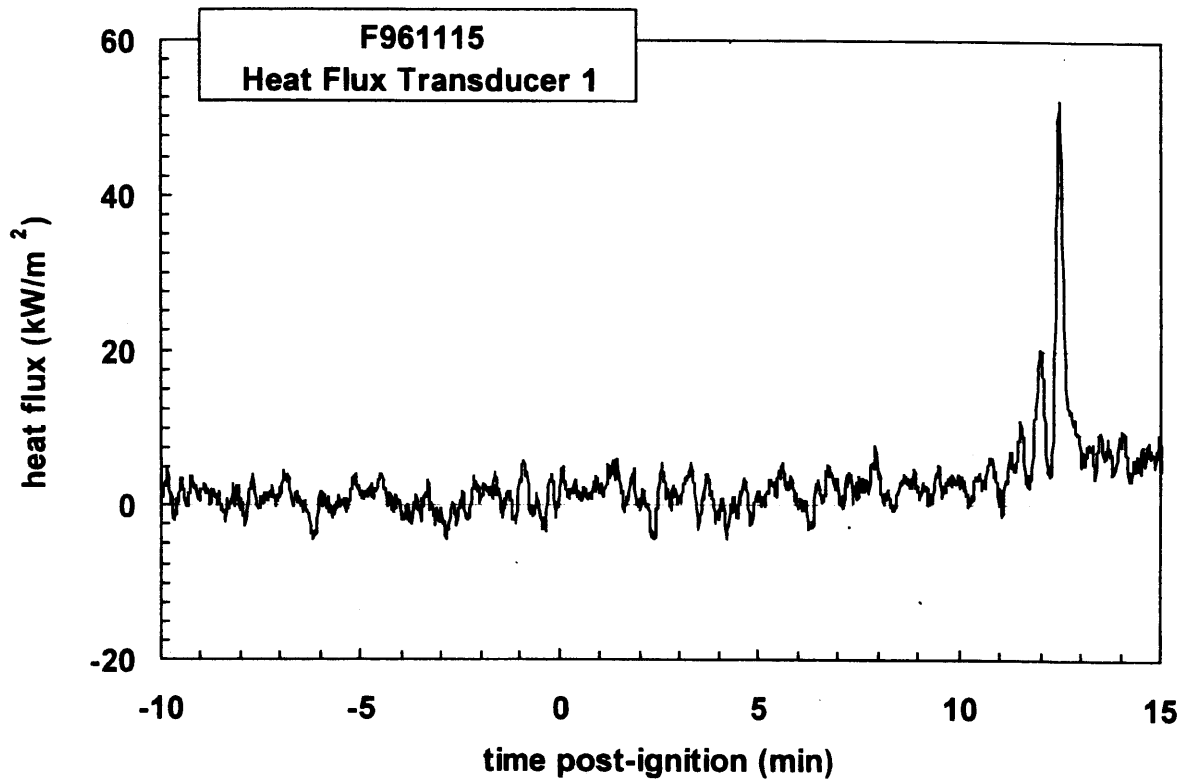
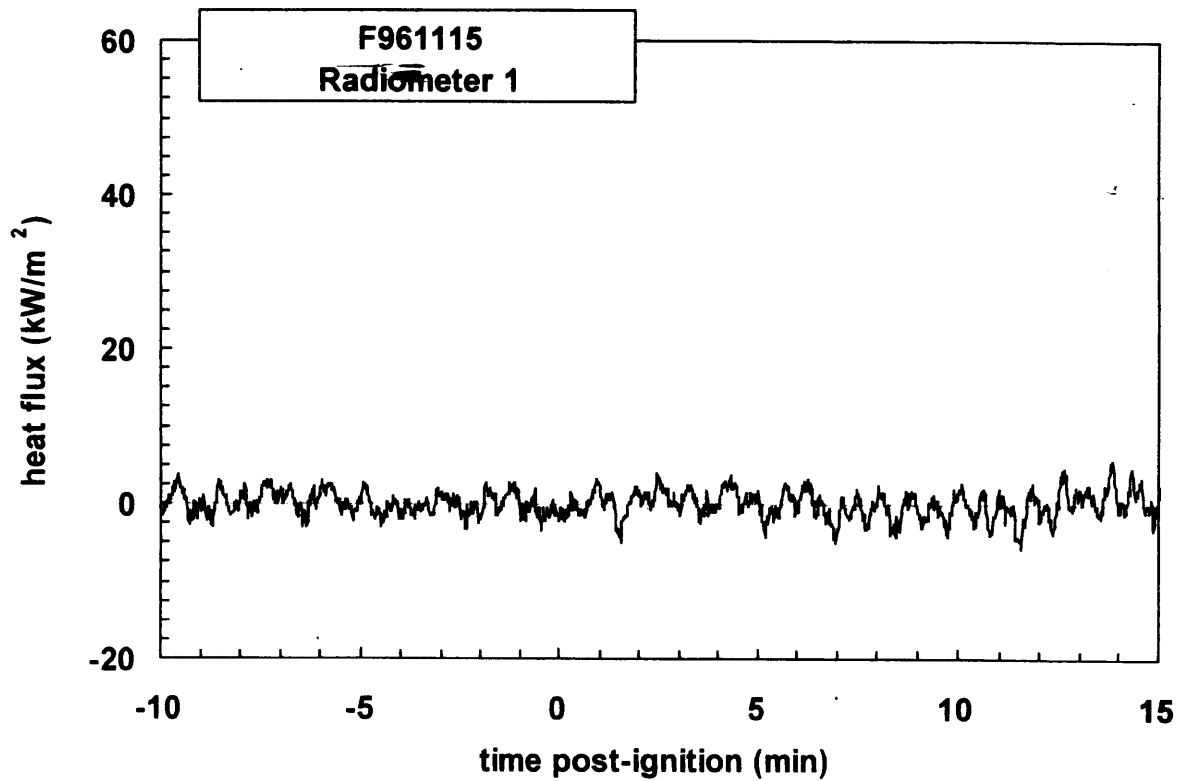


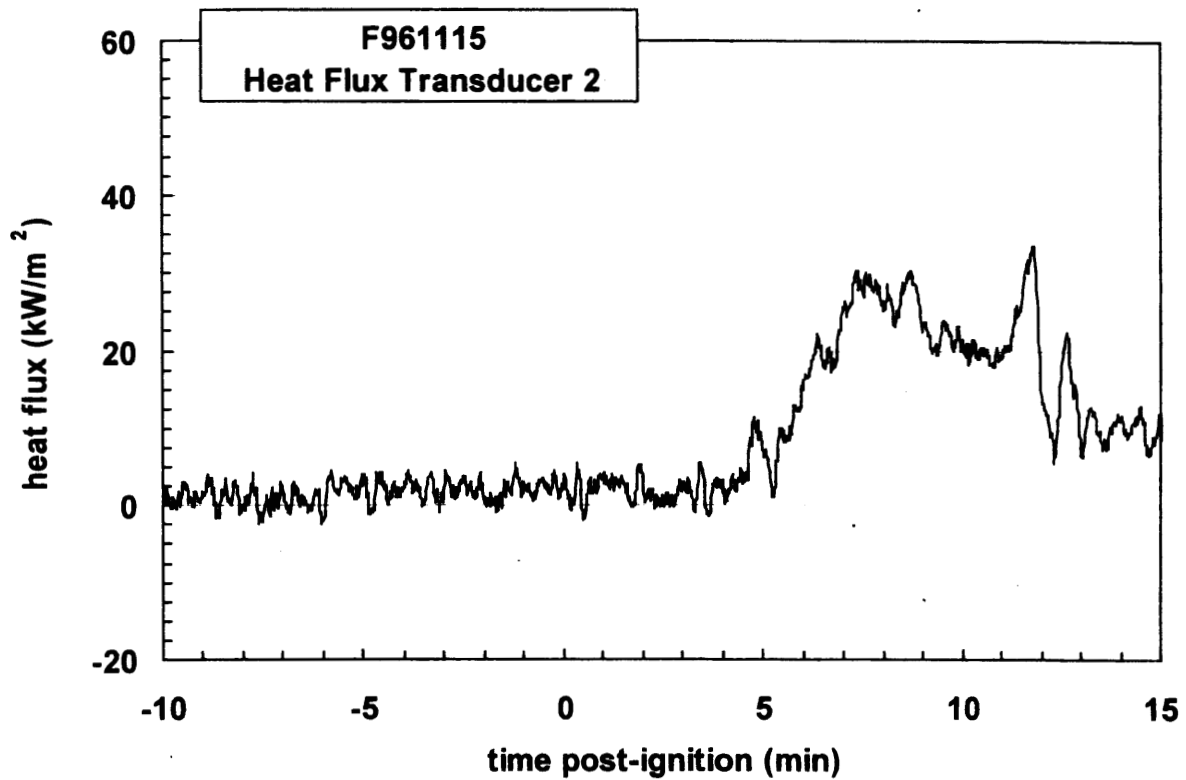
Figure E1. Fire Test F961115. Interior view of the front of the test vehicle showing the approximate locations of heat flux transducer/radiometer (HFT) assemblies in the dash panel. HFT assemblies #1, #2, #3, #4, and #6 extended through the dash panel and engine compartment dash panel silencer pad into the engine compartment, so that each transducer measured heat transfer from the engine compartment to the exterior face of the dash panel silencer pad. HFT assembly #5 was located in the HVAC air intake duct under the instrument panel support deck and directly rearward of the battery and power distribution center.



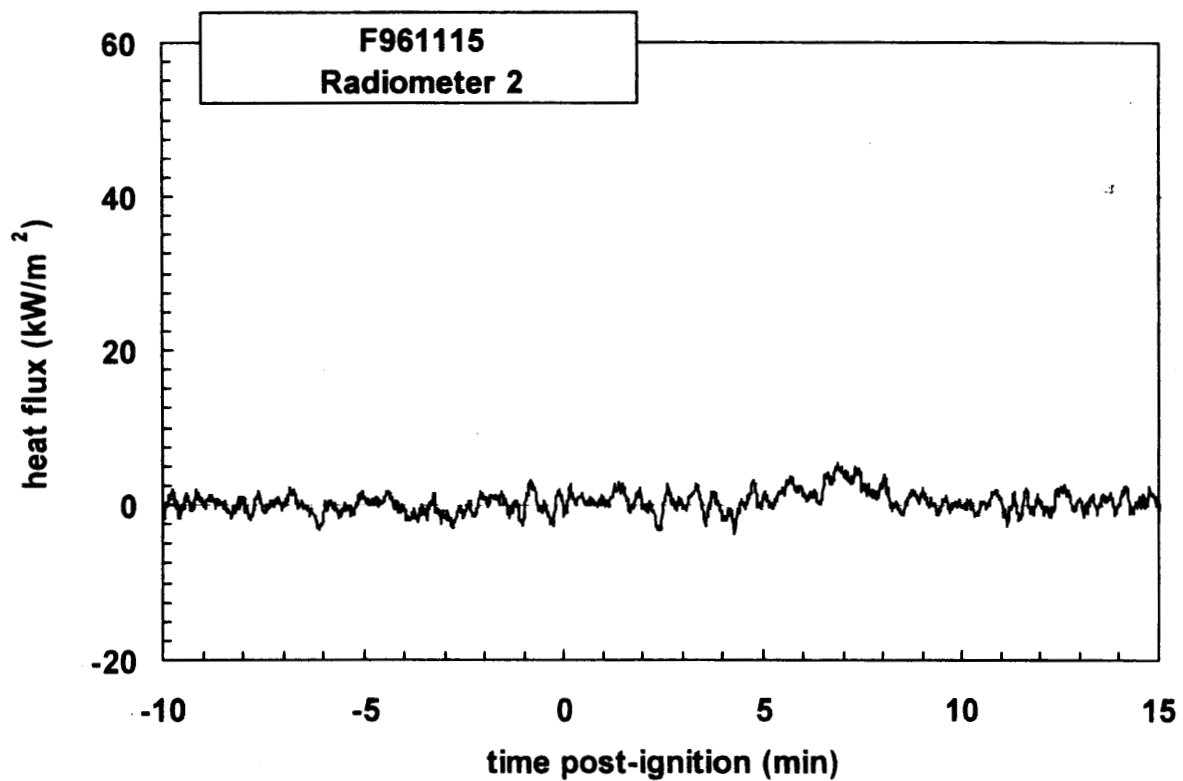
Plot E1. Fire Test F961115. Data plot from Heat Flux Transducer 1.



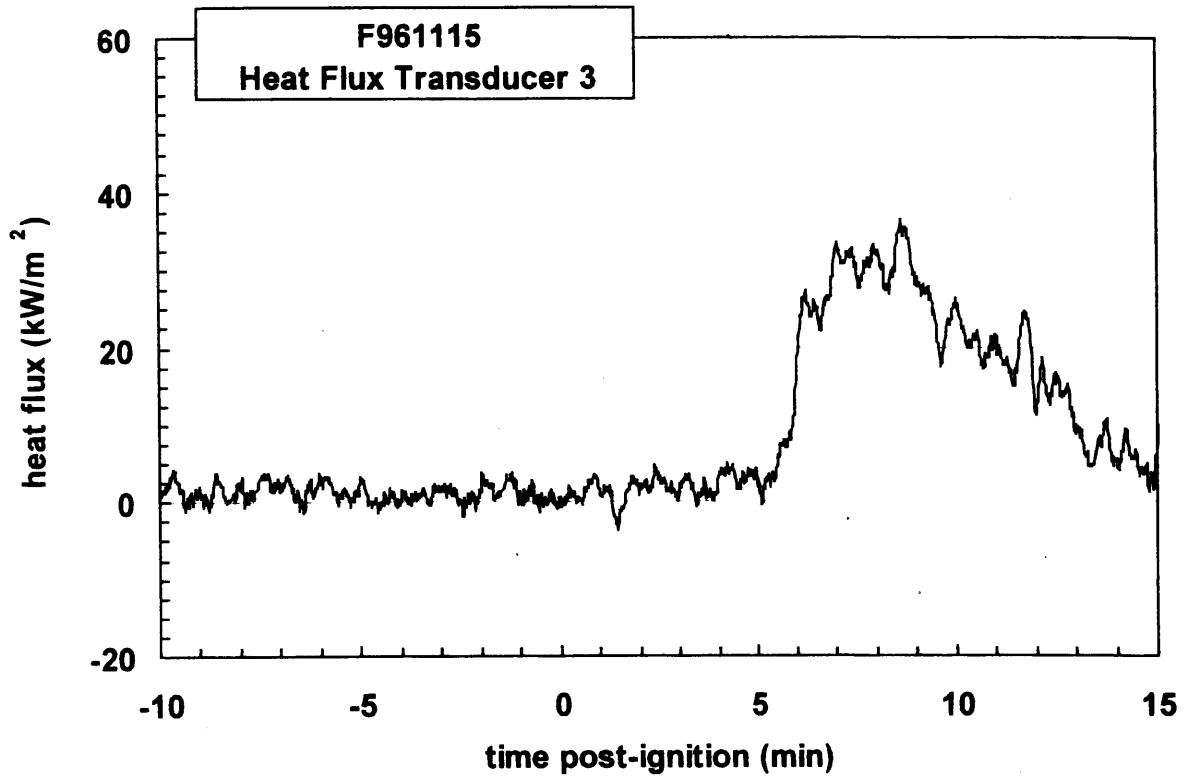
Plot E2. Fire Test F961115. Data plot from Radiometer 1.



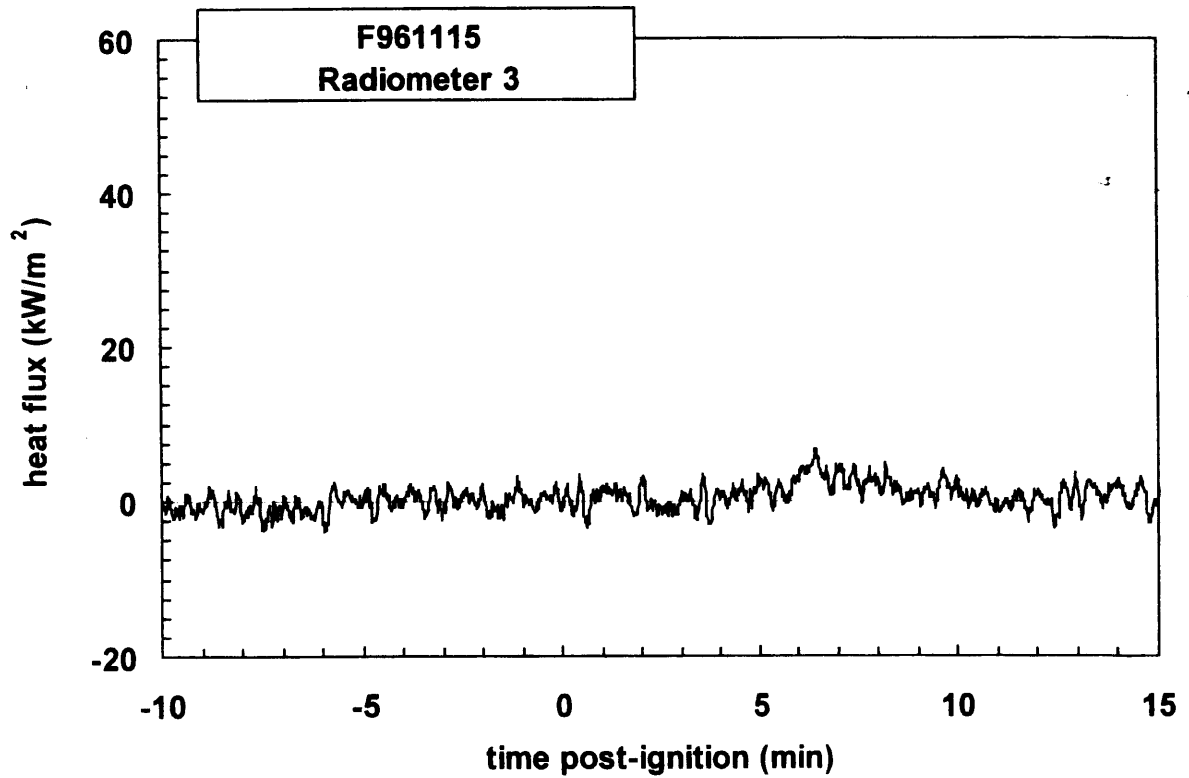
Plot E3. Fire Test F961115. Data plot from Heat Flux Transducer 2.



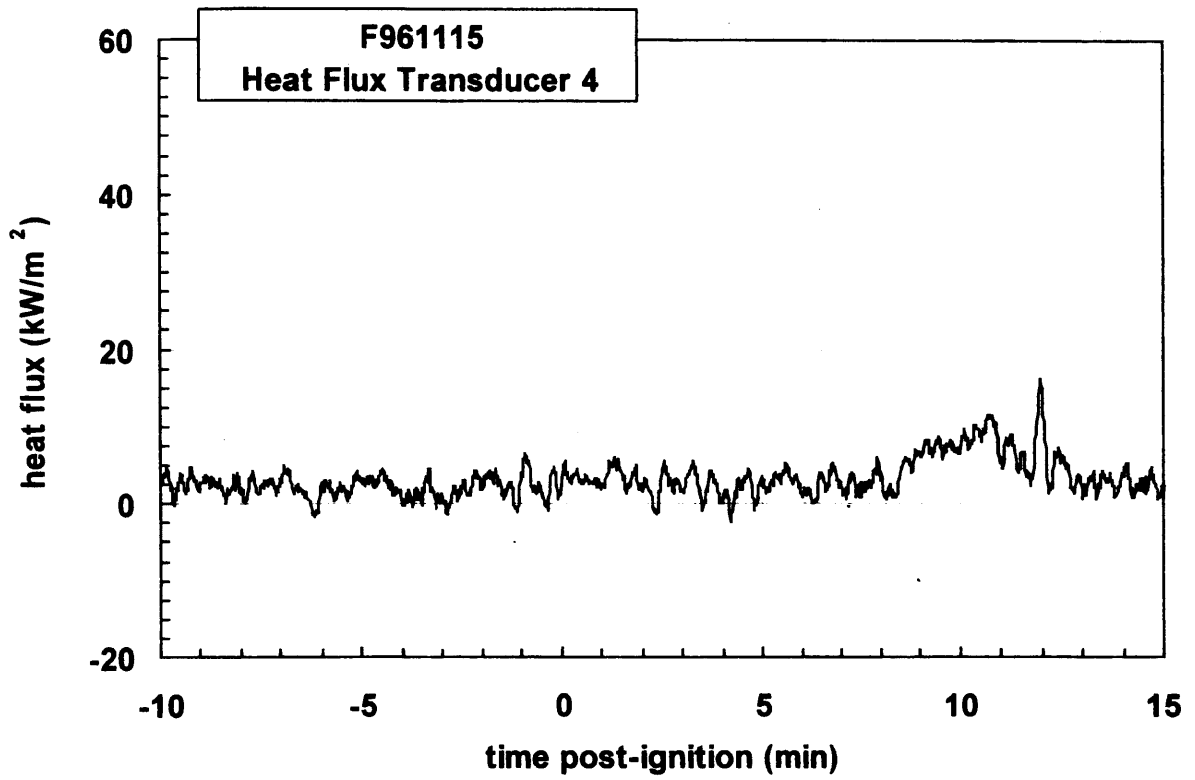
Plot E4. Fire Test F961115. Data plot from Radiometer 2.



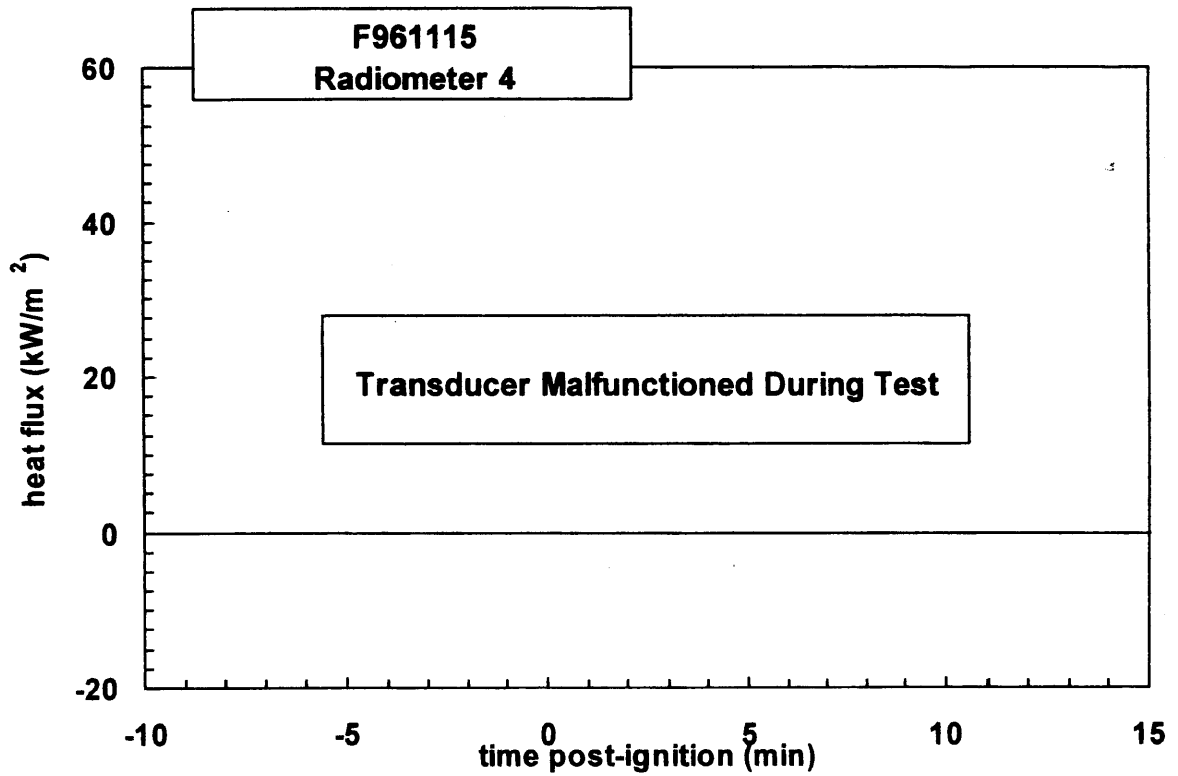
Plot E5. Fire Test F961115. Data plot from Heat Flux Transducer 3.



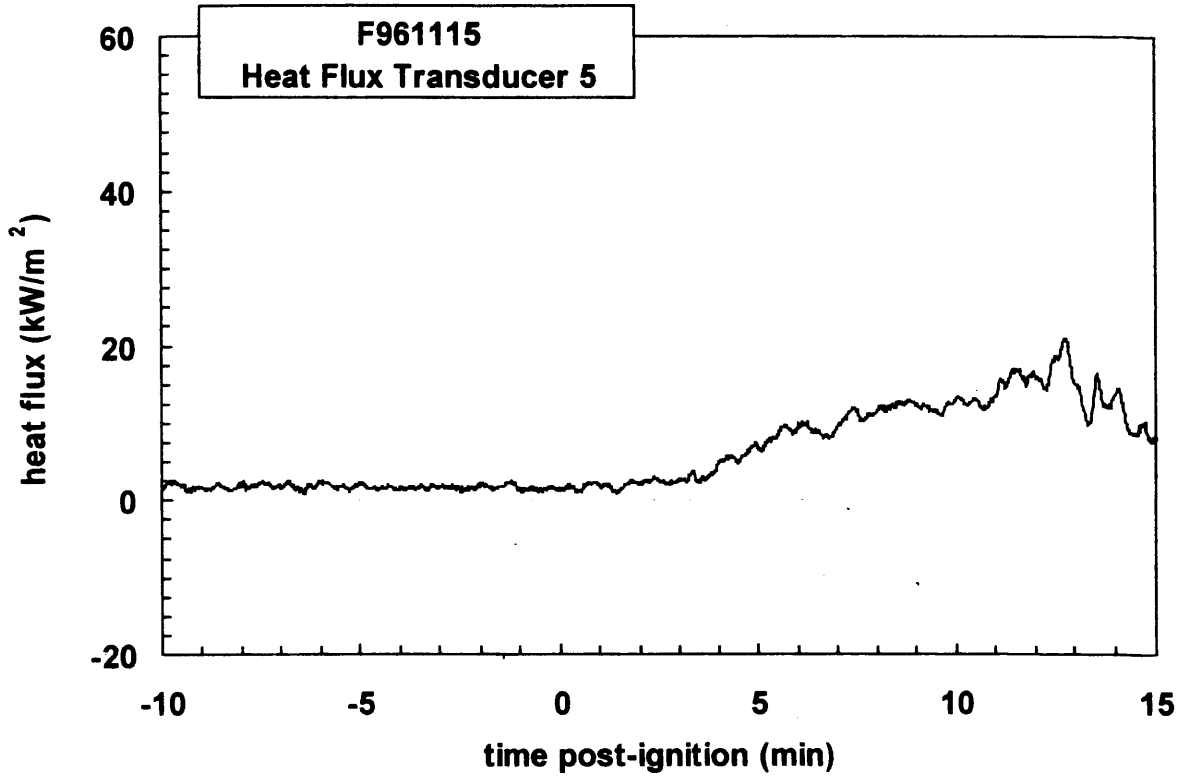
Plot E6. Fire Test F961115. Data plot from Radiometer 3.



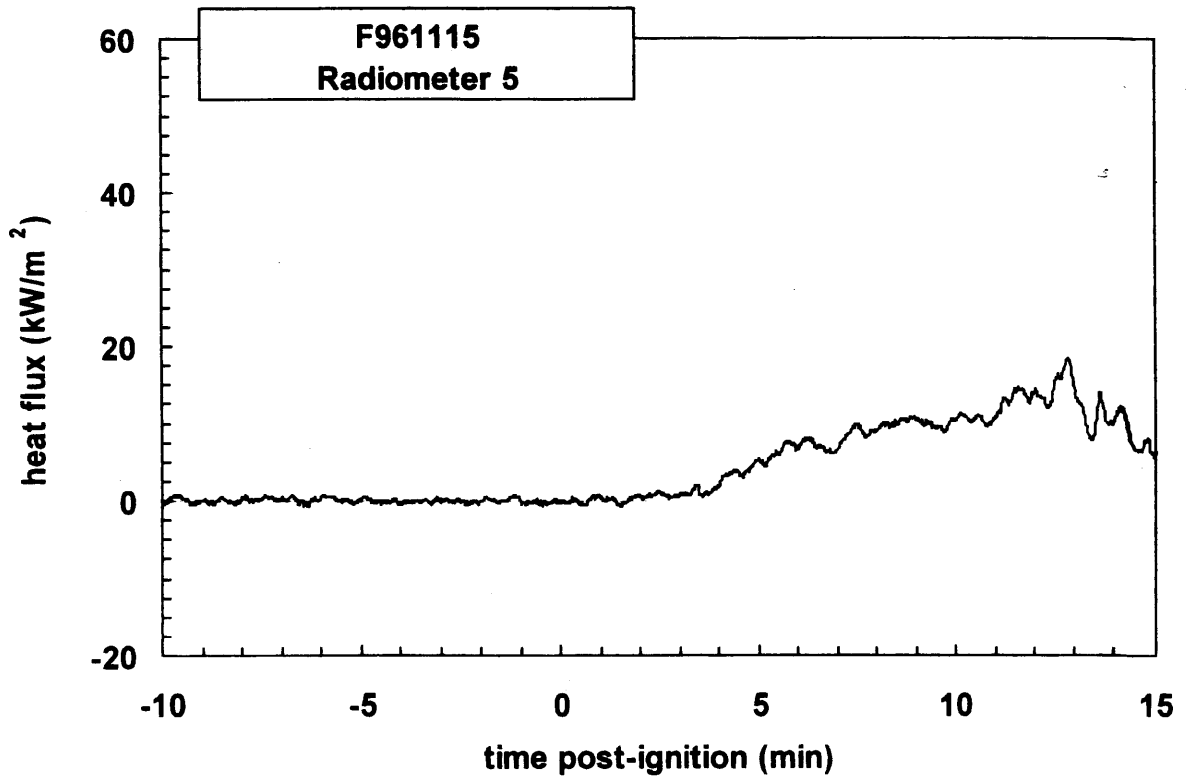
Plot E7. Fire Test F961115. Data plot from Heat Flux Transducer 4.



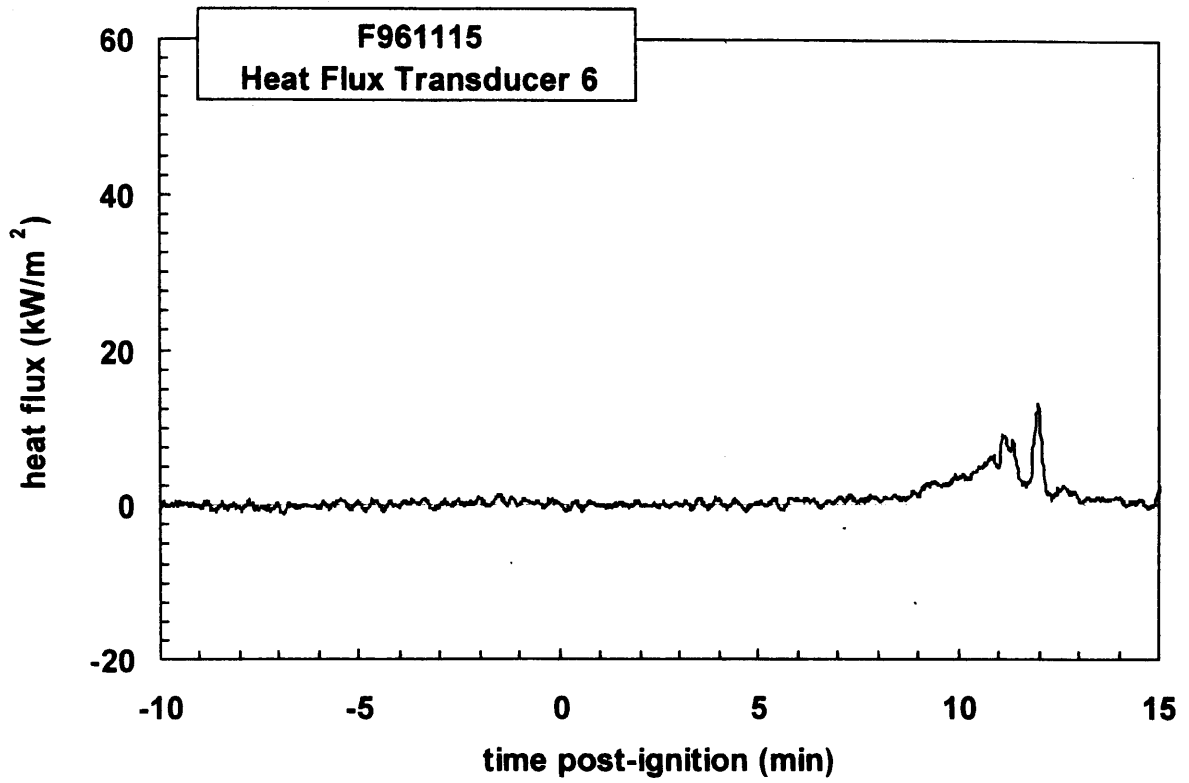
Plot E8. Fire Test F961115. Data plot from Radiometer 4.



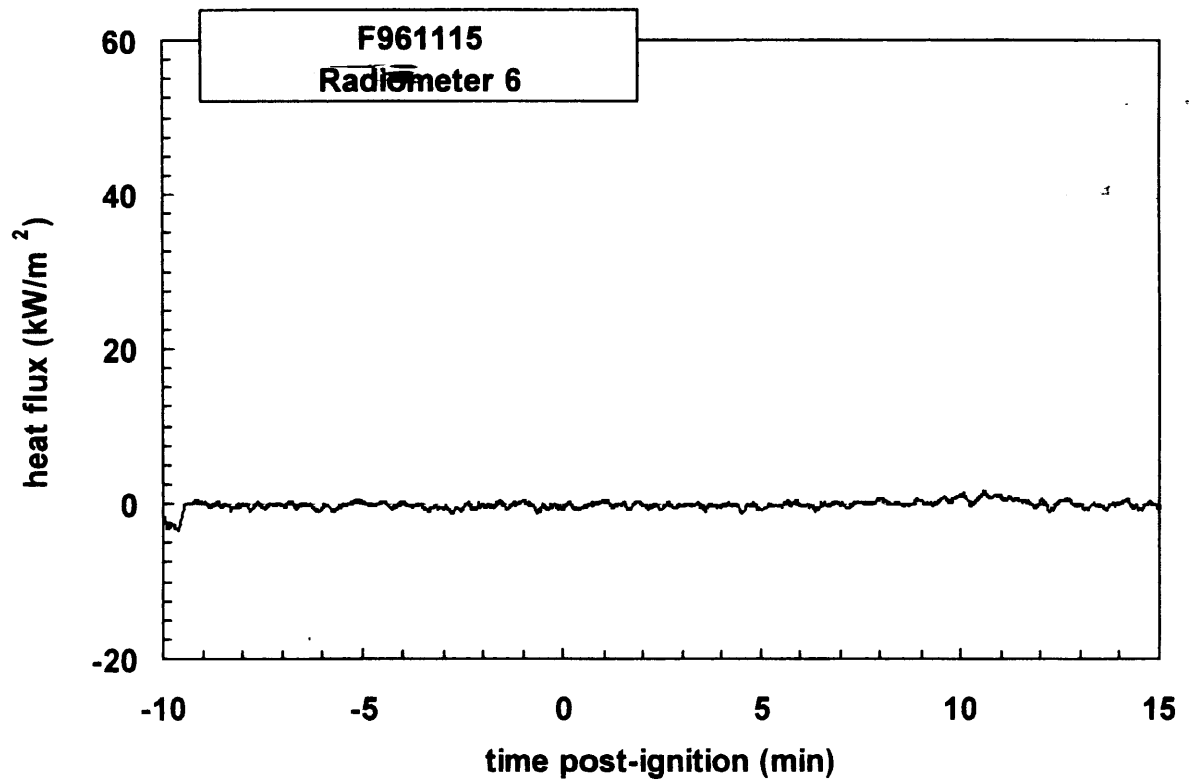
Plot E9. Fire Test F961115. Data plot from Heat Flux Transducer 5.



Plot E10. Fire Test F961115. Data plot from Radiometer 5.



Plot E11. Fire Test F961115. Data plot from Heat Flux Transducer 6.



Plot E12. Fire Test F961115. Data plot from Radiometer 6.

**APPENDIX F  
PRESSURE AND FLOW DATA**

Air pressure was measured at the exterior- and interior-surfaces of the dash panel. Figures F1 and F2 show the approximate locations of the pressure tapes on the dash panel of the test vehicle.

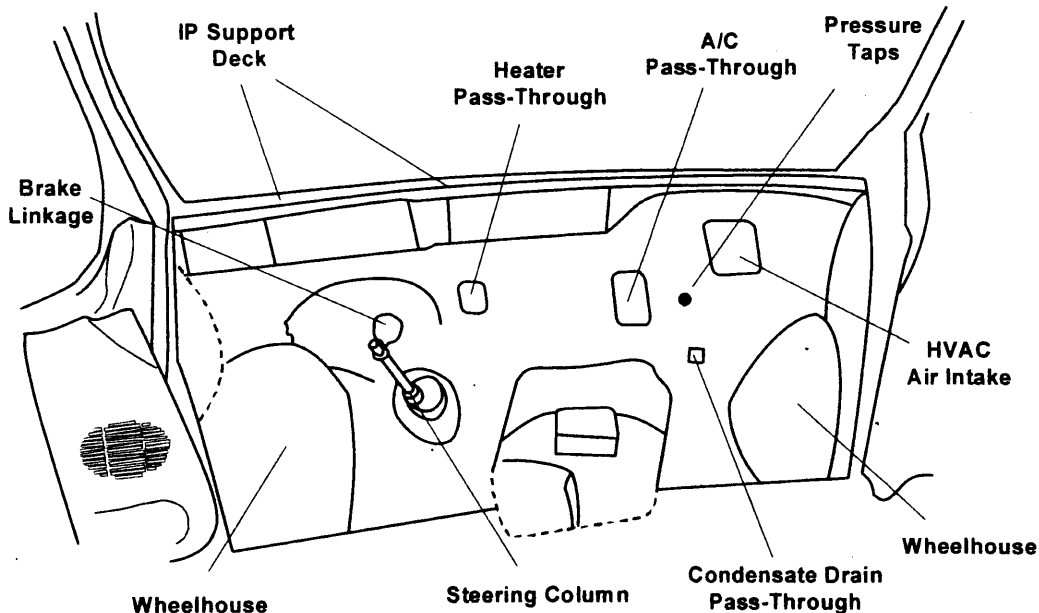


Figure F1. Fire Test F961115. View inside of the dash panel of the test vehicle showing the approximate locations of the pressure tapes relative to the A/C pass-through and HVAC air intake.

The pressure taps consisted of two section of stainless steel tubing (o.d. = 0.250 in.). One end of each of tubing contained a union-T fitting with compression-type couplings (Swage Union-T). The end of one section of tubing containing the union-T fitting was located on the interior surface of the dash panel. The other section of tubing was inserted through a hole drilled in the dash panel so that the union-T fitting was adjacent to the surface of the engine compartment dash panel silencer pad. Each pressure tap was connected to pressure gauges (Model C-264, Setra Systems, Acton, MA) with solvent-resistant flexible tubing (Tygon Masterflex® 6049; i.d. = 0.250 in.; o.d. = 0.438 in.) as shown in Figure F2. The total length of each pressure sampling line was approximately 10 m.

Pressure gauges with two pressure ranges were used for this test: - 0.5 to 0.5 ( $\pm 0.0013$ ) in. W.C. (-124.5 to 124.5 Pascal) and -0.1 to 0.1 ( $\pm 0.0003$ ) in. W. C. (-24.9 to 24.9 Pascal). Both gauges were accurate to 0.25% full scale. The gages were powered with a 24 volt non-regulated power supply (Setra Systems). The low- and high-range gages (P2 and P6, respectively) were connected in parallel to provide duplicate pressure measurement of the differential pressure

across the dash panel. The low range gauge was used to maximize the sensitivity for measuring small pressure differences across the dash panel. The high range gauge was used to increase the dynamic range of the measurement in case the pressure difference across the dash panel exceeded 25 pascal. Pressure gauges P1 and P7 were high range pressure gauges used to measure static pressure at the interior- and exterior surfaces of the dash, respectively. The low-pressure inputs of P1 and P7 were left open to the atmosphere to provide a common reference pressure during the test.

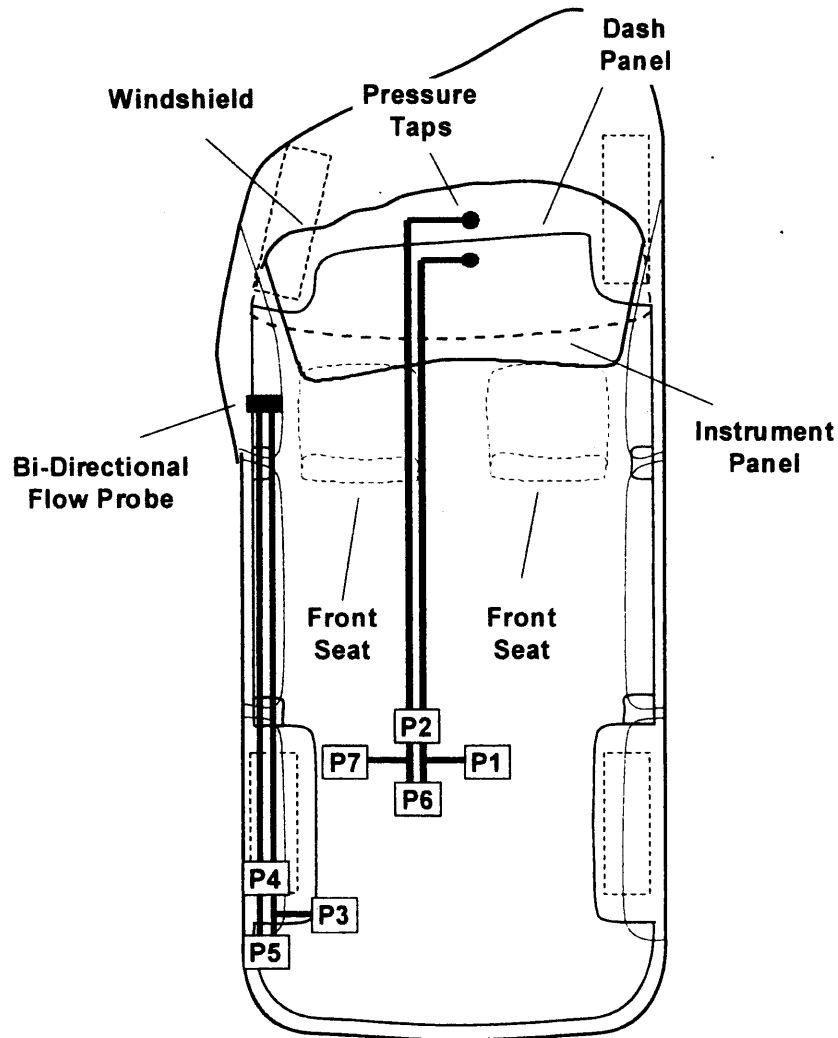


Figure F2. Fire Test F961115. Top view of test vehicle showing the approximate locations of the pressure taps on the dash panel and the bi-directional probe in the driver's window. Pressure gauges P2 and P6 measured the pressure difference across the dash panel. Pressure gauges P1 and P7 measured the pressure at the inner- and outer-surfaces of the dash panel, respectively, relative to atmospheric pressure. Atmospheric pressure was measured at a height of approximately 1 m above the floor of the test facility and about 5 m from the vehicle.

The velocity and direction of gas flow through the open window in the driver's door (the glass was broken in the crash test) was measured using a bi-directional flow probe (Fig.'s F2 and F3).

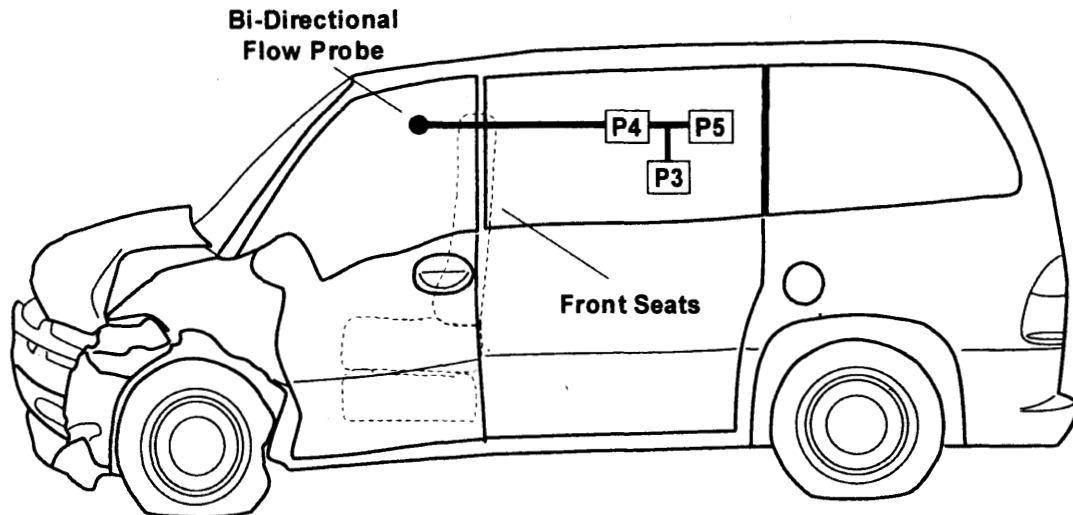


Figure F3. Fire Test F961115. Side view of test vehicle showing the approximate location of the bi-directional flow probe in the driver's side window. Pressure gauges P4 and P5 measured the pressure difference across the probe. Pressure gauge P3 measured the pressure at the inside of the bi-directional probe relative to atmospheric pressure. Atmospheric pressure was measured at a height of approximately 1 m above the floor of the test facility and about 5 m from the vehicle.

The bi-directional flow probe was centered horizontally and approximately 10 cm below the upper edge of the opening. The outlets of the pressure taps in the flow probe were connected to pressure gauges with solvent-resistant flexible tubing (Tygon Masterflex<sup>®</sup> 6049; i.d. = 0.250 in.; o.d. = 0.438 in.) as shown in Figures 2 and 3. The total length of tubing was approximately 10 m. Low- and high-range gages (P4 and P5, respectively) were connected in parallel to provide duplicate pressure measurements of the pressure difference across the bi-directional flow probe. Pressure Gauge P3 was a low-range gauge connected to the pressure tap on the interior side of the bi-directional flow probe. The low pressure input of this gauge was left open to atmosphere and was used to measure static pressure just inside the upper section of the window opening in the driver's door.

The velocity of gas flow through the window opening in the driver's door was calculated from the pressure difference measured across the bi-directional probe using the following relationship:

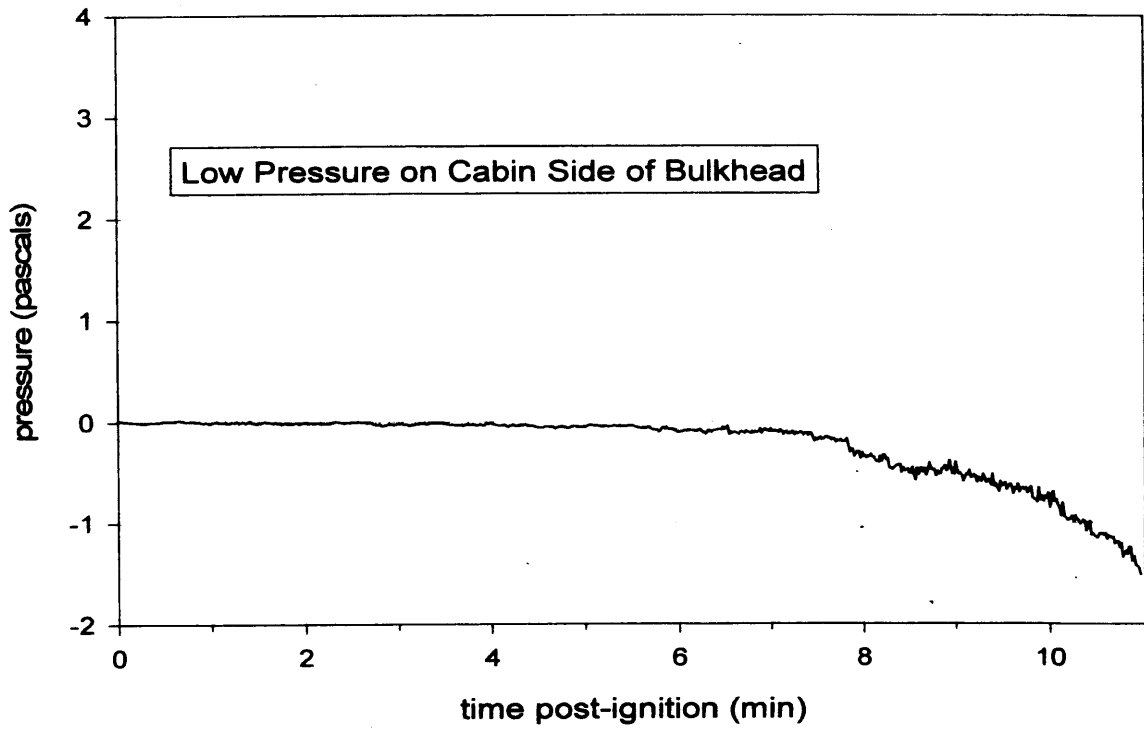
$$V = 0.070\sqrt{T\Delta p} \quad (F1)$$

where  $V$  is the gas velocity in m/s,  $T$  is the gas temperature in degrees Kelvin, and  $\Delta p$  is the pressure difference in Pascals ( $\text{N/m}^2$ ) [F1 and F2].

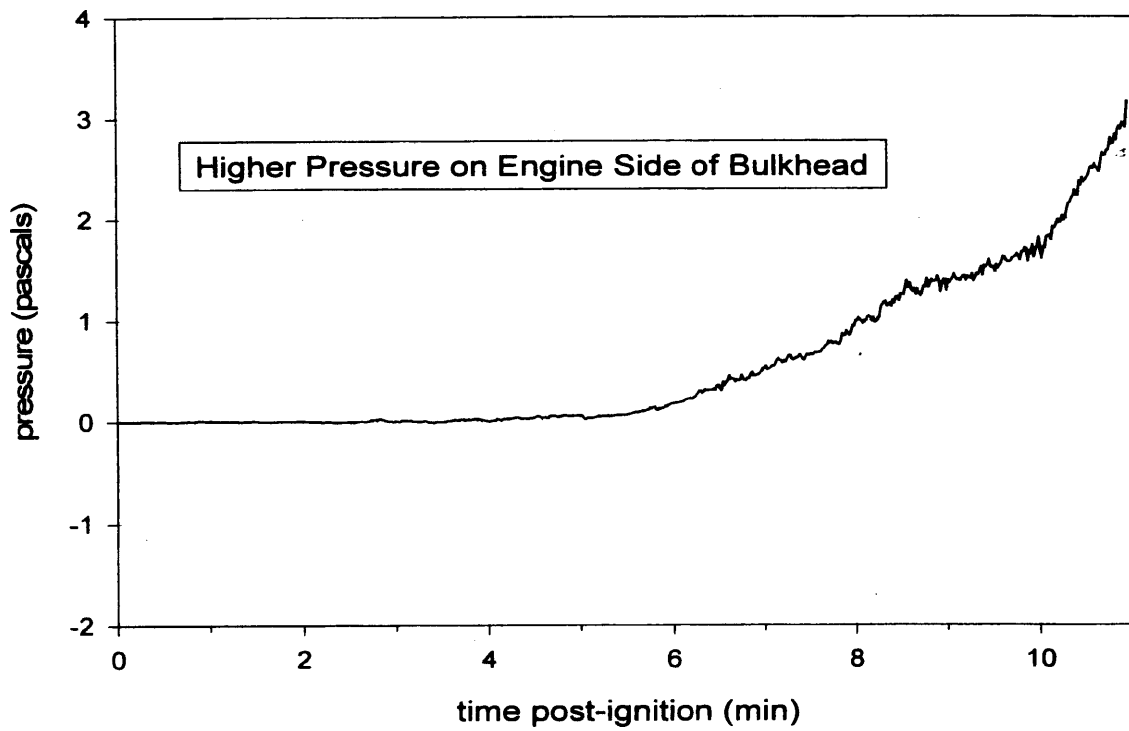
A PC-based data system was used to acquire data from these transducers during this test. The signal leads from the pressure transducers were connected to a low-gain analog-input multiplex expansion card (DBK12, IOtech) interfaced to a 16-bit, 100 kHz I/O board with 16 analog input channels (DaqBoard 200A, IOtech). The data acquisition software (DaqView Software version 4.10, IOtech) was configured to sample each channel at a rate of 100 Hz and store the data in 100-point block-averages.

#### REFERENCES

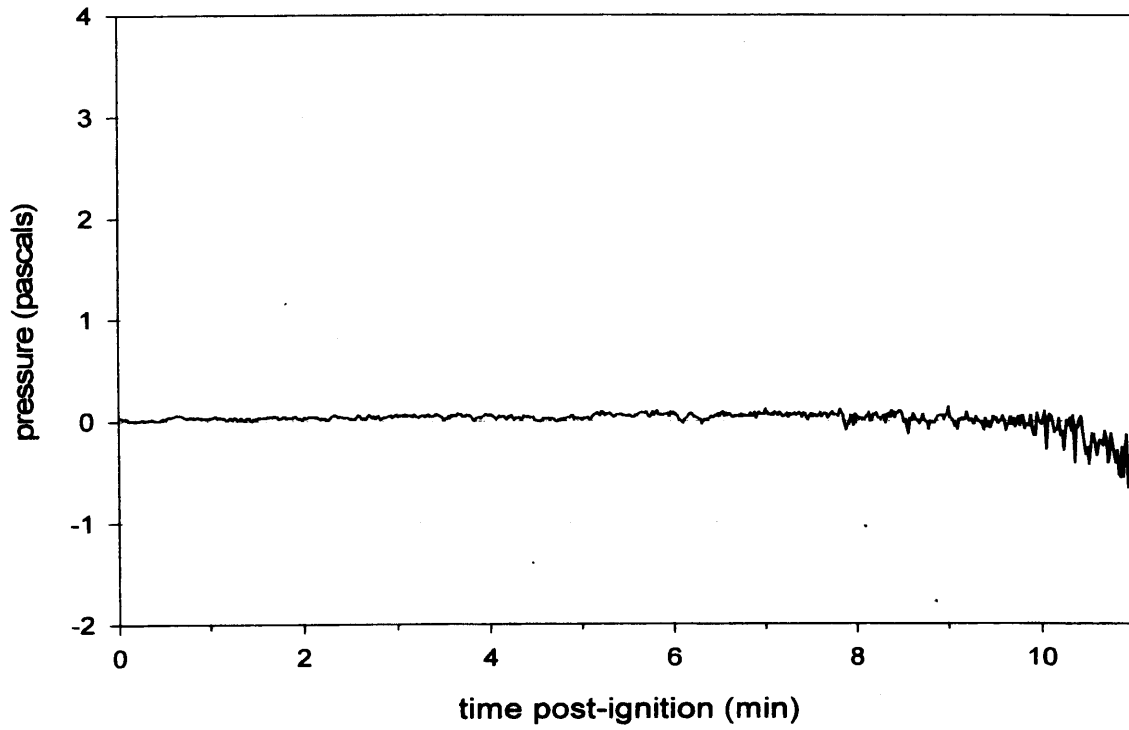
- F1. N. R. Keltner and J. L. Moya. Defining the thermal environment in fire tests. *Fire and Materials* **14**: 133-138, 1989.
- F2. B. J. McCaffrey and G. A. Heskestad. Robust bidirectional low-velocity probe for flame and fire application. *Combustion and Flame* **26**: 125-127, 1976.



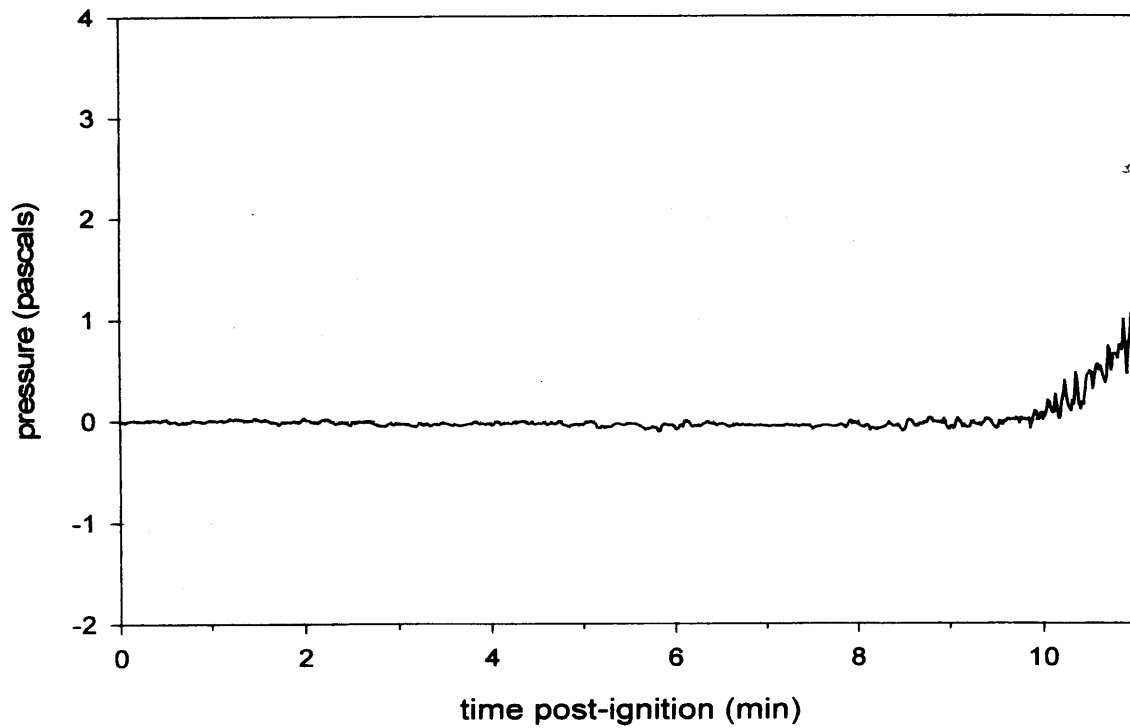
Plot E1. Fire Test F961115. Pressure at the interior face of the dash panel relative to atmosphere measured with P1.



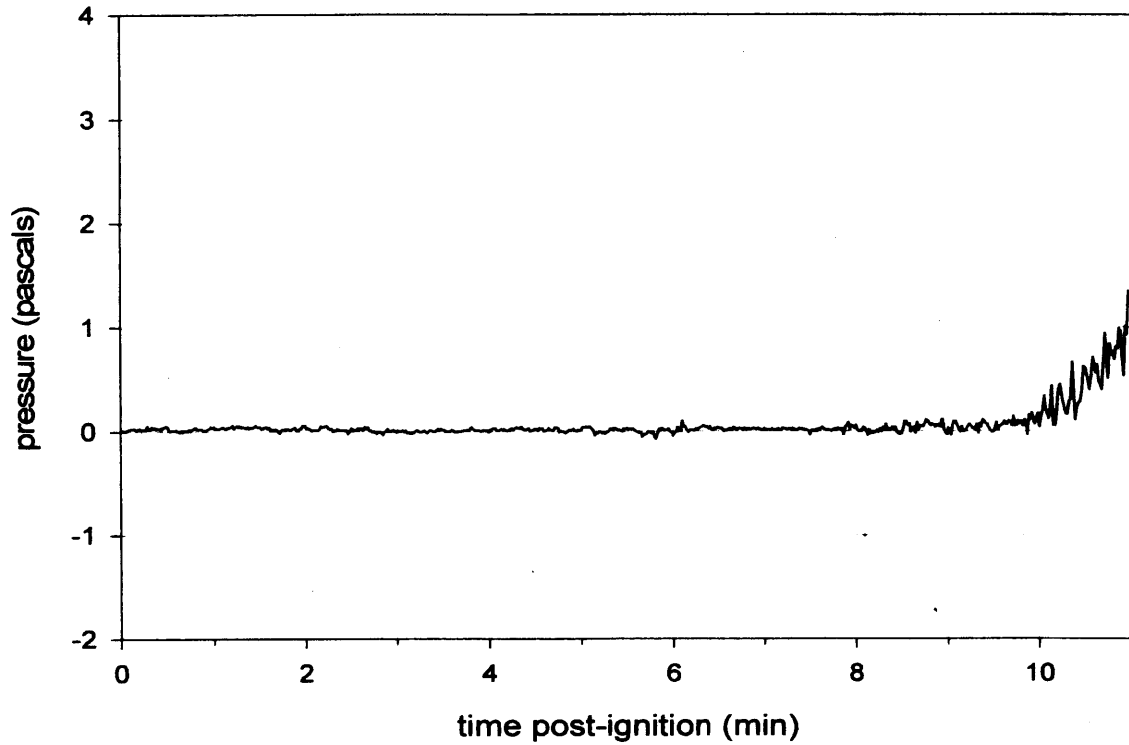
Plot E2. Fire Test F961115. Differential pressure across the dash panel measured with P2.



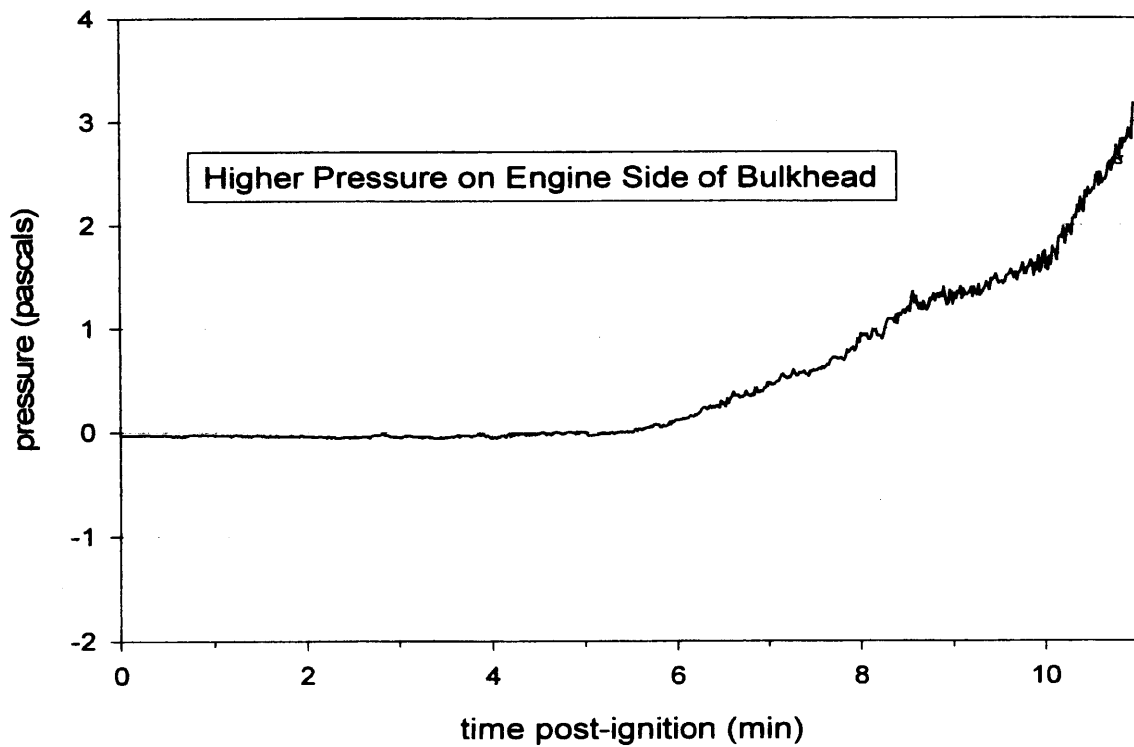
Plot E3. Fire Test F961115. Pressure relative to atmospheric air pressure measured at P3.



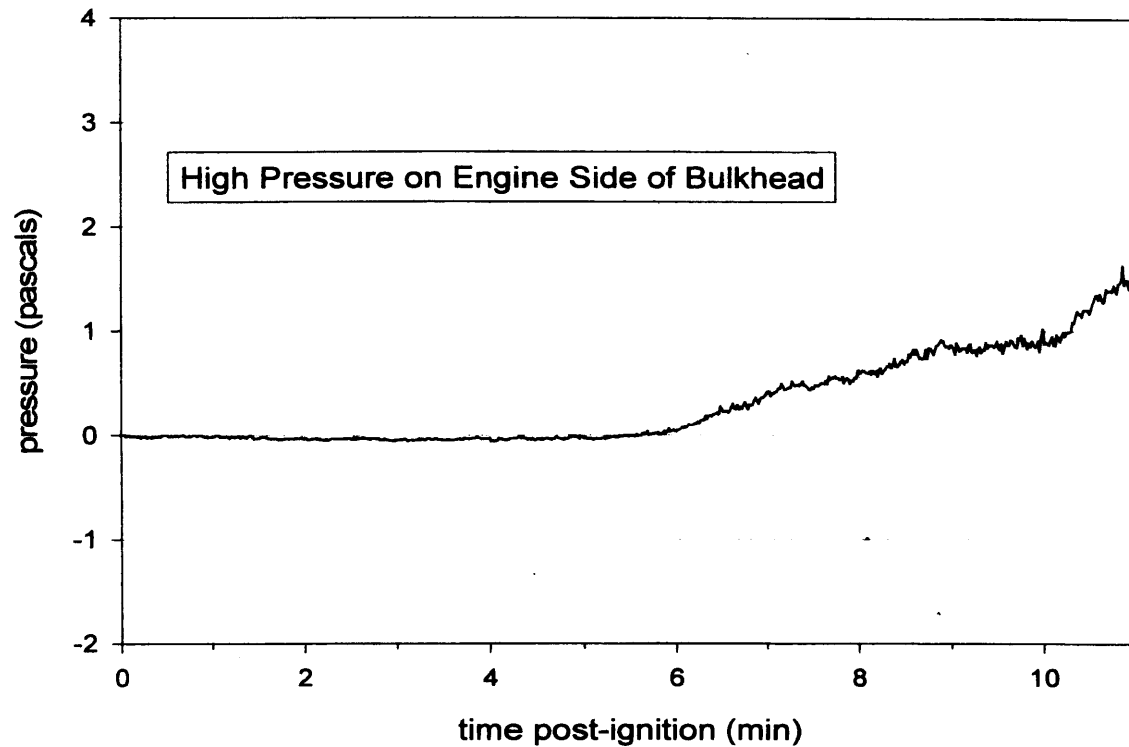
Plot E4. Fire Test F961115. Differential pressure across the bi-directional probe measured with P4.



Plot D5. Fire Test F961115. Differential pressure across the bi-directional probe measured with P5.



Plot E6. Fire Test F961115. Differential pressure across the dash panel measured with P6.



Plot E7. Fire Test F961115. Pressure at the exterior face of the dash relative to atmosphere measured with P7.

**APPENDIX G**  
**DIRECTIONAL FLAME THERMOMETER MEASUREMENTS,**  
**TIME-COMPENSATED ASPIRATED THERMOCOUPLE MEASUREMENTS,**  
**AND ESTIMATED HEAT FLUXES**

Directional Flame Thermometers (DFT) (also known as slug calorimeters) were used to measure convective and radiative heat transfer [A6 and A7] to six locations in the passenger compartment. These devices were made by intrinsically welding a Type-K thermocouple (30 AWG, o.d. = 0.16 cm) to the unexposed side of a stainless steel disk (diameter = 2.54 cm; thickness = 0.06 cm). The unexposed side of the disk containing the intrinsically welded thermocouple was then insulated with 0.3 cm Fiberfrax paper (Carborundum Co., Niagara Falls, NY) and backed with another stainless steel disk. The exposed side of the DFT was coated with high temperature optical black coating with an absorptance of 0.92 from 0.5 to 20  $\mu\text{m}$  (Medtherm Corp., Huntsville, AL). The thermocouple lead was enclosed in a stainless steel sheath and insulated with magnesium oxide. Refer to Figures G1 and G2 for the locations of the DFTs in the test vehicle.

Directional Flame Thermometers are passive devices that respond to both radiative and convective heating. The response-time of these devices was considerably longer than that of the water-cooled heat flux transducers described above. Radiative heat flux to the DFT was estimated from the first derivative of the temperature curve of the DFT. Convective heat flux to the DFT was estimated from the air temperature measured by the aspirated thermocouple probe. The use of the derivative in these calculations magnifies noise in the DFT-signal, therefore, an auto-recursive-moving-average (5 points) low pass filter was used to reduce electronic noise in the DFT signals. The first derivative of the filtered DFT-signal was calculated using the Lagrangian method with 5 data points. The hot wall heat flux is given by the following relationship:

$$q_h = \rho \cdot C_p \cdot \delta \cdot \frac{dT}{d\tau} \quad (G1)$$

where  $q$  is the heat flux in  $\text{kW/m}^2$ ;  $\rho$  is the density of the metal disc in  $\text{kg/m}^3$ ;  $\delta$  is the thickness of the metal disc in m;  $C_p$  is the specific heat of the metal disc in  $\text{J/kg}\cdot\text{K}$ ; and  $dT/d\tau$  is the rate of temperature rise on the back disc in  $\text{K/s}$ . The heat flux was cold-wall corrected using a linearized radiation heat transfer coefficient obtained from calibration experiments.

$$q_c = \kappa_c \cdot (T_i - T_o) \quad (G2)$$

The natural convection coefficient for cooling ( $\kappa_c$ ) was calculated using the software "One Minute Convection", Genium Publishing Corp. to be  $11 \text{ W/}[\text{m}^2\cdot\text{K}]$ . The radiative emission from the DFT is:

$$q_r = \sigma \cdot \varepsilon \cdot (T_i^2 + T_o^2) \cdot (T_i + T_o) \cdot (T_i - T_o) \quad (G3)$$

where  $\sigma$  is the Stefan-Boltzmann constant of  $5.67 \times 10^{-8} \text{ W}/[\text{m}^2 \cdot \text{K}^4]$ ,  $\varepsilon$  is the emissivity of the DFT surface (0.92) and temperatures are in Kelvin. The cold-wall corrected heat flux is:

$$q_t = q_h + q_r + q_c \quad (G4)$$

where  $q_h$  is the measured hot wall heat flux,  $q_r$  is the correction for radiative emission and  $q_c$  is the correction for convective heat loss from the DFT.

Six directional flame thermometers (DFT) were positioned in the passenger compartment to measure heat fluxes to the front occupant positions in the test vehicle during this fire test (Fig.'s G1 and G2).

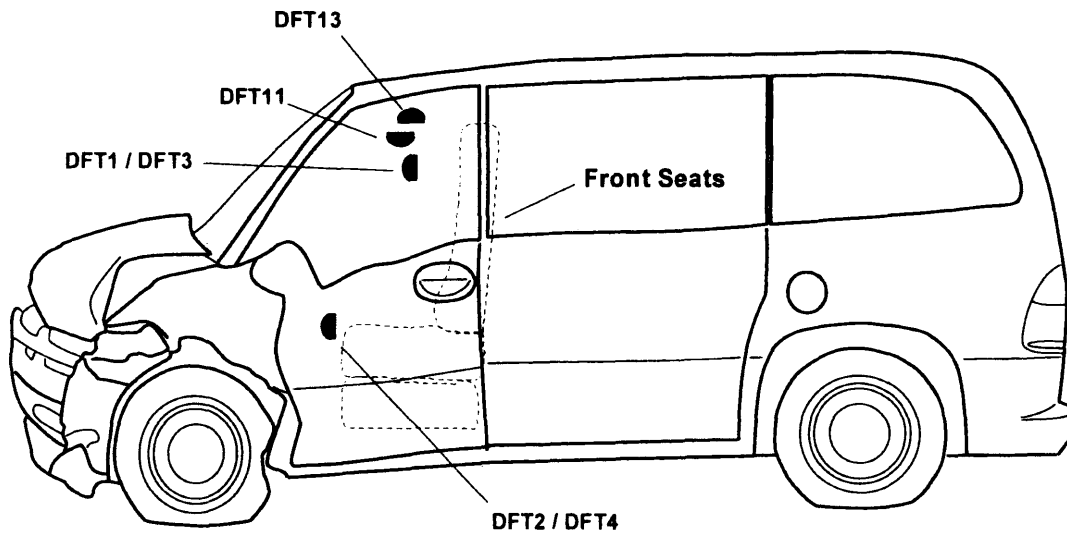


Figure G1. Fire Test F961115. Side view of the test vehicle showing the approximate locations of the DFT's in the passenger compartment. The blue surface is the heat-absorbing front of the DFT. The black surface is the insulated back of the DFT.

DFT1 and DFT3 were located above the front passenger's and driver's seats, respectively, and were facing forward. DFT 2 and DFT4 were located just in front of the seat cushions in the front passenger's and driver's seats, respectively, and were facing forward. DFT11 was located between the driver's and front passenger's seats and was facing upward. DFT13 was located between the driver's and front passenger's seats and was facing downward.

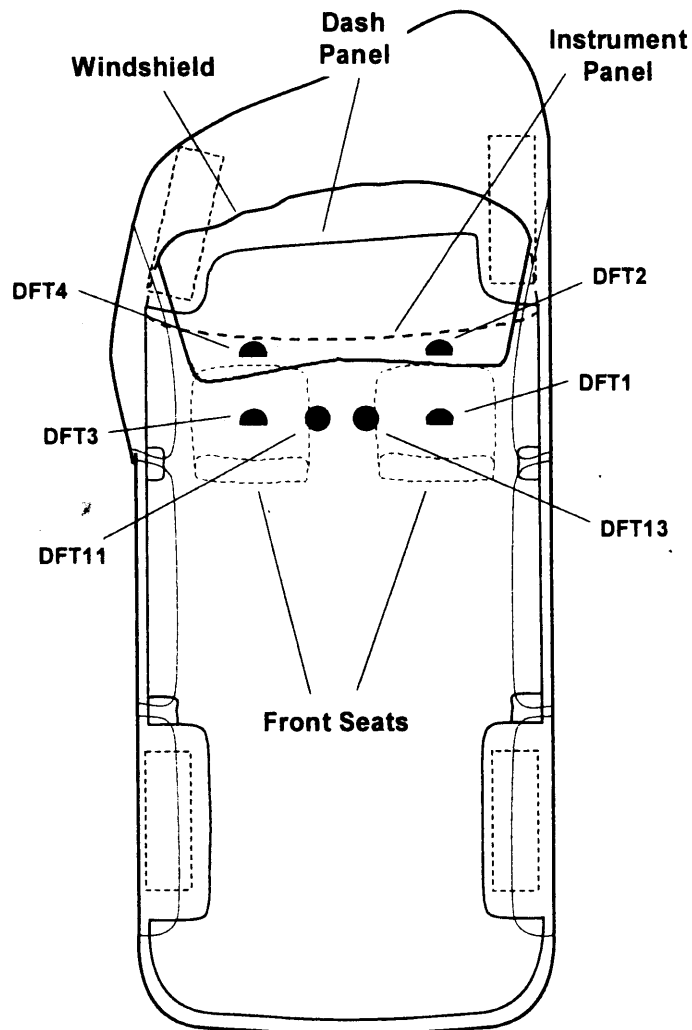
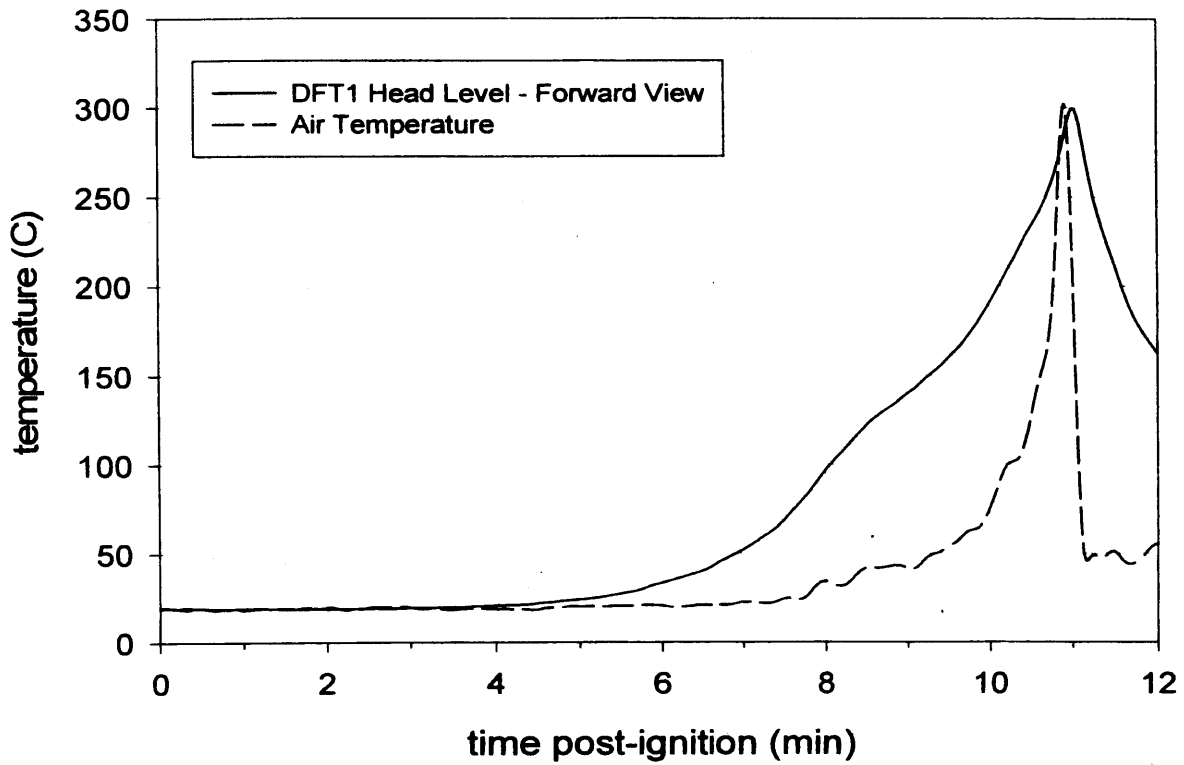


Figure G2. Fire Test F961115. Top view of the test vehicle showing the approximate locations of the DFT's in the passenger compartment. The blue surface is the heat-absorbing front of the DFT and the black surface is the insulated back of the DFT.

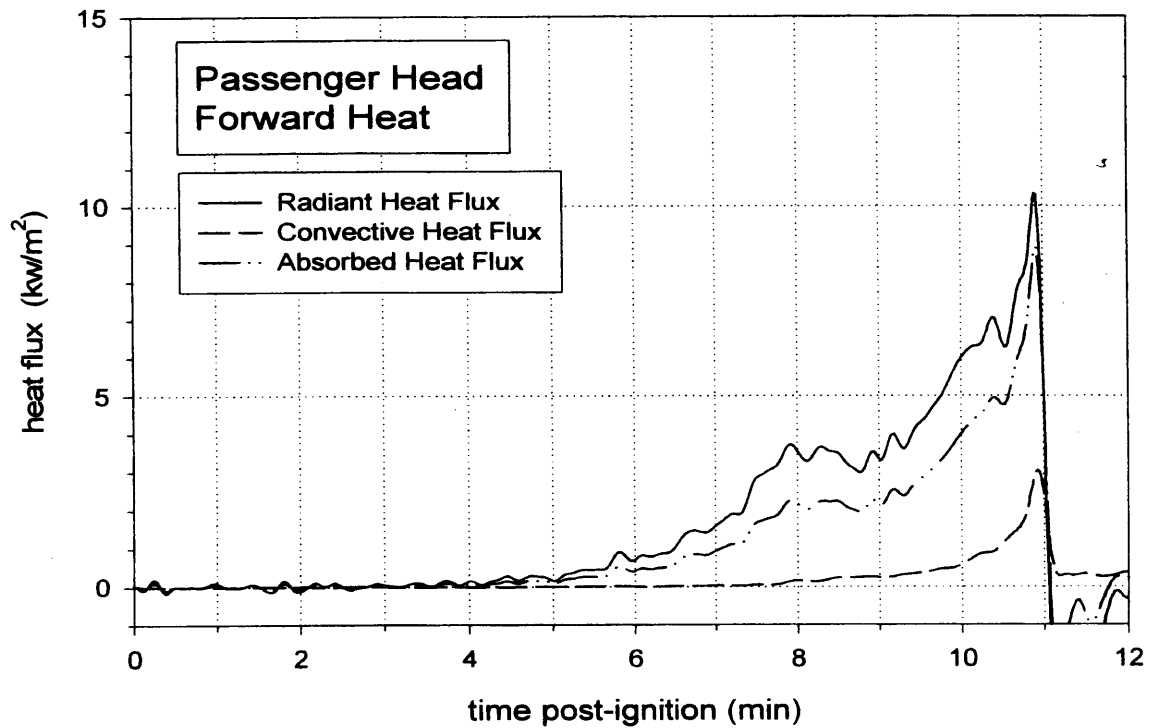
A PC-based data system was used to acquire data from these transducers during this test. The signal leads from the DFT's were connected to a thermocouple multiplex expansion card (DBK-19, IOtech) interfaced to a 16-bit, 100 kHz I/O board with 16 analog input channels (DaqBoard 200A, IOtech). The data acquisition software (DaqView Software version 4.10, IOtech) was configured to sample each channel at a rate of 100 Hz and store the data in 100-point block-averages.

Plots G1, G3, G5, G7, G9, and G11 show the temperatures recorded by DFT1, DFT2, DFT3, DFT4, DFT11, and DFT13, respectively. The temperature recorded by each DFT and the air temperatures around each DFT (estimated from the temperatures recorded by the aspirated thermocouples) were used to estimate the convective and radiative heat fluxes to each DFT. The estimated heat fluxes are shown in plots G2, G4, G6, G8, G10, and G12.

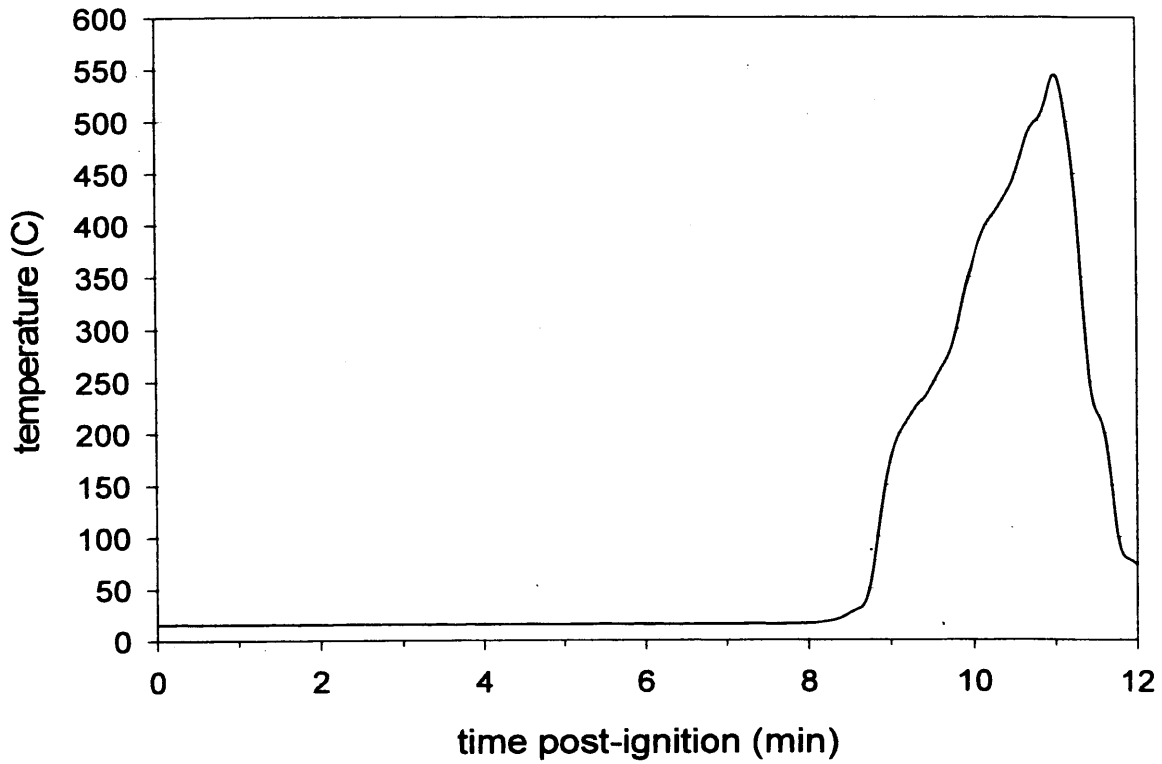
Except for DFT2, the heat fluxes to the DFT's increased exponentially starting at approximately 5 minutes post-ignition. The DFT located near the front passengers knees recorded a rapid increase in heat at about 8 ½ minutes post-ignition (Plot G3), coincident with ignition of the seat cushion and inboard arm rest on the front passenger's seat, and the deployed passenger air bag at about 7 min post-ignition. Rapid rises in the heat fluxes to all horizontal and vertical surfaces at head level were recorded during the final minute of the test, which were coincident with flame-spread across the headliner.



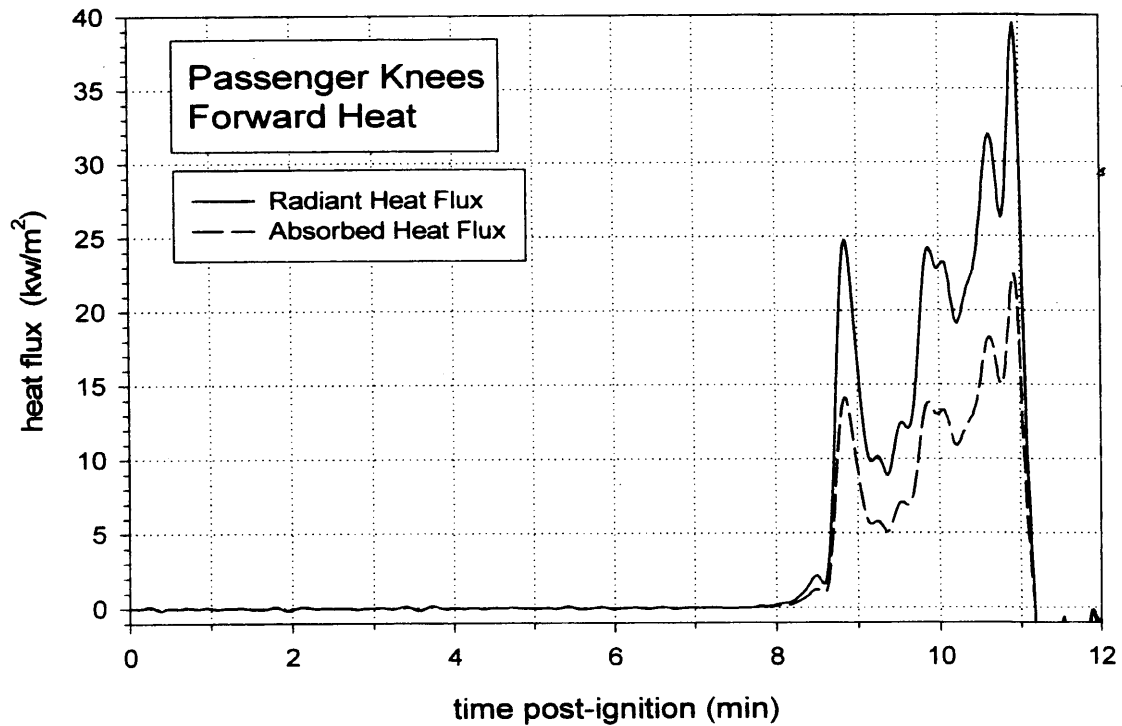
Plot G1. Fire Test F961115. Response of DFT1 and the average of the time-compensated responses of ASP1 and ASP2.



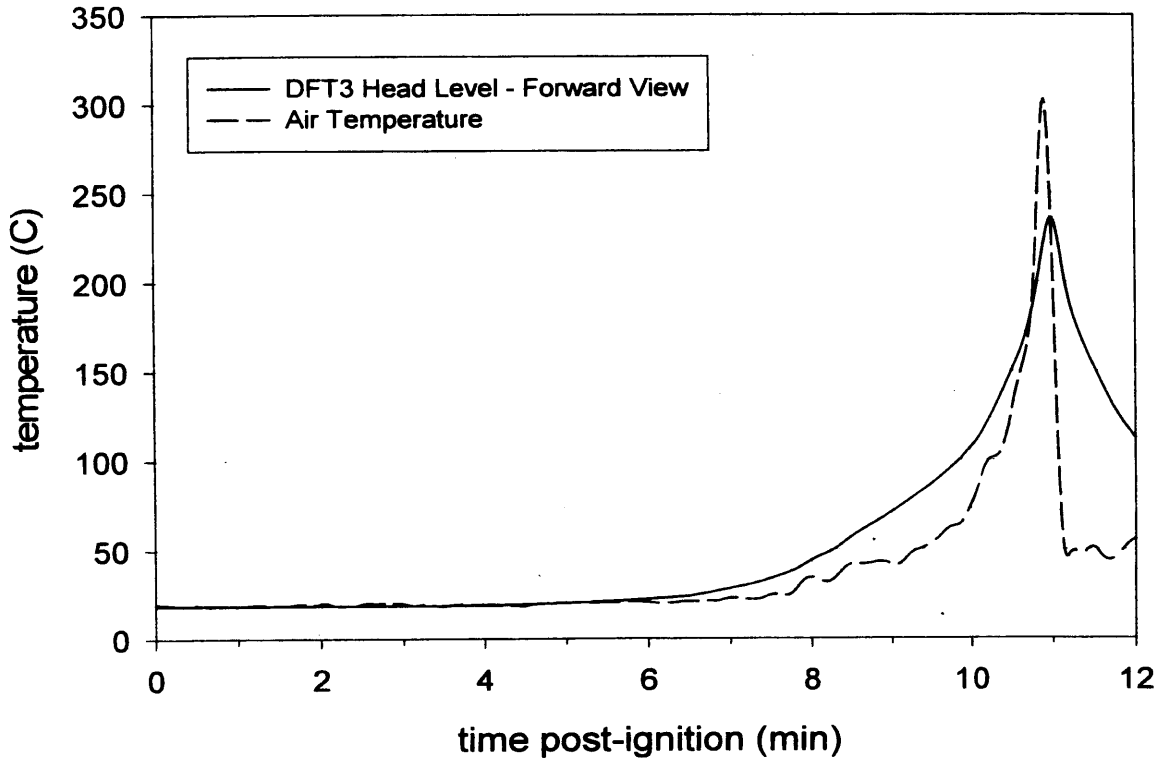
Plot G2. Fire Test F961115. Absorbed heat flux estimated from the response of DFT1 and the average of the time-compensated responses of ASP 1 and ASP2.



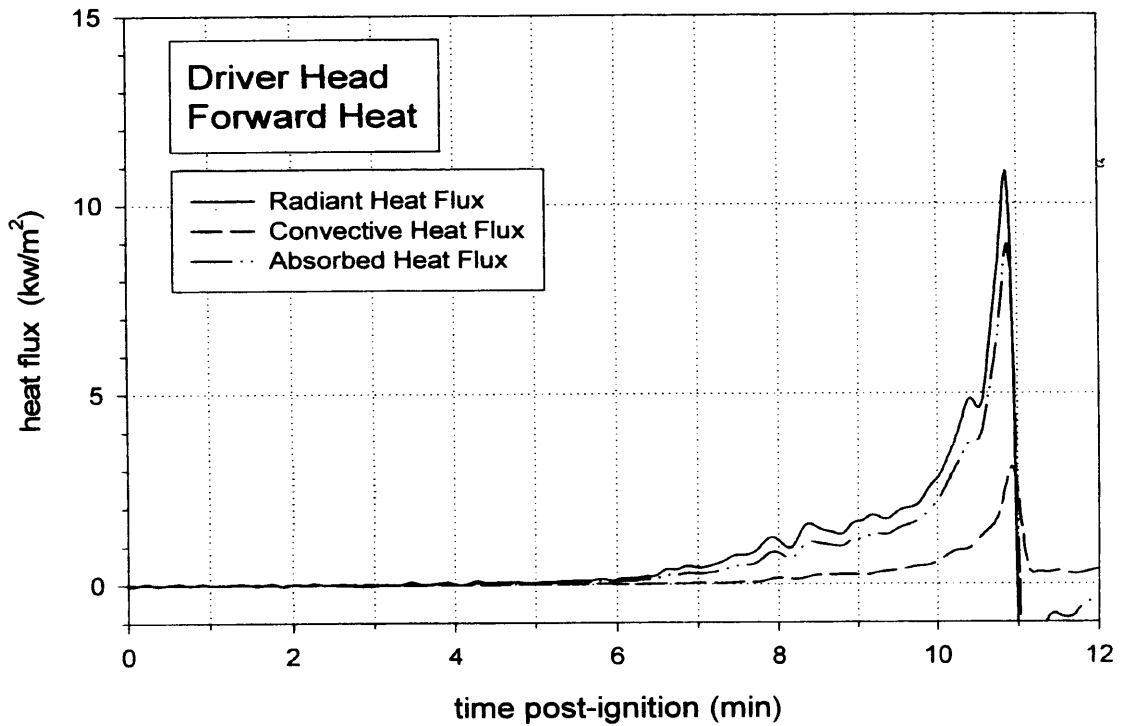
Plot G3. Fire Test F961115. Response of DFT2.



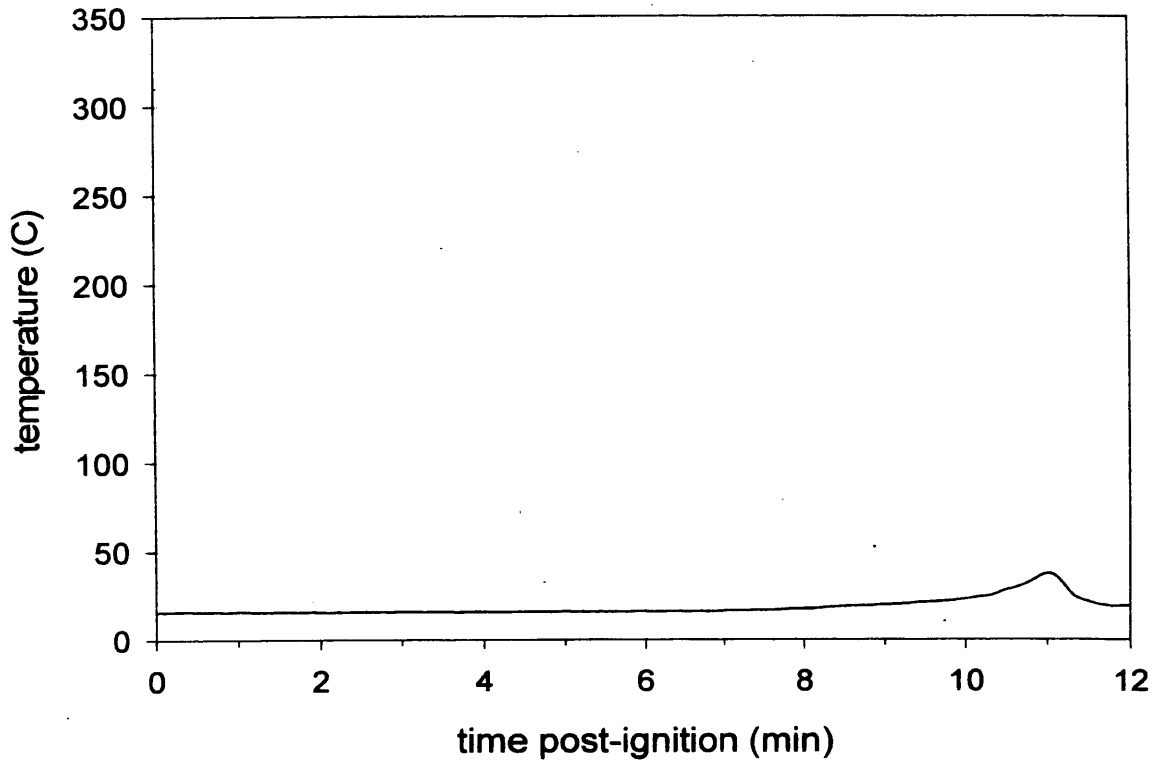
Plot G4. Fire Test F961115. Absorbed heat flux estimated from the response of DFT2.



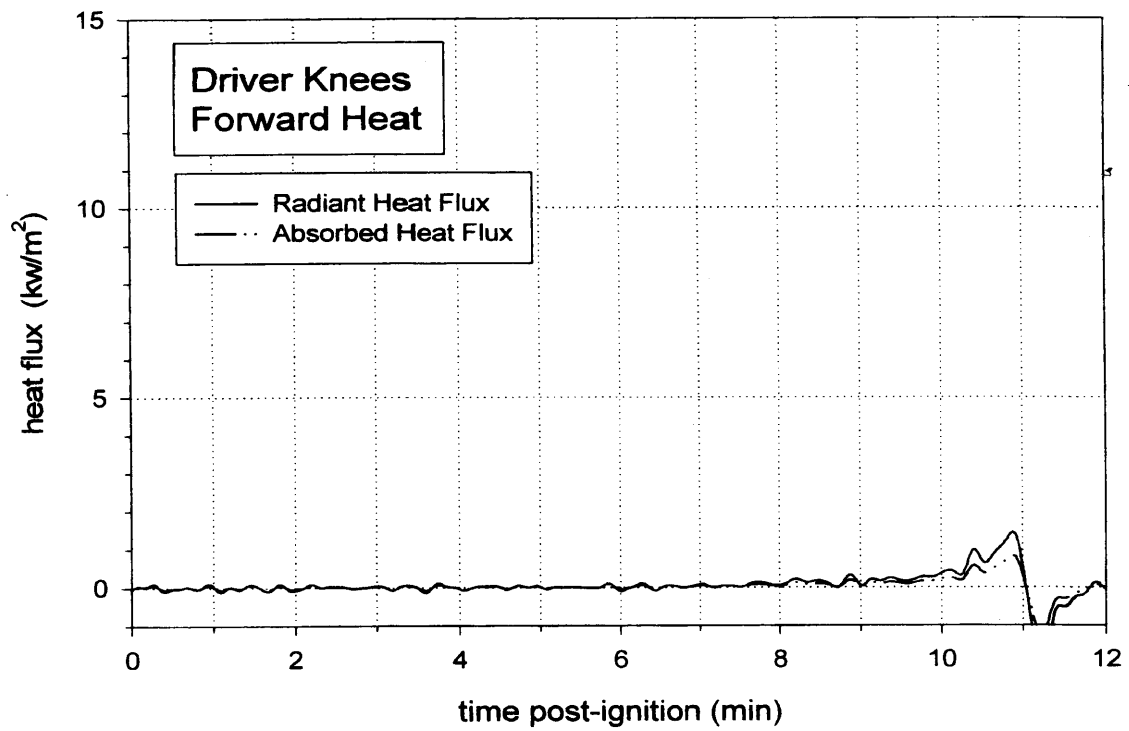
Plot G5. Fire Test F961115. Response of DFT3 and the average of the time-compensated responses of ASP1 and ASP2.



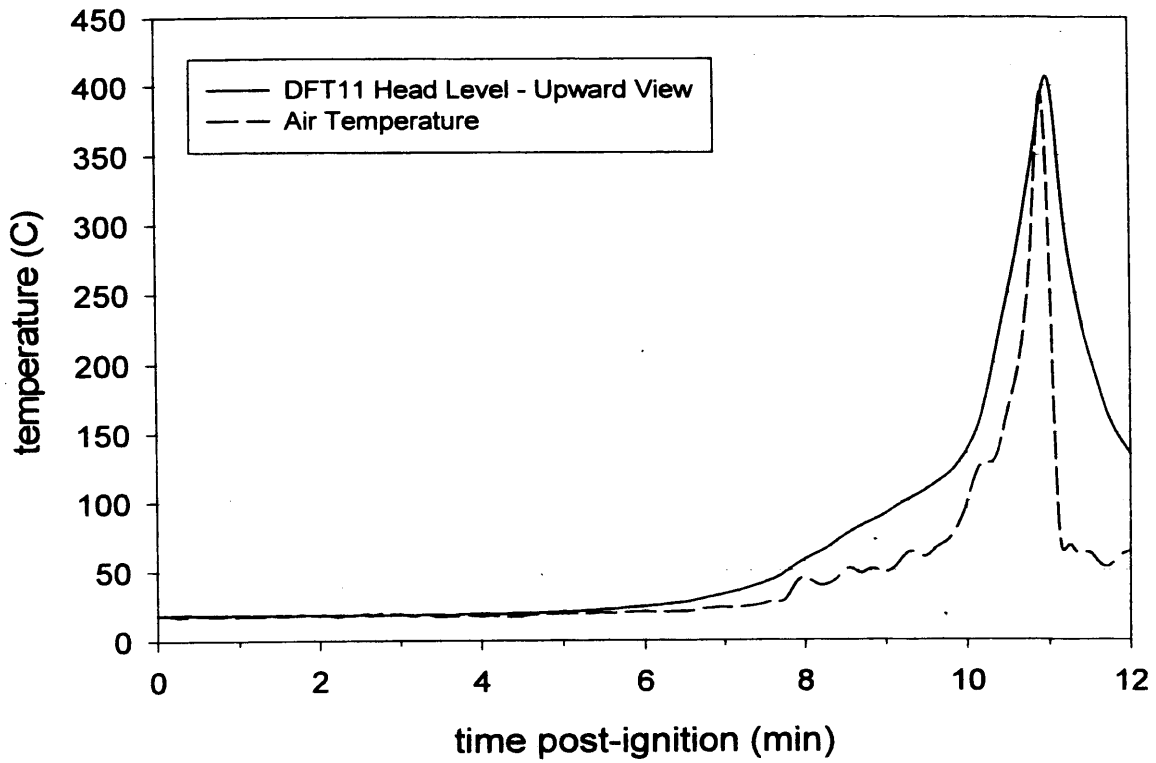
Plot G6. Fire Test F961115. Absorbed heat flux estimated from the response of DFT3 and the average of the time-compensated responses of ASP 1 and ASP2.



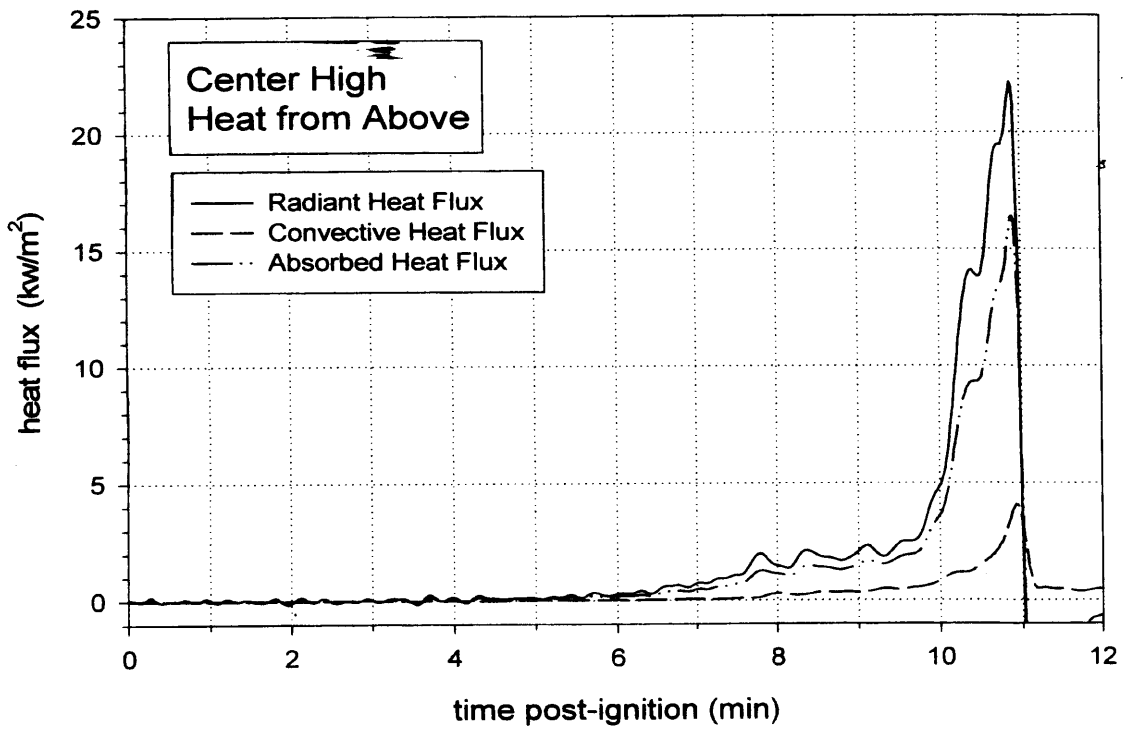
Plot G7. Fire Test F961115. Response of DFT4.



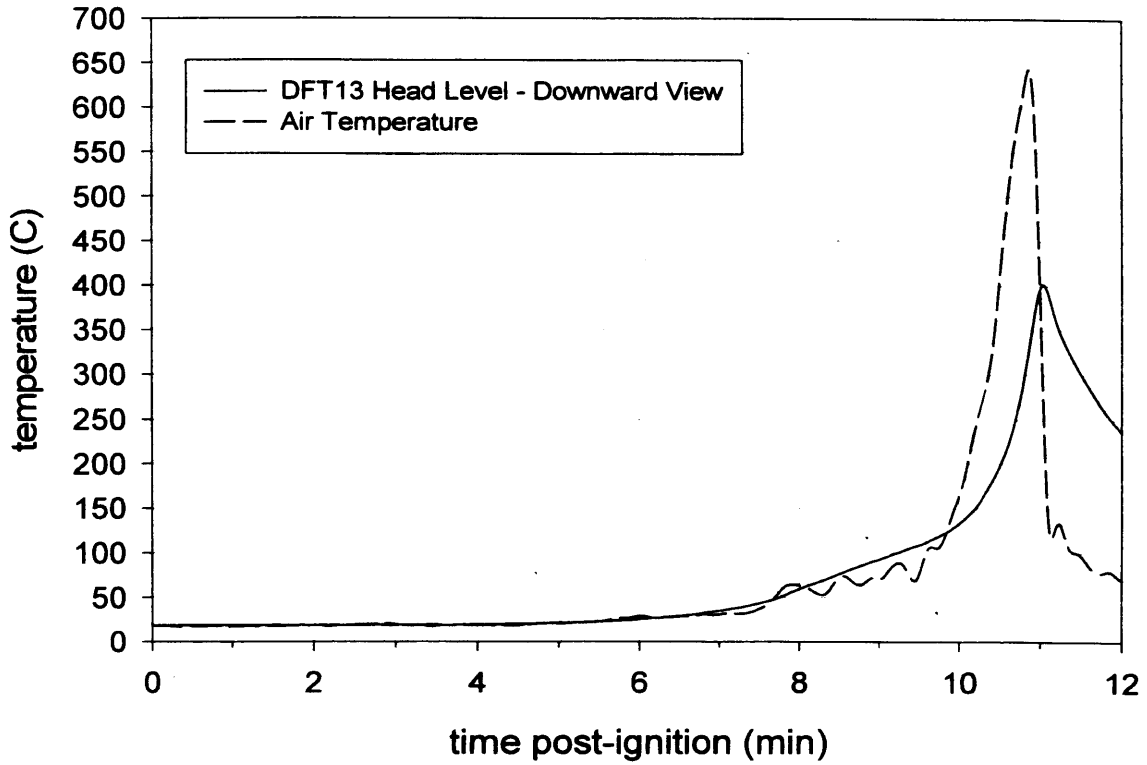
Plot G8. Fire Test F961115. Absorbed heat flux estimated from the response of DFT4.



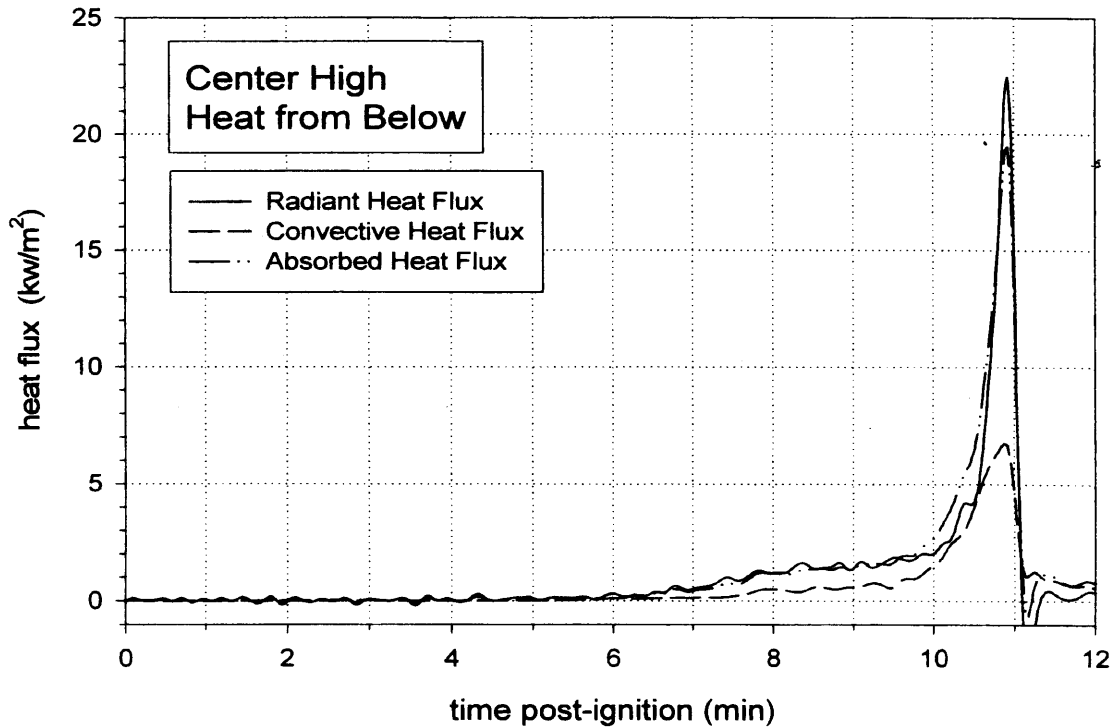
Plot G9. Fire Test F961115. Response of DFT11 and the time-compensated response of ASP3.



Plot G10. Fire Test F961115. Absorbed heat flux estimated from the response of DFT11 and the time-compensated response of ASP3.



Plot G11. Fire Test F961115. Response of DFT13 and the average of the time-compensated responses of ASP4 and ASP5.



Plot G12. Fire Test F961115. Absorbed heat flux estimated from the response of DFT13 and the average of the time-compensated responses of ASP4 and ASP5.

**APPENDIX H  
FIRE PRODUCTS COLLECTOR DATA**

Scientific and technical personnel from Factory Mutual Research Corporation were primarily responsible for obtaining and analyzing data from the Fire Products Collector (FPC) at the Factory Mutual Test Center.

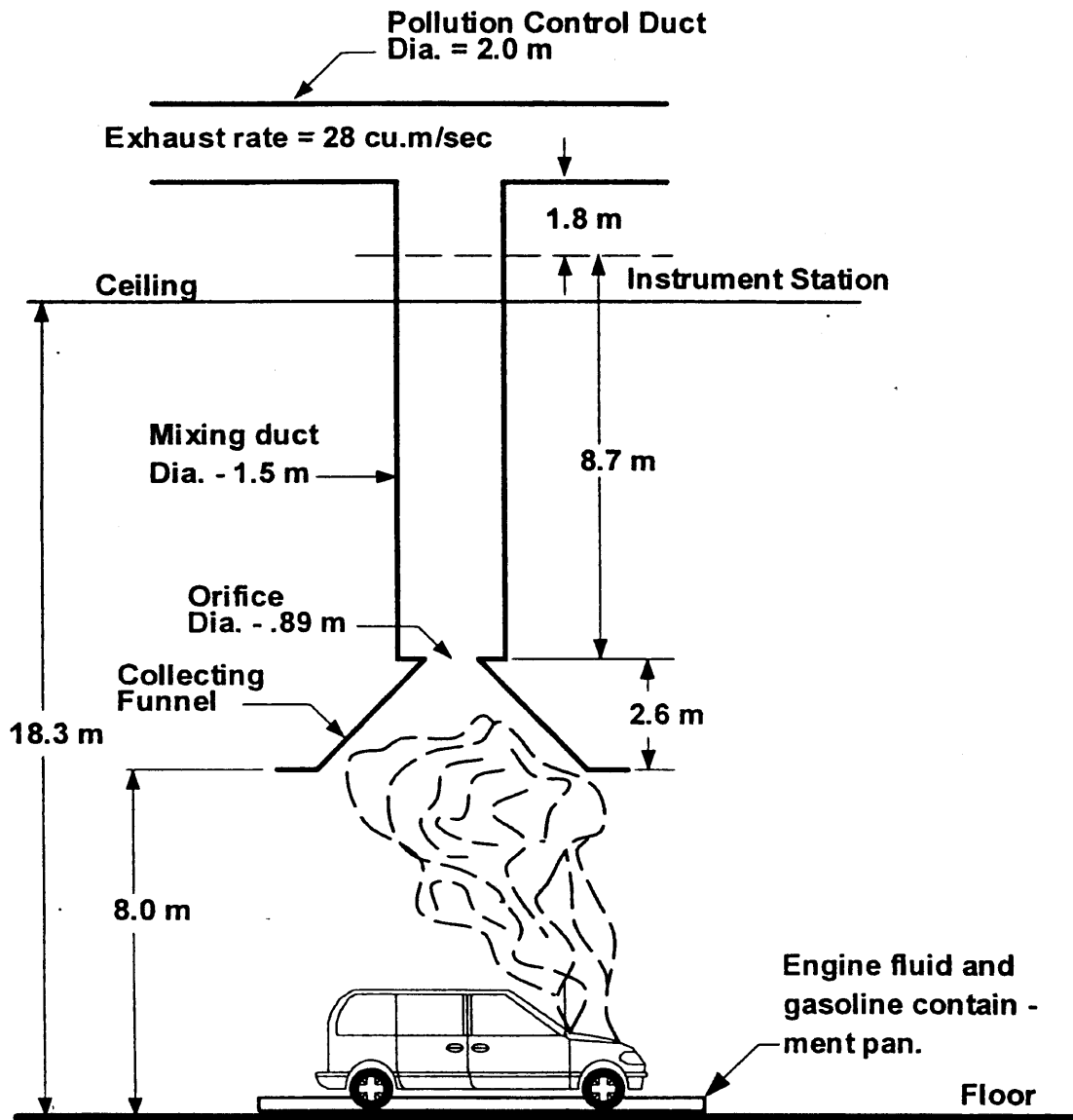


Figure H1. Fire Test F961115. Diagram of the test vehicle under the fire products collector at the Factory Mutual Test Center.

The Fire Products Collector was used to measure heat and combustion gases generated by the burning vehicles during these tests (Fig. H1). The FPC consisted of a collection funnel (diameter = 6.1 m), an orifice plate (hole = 0.9 m), and a vertical stainless steel sampling duct (diameter =

1.5 m). The sampling duct was connected to the air pollution control system of the Test Center. The blower of the air pollution control system induces gas flow through the sampling duct. Air enters the sampling duct via the orifice plate. The temperature, linear velocity, optical transmission, and chemical composition of the entrained gas were measured in the center of the sampling duct 8.66 m (5.7 duct diameters) downstream from the orifice plate, ensuring a flat velocity profile at the sampling location. The data acquisition system consisted of a Hewlett Packard 2313B analog-to-digital conversion sub-system interfaced to a Hewlett Packard 1000 computer.

Gas temperature in the sampling duct was measured with two Type-K thermocouples (30 gage) with exposed bead-type junctions. The thermocouple leads were housed in stainless steel tubes (o.d. = 6.4 mm). Ambient air temperature in the facility was measured by five Type-K thermocouples attached to the external surface of the duct at 2.44, 5.49, 9.14, 12.8, and 15.9 m above the floor. These thermocouples were shielded from radiation from the fire.

The linear velocity of the gas entrained in the sampling duct was measured with a Pitot ring consisting of four Pitot tubes. A static pressure tap was mounted on the inside wall of the sampling duct. The pressure difference between the Pitot ring and the static wall tap was measured with an electronic manometer (Barocel Model 1173, CGS Scientific Corporation).

The particulate concentration in the entrained air was determined from the optical transmission across the duct measured at 0.4579  $\mu\text{m}$  (blue), 0.6328  $\mu\text{m}$  (red), and 1.06  $\mu\text{m}$  (infrared). The optical path length across the duct was 1.524 m. Gas was withdrawn from the sampling duct through a stainless steel tube (o.d. = 3.9 mm) at a flow rate of  $0.17 \times 10^{-3} \text{ m}^3/\text{s}$  for chemical analysis. The gas flowed through a particulate filter, a water condenser, and a drying agent before entering the analyzers. Carbon dioxide ( $\text{CO}_2$ ) and carbon monoxide (CO) were measured with two dedicated non-disperse infrared analyzers (Beckman Model 864 Infrared Analyzers). Oxygen ( $\text{O}_2$ ) was measured with a paramagnetic oxygen analyzer (Beckman Model 755 Paramagnetic Oxygen Analyzer). Total gaseous hydrocarbons were measured with a flame ionization analyzer (Beckman Model 400 Flame Ionization Analyzer).

The rate of product release was calculated using the following relationship:

$$\left( \frac{dR_j}{dt} \right) = f_j \left( \frac{dV}{dt} \right) \rho_j = f_j \left( \frac{dW}{dt} \right) \left( \frac{\rho_j}{\rho_g} \right) \quad (\text{H1})$$

where  $d(R_j)/dt$  is the mass release rate of product  $j$  in kg/s;  $f_j$  is the volume fraction of product  $j$ ;  $dV/dt$  is the total volume flow rate of the gas entrained in the sampling duct in  $m^3/s$ ;  $dW/dt$  is the total mass flow rate of the gas entrained in the sampling duct in kg/s;  $\rho_j$  is the density of product  $j$  in  $g/m^3$ ; and  $\rho_g$  is the density of the gas entrained in the concentration measurements. The rate of oxygen consumption was calculated using equation (A1), where the volume fraction of oxygen consumed was substituted for  $f_j$ .

The volume fraction of smoke particulate was calculated from the following relationship:

$$f_s = \frac{D\lambda \times 10^{-6}}{\Omega} \quad (H2)$$

where  $f_s$  is the volume fraction of smoke,  $\lambda$  is the wavelength of the light source,  $\Omega$  is the extinction coefficient of particulate (a value of 0.7 was used in these calculations), and  $D$  is the optical density at each of the three wavelengths at which measurements were made:

$$D = \frac{\ln\left(\frac{I_0}{I}\right)}{L} \quad (H3)$$

where  $I_0$  is the intensity of light transmitted through clean air,  $I$  is the intensity of light transmitted through air containing smoke particulate, and  $L$  is the optical pathlength, which was equal to 1.524 m. A value of  $1.1 \times 10^6$   $g/m^3$  was used for the density of smoke particulate ( $\rho_j$ ) in equation (H1).

The convective heat release rate was calculated using the following relationship:

$$\left(\frac{dE_{conv}}{dt}\right) = \left(\frac{dW}{dt}\right) \times c_p \times (T_g - T_a) \quad (H4)$$

where  $d(E_{conv})/dt$  is the convective heat release rate in kW;  $dW/dt$  is the mass flow rate of the gas entrained in the sampling duct in kg/s;  $c_p$  is the heat capacity of the gas entrained in the sampling duct at the gas temperature in  $kJ/(kg \times K)$ ;  $T_g$  is the temperature of the gas entrained in the sampling duct in K; and  $T_a$  is the ambient air temperature in K.

The chemical heat release rate was calculated from the release rates of carbon dioxide and carbon monoxide as follows:

$$\left(\frac{dE_{ch}}{dt}\right) = \Delta H_{CO_2}^* \times \left(\frac{dR_{CO_2}}{dt}\right) + \Delta H_{CO}^* \times \left(\frac{dR_{CO}}{dt}\right) \quad (H5)$$

where  $d(E_{ch})/dt$  is the chemical heat release rate in kW;  $\Delta H^*$  is the net heat of complete combustion per unit mass of carbon dioxide or carbon monoxide released in the fire in kJ/g; and  $dR/dt$  is the mass release rate of carbon dioxide or carbon monoxide in kg/s. Values of  $\Delta H^*$  for carbon dioxide and carbon monoxide were obtained from the literature [H1 and H2].

The chemical heat release rate also was calculated from the oxygen consumption rate as follows:

$$\left(\frac{dE_{ch}}{dt}\right) = \Delta H_O^* \left(\frac{dC_O}{dt}\right) \quad (H6)$$

where  $d(E_{ch})/dt$  is the chemical heat release rate in kW;  $\Delta H_O^*$  is the net heat of complete combustion per unit mass of  $O_2$  consumed in kJ/g; and  $d(C_O)/dt$  is the consumption rate of oxygen in kg/s. The value for  $\Delta H_O^*$  was obtained from the literature [H1 and H2].

The radiative heat release rate was the difference between the chemical heat release rate and the convective heat release rate:

$$\left(\frac{dE_{rad}}{dt}\right) = \left(\frac{dE_{ch}}{dt}\right) - \left(\frac{dE_{conv}}{dt}\right) \quad (H7)$$

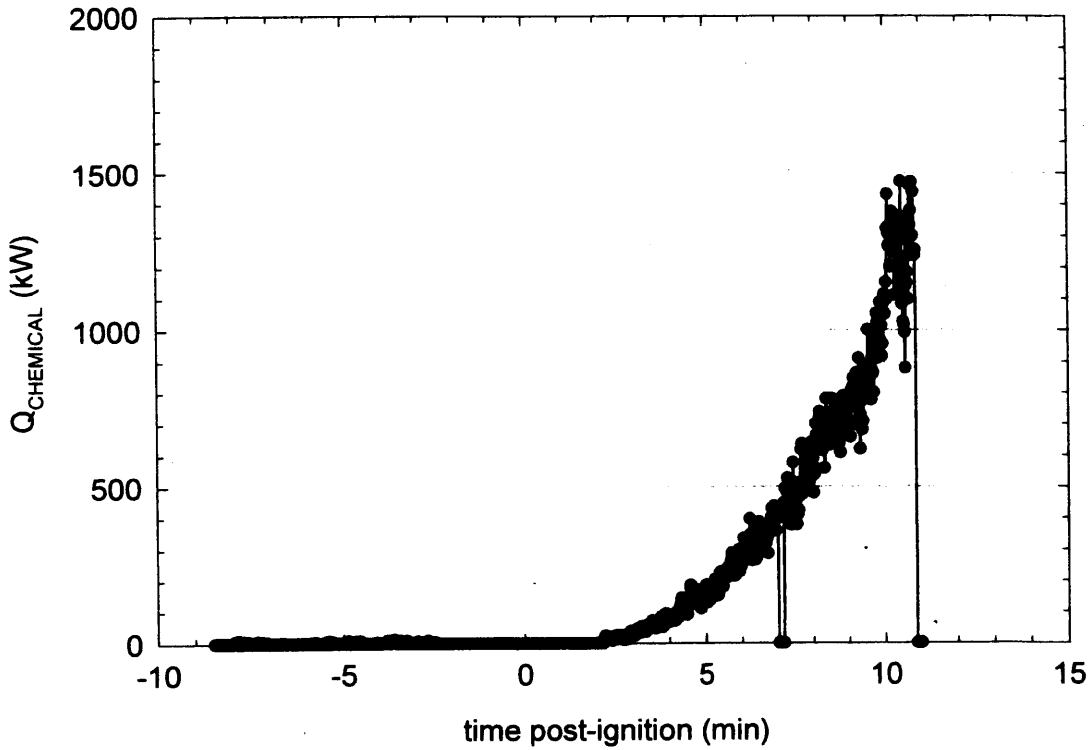
where  $d(E_{rad})/dt$  is the radiative heat release rate; and  $d(E_{ch})/dt$  is the average chemical heat release rate calculated using equations (H5) and (H6).

Data from the fire-products collector are shown in Plots H1 through H5. The Fire Products Collector did not detect a fire plume until 10 seconds after ignition. The chemical, convective, and radiative heat release rates increased uniformly from approximately 10 seconds after ignition until the fire was extinguished (Plots H1 through H3, respectively). The maximum chemical heat rate measured during the test was approximately 1500 kW (Plot H1). The carbon monoxide and carbon dioxide release rates also increased uniformly from the time of ignition until the fire was

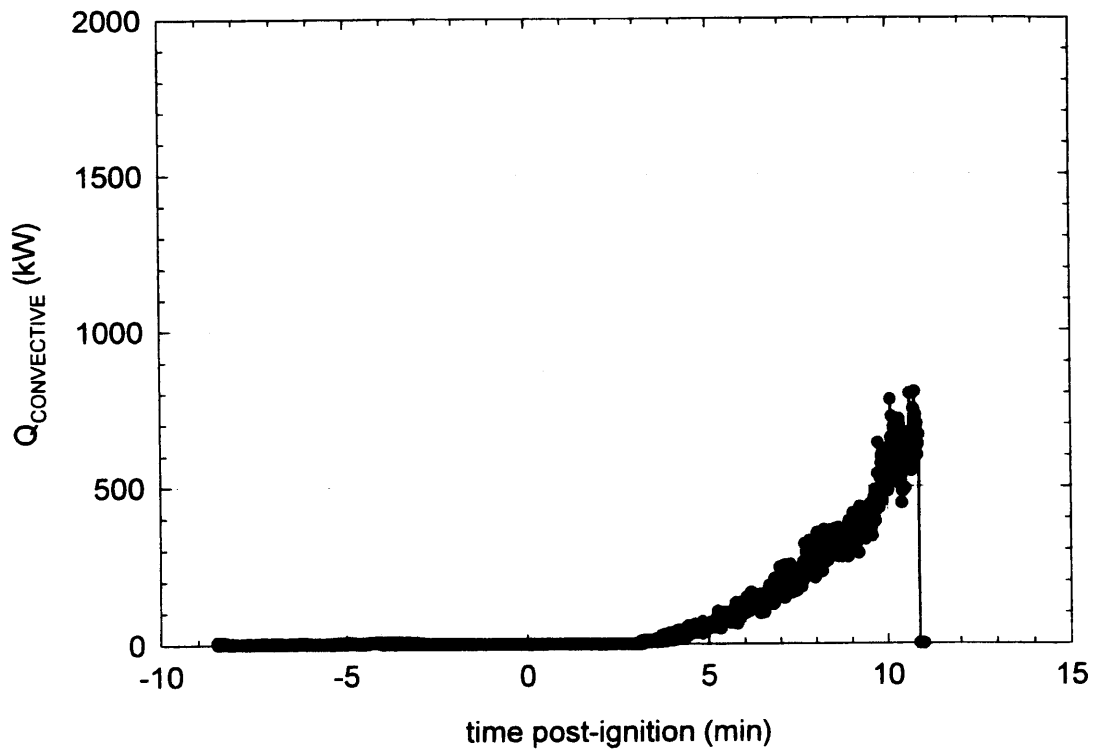
extinguished. The maximum carbon dioxide and carbon monoxide release rates were 0.11 and 0.0013 kg/s, respectively (Plots H4 and H5, respectively).

#### REFERENCES

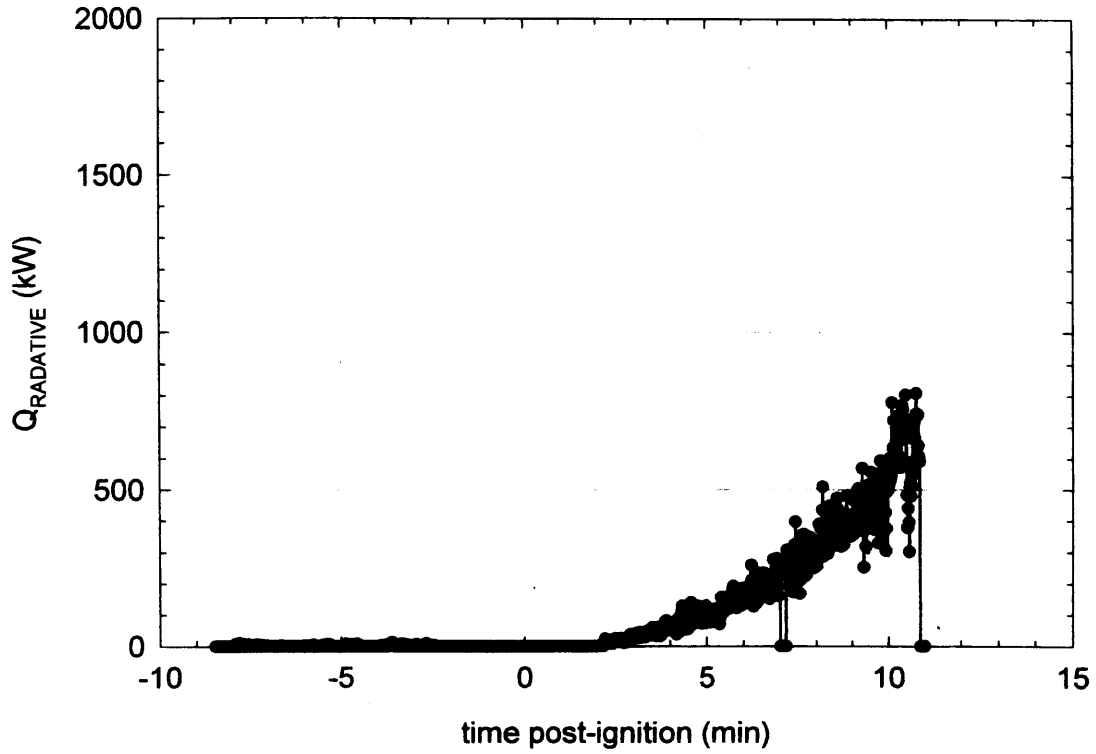
- H1. G. Heskestad. A Fire Products Collector for Calorimetry into the MW Range, Technical Report J.I. OC2E1.RA. Factory Mutual Research Corporation, Norwood, MA. June, 1981.
- H2. Archibald Tewarson. "Generation of Heat and Chemical Compounds in Fires" Section 3/Chapter 4, SFPE Handbook of Fire Protection Engineering, 2nd Edition, 1995, pp. 3:53-124.



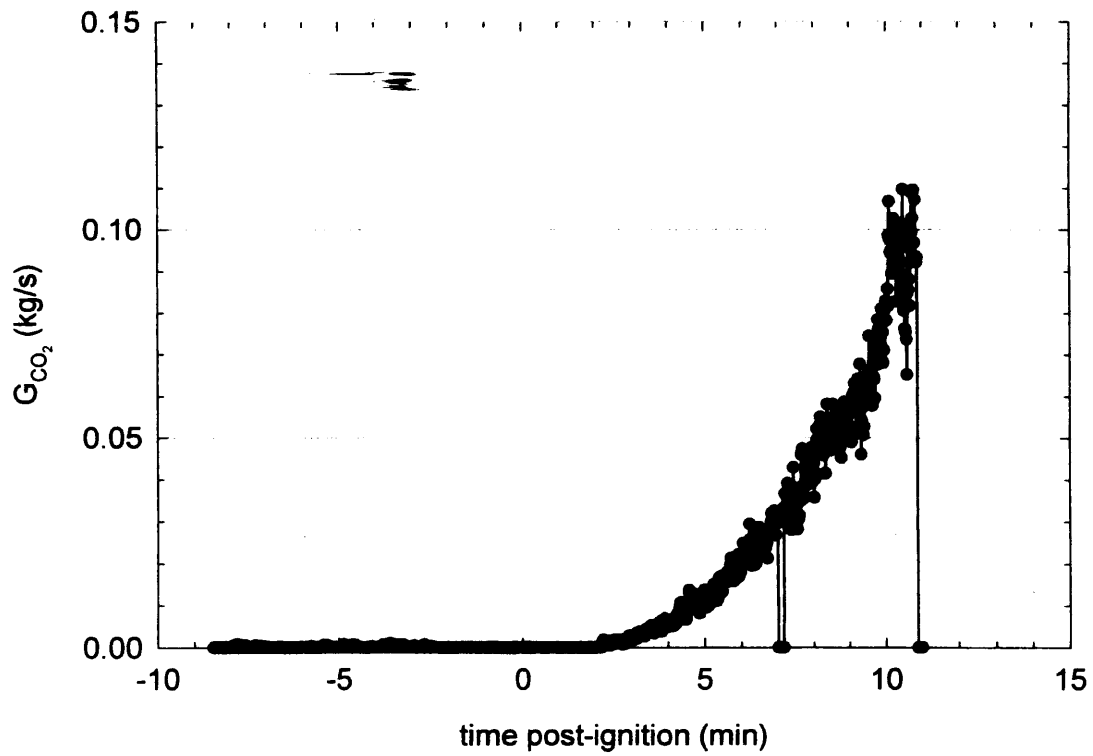
Plot H1. Fire Test F961115. Chemical heat release rate measured using the Fire Products Collector.



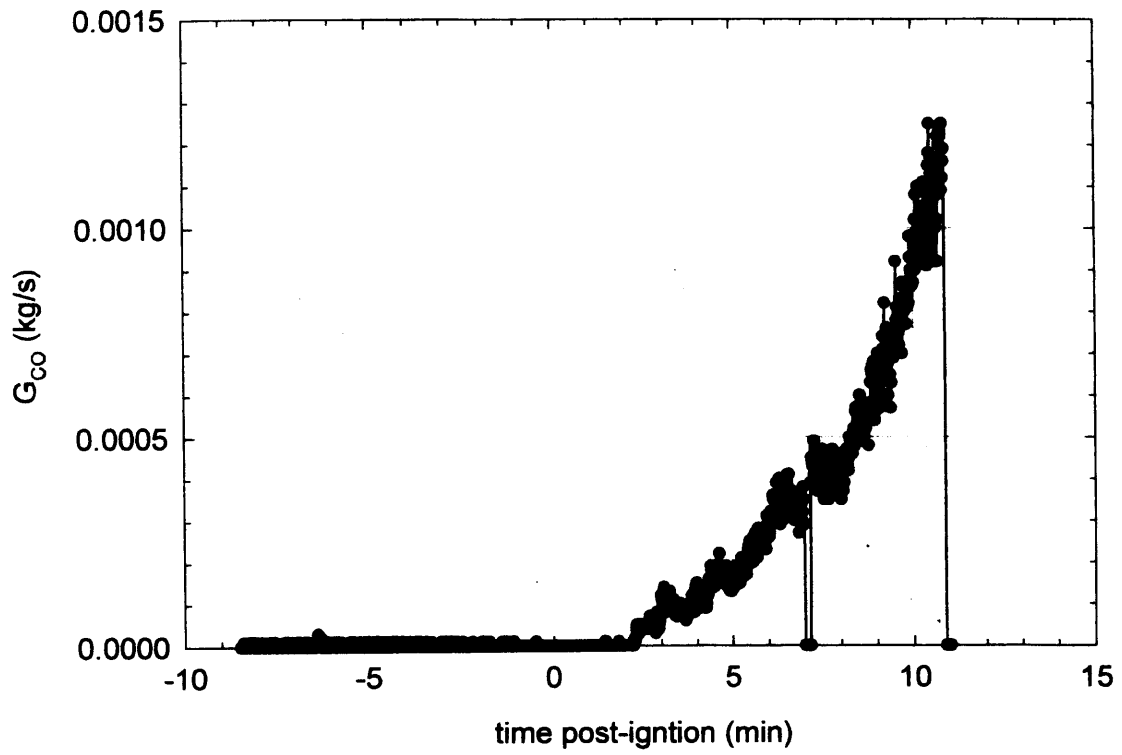
Plot H2. Fire Test F961115. Convective heat release rate measured using the Fire Products Collector



Plot H3. Fire Test F961115. Radiative heat release rate measured using the Fire Products Collector.



Plot H4. Fire Test F961115. Carbon dioxide release rate measured using the Fire Products Collector



Plot H5. Fire Test F961115. Carbon monoxide release rate measured using the Fire Products Collector.

**APPENDIX I**  
**PASSENGER COMPARTMENT COMBUSTION GAS DATA**  
**FOURIER TRANSFORM INFRARED SPECTROSCOPY**

Combustion gases in the passenger compartment were measured by Fourier transform infrared (FTIR) spectrometry. A single sampling-line was used to acquire air samples from the passenger compartment. The sampling-line consisted of a stainless-steel tube (o.d. = 0.250 in. (6.4 mm), i.d. = 0.125 in. (3.2 mm), l = 20 ft (6.1 m)) was inserted through the roof along the longitudinal midline of the vehicle between the front occupant positions. The inlet of the sample-tube extended 25 cm below the headliner (Fig.'s I1 and I2). The tube was not heated. The outlet of the sample tube was connected to a heated Teflon® transfer-line (o.d. = 0.250 in. (6.4 mm), i.d. = 0.125 in. (3.2 mm), l = 75 ft. (23 m)), which was connected to the gas cell of the FTIR spectrometer and to a sampling manifold containing five sorbent cartridges. The transfer-line was heated to 125°C during the test to prevent condensation of water and water-soluble gases (e.g., HCl, HCN, NO, and NO<sub>2</sub>). An in-line stainless steel filter holder containing a quartz fiber filter (o.d. = 47 mm) was placed between the sample-tube and the transfer-line to prevent smoke particles from contaminating analytical instrumentation.

The FTIR spectrometer was an Model I-1000 Series FTIR Spectrometer (MIDAC Corporation, Riverside, California), with a KBr beam-splitter; a liquid nitrogen-cooled Mercury-Cadmium-Telluride detector; and gold-surfaced aluminum optics. This instrument was fitted with a stainless steel, multiple-reflectance gas cell (path length = 10 m) with zinc selenide windows. The gas cell was heated to 125°C. The optical bench was filled with clean, dry argon and hermetically sealed. The usable spectral range of this instrument was approximately 7400-700 cm<sup>-1</sup>. Pressure in the gas cell during the fire tests was measured with a Baratron pressure gauge (MKS Instruments, Burlington, MA). The spectrometer was operated at a spectral resolution of 0.5 cm<sup>-1</sup>.

The sampling line and gas cell were equilibrated to 125°C for at least 60 minutes before sample acquisition. A reference spectrum was acquired while the gas cell was evacuated. During the fire tests, the gas cell was purged continuously with air withdrawn from the passenger compartment at a flow rate of 7 L/min. Single-scan absorbance spectra were acquired and stored to disk at intervals of 7 s. The stored spectra were analyzed after the test using the quantitative analysis software provided by the instrument manufacturer (AutoQuant, MIDAC). This software used a Classical Least Squares algorithm to determine gas concentrations. The method developed for analysis of combustion gases was calibrated with gas standards (Scott Specialty Gases, Inc., Troy, MI). The standards were either NIST-traceable or produced by a gravimetric blending process.

The gaseous combustion products measured in the passenger compartment during this test included carbon dioxide, carbon monoxide, methane, ethylene, acetylene, hydrogen cyanide, nitric oxide, and hydrogen chloride (Plots I1 through I8). Except for carbon dioxide, which has a

background concentration in air of approximately 0.05 %, the concentrations of all of these gases were less than their respective lower limits of detection from the start of the test to 6 minutes post-ignition. Carbon dioxide, carbon monoxide, and the light hydrocarbons started to accumulate in the passenger compartment between 6 and 7 minutes post-ignition (Plots I1 through I5). Hydrogen cyanide (Plot I6) and nitric oxide (Plot I7) started to accumulate in the passenger compartment between 9 and 10 minutes post-ignition. Hydrogen chloride (HCl) was not detected in the air sampled from the passenger compartment (Plot I8).

The Infrared spectra also contained a broad absorbance band between 2800 and 3200  $\text{cm}^{-1}$ , indicating the presence of a mixture of unsaturated aliphatic hydrocarbons in the air samples from the passenger compartment. The intensity of this absorbance band generally followed the same time-course as that of methane (Plot I3). This broad band appeared to contain absorbances from ethane, propane, and butane. However, all of the gaseous species contributing to this absorbance band could not be identified or accurately quantified.

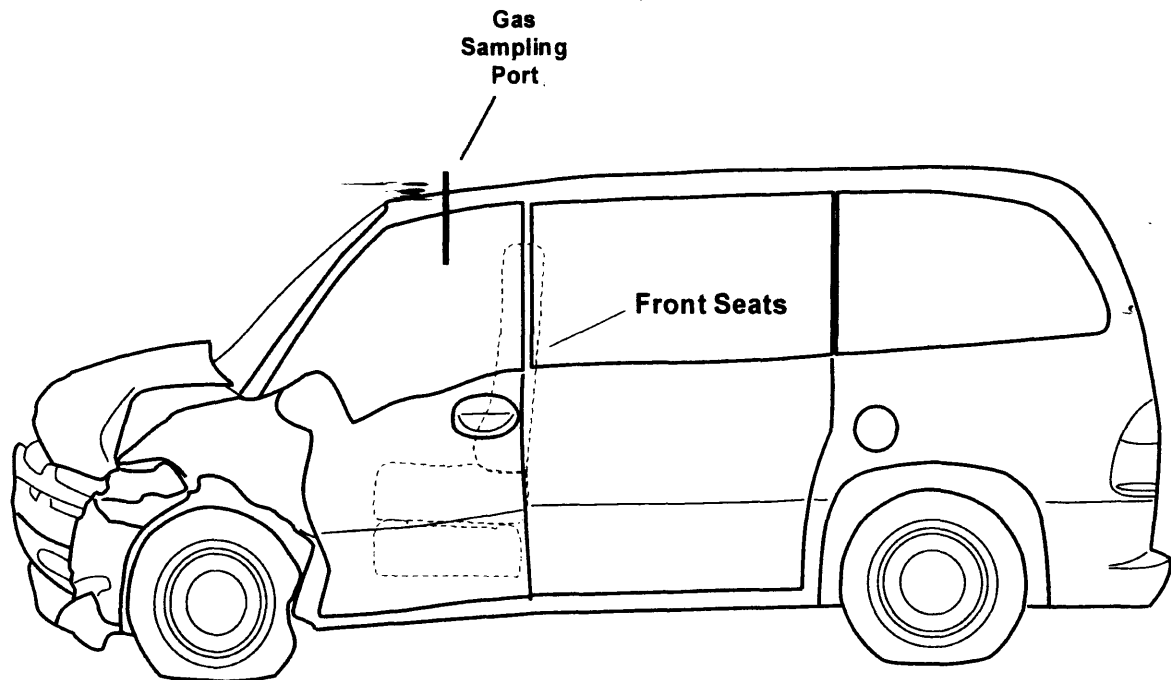


Figure I1. Fire Test F961115. Side view of the test vehicle show the approximate location of the gas sampling port in the passenger compartment.

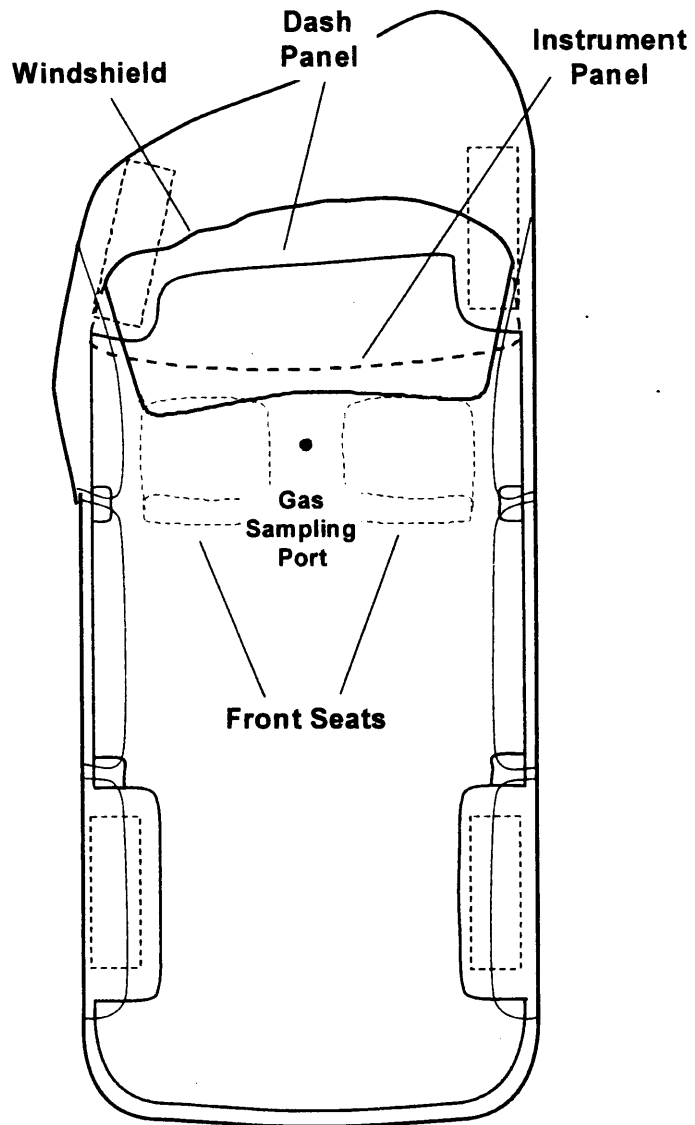
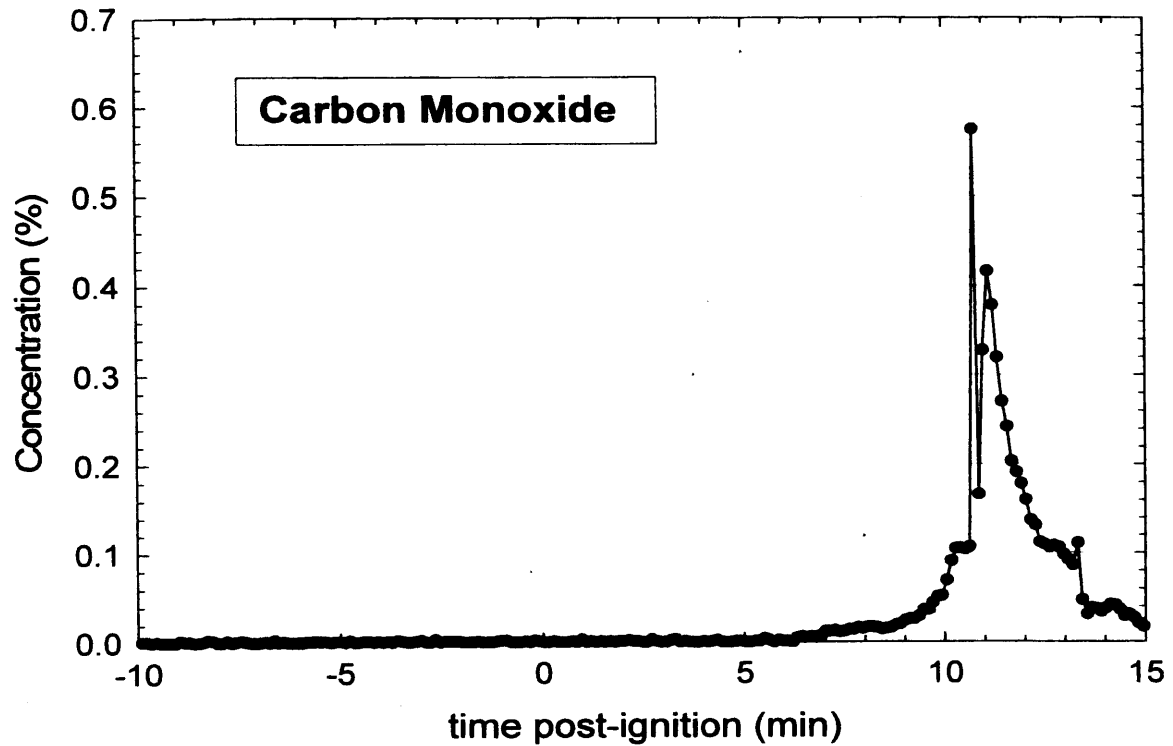
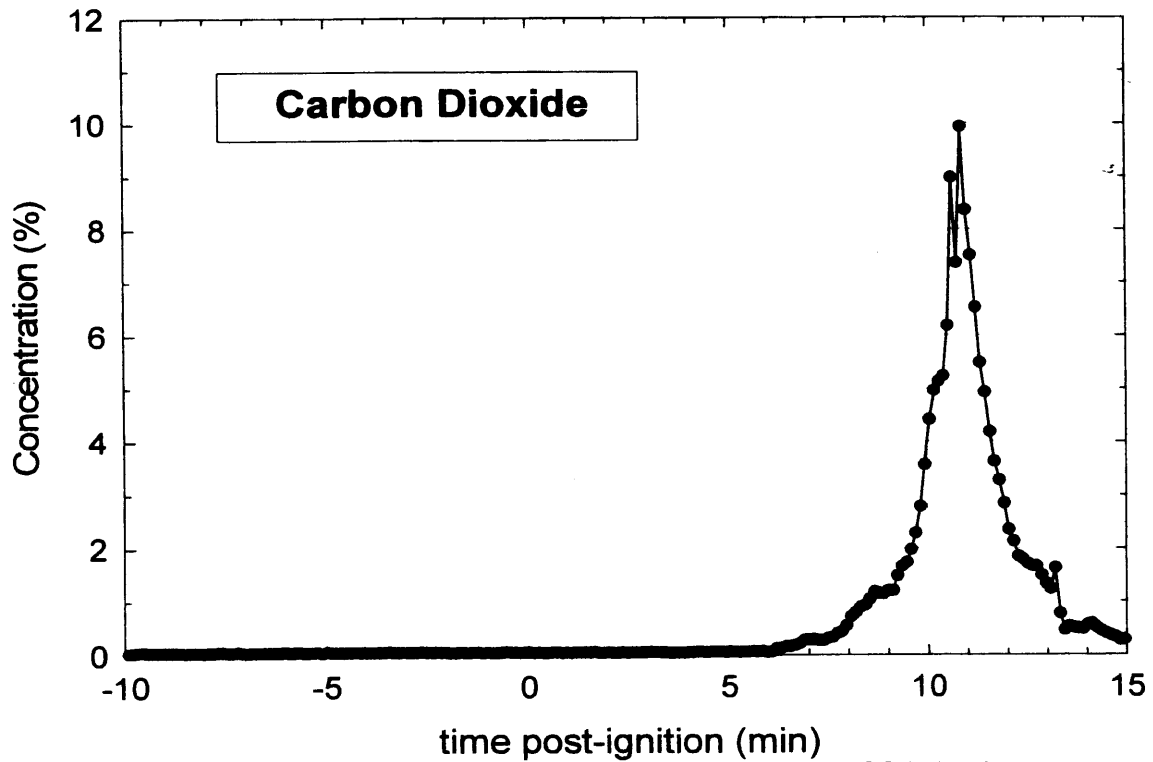


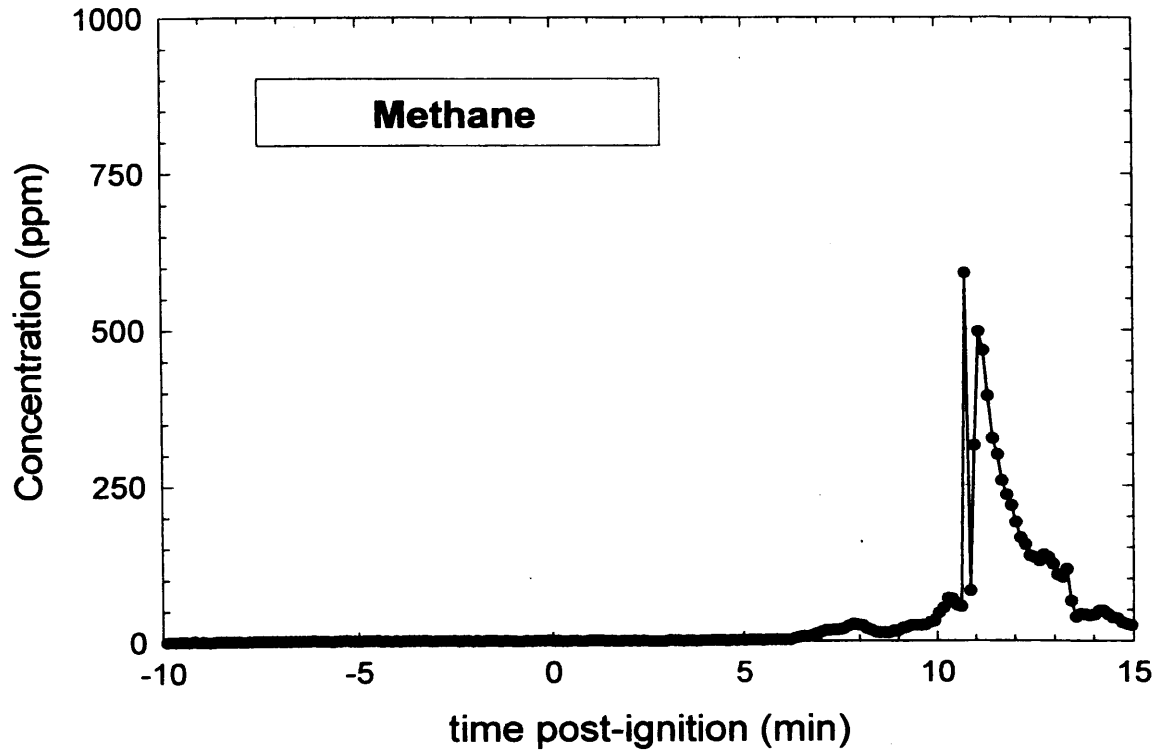
Figure 12. Fire Test F961115. Top view of the test vehicle showing the approximate location of the gas sampling port in the passenger compartment.



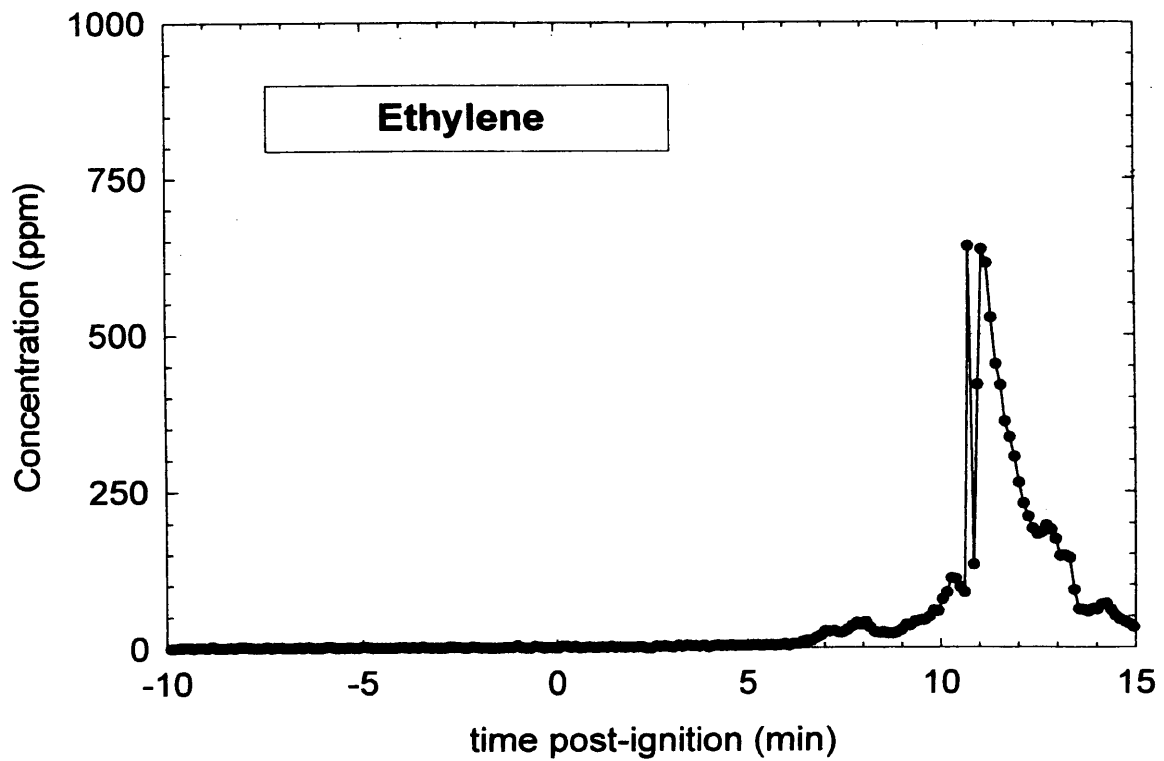
Plot I1. Fire Test F961115. Concentration of carbon monoxide (CO) in the passenger compartment measured by FTIR analysis.



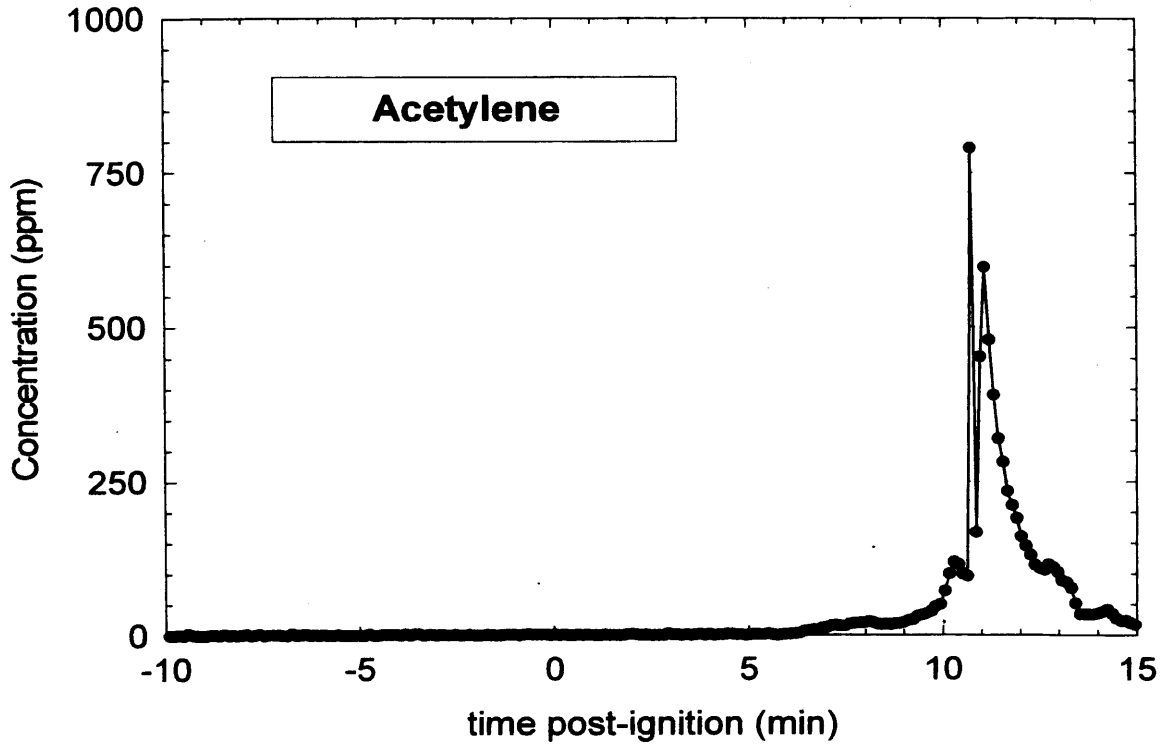
Plot I2. Fire Test F961115. Concentration of carbon dioxide (CO<sub>2</sub>) in the passenger compartment measured by FTIR analysis.



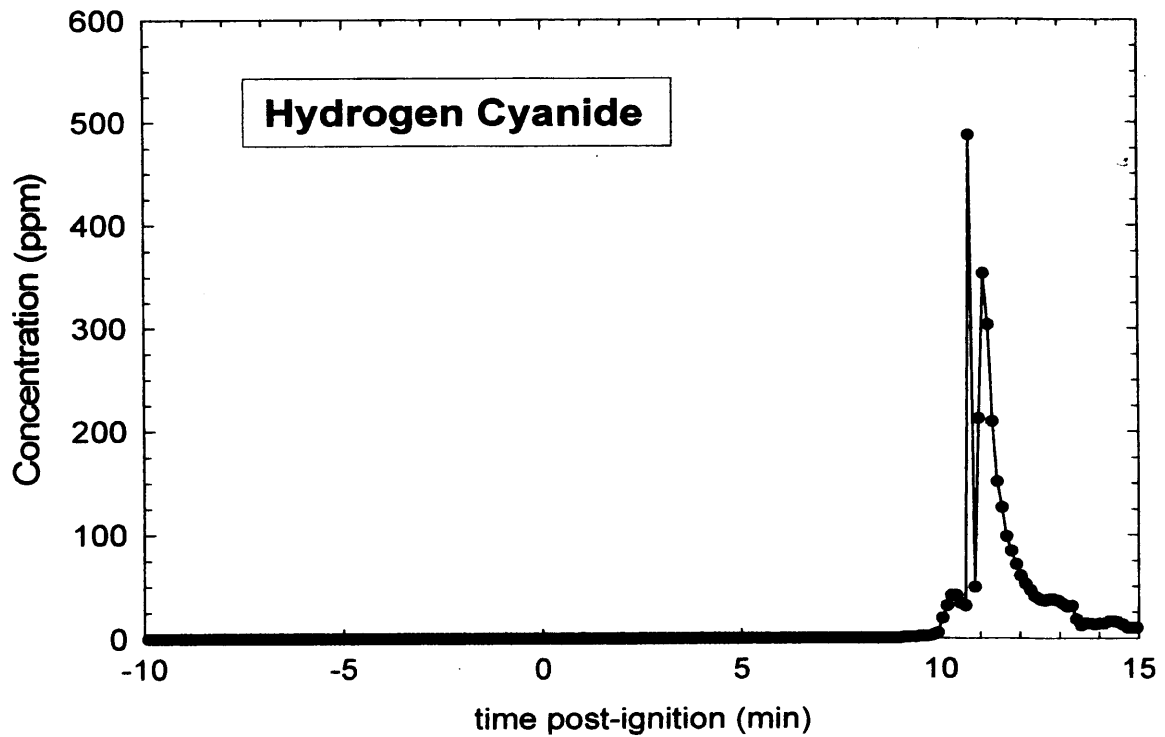
Plot I3. Fire Test F961115. Concentration of methane ( $\text{CH}_4$ ) in the passenger compartment measured by FTIR analysis.



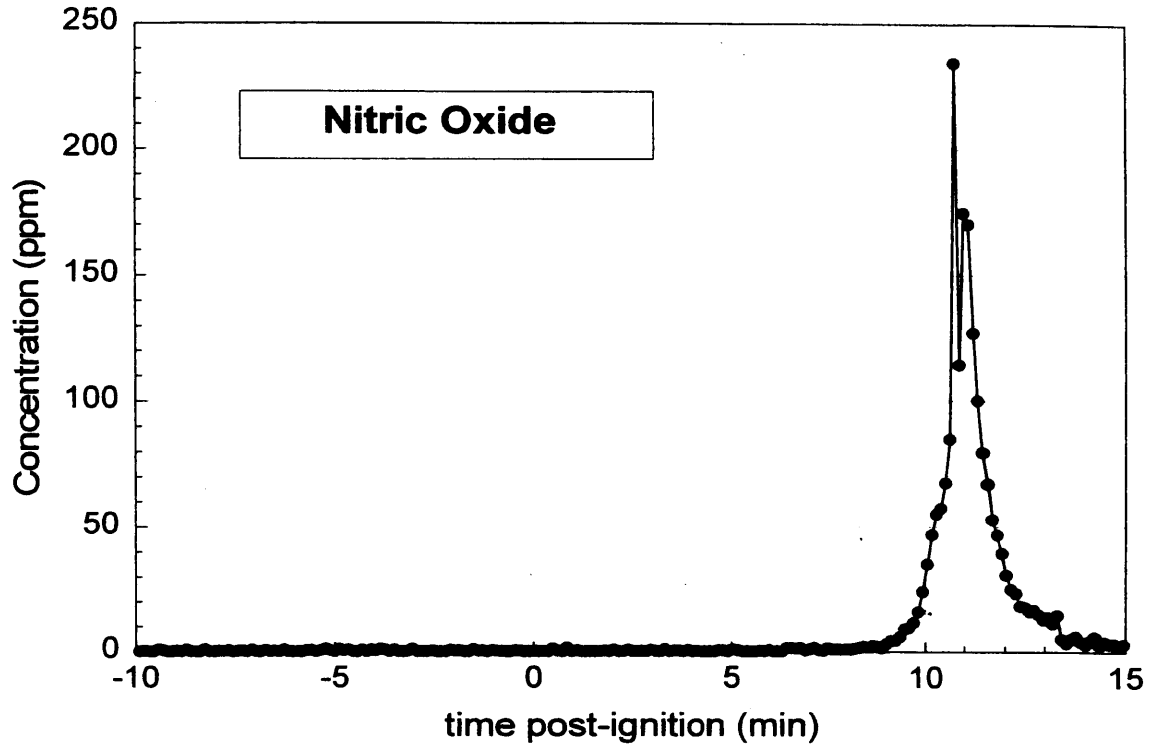
Plot I4. Fire Test F961115. Concentration of ethylene ( $\text{C}_2\text{H}_4$ ) in the passenger compartment measured by FTIR analysis.



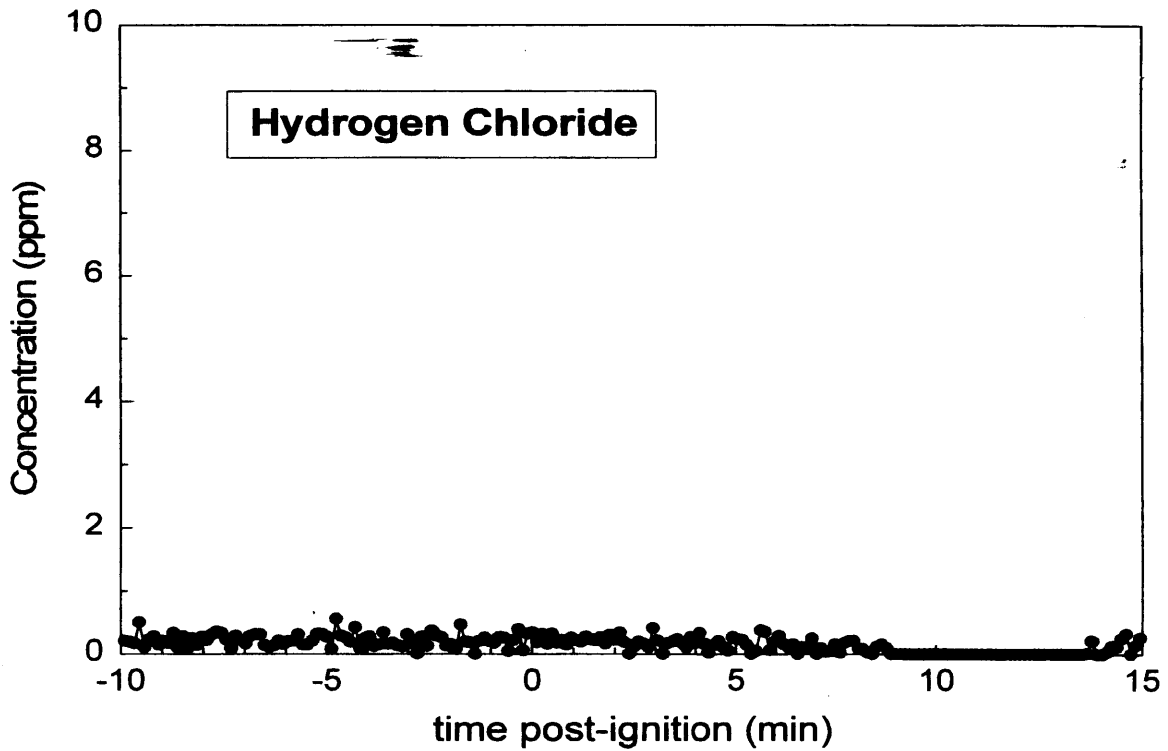
Plot 15. Fire Test F961115. Concentration of acetylene ( $C_2H_2$ ) in the passenger compartment measured by FTIR analysis.



Plot 16. Fire Test F961115. Concentration of hydrogen cyanide (HCN) in the passenger compartment measured by FTIR analysis.



Plot 17. Fire Test F961115. Concentration of nitric oxide (NO) in the passenger compartment measured by FTIR analysis.



Plot 18. Fire Test F961115. Concentration of hydrogen chloride (HCl) in the passenger compartment measured by FTIR analysis

**APPENDIX J**  
**PASSENGER COMPARTMENT COMBUSTION GAS DATA**  
**GAS CHROMATOGRAPHY/MASS SPECTROSCOPY**

A manifold containing five sorbent cartridges in parallel was attached to the gas sampling line used for FTIR analysis (see **APPENDIX I**). The cartridges were glass-lined stainless steel tubes (i.d. = 4 mm; length = 10 cm; Scientific Instrument Services, Inc, Ringoes, NJ) packed with 25 mg of Carbotrap™ C Graphitized Carbon Black (Supelco, Inc.; Bellefonte, PA) in series with 15 mg of Carbotrap™ Graphitized Carbon Black (Supelco). Airflow was directed sequentially through the sorbent cartridges by a solenoid-actuated gas-switching manifold. The sampling rate was 25 mL/min.

The sorbent cartridges were analyzed by thermal desorption/gas chromatography/mass spectrometry. Deuterated standards dissolved in deuterated methanol were added to each sorbent cartridge to monitor sample recovery. The thermal desorption analyzer was a Model TD-2 Short Path Thermal Desorption Analyzer and a Model 961 Cryo-Trap (Scientific Instrument Services). The gas chromatograph was a Model 5890A Gas Chromatograph (Hewlett Packard, Palo Alto, CA). The mass spectrometer was a Packard Model 5971 Mass Selective Detector (Hewlett Packard). The thermal desorption unit was interfaced directly to the split/splitless injector of the gas chromatograph. The injector was operated in the splitless mode with a purge flow of approximately 5 mL/min. The trapping blank was a section of deactivated fused silica capillary tubing (15 cm x 0.53 mm) attached to the head of the chromatographic column. The chromatographic column was a fused silica capillary column coated with 100% methyl silicone (HP-1 ; length = 30 m; i.d. = 0.25 mm; film thickness = 0.25  $\mu$ m).

The sample was desorbed at 300°C for 10 min, and cryofocused onto the trapping blank at -80°C. The temperature of the analytical column was maintained at 0°C while the sample was desorbed. At the end of the desorption period, the temperature of the trapping blank was programmed to 300°C at a rate of approximately 15°C/sec. The column temperature was programmed from 0 to 250°C at a rate of 2.5°C/min. Mass spectra were obtained by scanning from m/z 40 to 600 at a rate of 1.2 scan/s. Components of each sample were identified by performing a search of a commercial mass spectral library (Wiley 275K Mass Spectral Library). When the quality of the match to the library spectra was low, components were identified by interpretation of the mass spectra.

The mass chromatograms from GC/MS analysis of gas samples taken from the passenger compartment before (blank) and during this test are shown in Plots J1 through J6. Tables J1 through J6 contain peak identifications for these analyses.

These analyses showed that combustion gases started to accumulate in the passenger compartment about 4 minutes post-ignition. The gaseous organic species in Samples 1 and 2

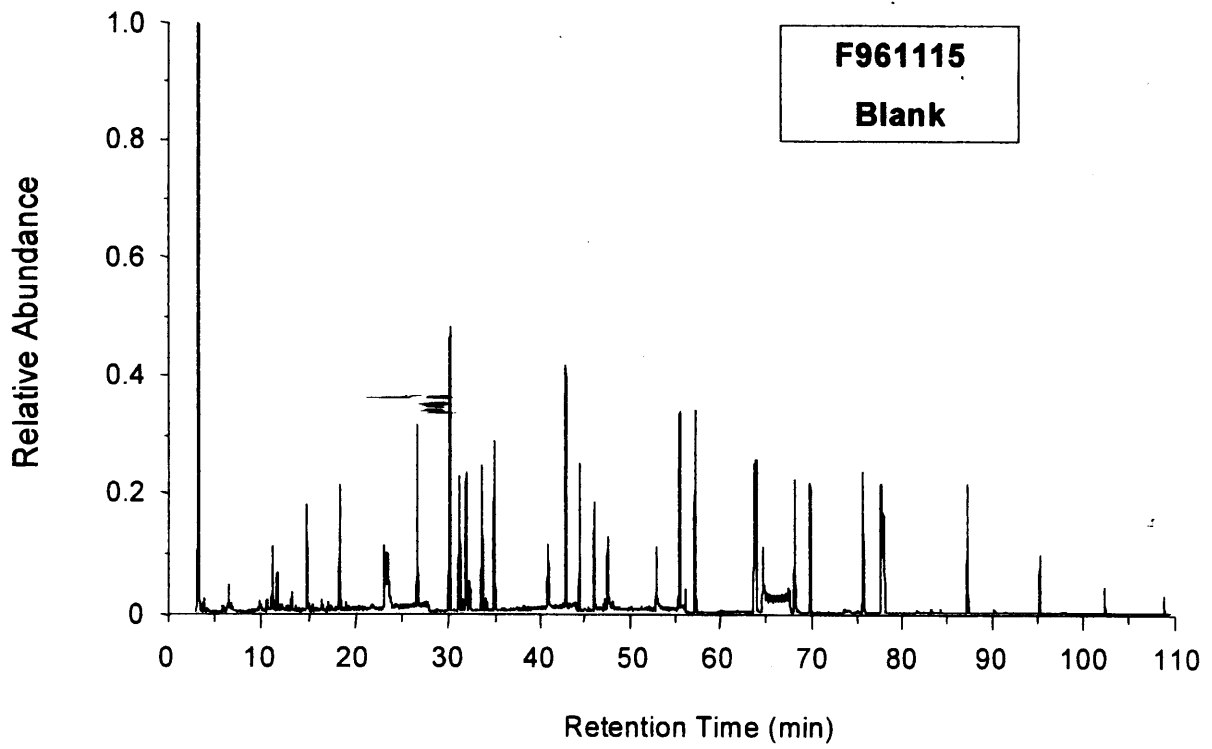
(Plots J2 and J2, and Tables J2 and J3, respectively) were similar to those detected in the blank (Plot J1 and Table J1).

Samples 3 and 4 (Plots J4 and J5, and Tables J4 and J5, respectively) contained compounds that were produced by thermal decomposition of natural rubber, ethylene-containing polymers, propylene containing polymers, and styrene-containing polymers. These compounds include 2-methyl-1,3-pentadiene (isoprene), 1,3-cyclopentadiene, 6-methyl-bicyclo[3.1.0]hexane, 4,4-dimethyl-1,2-pentadiene, benzene, toluene, ethylbenzene, xylenes, ethenylbenzene (styrene), and 1-methylethenyl)-benzene ( $\alpha$ -methylstyrene). These compounds were not detected in Sample 5.

Sample 5 also contained a number of fragments from silicon polymers (polymers containing dimethyl siloxane). The blank and Samples 1 through 4 contained a number of cyclic dimethylsiloxanes, which could be attributed to cryo-focusing column-bleed during the sample-desorption stage of the analysis. (Column-bleed is a term that describes the slow thermal decomposition of the stationary phase (bonded dimethylsiloxane) in the gas chromatographic column. This process causes low-level contamination of the mobile phase with a homologous series of cyclic dimethylsiloxanes, such as hexamethyl cyclotrisiloxane, which can be seen in the mass chromatograms of the Blank and all of the samples.) The presence of relatively large amounts of many siloxane species not detected in the Blank suggests they were produced by thermal decomposition of silicone polymers in the test vehicle during the fire.

A complex mixture of hydrocarbons in the in the range of  $C_{15}$  to  $C_{22}$  also was detected in the Samples 3 through 5 (Plots J4 through J6, and Tables J4 through J6). Pristane and phytane were positively identified in Sample 5. These compounds are so-called biomarkers for petroleum products, and their presence in Sample 5 suggests that that the gaseous hydrocarbons in the passenger compartment during the later stages of the fire were produced by vaporization of the hydrocarbon oils poured under the vehicle before the test.

Sample 5 also contained a number of common polymer additives. These included: diethyl phthalate, dibutyl phthalate, N-butyl-benzenesulfonamide, and BHT-aldehyde (an oxidation product of BHT).



Plot J1. Fire Test F961115. Mass chromatogram from GC/MS analysis of the blank acquired for 10 minutes before the test.

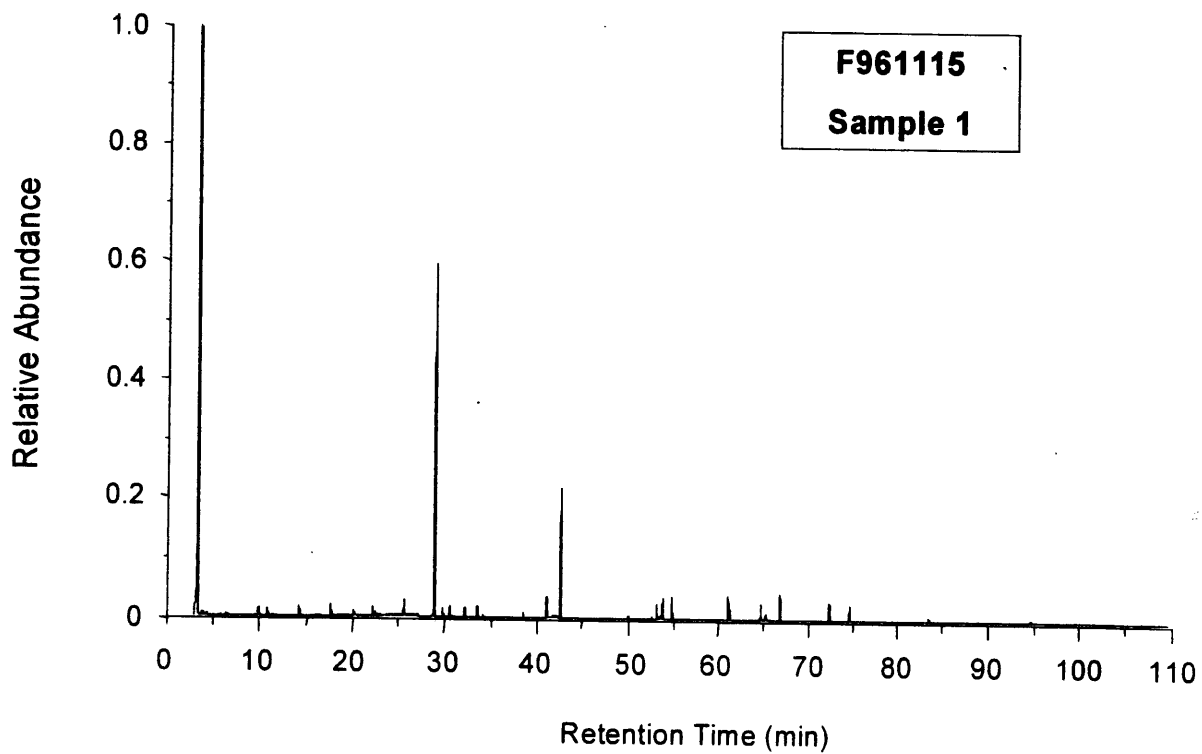
**Table J1**  
**Peak Identification for Fire Test F961115 Blank**

$t_R$	Compound	CAS Number
3.32	carbon dioxide	000124-38-9
3.80	difluorodimethylsilane	000353-66-2
6.23	n-pentane-d <sub>12</sub> (IS) <sup>1</sup>	002031-90-5
6.44	n-pentane	000109-66-0
9.28	2-methylpentane	000107-83-5
9.97	3-methylpentane	000096-14-0
10.53	n-hexane-d <sub>14</sub> (IS) <sup>1</sup>	021666-38-6
10.98	n-hexane	000110-54-3
12.37	methylcyclopentane	000096-37-7
13.82	benzene-d <sub>6</sub> (IS) <sup>1</sup>	001076-43-3
13.96	benzene	000071-43-2
17.05	n-heptane-d <sub>16</sub> (IS) <sup>1</sup>	033838-52-7
21.38	toluene-d <sub>8</sub> (IS) <sup>1</sup>	002037-26-5
21.65	toluene	000108-88-3
24.62	n-octane-d <sub>18</sub> (IS) <sup>1</sup>	017252-77-6
27.84	Hexamethylcyclotrisiloxane <sup>2</sup>	000541-05-9
28.79	benzene, ethyl-d <sub>10</sub> (IS) <sup>1</sup>	025837-05-2
29.14	benzene, ethyl-	000100-41-4
29.48	p-xylene-d <sub>10</sub> (IS) <sup>1</sup>	041051-88-1
29.80	p-xylene	000106-42-3
31.06	o-xylene-d <sub>10</sub> (IS) <sup>1</sup>	056004-61-6
31.45	m-xylene	000108-38-3
32.27	n-nonane-d <sub>20</sub> (IS) <sup>1</sup>	121578-11-8
37.74	phenol-d <sub>5</sub> (IS) <sup>1</sup>	004165-62-2
39.53	n-decane-d <sub>22</sub> (IS) <sup>1</sup>	016416-29-8
40.97	octamethylcyclotetrasiloxane <sup>2</sup>	000556-67-2
42.46	4-methylphenol-d <sub>8</sub> (IS) <sup>1</sup>	
43.84	2-methylphenol-d <sub>8</sub> (IS) <sup>1</sup>	
48.78	2,4-dimethyl phenol-d <sub>3</sub> (IS) <sup>1</sup>	
51.11	naphthalene-d <sub>8</sub> (IS) <sup>1</sup>	001146-65-2
52.67	n-dodecane-d <sub>26</sub> (IS) <sup>1</sup>	121578-12-9
58.61	n-tridecane-d <sub>28</sub> (IS) <sup>1</sup>	121578-12-9
58.78	1-methylnaphthlene-d <sub>10</sub> (IS) <sup>1</sup>	038072-94-5
59.49-62.08	methylsiloxane polymers <sup>2</sup>	000540-97-6
62.64	biphenyl-d <sub>10</sub> (IS) <sup>1</sup>	001486-01-7
64.18	n-tetradecane-d <sub>30</sub> (IS) <sup>1</sup>	

**Table J1, continued**  
**Peak Identification for Fire Test F961115 Blank**

$t_R$	Compound	CAS Number
69.45	n-pentadecane-d <sub>32</sub> (IS) <sup>1</sup>	036340-20-2
71.22	methylsiloxane polymer <sup>2</sup>	
71.51	methylsiloxane polymer <sup>2</sup>	
79.97	tetradecamethylcycloheptasiloxane	078979-94-3
87.29	methylsiloxane polymer <sup>2</sup>	

<sup>1</sup>Deuterated internal standard added to the sample before analysis. <sup>2</sup>Column-bleed introduced during cryo-focusing.



Plot J2. Fire Test F961115. Mass chromatogram from GC/MA analysis of Sample 1 acquired from -10:00 to 0:03 (min:sec) post-ignition.

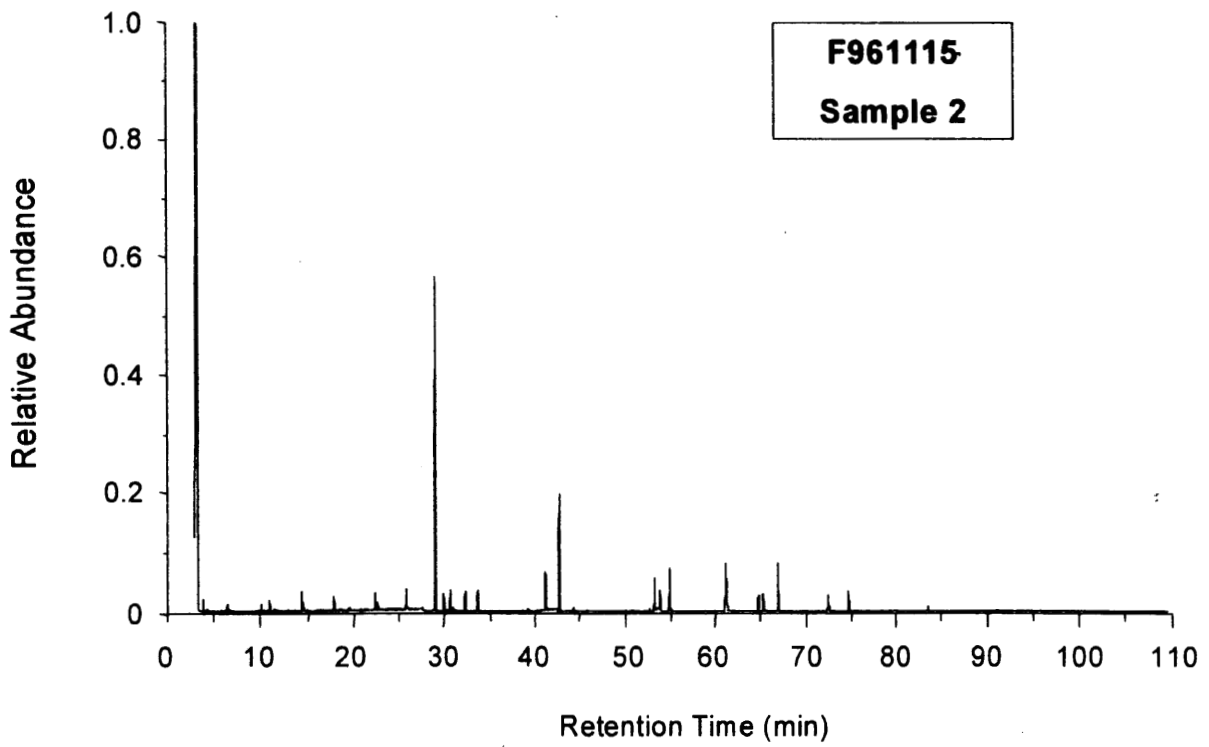
**Table J2**  
**Peak Identification for Fire Test F961115 Sample 1**

$t_R$	Compound	CAS No.
3.48	urea	000057-13-6
3.72	difluorodimethylsilane	000353-66-2
4.01	acetaldehyde	000075-07-0
4.15	1-propene, 2-methyl-	000115-11-7
6.15	n-pentane-d <sub>12</sub> (IS) <sup>1</sup>	002031-90-5
6.39	4(1H)-pyrimidinone	004562-27-0
9.55	6-methylene-bicyclo[3.1.0]hexane	054211-16-4
10.42	n-hexane-d <sub>14</sub> (IS) <sup>1</sup>	21666-38-6
10.89	n-hexane	000110-54-3
13.71	benzene-d <sub>6</sub> (IS) <sup>1</sup>	001076-43-3
13.85	benzene	000071-43-2
17.02	n-heptane-d <sub>16</sub> (IS) <sup>1</sup>	33838-52-7
21.35	toluene-d <sub>8</sub> (IS) <sup>1</sup>	002037-26-5
21.62	toluene	000108-88-3
24.63	n-octane-d <sub>18</sub> (IS) <sup>1</sup>	017252-77-6
27.84	hexamethylcyclotrisiloxane <sup>2</sup>	000541-05-9
28.65	ethylbenzene-d <sub>10</sub> (IS) <sup>1</sup>	025837-05-2
29.37	p-xylene-d <sub>10</sub> (IS) <sup>1</sup>	041051-88-1
29.69	p-xylene	000106-42-3
30.94	o-xylene-d <sub>10</sub> (IS) <sup>1</sup>	056004-61-6
32.27	n-nonane-d <sub>20</sub> (IS) <sup>1</sup>	121578-11-8
37.11	2-anthracenamine	000613-13-8
39.53	n-decane-d <sub>22</sub> (IS) <sup>1</sup>	016416-29-8
41.01	octamethylcyclotetrasiloxane <sup>2</sup>	000556-67-2
50.56	1,5-dihydro-1-(4-methoxyphenyl)-5,5-diphenyl)-2H-pyrrol-2-one	053774-23-5
51.10	naphthalene-d <sub>8</sub> (IS) <sup>1</sup>	001146-65-2
51.70	decamethylcyclopentasiloxane <sup>2</sup>	000541-02-6
52.69	n-dodecane-d <sub>26</sub> (IS) <sup>1</sup>	121578-12-9
58.66	n-tridecane-d <sub>28</sub> (IS) <sup>1</sup>	121578-12-9
58.79	1-methylnaphthlene-d <sub>10</sub> (IS) <sup>1</sup>	038072-94-5
62.21	docecamethylcyclohexasiloxane <sup>2</sup>	000540-97-6
62.67	biphenyl-d <sub>10</sub> (IS) <sup>1</sup>	001486-01-7
64.22	n-tetradecane-d <sub>30</sub> (IS) <sup>1</sup>	
69.50	n-pentadecane-d <sub>32</sub> (IS) <sup>1</sup>	036340-20-2
71.66	1,1,1,5,5,5-hexamethyltrisiloxane <sup>2</sup>	003555-47-3

**Table J2, continued**  
**Peak Identification for Fire Test F961115 Sample 1**

$t_R$	Compound	CAS No.
80.08	methyloxane polymer <sup>2</sup>	
90.72	bis(trimethylsilyl)-mercaptoacetic acid	

<sup>1</sup>Deuterated internal standard added to the sample before analysis. <sup>2</sup>Column-bleed introduced during cryo-focusing.

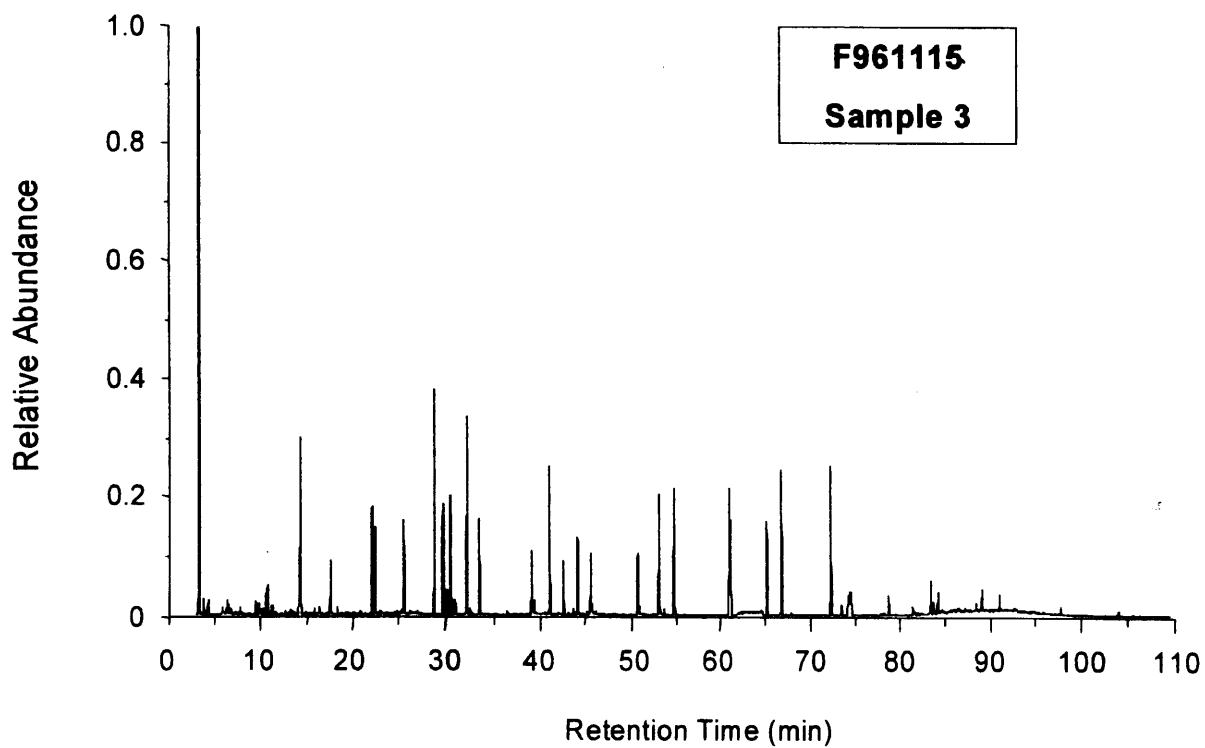


Plot J3. Fire Test F961115. Mass chromatogram from GC/MS analysis of Sample 2 acquired from 0:03 to 4:01 (min:sec) post-ignition.

**Table J3**  
**Peak Identification for Fire Test F961115 Sample 2**

$t_R$	Compound	CAS No.
3.59	difluorodimethylsilane	000353-66-2
4.01	1-propene, 2-methyl-	000115-11-7
6.09	n-pentane-d <sub>12</sub> (IS) <sup>1</sup>	002031-90-5
9.56	6-methylene-bicyclo[3.1.0]hexane	054211-16-4
9.87	4,4-dimethyl-1,2-pentadiene	026981-77-1
10.42	n-hexane-d <sub>14</sub> (IS) <sup>1</sup>	021666-38-6
10.88	n-Hexane	000110-54-3
13.72	benzene-d <sub>6</sub> (IS) <sup>1</sup>	001076-43-3
13.86	benzene	000071-43-2
17.04	n-heptane-d <sub>16</sub> (IS) <sup>1</sup>	033838-52-7
21.38	toluene-d <sub>8</sub> (IS) <sup>1</sup>	002037-26-5
21.65	toluene	000108-88-3
24.65	n-octane-d <sub>18</sub> (IS) <sup>1</sup>	017252-77-6
27.84	hexamethylcyclotrisiloxane <sup>2</sup>	000541-05-9
28.68	ethylbenzene-d <sub>10</sub> (IS) <sup>1</sup>	025837-05-2
29.06	ethylbenzene	000100-41-4
29.40	p-xylene-d <sub>10</sub> (IS) <sup>1</sup>	041051-88-1
29.72	p-xylene	000106-42-3
30.97	o-xylene-d <sub>10</sub> (IS) <sup>1</sup>	056004-61-6
32.29	n-nonane-d <sub>20</sub> (IS) <sup>1</sup>	121578-11-8
39.55	n-decane-d <sub>22</sub> (IS) <sup>1</sup>	016416-29-8
41.04	octamethylcyclotetrasiloxane <sup>2</sup>	000556-67-2
51.13	naphthalene-d <sub>8</sub> (IS) <sup>1</sup>	001146-65-2
51.72	decamethylcyclopentasiloxane <sup>2</sup>	000541-02-6
52.71	n-dodecane-d <sub>26</sub> (IS) <sup>1</sup>	121578-12-9
58.68	n-tridecane-d <sub>28</sub> (IS) <sup>1</sup>	121578-12-9
58.81	1-methylnaphthlene-d <sub>10</sub> (IS) <sup>1</sup>	038072-94-5
62.22	docecamethylcyclohexasiloxane <sup>2</sup>	000540-97-6
62.69	biphenyl-d <sub>10</sub> (IS) <sup>1</sup>	001486-01-7
64.25	n-tetradecane-d <sub>30</sub> (IS) <sup>1</sup>	
69.53	n-pentadecane-d <sub>32</sub> (IS) <sup>1</sup>	036340-20-2
71.68	1,1,1,5,5,5-hexmethyltrisiloxane <sup>2</sup>	003555-47-3
80.10	methylsiloxane polymer <sup>2</sup>	

<sup>1</sup>Deuterated internal standard added to the sample before analysis. <sup>2</sup>Column-bleed introduced during cryo-focusing.



Plot J4. Fire Test F961115. Mass chromatogram from GC/MS analysis of Sample 3 acquired from 4:01 to 9:03 (min:sec) post-ignition.

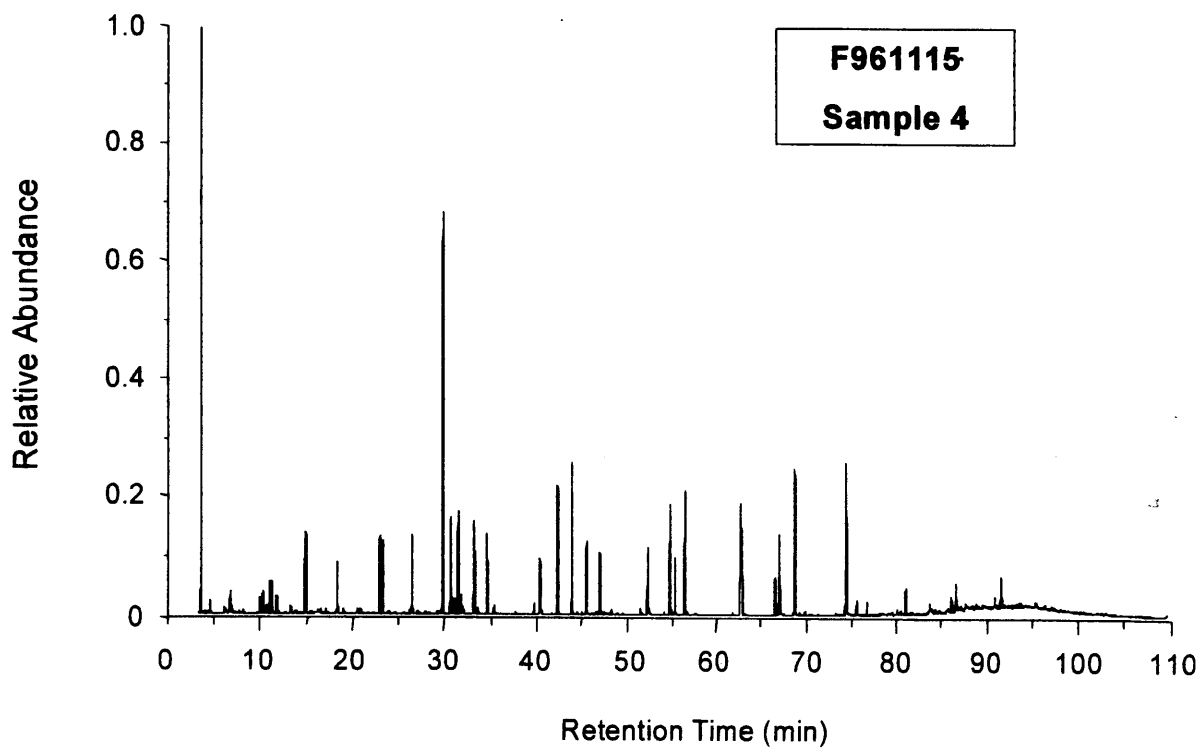
**Table J4**  
**Peak Identification for Fire Test F961115 Sample 3**

$t_R$	Compound	CAS No.
3.74	difluorodimethylsilane	000353-66-2
4.17	2-methyl-1-Propene	000115-11-7
6.17	n-pentane-d <sub>12</sub> (IS) <sup>1</sup>	002031-90-5
6.38	n-pentane	000109-66-0
6.53	2-methyl-1,3-butadiene (isoprene)	000078-79-5
7.50	1,3-cyclopentadiene	001574-40-9
9.17	6-methylene-bicyclo[3.1.0]hexane	054211-16-4
9.52	butanal	000123-72-8
9.88	4,4-dimethyl-1,2-pentadiene	026981-77-1
10.25	1-hexene	000592-41-6
10.42	n-hexane-d <sub>14</sub> (IS) <sup>1</sup>	021666-38-6
10.88	n-hexane	000110-54-3
13.73	benzene-d <sub>6</sub> (IS) <sup>1</sup>	001076-43-3
13.86	benzene	000071-43-2
17.00	n-heptane-d <sub>16</sub> (IS) <sup>1</sup>	033838-52-7
21.33	toluene-d <sub>8</sub> (IS) <sup>1</sup>	002037-26-5
21.61	toluene	000108-88-3
24.61	n-octane-d <sub>18</sub> (IS) <sup>1</sup>	017252-77-6
27.73	hexamethylcyclotrisiloxane <sup>2</sup>	000541-05-9
28.61	ethylbenzene-d <sub>10</sub> (IS) <sup>1</sup>	025837-05-2
28.98	ethylbenzene	000100-41-4
29.33	p-xylene-d <sub>10</sub> (IS) <sup>1</sup>	041051-88-1
29.65	p-xylene	000106-42-3
30.92	o-xylene-d <sub>10</sub> (IS) <sup>1</sup>	056004-61-6
31.02	ethenylbenzene (styrene)	000100-42-5
32.25	n-nonane-d <sub>20</sub> (IS) <sup>1</sup>	121578-11-8
37.64	phenol-d <sub>5</sub> (IS) <sup>1</sup>	004165-62-2
37.87	(1-methylethenyl)-benzene ( $\alpha$ -methylstyrene)	000098-83-9
39.51	n-decane-d <sub>22</sub> (IS) <sup>1</sup>	016416-29-8
40.97	octamethylcyclotetrasiloxane <sup>2</sup>	000556-67-2
42.46	4-methylphenol-d <sub>8</sub> (IS) <sup>1</sup>	
43.83	2-methylphenol-d <sub>8</sub> (IS) <sup>1</sup>	
48.81	2,4-dimethyl phenol-d <sub>3</sub> (IS) <sup>1</sup>	
51.10	naphthalene-d <sub>8</sub> (IS)	001146-65-2
52.69	n-dodecane-d <sub>26</sub> (IS) <sup>1</sup>	121578-12-9
58.64	n-tridecane-d <sub>28</sub> (IS) <sup>1</sup>	121578-12-9

**Table J4, continued**  
**Peak Identification for Fire Test F961115 Sample 3**

$t_R$	Compound	CAS No.
58.80	1-methylnaphthlene-d <sub>10</sub> (IS) <sup>1</sup>	038072-94-5
62.66	biphenyl-d <sub>10</sub> (IS) <sup>1</sup>	001486-01-7
64.22	n-tetradecane-d <sub>30</sub> (IS) <sup>1</sup>	
69.50	n-pentadecane-d <sub>32</sub> (IS) <sup>1</sup>	036340-20-2
70.59	pentadecane	000629-62-9
71.55	1,1,1,5,5,5-hexamethyltrisiloxane <sup>2</sup>	003555-47-3
75.58	hexadecane	000544-76-3
76.00-96.00	aliphatic hydrocarbons	

<sup>1</sup>Deuterated internal standard added to the sample before analysis. <sup>2</sup>Column-bleed introduced during cryo-focusing.



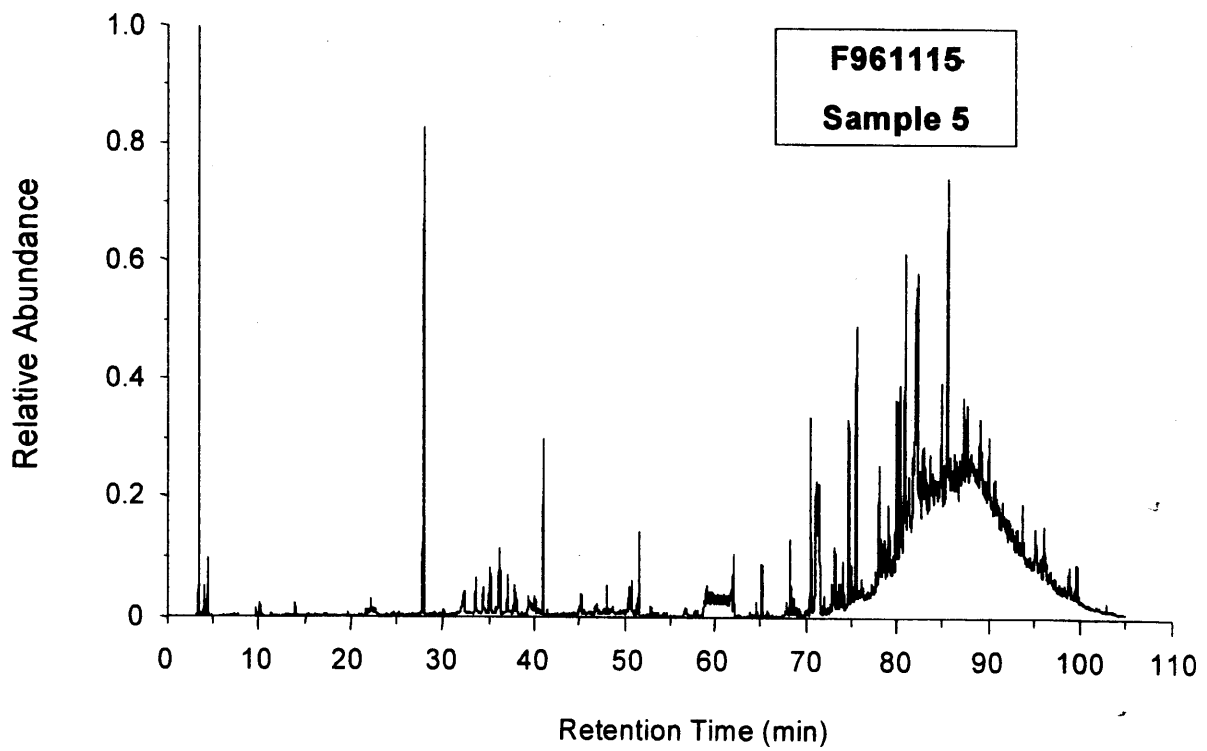
Plot J5. Fire Test F961115. Mass chromatogram from GC/MS analysis of Sample 4 acquired from 9:03 to 10:30 (min:sec) post-ignition.

**Table J5, continued**  
**Peak Identification for Fire Test F961115 Sample 4**

$t_R$	Compound	CAS No.
58.69	n-tridecane-d <sub>28</sub> (IS) <sup>1</sup>	121578-12-9
58.83	1-methylnaphthlene-d <sub>10</sub> (IS) <sup>1</sup>	038072-94-5
62.24	dodecamethylcyclohexasiloxane <sup>2</sup>	000540-97-6
62.71	biphenyl-d <sub>10</sub> (IS) <sup>1</sup>	001486-01-7
64.28	n-tetradecane-d <sub>30</sub> (IS) <sup>1</sup>	
69.54	n-pentadecane-d <sub>32</sub> (IS) <sup>1</sup>	036340-20-2
70.64	pentadecane	000629-62-9
71.69	1,1,1,5,5,5-hexmethyltrisiloxane <sup>2</sup>	
75.63	hexadecane	000544-76-3
70.00-92.00	aliphatic hydrocarbons	

**Table J5**  
**Peak Identification for Fire Test F961115 Sample 4**

$t_R$	Compound	CAS No.
4.19	2-methyl-1-propene	000115-11-7
5.67	2-methyl butane	000078-78-4
6.20	n-pentane-d <sub>12</sub> (IS) <sup>1</sup>	002031-90-5
6.41	n-pentane	000109-66-0
7.55	1,3-cyclopentadiene	001574-40-9
9.25	6-methylenebicyclo[3.1.0]hexane	054211-16-4
9.55	butanal	000123-72-8
9.94	3-methylpentane	000096-14-0
10.32	1-hexene	000592-41-6
10.49	n-hexane-d <sub>14</sub> (IS) <sup>1</sup>	021666-38-6
10.95	n-hexane	000110-54-3
12.37	methylcyclopentane	000096-37-7
13.78	benzene-d <sub>6</sub> (IS) <sup>1</sup>	001076-43-3
13.92	benzene	000071-43-2
17.07	n-heptane-d <sub>16</sub> (IS) <sup>1</sup>	033838-52-7
21.40	toluene-d <sub>8</sub> (IS) <sup>1</sup>	002037-26-5
21.67	toluene	000108-88-3
24.67	n-octane-d <sub>18</sub> (IS) <sup>1</sup>	017252-77-6
27.86	hexamethylcyclotrisiloxane <sup>2</sup>	000541-05-9
28.67	ethylbenzene-d <sub>10</sub> (IS) <sup>1</sup>	025837-05-2
29.04	ethylbenzene	000100-41-4
29.40	p-xylene-d <sub>10</sub> (IS) <sup>1</sup>	041051-88-1
29.71	p-xylene	000106-42-3
30.98	o-xylene-d <sub>10</sub> (IS) <sup>1</sup>	056004-61-6
31.05	ethenylbenzene (styrene)	000100-42-5
31.40	o-xylene	000095-47-6
32.30	n-nonane-d <sub>20</sub> (IS) <sup>1</sup>	121578-11-8
37.74	phenol-d <sub>5</sub> (IS) <sup>1</sup>	004165-62-2
39.56	n-decane-d <sub>22</sub> (IS) <sup>1</sup>	016416-29-8
41.05	octamethylcyclotetrasiloxane <sup>2</sup>	000556-67-2
42.54	4-methylphenol-d <sub>8</sub> (IS) <sup>1</sup>	
43.92	2-methylphenol-d <sub>8</sub> (IS) <sup>1</sup>	
48.88	2,4-dimethyl phenol-d <sub>3</sub> (IS) <sup>1</sup>	
51.18	naphthalene-d <sub>8</sub> (IS) <sup>1</sup>	001146-65-2
51.74	decamethylcyclopentasiloxane <sup>2</sup>	000541-02-6
52.74	n-dodecane-d <sub>26</sub> (IS) <sup>1</sup>	121578-12-9



Plot J6. Fire Test F961115. Mass chromatogram from GC/MA analysis of Sample 5 acquired from 10:30 to 11:43 (min:sec) post-ignition.

**Table J6**  
**Peak Identification for Fire Test F961115 Sample 5**

$t_R$	Compound	CAS No.
13.82	benzene	000071-43-2
27.83	hexamethylcyclotrisiloxane <sup>2</sup>	000541-05-9
32.29	unknown	
33.54	unknown	
34.34	methylsiloxane polymer	
35.10	methylsiloxane polymer	
36.20	methylsiloxane polymer	
37.11	methylsiloxane polymer	
37.81	methylsiloxane polymer	
38.01	methylsiloxane polymer	
40.97	octamethylcyclotetrasiloxane <sup>2</sup>	000556-67-2
50.51	methylsiloxane polymer	
50.63	methylsiloxane polymer	
50.79	methylsiloxane polymer	
51.66	decamethylcyclopentasiloxane <sup>2</sup>	000541-02-6
58-62	methylsiloxane polymers	
61.16	dodecamethylcyclohexasiloxane <sup>2</sup>	000540-97-6
62.71	biphenyl-d <sub>10</sub> (IS) <sup>1</sup>	001486-01-7
64.28	n-tetradecane-d <sub>30</sub> (IS) <sup>1</sup>	
65.29	n-tetradecane	
69.54	n-pentadecane-d <sub>32</sub> (IS) <sup>1</sup>	036340-20-2
70.64	pentadecane	000629-62-9
71.69	1,1,1,5,5,5-hexamethyltrisiloxane <sup>2</sup>	
73.27	1,2benzenedicarboxylic acid, diethyl ester	000084-66-2
75.64	n-hexadecane	000544-76-3
80.42	n-heptadecane	000629-78-7
80.93	2,6,10,14-tetramethylpentadecane (pristane)	001921-70-6
82.09	2,6-di(t-butyl)-4-hydroxybenzaldehyde (BHT-aldehyde)	
82.15	N-butyl-benzenesulfonamide	000362-84-2
85.60	2,6,10,14-tetramethylhexadecane (phytane)	000638-36-8
90.04	1,2-benzenedicarboxylic acid, dibutyl ester	000084-74-2

<sup>1</sup>Deuterated internal standard added to the sample before analysis. <sup>2</sup>Column-bleed introduced during cryo-focusing